The Electrochemical Leaf:

Driving and Observing

Nanoconfined Enzyme Cascades



Giorgio Morello

Trinity Term 2020

A Thesis submitted for the degree of

Doctor of Philosophy, University of Oxford

© Giorgio Morello 2020

A Rosalba

ABSTRACT

The co-localisation of cooperating enzymes within nanozones is crucial in biological catalytic processes to ensure fast and efficient catalysis. The Electrochemical Leaf is a novel electrode which mimics that principle. Entrapping two cooperating enzymes, Ferredoxin $NADP^+$ reductase (FNR) and a NADPH-dependent dehydrogenase, within the nanopores of an Indium-Tin-Oxide (ITO) electrode produces a massive catalytic enhancement. Upon application of a small potential FNR catalyses the interconversion of $NADP^+$/NADPH, while the NADP(H)-dependent dehydrogenase uses the produced cofactor to catalyse the oxidation or reduction of a substrate. By nanoconfining the two catalysts the effective concentration of the enzymes is greatly increased, and diffusion distances of the cofactor minimized. The system makes it possible to drive and monitor complex biotransformations. This Thesis shows that by incorporating the NADPH-dependent Malic Enzyme (ME), the resulting electrode, (FNR+ME)@ITO/Support, is able to drive reductive CO_2 incorporation into pyruvate (C3) forming malate (C4). The favourable catalysis within the electrode pores allows for the design of a system which mimics biological oxygenic photosynthesis by incorporating a PEC-PV system with a photoanode in conjunction with a 0.5 V Silicon solar cell. For the first time the Electrochemical Leaf was exploited to drive multi-enzyme cascade reactions where the overall rate is measured directly as an electric current through the FNR-NADPH-dependent dehydrogenase couple. As a proof of concept, the reversible amination of pyruvate (C3) to L-aspartate (C4) was investigated by entrapping FNR, ME, carbonic anhydrase, fumarase and L-aspartate ammonia

lyase. The Electrochemical Leaf can be coupled to any natural or artificial multienzyme cascade provided one enzyme is NAD(P)(H) dependent. The implications are numerous for synthesis, biosensing and fundamental investigation of systems catalysis.

ACKNOWLEDGEMENTS

I would like to thank Prof. Fraser Armstrong for giving me the great opportunity of carrying out research in his lab, for constantly showing encouragement and support to me and my work.

Thanks to all the Armstrong group throughout these 3.5 years for scientific and non-scientific support. It was a great adventure and you made this journey lighter! Importantly thanks to the people actively involved in the Friday discussions Clare, Bhavin, Stephen, Non and Koroush. Special thanks to Clare, Bhavin and Non for sharing several late evenings in the lab, weekends and to be always available for questions and help. Special mention to Clare for all the food, help and being a very good friend. Many thanks to Kavita for smiling every day, and thanks to the rest of the people in the group Lei, Beichen and Ryan. Thanks to Liyun for your constant enthusiasm and for being a great travel company in LA. I will never forget your peculiar way of taking pictures. Oliver, Matteo and Leonie it was great to have you here in the Armstrong group!

To the proofreaders of this Thesis and their commitment even during difficult times, thank you Clare, Non, Sven, Fraser and Bhavin. Your suggestions were very helpful and crucial.

Thanks to Sven for literally everything and everyday support. Everything is simpler with you, even pandemic outbreaks and PhD.

Thanks to my parents for encouragements since I was a little child and to the rest of the family. The funding support was essential so many thanks to the Wadham College for awarding me the Oxford-Richards Graduate Scholarship and to Fraser for a further funding extension pre- and during pandemic. Special thanks also to

Terry and her electrochemical cells, without you this project would have been much harder.

PUBLICATIONS

- **G. Morello**, C. F. Megarity, F. A. Armstrong. The power of electrified nanoconfinement for energising, controlling and observing long enzyme cascades. *Nat. commun*, **12**, 340 (2021).

- C. F. Megarity, B. Siritanaratkul, R. A. Herold, **G. Morello,** F. A. Armstrong. Electron flow between the worlds of Marcus and Warburg. *J. Chem. Phys*, **153**, 225101 (2020).

- **G. Morello**, B. Siritanaratkul, C. F. Megarity, F. A. Armstrong. Efficient Electrocatalytic CO_2 Fixation by Nanoconfined Enzymes via a C3-to-C4 Reaction That Is Favored over H_2 Production. *ACS Catal.* **9**, 11255–11262 (2019).

- C. F. Megarity, B. Siritanaratkul, B. Cheng, **G. Morello**, L. Wan, A. J. Sills, R. S. Heath, N. J. Turner, F. A. Armstrong. Electrified Nanoconfined Biocatalysis with Rapid Cofactor Recycling. *ChemCatChem*, **11**, 5662–5670 (2019).

- C. Megarity, B. Siritanaratkul, R. Heath, L. Wan, **G. Morello**, S. Fitzpatrick, R. Booth, A. Sills, A. Robertson, J. Warner, N. Turner, F. A. Armstrong. Electrocatalytic Volleyball: Rapid Nanoconfined Nicotinamide Cycling for Organic Synthesis in Electrode Pores. *Angew. Chemie Int. Ed.* **58**, 4948–4952 (2019).

ABBREVIATIONS

A	Absorbance
A	Area
ADH	Alcohol dehydrogenase
AP	Artificial photosynthesis
AspA	L-aspartate amino-lyase
ATP	Adenosine triphosphate
BDD	Boron doped diamond
BV	Benzyl viologen
C	Capacitance
CA	Carbonic anhydrase
CAR	Carboxylic acid reductase
CB	Conduction band
CE	Counter electrode
CNT	Carbon nanotubes
CODH	Carbon monoxide dehydrogenase
CRISPR	Clustered regularly interspaced short palindromic repeats
CV	Cyclic voltammetry
FRET	Förster resonance energy transfer
dd	Doublet of doublets
dNTPs	Deoxyribonucleotide triphosphate
ds	Double strand
DSSC	Dye-sensitised solar cell
DTT	Dithiothreitol
E	Potential
E1	Enzyme 1
E2	Enzyme 2
E2A	Enzyme 2A
E3	Enzyme 3
E4	Enzyme 4
E_{app}	Potential applied
EDTA	Ethylenediaminetetraacetic acid
ee	Enantiomeric excess
E_F	Fermi level
E_{fb}	Flat band potential
E_g	Band gap

EPD	Electrophoretic deposition
epPCR	Error prone PCR
F	Faraday constant
FACS	Fluorescence-activated cell sorting
FAD	Flavin adenine dinucleotide
Fd	Ferredoxin
FDH	Formate dehydrogenase
FE	Faradaic efficiency
$FE_{coll\ eff}$	Collection efficiency
FNR	Ferredoxin $NADP^+$ reductase
FTO	Fluorine-doped tin oxide
FumC	Fumarase C from *E. coli*
G3P	Glyceraldehyde 3-phosphate
GC	Gas chromatography
g-C_3N_4	Graphitic carbon nitride
GDH	Glucose dehydrogenase
GHG	Greenhouse gas
GLDH	Glutamate dehydrogenase
GMO	Genetically modified organism
GOx	Glucose oxidase
h^+	Hole
Hase	Hydrogenase
HIV	Human immunodeficiency viruses
HOMO	Highest occupied molecular orbital
HPLC	High Performance Liquid Chromatography
HRP	Horse radish peroxidase
i	Current
IDH	Isocitrate dehydrogenase
IPTG	Isopropyl β- d-1-thiogalactopyranoside
ITO	Indium-doped tin oxide
J	Current density
KRED	Ketoreductase
LB	Lysogeny broth
LDH	Lactate dehydrogenase
LHC	Light harvesting complex
LSV	Linear sweep voltammetry
MDH	Malate dehydrogenase
ME	Malic enzyme
Med	Mediator

MFC	Mass flow controller
MO	Metal oxide
MOF	Metal organic framework
MSD	Mean square displacement
MV	Methyl viologen
MW	Molecular weight
N	Number of moles
NADP	Nicotinamide adenine dinucleotide phosphate
NMR	Nuclear magnetic resonance
OEC	Oxygen evolving complex
OER	Oxygen evolving reaction
ORF	Open reading frame
PCR	Polymerase chain reaction
pdb	Protein data bank
PEC	Photoelectrochemical
PEP	Phosphoenolpyruvate
PFE	Protein film electrochemistry
PGE	Pyrolytic graphitic electrode
Pheo	Pheophytin
pI	Isoelectric point
PQ	Plastoquinone
PS	Polystyrene
PSI	Photosystem I
PSII	Photosystem II
Pt	Platinum
PV	Photovoltaics
Q	Charge passed
Q_{col}	Charge at the collector
QD	Quantum dots
Q_{gen}	Charge at the generator
R	Gas constant
RC	Reaction centre
RE	Reference electrode
RedAm	Reductive aminase
RHE	Reversible hydrogen electrode
rt	Room temperature
RubisCO	Ribulose-1,5-bisphosphate carboxylase/oxygenase
SCE	Standard calomel electrode
SDS	Sodium dodecyl sulfate

SEM	Scanning electron microscopy
sgRNA	Single guided RNA
SHE	Standard hydrogen electrode
ss	Single strand
T	Temperature
TEA	Triethylamine
Ti foil	Titanium foil
TMSP	Trimethylsilylpropanoic acid
TOF	Turnover frequency
TST	Transition theory
TTN	Total turnover number
v	Scan rate
VB	Valence band
WE	Working electrode
z	Number of electrons
ZF	Zinc fingers
ε	Extinction coefficient
τ-values	Tau-values

TABLE OF CONTENTS

Abstract IV

Acknowledgements VI

Publications VIII

Abbreviations IX

Table of Contents XIII

Chapter I 1

1. Introduction 2

1.1. The Energy Problem 2

1.2. Oxygenic Photosynthesis 3

1.3. Biotechnological Solutions 7

1.4. Artificial Photosynthesis 9

1.5. Biocatalysis 19

1.5.1. Cofactor regeneration systems 21

1.5.2. Whole cell cofactor regeneration systems 21

1.5.3. Enzymatic based cofactor regeneration methods 22

1.5.4. Electrochemical methods for cofactor regeneration 24

1.6. The electrochemical leaf 27

1.6.1. Ferredoxin $NADP^+$ reductase 27

1.6.2. Electrochemical results using the electrochemical leaf 32

1.6.3. The nanoconfinement effect 38

1.7. Outline 43

Chapter II 45

2. Introduction of the malic enzyme in the electrochemical leaf 46

2.1. Abstract 46

2.2. Introduction 47

2.3. Aim of the Chapter 51

2.4. Results and Discussion 52

2.4.1. Cloning and expression of MaeB 52

2.4.2. Electrochemical results 56

2.4.2.1. Optimizing conditions 56

2.4.2.2. Reductive carboxylation 65

2.4.2.3. CO_2 titration 67

2.4.2.4. Product analysis 70

2.4.2.5. Bulk electrolysis and nanoconfinement of enzymes 72

2.5. Conclusion 83

Chapter III 87

3. Light-driven reductive carboxylation 88

3.1. Abstract 88

3.2. Introduction 89

3.3. Aim of the Chapter 93

3.4. Results and Discussion 94

3.4.1. Preparation of the photoanode and PEC results 94
3.4.2. Light-driven $NADP^+$ reduction 99
3.4.3. Development of a *Z*-scheme without external bias 110
3.4.4. System with a single light absorber 110
3.4.4.1. Assembly of a Z-scheme 113
3.4.5. Oxygen detection 116
3.4.6. Light-driven reductive carboxylation 120
3.4.7. Faradaic efficiency-dependence on potential applied 128
3.5. Conclusion 131
Chapter IV 133
4. Wiring nanoconfined cascades: a five-enzyme cascade 134
4.1. Abstract 134
4.2. Introduction 135
4.3. Aim of the Chapter 142
4.4. Part 1: Results and Discussion 143
4.4.1. The 5-enzyme cascade in action 143
4.4.2. The cascade model and nanoconfinement of intermediates 146
4.4.3. Reversible reduction and oxidation: product analysis 151
4.5. Part 1: Conclusion 160
4.6. Part 2: The 5-enzyme cascade, further results 162
4.6.1. 5-enzyme cascade in the unbuffered condition and the role of CA in the downstream direction. 163

4.6.2. Reductive amination catalysed by the 5-enzyme cascade using smaller, catalytic amounts of $NADP^+$. 165

4.6.3. The role of CA and nanoconfinement in the upstream direction. 167

4.6.4. The gradual current growth in the upstream direction 169

4.6.5. Varying enzyme ratios 173

4.6.6. Steady state kinetic data for ME, FumC and AspA..... 180

4.6.7. Comparison between the electrified nanoconfined cascade and the cascade in solution 182

4.7. Part 2: Conclusions 189

Chapter V 192

5. Exploitation of the electrochemical leaf as a sensor for biocatalyst discovery and evolution..... 193

5.1. Abstract..... 193

5.2. Introduction 194

5.3. Aim of the Chapter 198

5.4. Results and Discussion..... 199

5.4.1. Further results 204

5.5. Conclusion and future perspective..... 208

Chapter VI 210

6.1 Conclusions..... 211

6.1.1 Introduction of the malic enzyme in the electrochemical leaf..... 212

6.1.2 The light driven reductive carboxylation 213

6.1.3 Wiring nanoconfined cascades: a five-enzyme cascade 213
6.1.4 Exploitation of the electrochemical leaf as a sensor for biocatalyst discovery and evolution 214
6.2 Future perspectives 215
6.2.1 Concentration of E2, E3 and product inhibition 215
6.2.2 Generation of pores of controlled size 217
6.2.3 Scale-up of the system and use of cell lysate to drive synthesis ... 219
6.2.4 Development of a directed evolution system 220
6.2.5 Using the sensor for metabolite detection 221
Chapter VII 223
7 Electrochemical theory 224
7.1.1 Protein film electrochemistry 224
7.1.2 Electrochemical setup 226
7.1.3 Nonfaradaic current 228
7.1.4 Faradaic current 229
7.1.5 Cyclic voltammetry 231
7.1.6 Catalytic current 235
7.1.7 Reversibility 239
7.1.8 Chronoamperometry 240
7.1.9 Diffusion 241
7.2 Semiconductor theory 243
7.3 Experimental methods 249

7.3.1 Molecular Biology 249
7.3.1.1 ME cloning 249
7.3.1.2 Ligation independent cloning 250
7.3.1.3 AspA cloning 250
7.3.1.4 Transformation 251
7.3.1.5 Miniprep 251
7.3.1.6 ME expression and purification 252
7.3.1.7 FNR expression and purification 253
7.3.1.8 AspA expression and purification 254
7.3.1.9 FumC expression 254
7.3.1.10 Protein concentration: Bradford method 255
7.3.1.11 SDS gel 255
7.3.1.12 Solution assay 255
7.3.2 Electrode preparation 257
7.3.2.1 Cathode preparation 257
7.3.2.1.1 Electrophoretic deposition (EPD) 257
7.3.2.1.2 PGE electrodes 258
7.3.2.1.3 Introduction of controlled-size pores (Doctor blade) 258
7.3.2.2 Photoanode preparation 259
7.3.2.2.1 Hematite 259
7.3.2.2.2 Bismuth Vanadate 259

7.3.2.3 FNR loading 260
7.3.2.4 Loading of 4-enzyme and 5-enzyme cascade 260
7.3.3 Electrochemistry of the cathode: 261
7.3.3.1 Cyclic voltammetry 261
7.3.3.2 Chronoamperometry 262
7.3.3.3 Solution exchange 262
7.3.3.4 CO_2 titration 263
7.3.3.5 Rotation dependence experiment with the five-enzyme cascade…. ..... ….264
7.3.4 Nuclear magnetic resonance (NMR) 264
7.3.5 Linear sweep of the photoanode 265
7.3.6 Light-driven NADPH production 265
7.3.7 Light-driven reductive carboxylation 266
7.3.8 Oxygen and hydrogen gas detection 266
7.3.9 Faradaic efficiency dependence on the applied potential 267
7.3.10 Development of a sensor for biocatalyst discovery 268
7.3.10.1 Preparation of cell lysate 268
7.3.10.2 Electrochemical experiments with the proposed sensor 268
7.3.11 Light-driven $NADP^+$ reduction using FNR-g-C_3N_4 composite .. 269
Appendix 270
A.1. Cloning and purification of AspA 271
A.2. Cloning and purification of Fumarase 274

A.3. Malate oxidative decarboxylation in the absence of CO_2 280

References 281

Chapter I

1. Introduction

1.1. The Energy Problem

Of the most alarming challenges facing humanity today are environmental pollution and climate change. Fossil fuel emissions of particulates and greenhouse gases (GHG), such as carbon dioxide (CO_2), sulfur dioxide (SO_2), nitrogen oxide (NO) and carbon monoxide (CO) is generally considered to be one of the causes of global temperature rise in recent decades.[1,2] Fossil fuels are currently used in each sector of society, from transport, which accounts for 25%, to agriculture and industry.[2] Moreover, as the population is predicted to increase, especially in developing countries, the energy requirement will follow, thus requiring higher fossil fuel consumption, unless a suitable alternative can be found.[3] Currently, 92% of the human population is living in places with an air quality declared unsafe.[4] That is alarming, as air quality is considered responsible for the death of over seven million people per year worldwide.[4] The link between pollution increase and climate change is generally accepted by the scientific community.[4] Thus, in order to meet the limit of a 1.5°C temperature increase above pre-industrial levels, as decided in the Paris Agreement,[5] significant actions have to be taken as a matter of urgency. It is projected that if the temperature increase is being kept below that limit, damages linked to health and the economy will be reduced.

Polluting energy systems that provide energy sources and chemical feedstocks are one of the main sources of GHG and particulate generation.[4] New energy sources and chemical production methods must be developed to supply current demands and to avoid what is generally referred to as ‘happy degrowth’ (moving into a temporary degrowth phase).[6] In terms of renewable electricity, solar

energy is one of the most promising technologies thanks to the very low cost of Si-solar cells ($1.8 in 2010[7]) and their high efficiency (>40%[8,9]). Photovoltaic (PV) technology has seen an exponential increase in efficiency from 1% in 1940 to 40% in 2008 and a decrease in cost, from $100 per watt in the 1970's to $0.21 per watt as of 2019.[7,10] However, currently the main issue with PV technology or any other renewable energy technology is their intermittent nature, which then necessitates storage of the energy harnessed, either in a battery or in a fuel to ensure continuous supply. This is particularly important during night and in the winter months and in areas of the world where sunlight is extremely scarce.[11]

Storing solar energy is the key to ensure the transition to a renewable energy-based society. If we could gather all the solar illumination which is reaching the earth in 1 hour we would have enough energy to sustain the whole current world consumption for a year.[12,13] Batteries could give a solution to the problem of energy storage. However, Nature provides a different way for storage; she has evolved a process, oxygenic photosynthesis, to store solar energy efficiently using the extremely abundant feedstocks water and CO_2.

1.2. Oxygenic Photosynthesis

The evolution of oxygenic photosynthesis had an enormous impact on the earth because of the release of oxygen in the atmosphere, which allowed for the development of life as we know it. Oxygenic photosynthesis is a metabolic process which occurs in plants and green algae inside organelles called chloroplasts or in the cyanobacterial membrane.[14] The process is divided into light-dependent and light-independent reactions. The chloroplast matrix, known as the stroma, contains the enzymes responsible for the light-independent reactions. Additionally, the

chloroplast and cyanobacteria have a complex set of membranes that form structures called thylakoids.[15] Thylakoids are the core of the light-dependent reactions as they contain the key pigments and proteins (see below) required for the photochemistry.[16] During oxygenic photosynthesis water is effectively oxidized to O_2 while CO_2 is reduced to carbohydrates (Equation 1.1)[14].

$$H_2O + CO_2 \rightarrow O_2 + C_nH_{2n}O_n \quad (1.1)$$

The thylakoid membrane is rich in enzymes and pigments containing proteins, such as light harvesting complexes (LHC) used for light absorption (antenna).[17] Their role is to absorb light energy and to transfer the excitation energy to the reaction centres (RCs), where light is transformed into chemical energy.[18] In plants and cyanobacteria the RCs are held within two enzymes, Photosystem II (PSII) and Photosystem I (PSI). [19] PSII is a dimeric protein of 700 kDa molecular weight and is found bound to the thylakoid membrane. Each monomer of PSII contains 20 protein subunits, including chlorophyll binding proteins; chlorophylls, plastoquinones (PQ), carotenoids and the Mn_4Ca cluster where water oxidation takes place.[20] Within PSII, the redox reactions are contained in a heterodimer of large proteins called D1 and D2. Importantly, the protein D1 contains P680 RC, which is the chlorophyll responsible for the charge separation within PSII.[21] The heterodimer performs water oxidation at the lumen side and reduces the PQ pool (equation 1.2).[16]

$$2H_2O + 2PQ \rightarrow 2O_2 + 2PQH_2 \quad (1.2)$$

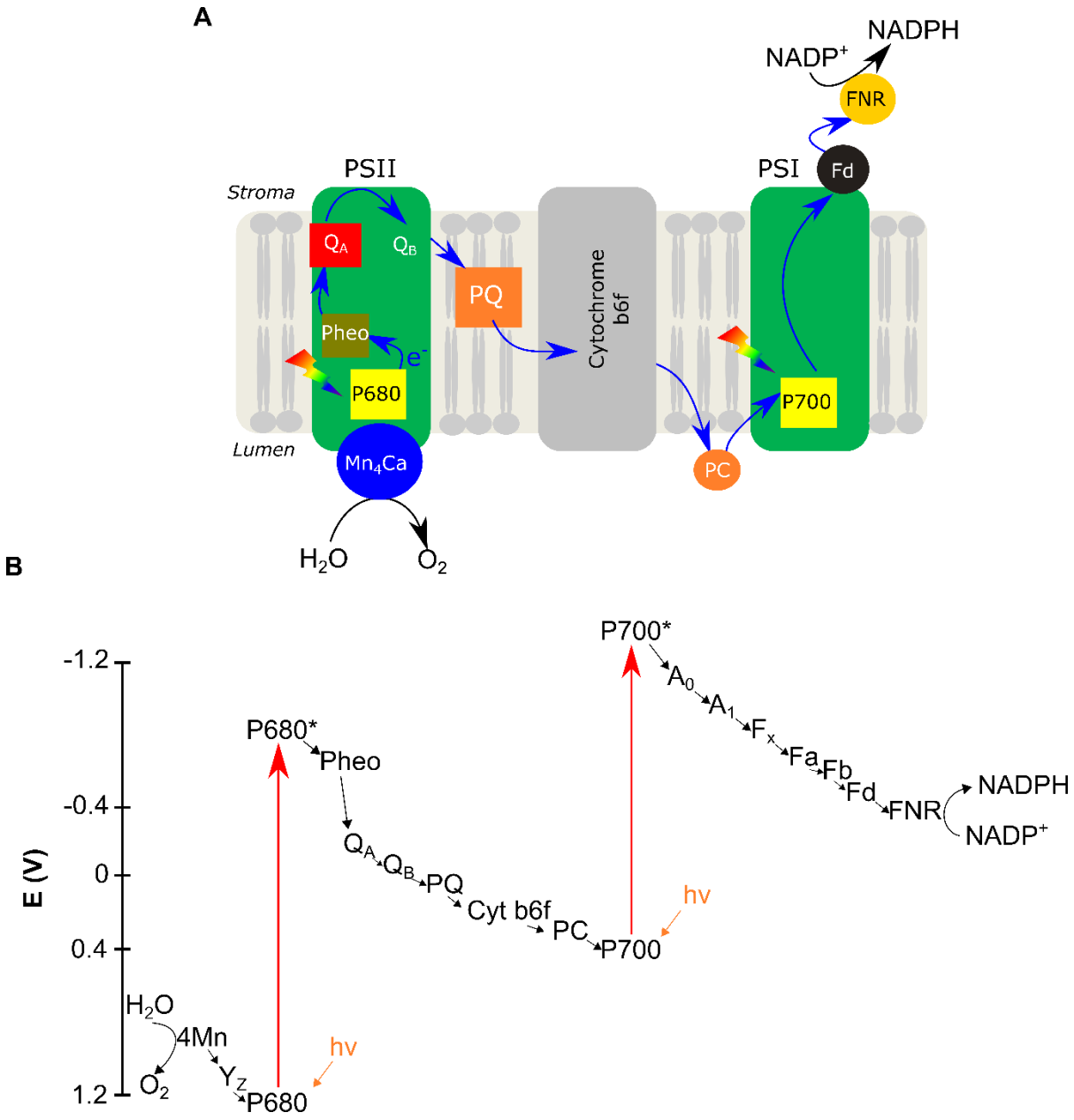


Figure I-1. Z-scheme of oxygenic photosynthesis. A. Light reactions of photosynthesis occur in the thylakoid membrane in plants, cyanobacteria and algae. PSII and PSI are the two main proteins responsible for the light reaction. PSII catalyses the oxidation of water through the oxygen-evolving complex (OEC), which is a Mn_4Ca cluster responsible for replenishing the hole (h^+) in the reaction centre. The excited electron from P680* can reduce Pheophytine, Q_A and then Q_B. After receiving two electrons, Q_B leaves the PSII binding site and merges into the PQ pool, which indirectly replenishes the hole left in PSI after charge separation. The excited electron of PSI mediates reduction of Fd, via several intermediate electron acceptors (A_0 to F_b). Fd is the natural electron donor for FNR to catalyse $NADP^+$ reduction. **B**. Z-scheme of oxygenic photosynthesis. A second light absorber is needed to reduce the terminal electron acceptor $NADP^+$, because the reduction potential of P680* is not negative enough to reduce the nicotinamide cofactor.

Figure I-1 describes the mechanism of oxygenic photosynthesis. Upon light excitation, the antenna transfers the excitation to the reaction centre, where charge separation occurs. The resulting radical P680* is able to reduce Pheophytin (Pheo), which then transfers the electron to the primary quinone Q_A. Q_A then reduces Q_B, which can accept two electrons, and leaves the PSII-binding site after protonation to enter the PQ pool in the thylakoid lumen.[22] Reduced Q_B must leave the PSII binding site to allow for the light reactions to proceed. The hole left in P680 generates the species $P680^+$, which is the most oxidizing species known in biology with a reduction potential of +1.25 eV.[21] $P680^+$ is able to oxidize $TyrZ^{\bullet}$,[23,24] which receives an electron from the Mn_4Ca cluster following water oxidation. The time requirements of the above reactions are in the picosecond range, where the fastest step is the reduction of Pheo (3–4 ps), followed by the second reduction event (reduction of Q_A, 300 ps). The slowest reaction is the step required for Q_B to leave PSII and merge the PQ pool (ms range).[20,23]

The excited state generated in PSII is not negative enough to drive CO_2 reduction. Therefore, a second light absorber – PSI – is required, which absorbs light to trigger a reduction cascade which ultimately leads to the reduction of a small iron-sulfur cluster-containing protein – ferredoxin (Fd). The hole left in PSI is replenished through the PQ pool that reduces cytochrome b6f, plastocyanin and then $P700^+$ (**Figure I-1-A**). The resulting scheme is commonly known as Z-scheme (**Figure I-1-B**).[25] Ferredoxin is the natural redox partner of Ferredoxin $NADP^+$ reductase (FNR), which catalyses the reduction of the terminal electron acceptor, the nicotinamide adenine dinucleotide phosphate, $NADP^+$, to NADPH. Along with adenosine triphosphate (ATP), NADPH is required for the reactions of the Calvin cycle. Adenosine triphosphate is produced by ATP synthase which uses a proton

gradient across the thylakoid membrane as the driving force. Through the reactions of the Calvin cycle, CO_2 is reduced to carbohydrates by ribulose biphosphate carboxylase (RubisCO) in the stroma. This enzyme incorporates CO_2 into ribulose-1,5-biphosphate (5 carbons) to generate a hexose-intermediate (6 carbons) which hydrolyses to two molecules of 3-phosphoglycerate (2×3 carbons).[14,16] The byproduct of the cycle, glyceraldehyde-3-phosphate (G3P) is then used to generate starch, sucrose and ribulose-1,5-biphosphate which is re-introduced into the Calvin cycle.[26] The Calvin cycle is also referred to as the light-independent reactions of photosynthesis. Equations below show the relation between light-dependent (1.3) and light-independent reactions (1.4) in oxygenic photosynthesis.

Light-dependent:

$$H_2O + NADP^+ + ADP + P_i + h\nu \rightarrow O_2 + NADPH + H^+ + ATP \qquad (1.3)$$

Light-independent:

$$3CO_2 + 6NADPH + 9ATP + H^+ \rightarrow G3P + 6NADP^+ + 9ADP + 8P_i + H_2O \qquad (1.4)$$

1.3. Biotechnological Solutions

Mimicking or using photosynthesis is of great interest in the field of future energy technologies because its principles allow for the storage of solar energy in the form of an energy carrier. By using an energy carrier-based system, a more sustainable and fossil fuel-independent society could be built. Photosynthetic microorganisms such as algae and cyanobacteria can be used as their wild type (*wt*) forms, or alternatively, genetically engineered for the efficient conversion of solar energy and production of fine chemicals.[13,27] A typical example is in the use of the monocellular model organism *Chlamydomonas reinhardtii*, a green alga, for

the production of hydrogen gas. Green algae can typically express an [FeFe]-hydrogenase (*e.g. C.r* HydA1), to reduce protons to hydrogen gas at very high turnover numbers.[28] However, this hydrogenase is extremely sensitive to oxygen and is irreversibly damaged in its presence.[29] Thanks to a pioneering work by Melis *et al.* in 2001, it was observed that by depriving sulfur from *C. reinhardtii* growth medium and sealing the bioreactor, the microalga undergoes an extensive downregulation of PSII and RubisCO; the rate of respiration (O_2 consumption) becomes higher than the rate of water oxidation (O_2 production), so that anaerobic conditions are established, and consequently, high rate H_2 production can occur. The main reason behind this severe response is that PSII is prone to extensive photodamage and the only way for the cell to survive is by continuously replacing the damaged protein.[28,30,31] The protein D1 (see Section 1.2), a cysteine-rich protein, has a half-life time smaller than 1 h[32] under standard growth conditions, hence a lack of sulfur in the medium could be detrimental since the cells keep growing in the first stage of the sulfur deprivation.[28,33,34] Hydrogen gas production in *C. reinhardtii* involves three electron sources: one comes from starch through PQ-type II NADPH dehydrogenase (Nda2) (starch is accumulated during standard growth), the second from the remaining PSII activity (suggested to be the main route[35]), the last route is by anaerobic fermentation.[23,36,37] The main problem of using sulfur deprivation for biotechnological production of H_2 is that the lack of sulfur leads to cell death after 1 week. Even though it was discovered by Kosourov *et al.* that the algal culture can be restored by introducing sulfur to start a new cycle of sulfur deprivation experiment, the final yield of H_2 production decreased at each new cycle. [34] Encouragingly, Krishna *et al.* suggested that it is possible to achieve continuous H_2 production by using a strain of *C. reinhardtii* with an imbalanced PSII

and PSI ratio, without the need for sulfur deprivation. However, the rates of H_2 production are slower.[38] This is probably because the complex response given by sulfur deprivation leads to the unavailability of important electron sinks, such as the reduction of CO_2 via FNR (see Section 1.2).[38]

Algae and cyanobacteria could be used as a production platform for other commodities, such as butanol, lipids, and isoterpenoids. Genetic engineering tools are currently being developed for these photosynthetic organisms.[39] However, the lack of established methods is the reasons why final yields for higher value metabolites are not as high as in heterotrophs.[40] Remarkable cases have been reported in cyanobacteria: Miao *et al.*[41] reported the production of 1-butanol in *Synechocystis* PCC 6803 with a final yield of 4.8 g L^{-1}. Promising results have also been reported for isoprene and more complex terpenes.[42] In microalgae instead, genetic engineering is still a limitation and mainly abiotic factors are used to change or redirect the metabolic flux in the cell metabolism.[40]

1.4. Artificial Photosynthesis

Artificial photosynthesis (AP) has an ambitious goal: to harness sunlight and use the energy captured to drive relevant reactions such as proton or CO_2 reduction. The challenge is to use cheap and abundant sources and materials, such as visible light and water as electron donor, to potentially achieve higher solar-to-chemical efficiencies than in natural oxygenic photosynthesis (1%).[43] Importantly, mimicking photosynthesis does not necessarily mean mimicking the structural natural components, but mimicking the fundamental principles and chemical processes of photosynthesis.[44]

Crucial for the field of AP was the discovery by Honda and Fujishima in 1972 where the authors reported the ability of TiO_2 to drive proton reduction using water as the electron donor under UV light illumination.[45] However, UV light constitutes only 6% of the total spectrum of the sun, therefore visible light, which accounts for 43% of the spectrum, should be used to increase solar to chemical efficiency.[13] Ideally, all the spectrum should be used including IR (51% of the sun spectrum)[13], which naturally does not influence photosynthesis. Currently, charge separation during far red illumination in plants is being studied.[24]

An artificial photosynthesis device includes a light absorber, for example a semiconductor material (replacing PSII in oxygenic photosynthesis), a catalyst for water oxidation (replacing the Mn_4Ca cluster) and a catalyst for the reduction of interest (in photosynthesis FNR). Semiconductor chemistry is explained with the energy band model (detailed semiconductor theory is introduced in Section 7.2). Briefly, the highest occupied energy level is called the valence band (VB) and the lowest unoccupied energy level the conduction band (CB). The difference between these two bands is defined as the band-gap (E_g). Charge separation (see below) occurs upon light absorption when the energy of the photon is equal or higher than E_g. Thus, the band gap needs to be below 2.9 eV for the transition to happen under visible light (420 nm < λ > 750 nm = 2.9 eV < *hv* > 1.77 eV). Upon charge separation, an electron migrates to the semiconductor conduction band (CB) leaving a hole (h^+) in the semiconductor valence band (VB). Oxidation of water (or any suitable electron donor) can refill the vacancy left in the material.

When choosing the semiconductor for AP devices to drive water splitting (hydrogen evolution and H_2O oxidation), there are important prerequisites to consider. A summary is given in **Figure I-2** which uses TiO_2 as an example to

illustrate those considerations. Ideally, the material has to absorb visible light to increase solar to chemical efficiency, *i.e.* E_g < 2.9 eV. Moreover, the VB potential should be more positive than the water oxidation potential ($E^{O2/H2O}$, 1.23 eV vs. RHE) and the CB potential should be more negative than the potential of the reduction reaction of interest (proton reduction in **Figure I-2**). Furthermore, the chosen material should be very conductive, and the diffusion holes' mobility not too small.[46] This factor describes the distance a hole, generated after charge separation, can migrate before recombination occurs. For instance, this distance is high for Silicon (100 µm), but extremely short (2–4 nm) for hematite (Fe_2O_3).[47,48] **Figure I-2** shows the band gap, VB and CB potentials relative to $E^{O2/H2O}$ and $E^{H2/H+}$ of the well-studied semiconductor TiO_2. Clearly, this semiconductor can drive overall water splitting, but only upon UV-light absorption because of its wide-band gap of 3.2 eV.

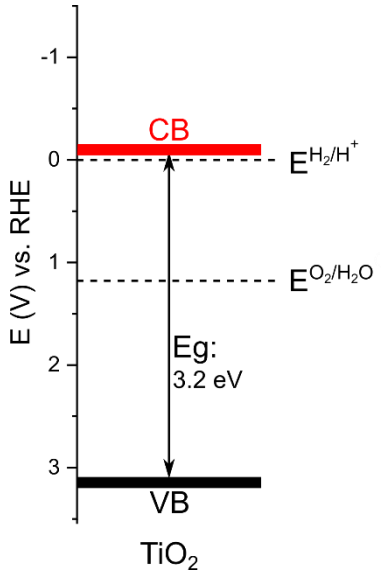


Figure I-2. Requisites to consider when choosing a semiconductor to catalyse light-driven water splitting. The potential of the material's valence band (black rectangle) and conduction band (red rectangle) is shown relative to the potential of water oxidation and H^+ reduction. E_g is the difference between VB and CB potential. In the example: wide band-gap semiconductor TiO_2.

Before explaining more details on semiconductor materials, it is important to discuss typical examples of devices developed so far in AP, using water splitting as a reaction example. A summary of selected devices is shown in **Figure I-3**. The used systems are typically divided into: photoelectrochemical (PEC, **Figure I-3**, Panel A to C), PV-electrolyser (**Figure I-3**, D) and photocatalytic or particulate systems (**Figure I-3**, E and F).

In PEC systems, light absorbers are deposited on conducting solid supports, such as fluorine tin oxide (FTO) and indium tin oxide (ITO) coated glass, and the redox reaction (oxidation of water or reduction of H^+) occurs at the solid/liquid interface; in **Figure I-3-A** an *n*-type semiconductor is deposited on an electrode and the resulting construct is defined as photoanode (for more details see Section 7.2). Upon light absorption, charge separation occurs, thus an electron transitions to the CB leaving a hole (h^+) in the VB. Because of band bending (magenta line, **Figure I-3-A**), the electron migrates to the back contact while the h^+ moves to the hole/semiconductor junction: h^+ can be filled by water oxidation. In **Figure I-3-B**, a *p*-type semiconductor is deposited on an electrode generating a photocathode. After charge separation, an excited electron migrates towards the semiconductor/electrolyte junction to drive H^+ reduction while the hole moves to the back contact. Note the differences between **Figure I-3-A** and **-B**, in terms of the reactions catalysed by photoanode and photocathode (oxidation and reduction, respectively), by the counter electrode, the Fermi level (the dotted line, see Section 7.2) and the band bending (magenta line); the last two differences are due to the different material used (*n*-type for the photoanode and *p*-type for the photocatode). Because of the position of the CB, a potential can be applied in case the photoanode cannot thermodynamically drive H^+ reduction (**Figure I-3-A**, applied

potential > E_{fb}, flat band potential, see Section 7.2). Likewise, a potential can be applied for a photocathode not meeting the thermodynamic requirements (**Figure I-3-B**, applied potential < E_{fb}). Otherwise, a Z-scheme can be built as for natural oxygenic photosynthesis. This case is described in **Figure I-3-C**, where two light absorbers, a photoanode for water oxidation and a photocathode for H^+ reduction, are included.

Figure I-3-D shows a different situation where two catalyst materials, a catalyst for water oxidation such as iridium oxide[49] and one for proton reduction, such as NiMoZn[50], are deposited on the conducting supports to generate an anode for the oxidation and a cathode for the reduction reaction. The system can be energized by providing a high voltage through a potentiostat or a solar cell (PV element).[50] In all examples from **Figure I-3**, **A–D**, the efficiency of the system can be monitored by measuring the electrical current.

Deposition of a material on a conductive support can increase the cost of the AP device and sometimes be inefficient (unstable film). Cost efficiency can be improved by using semiconductors directly in a solution (particulate system, not requiring deposition). For instance, **Figure I-3-E** shows a system using a single semiconductor for water splitting. In an analogous way to the Z-scheme shown before in **Figure I-3-C**, the same setup can be built in a particulate system, usually by including a soluble electron mediator, such as $Fe^{2+/3+(51)}$ but papers on unmediated particulate Z-scheme have also been published (**Figure I-3-F**).[12,52,53]

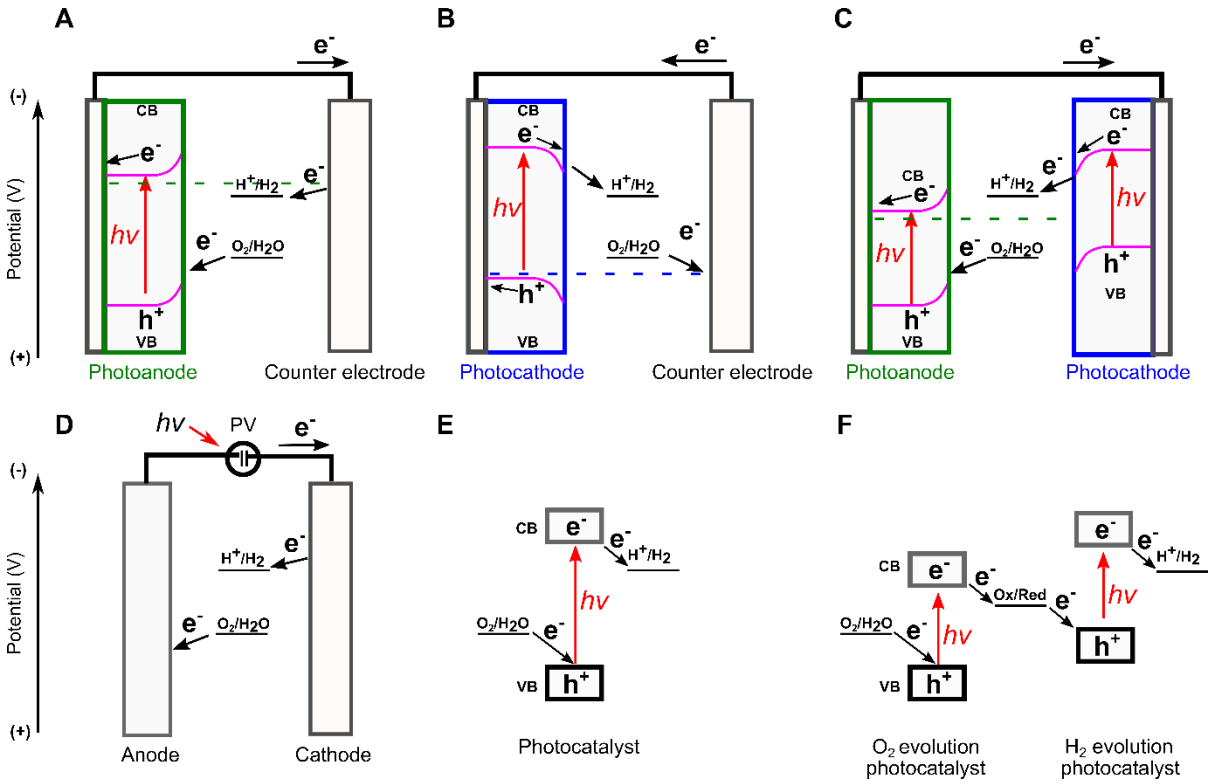


Figure I-3. Examples of different AP schemes from the literature. **A**. PEC with suitable photoanode to drive O_2 evolution with concurrent H^+ reduction at the counter electrode (CE); **B**. PEC with suitable photocathode able to drive H_2 evolution with concurrent water oxidation at the CE; **C**. Z-scheme using a photoanode able to drive O_2 evolution but not proton reduction so that introduction of a photocathode for H^+ reduction is required to drive the system only with light; **D**. A PV device provides the voltage to drive O_2 evolution at anode and H_2 evolution at the cathode; **E**. Photocatalyst in a particulate system able to drive water splitting upon light illumination; **F**. Particulate system with a photocatalyst for O_2 evolution and a photocatalyst for H_2 evolution. A soluble electron mediator is usually needed in this case. Dotted line represents the Fermi level (see Section 7.2). Figure was adapted from Hisatomi *et al*.[12]

In this thesis, a semi-artificial PEC system will be developed to drive the reduction of $NADP^+$ via an electrode-protein composite called the 'electrochemical leaf' (see Section 1.6). The light absorber deposited on a conducting support can be a sensitised electrode for visible light absorption, such as sensitised TiO_2 or another *n*-type semiconductor. **Figure I-4** shows a summary of *n*-type semiconductors and their CB and VB potentials relatively to potential of water oxidation and $NADP^+$ reduction.

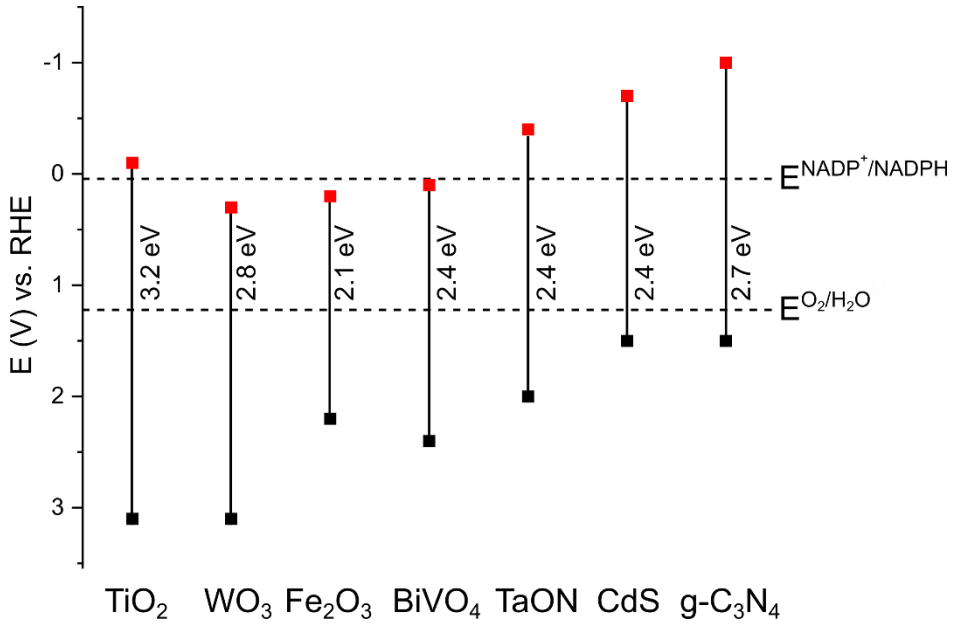


Figure I-4. Examples of selected semiconductors used for PEC applications. The potential of the material's VB (black squares) and CB (red squares) is shown relative to the potential of water oxidation and $NADP^+$ reduction. Adapted from Sivula and Van der Kroel.[46]

TiO_2 is a well-studied and very stable material, able to drive $NADP^+$ reduction just by using light.[45] However, its main limitation is its wide band gap (3.2 eV), meaning that charge separation would occur only in the presence of UV light. Efforts have been made to implement TiO_2 in a visible light-driven PEC system.[54–56] So far, sensitization (introduction of a dye absorbing visible light) and doping (introduction of a foreign element) were the main strategies used: for instance, the wide gap semiconductor has been sensitized in pivotal studies by Gratzel *et al*. to develop the Dye Sensitized Solar Cell (DSSC) and several other studies followed where other dyes such as tris(bipyridyl)ruthenium (RuP) have been covalently bound to drive proton reduction or CO_2 reduction, often using organic electron donors rather than water.[57–59] Another approach is to engineer the band gap of a wide band gap semiconductor to introduce a new intermediate band by doping. As an example, this result was achieved with Rh- or Al-doped $SrTiO_3$

electrodes as photocathodes, with the resulting material being able to absorb visible light, as opposed to the wide band gap $SrTiO_3$.[51,60]

Semiconductor materials like Fe_2O_3, $BiVO_4$ and WO_3 are very promising and under intense research. Their band gaps are 2.1, 2.4, 2.8 eV, respectively, but their conduction band is not negative enough to drive reductive reactions like H^+ to H_2, $NAD(P)^+$ to NADPH and CO_2 to CO (see **Figure I-4**). In order to study their properties for water oxidation, an additional bias needs to be added to the system. Hematite (Fe_2O_3) is extremely attractive because the material can absorb most of the visible light; in a PEC system the theoretical current density is 12 mA/cm^2 achievable after only 0.1 V of applied bias.[43,61] Moreover, iron is a widely abundant, and cheap material. However, the real measured performance of hematite is still far from reaching the numbers listed above, because of processes like electron-hole recombination and low conductivity which worsen current density and increase the onset potential for water oxidation (*i.e.* create an extra overpotential requirement before catalysis occurs, see Section 7.2).[43,62,63] Common strategies to improve the material's performance are to nanostructure the material (synthesize nanostructure such as nanotubes), doping and addition of under/over layers to increase current density and decrease the overpotential requirement.[48,54,64–66]

$BiVO_4$ can reach a smaller theoretical current density of 8 mA/cm^2, because of its wider band gap than hematite by 0.3 eV. However, higher photocurrents are normally achieved, due to (i) higher charge carrier mobility (70–200 nm) and (ii) position of the CB which almost straddles the potential for H^+ and $NADP^+$ reduction (and more negative than the hematite CB).[67–69]

There has been great interest and enthusiasm raised with the discovery of graphitic-carbon nitride (g-C_3N_4), tantalum oxynitride (TaON) and tantalum nitride

(Ta_3N_5). **Figure I-4** shows that those materials are thermodynamically capable of catalysing visible light-driven $NADP^+$ reduction without any need for any additional bias because of the suitable potentials of their VB and CB. Moreover, charge separation can occur upon visible-light absorption because their band gaps are 2.7, 2.4, and 2.1 eV, respectively.[46] However, tantalum is a rare material and synthesis of the (oxy)nitrides is challenging whilst the current density remains low at no applied potential.[70] Graphitic carbon nitride has extensive possibilities as a useful material in AP systems as it is metal-free, cheap and stable with a band gap of 2.4 to 2.7 eV, depending on the synthesis. However, g-C_3N_4 suffers from low conductivity and intense research is being carried out to improve its performance.[71] As a result, the photocurrent is still more than 1000× lower than the semiconductors discussed earlier.[72–75] Cadmium sulfide (CdS) is also able to drive overall water splitting with no applied potential, but it suffers from instability in neutral conditions and it is toxic. Nevertheless, CdS has been used in novel applications such as dinitrogen reduction and plastic degradation.[76,77]

The semiconductor performance in a PEC system is assessed by looking at the amplitude of the current density at the onset potential for the reaction under investigation (in this thesis the reaction is water oxidation; $E^{O2/H2O}$ is 1.23 V vs RHE). The onset potential is the potential where catalysis starts to occur (for further details see Section 7.2). Unfortunately, most of the materials so far discovered lack one or more of the requisites listed above.

Because of the characteristics listed above, the main materials used in this thesis are hematite and $BiVO_4$. Due to the CB position, it was necessary to apply a small additional potential (see Section 3.4.1. and Section 3.4.2.) or to build a Z-scheme by including a second light absorber (see Section 3.4.3.). For instance,

promising photocathodes are *p*-type semiconductors (see Section 7.2) such as Cu_2O, CuO, but a big drawback lies on the instability of Cu in the water oxidation condition because Cu is released into solution in the condition used.[78–81].

Typically, an oxygen evolving reaction (OER) catalyst is also included in AP systems, to increase the rates of oxygen evolution and decrease electron-hole recombination, increasing the overall efficiency of the system. In many cases this condition was achieved by depositing metal oxides, such as iridium, rhodium and ruthenium-based materials on the semiconductor surface. However, given the main goal of AP, that is to make fuel at generally low costs, it would be more ideal to use cheap materials. As such, the catalysts above provide insights but not practical solutions. Important breakthroughs were recently obtained by Nocera *et al.* with the discovery of Co- and Ni-based OER catalysts (CoPi or CoBi).[50,82,83] Application of these materials in a device comprising a triple junction solar cell allowed Nocera *et al.* to develop a technology called the "*Artificial Leaf*" reaching record and unprecedented current density for H_2 production of 100 mA cm^{-2}.[50] Other promising catalysts are Fe- and Ni- oxyhydroxide (FeOOH and NiOOH). These layers are also reported to generate a *pn*-junction, improving charge separation, with a positive effect on photocurrent and onset potential.[67,84,85]

Choosing an efficient catalyst for any reaction under investigation is crucial. For this purpose, enzymes provide an excellent platform to study and investigate how to improve and design catalysts. Moreover, as enzymes are already optimised by evolution to catalyse the reaction under investigation, they offer the opportunity to improve other components of the AP system, such as semiconductor material and reaction conditions.

Semi-artificial photosynthesis combines biocatalysts with semiconductor materials: several enzymes have been implemented such as hydrogenases, for H^+ reduction, CO dehydrogenase and formate dehydrogenase for CO_2 reduction.[59,72,86–89] Chapter III of this Thesis shows a semiartificial photosynthesis system for the light-driven reductive carboxylation of pyruvate (3 carbons) to malate (4 carbons) via NADPH cycling, in a system which resembles oxygenic photosynthesis. Importantly, the proposed AP system could become an important tool for biocatalysis, as it could work with any NADPH-dependent biocatalyst, given that the nicotinamide cofactor is involved.[90]

1.5. Biocatalysis

The use of enzymes as catalysts to drive reactions in AP systems offers several advantages over artificial inorganic catalysts, as they allow reactions to be driven in milder conditions, such as room temperature, atmospheric pressure and in an aqueous environment.[91] Moreover, enzymes display high selectivity, which is a very challenging feature to induce in conventional organic synthesis where protection groups have to be added to ensure formation of the right product.[92,93] Thus, using enzymes could make industrial processes cleaner, safer and in some cases cheaper. Consequently, enzymes are preferably being used for synthesis in industry if possible.[94]

The drawbacks of using enzymes are generally their instability, compared to inorganic catalysts, and rather contradictorily the limitation given by their substrate-selectivity and solvent compatibility. However, thanks to the development of directed evolution, it is now possible to improve an enzyme towards multiple desired functions, such as reversing enantio-selectivity,[95]

expanding the substrate scope,[96] increasing temperature and pH sensitivity,[97,98] changing cofactor specificity[99] and increasing stability in organic media.[100]

Oxidoreductases constitute one of the largest class of enzymes, and oxidation reactions are of high interest for industry.[91,92] These enzymes are already used in some cases in industrial synthesis, for example ketoreductase (KRED) has replaced its synthetic counterpart in the production of the cholesterol-lowering drug Lipitor.[101] The main issue with the use of oxidoreductases for large-scale synthesis is their need for a redox cofactor in catalysis. This is usually the cofactor nicotinamide adenine dinucleotide (NAD^+), or its phosphorylated counterpart $NADP^+$, which both act as an electron donor or acceptor, while a substrate is reduced or oxidized, respectively (**Figure I-5**). A reaction scheme of a NAD(P)(H)-dependent dehydrogenase is shown in **Figure I-5**. It is obvious that stochiometric amounts of cofactors are needed and because of the high price ($3000 per mol of NADH and $215,000 per mol of NADPH)[92] any process based on stochiometric supply would be economically unfeasible.[102] These cofactors are also crucial for the cell redox balance[103] and normally they are reduced during cell respiration and oxidized in the anabolic reactions[14]. *In vivo*, the cofactor is recycled efficiently but *in vitro*, a cofactor regeneration system is required (see Section 1.5.1.). Several methods have been used to date, but so far only enzyme-based methods have been implemented outside from the laboratory.[104] In the next section, several methods for cofactor regeneration will be discussed.

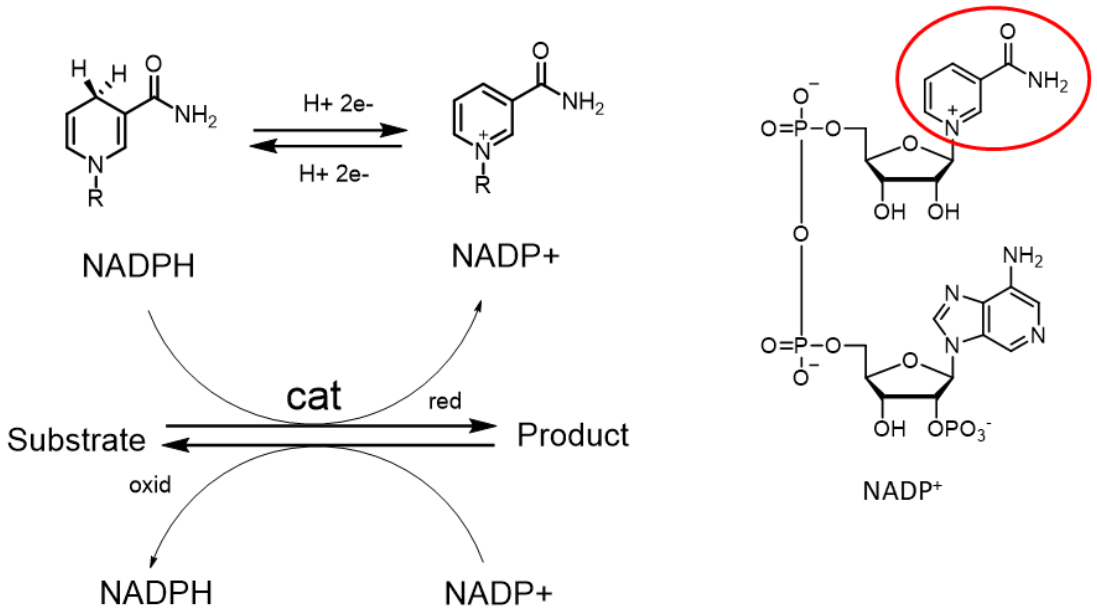


Figure I-5. Reaction scheme of NADPH dependent oxidoreductases. This class of enzymes drives oxidation (oxid) or reduction (red) reactions, requiring stochiometric amount of nicotinamide cofactor. The full chemical structure of $NADP^+$ is shown on the right side.

1.5.1. Cofactor regeneration systems

1.5.2. Whole cell cofactor regeneration systems

The simplest method for regenerating cofactor is to use whole cells either immobilised or in solution overexpressing the gene/s encoding for the required enzyme/s. This way, laborious enzyme purification as well as issues of enzyme instability can be avoided while the microorganism will continuously produce the enzyme and regenerate the cofactor. However, there are possible drawbacks with this whole cell approach, such as (i) genetically modified organisms (GMO) regulation, (ii) more difficult product purification because of likely occurring side-reactions, (iii) biomass waste disposal, (iv) possible synthesis of inhibitory products from the cell impairing the biocatalytic reaction. Moreover, the substrate for the biocatalytic reaction could be incompatible with the cell because of toxicity. Nevertheless, whole-cells are heavily used in industry and academia[105–108] such

as for the reduction of a ketone or alcohol oxidation by an alcohol dehydrogenase,[109,110] reduction of alyl-3-oxobutanoate by *E. coli* overexpressing the genes for carbonyl S1 reductase and glucose dehydrogenase[111], production of the precursor for antimalarial drug, artemisinin[112], and of a wide range of metabolites such as L-glutamate[108], bioethanol, butanol, lactic acid, bioplastic.[113–120]

1.5.3. Enzymatic based cofactor regeneration methods

Enzyme-based methods for cofactor regeneration are so far not only the best performing but also the only methods used on an industrial scale in combination with whole cells.[104]

Figure I-6 shows the most used enzyme-based systems reported in the literature. Briefly, they can be divided into two systems: (i) systems with one enzyme driving both the reaction under investigation and the recycling of the cofactor (**Figure I-6-A**) and (ii) systems with two separate enzymes (**Figure I-6**, **B** to **D**). For instance, alcohol dehydrogenases (ADHs) can be used both for the main reaction and for regeneration of the cofactor by using a co-substrate, such as an alcohol or ketone depending on the main reaction under investigation.[121] The use of one catalyst in the regeneration system decreases the overall cost, however it is difficult to optimise the enzyme activity for both reactions and very high concentration of co-substrates are required to drive the reaction towards the product. Moreover, a high amount of waste is usually produced.[122]

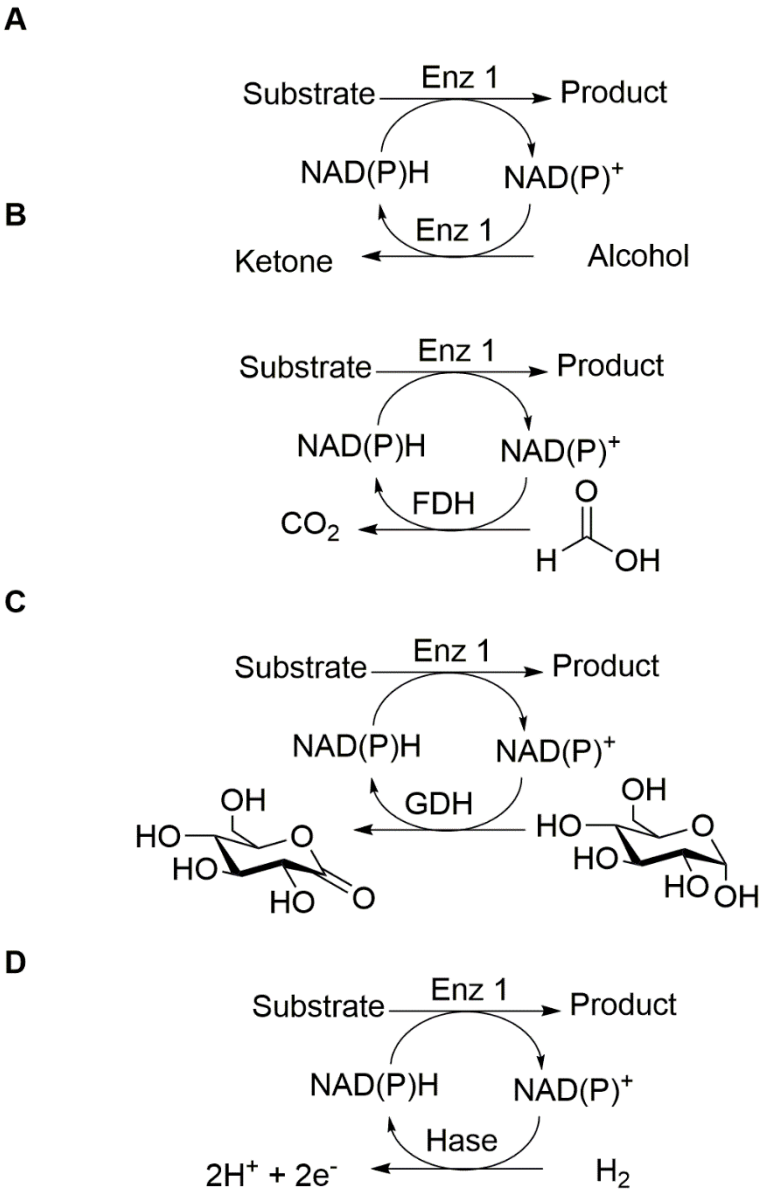


Figure I-6. Examples of enzyme-based cofactor regeneration systems. One-enzyme system: **A.** the enzyme drives both the main reaction and the cofactor regeneration. This system typically uses an alcohol dehydrogenase (ADH). Two-enzyme systems: **B.** FDH drives oxidation of formate to CO_2, while reducing the cofactor; **C.** GDH oxidizes glucose to gluconolactone (NAD^+ and $NADP^+$); **D.** Hydrogenase (Hase) oxidises H_2 to protons and electrons, used to reduce $NADP^+$.[123]

The use of a secondary enzyme is the most commonly implemented system, where for example, formate dehydrogenase (FDH) reduces the cofactor by oxidizing formic acid to CO_2 (**Figure I-6-B**). Glucose dehydrogenase (GDH) can also recycle the cofactor by oxidise glucose to gluconolactone (**Figure I-6-C**).[99,111] The main

advantage related to the use of FDH is that the coproduct, CO_2, is not a problem for product recovery, however the enzyme is not very active and CO_2 production slowly acidifies the reaction mixture.

Whilst GDH is widely used, excess glucose is necessary to shift the reaction towards the product which makes product recovery difficult and atom efficiency of the system low.[122]

Figure I-6-D shows another possibility which is the use of *Ralstonia eutropha* NAD/$NADP^+$-dependent hydrogenase, which can oxidize H_2 to $2H^+$ and $2e^-$ which are then used to reduce $NADP^+$ to NADPH.[124] The method is attractive as 100% atom efficiency is obtained and no waste is generated due to a co-substrate.

1.5.4. Electrochemical methods for cofactor regeneration

Electrochemical regeneration of the cofactor without the need for any other catalyst is of great interest because the resulting method would likely be stable, simple and cheap, considering the current costs of electricity.[125] Additionally, if the nicotinamide cofactor could be oxidized or reduced at the electrode surface there would be no need for using any enzyme or other type of catalyst, decreasing the overall cost of the process. Schematic electrochemical methods for NAD(P)H reduction are shown in **Figure I-7**.

It is known that the nicotinamide cofactor is reduced via two steps at the electrode: First, at –1.1 V vs. SCE a radical is formed, which is subsequently protonated at –1.7 V vs. SCE. However, the radical species can dimerize forming NAD(P) dimers and the protonation step is also not selective, as it can lead to the biologic inactive forms of 1,2 NAD(P)H and 1,6 NAD(P)H.[126] Low selectivity would make any application of the system unfeasible since over the course of few regeneration

cycles the overall efficiency of the system would drop dramatically. This would hinder any industrial process based on an electrochemical-only regeneration technology (scheme for the overall reaction in **Figure I-7-A**). Electrochemical methods using electron mediators (Med^{ox}, such as rhodium and iridium catalysts) have been researched for more than 30 years to solve some of the issues of electrochemical cofactor regeneration (scheme for the overall reaction in **Figure I-7-B**).[127]

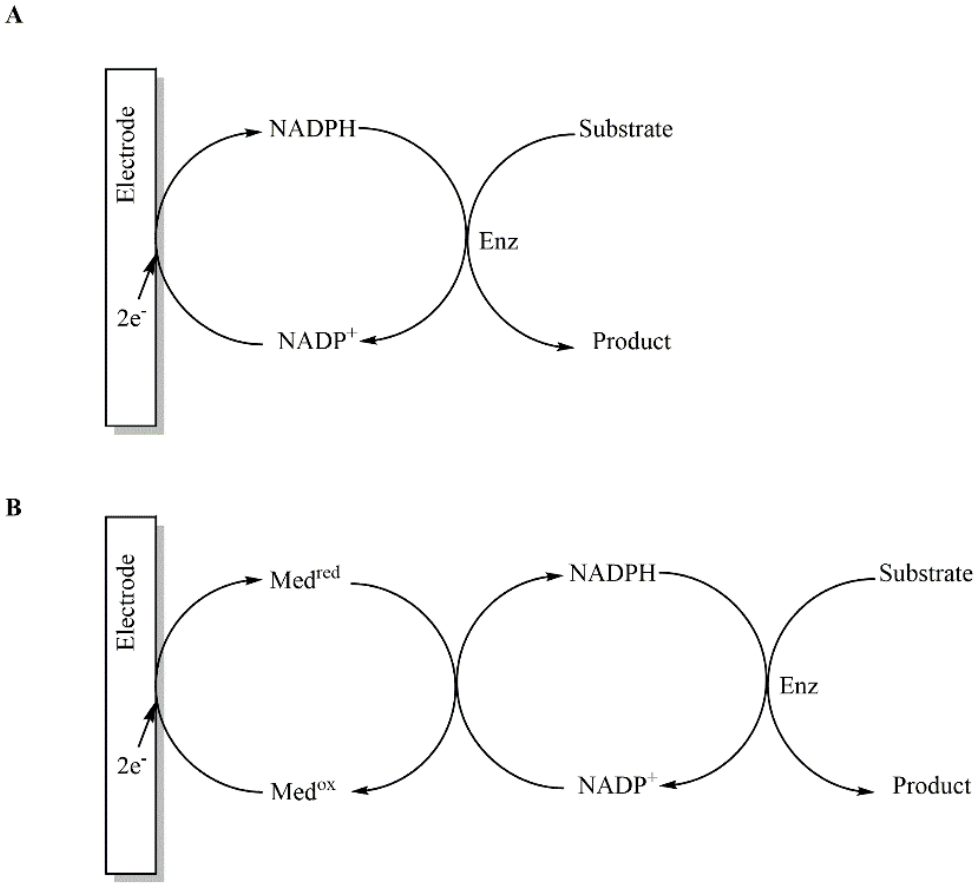


Figure I-7. Electrochemical methods for cofactor regeneration. A. Direct electrochemical reduction of the cofactor. **B**. Indirect electrochemical reduction via mediator.

The most promising catalysts are $[Cp^*Rh(bpy)(H_2O)]^{2+}$ and $[Rh(Cp^*)(bpy)Cl]^+$.[128] The advantages with using these catalysts are that (i) they can be used with both NAD^+ and $NADP^+$ thus increasing the scope of the system

for different chemical products, (ii) they are stable over a wide pH range (pH 4 to 7) and temperature range (up to 70°C) and (iii) they successfully stop the formation of NAD dimers. However, they are reported to inactivate the biocatalyst over the course of the reaction because of complexation with the enzyme.[128,129] The latter issue was solved by Minteer *et al.* with a system composed of a cobaltocene poly(allylamine) (Cc-PAA) redox polymer bound to a diaphorase.This system was also reported to be much more specific for the biological active form of NADPH (faradaic efficiency from 87% to 99%, while the Rh and Ir complexes have faradaic efficiencies of around 89%).[130] However, even with 99% efficiency, the specificity would drop to 81% after 20 cycles and to 36% after 100 cycles. Consequently, in related studies using mediated (indirect) electron transfer, high cofactor concentration (>1 mM) is always used, which decreases the total turnover number (TTN, defined as moles of product per moles of cofactor added at the beginning of the experiment). Eventually, for an industrially relevant regeneration system a 100% efficiency should be achieved for the process to be cost-sustainable with respect to the high cost of the cofactor.

1.6. The electrochemical leaf

1.6.1. Ferredoxin NADP$^+$ reductase

Ferredoxin NADP$^+$ reductase (FNR) is a monomeric protein which is found across all *phylia.*[131,132] This enzyme has a crucial role in the Calvin cycle in photosynthetic organisms, as it catalyses NADP$^+$ reduction, upon interaction with reduced Fd (Equation 1.5). In heterotrophs, the reaction is more favourable towards Fd reduction and it is involved in several anabolic reactions, such as synthesis of amino acids and deoxyribonucleosides and desaturation of fatty acids.[132] Ferredoxin is a small (13 kDa in *C. reinhardtii*) iron-sulfur containing protein, able to carry 1 e$^-$, while NADP$^+$ reduction requires 2 e$^-$ (nicotinamide structure is shown in **Figure I-8**). The presence of a non-covalently bound FAD (flavin adenine dinucleotide) within FNR, makes the reaction possible.

$$2\,Fd\,(Fe^{2+}) + NADP^+ + H^+ \rightleftarrows 2Fd\,(Fe^{3+}) + NADPH \qquad (1.5)$$

The FAD group contains an adenosine, bound to pyrophosphate and a ribityl moiety. The redox reactions occur at the isoalloxazine ring. This cofactor can exist in three forms: quinone, radical semiquinone and fully reduced hydroquinone. FNR provides a special environment for FAD reduction. Not only it shifts the two electron reduction potential by ≈200 mV from –0.22 V to –0.38 V vs. SHE (pH 8) but it partly stabilizes the semiquinone radical which otherwise would immediately disproportionate towards the stable forms: the potentials for FAD reduction in FNR are mildly crossed *i.e.* adding the first electron is slightly less favourable than adding the second hence allowing partly to trap the radical state. (**Figure I-8**).[132–134]

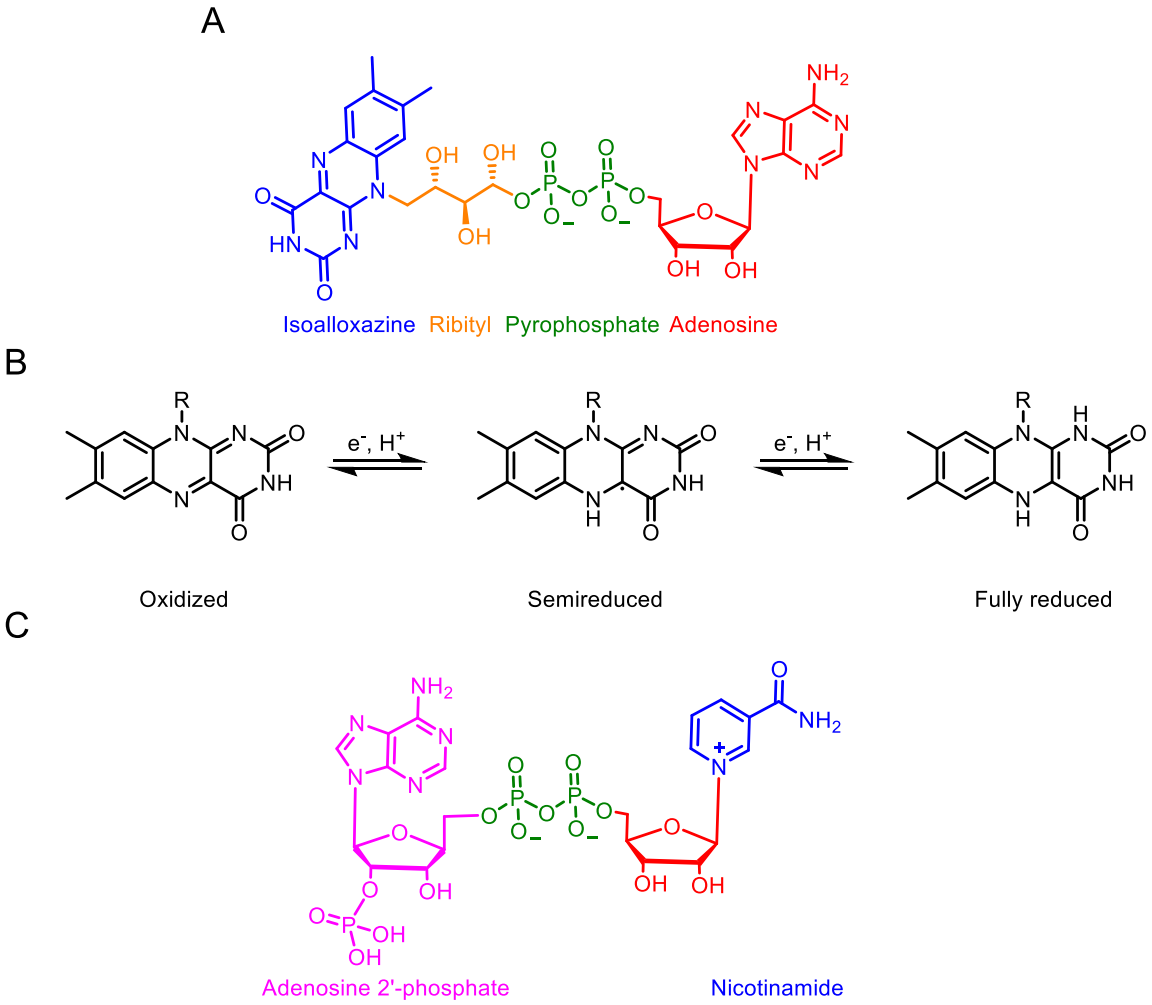


Figure I-8. FAD and NADP$^+$. A. Structure of FAD: the chemical active part is the isoalloxazine ring (blue). **B.** The FAD can exist in three different forms: fully oxidized (quinone), semi reduced (semiquinone) and fully reduced (hydroquinone).[132] **C.** Structure of NADP$^+$: in blue the chemically active moiety (nicotinamide) and in magenta the adenosine 2′-phosphate. The latter is the only structural difference between NADP$^+$ and NAD$^+$.

FNR contains two domains, the N-terminal is the FAD binding domain which is also responsible for the interaction with Fd and the C-terminal for NADP$^+$ binding.[135] **Figure I-9** shows the crystal structure of FNR from *Zea mais* (*pdb* 1GAQ: FNR-Fd complex) with bound FAD and NADP$^+$. In this thesis, FNR from *C. reinhardtii* was used: this enzyme has a high degree of similarity with the structure shown in **Figure I-9** (1GAQ, 58.6%, alignment carried out with Clustal Omega). Insight into the catalytic site of FNR can be helpful to understand the binding of

FAD and $NADP^+$. **Figure I-9** shows the catalytic site of FNR in *Z. mais* and in brackets the corresponding residues in *C. reinhardtii* identified after alignment. The isoalloxazine ring binds through π-stacking with Y95 and Y314 (Y124, Y346).[132] Binding of $NADP^+$ within FNR involves residues on the C-terminal of the enzyme. The phosphate group within $NADP^+$ is stabilised by basic residues such as Arg and Lys.[136] In *Z. mais* Ser234 and Arg244 (S267 and K277) interact with the phosphate at the 2′-position of the ribose. The nicotinamide binding site is occupied by a conserved C-terminal Tyr; therefore, binding of $NADP^+$ and electron transfer with FAD has to involve displacement of the C-terminal Tyr314 (Y346).[137] The interaction between the positively charged residues with the phosphate group of $NADP^+$ is enough to overcome the energy barrier given by the displacement of C-terminal tyrosine.[136] In case NAD^+ instead of $NADP^+$ is added (*i.e.* the structure does not contain a phosphate at the 2′-position of the ribose) catalysis can be impaired: as a matter of fact, the selectivity of FNR for NAD^+ is much lower than for $NADP^+$ (K_M for $NADP^+$ typically 8–39 µM[134,138], while for NAD^+ 4–11 mM and k_{cat} 100X lower[138]). Replacing C-terminal Tyr with a smaller amino acid can improve the binding of NAD^+. Variant Y346S (from *C. reinhardtii* reported by our group[139] based on previous mutant Y308S by Piubelli *et al.* from pea[137]) was able to use NAD^+ efficiently. Surprisingly, $NADP^+$ related catalysis was strongly impaired because of a dramatic decrease in k_{cat}, while K_M reached a smaller value (higher affinity) of 0.44 µM: Piubelli *et al*. reasoned that the high affinity between FNR and $NADP^+$ after removing the C-terminal Tyr was preventing the enzyme from releasing the product.[137]

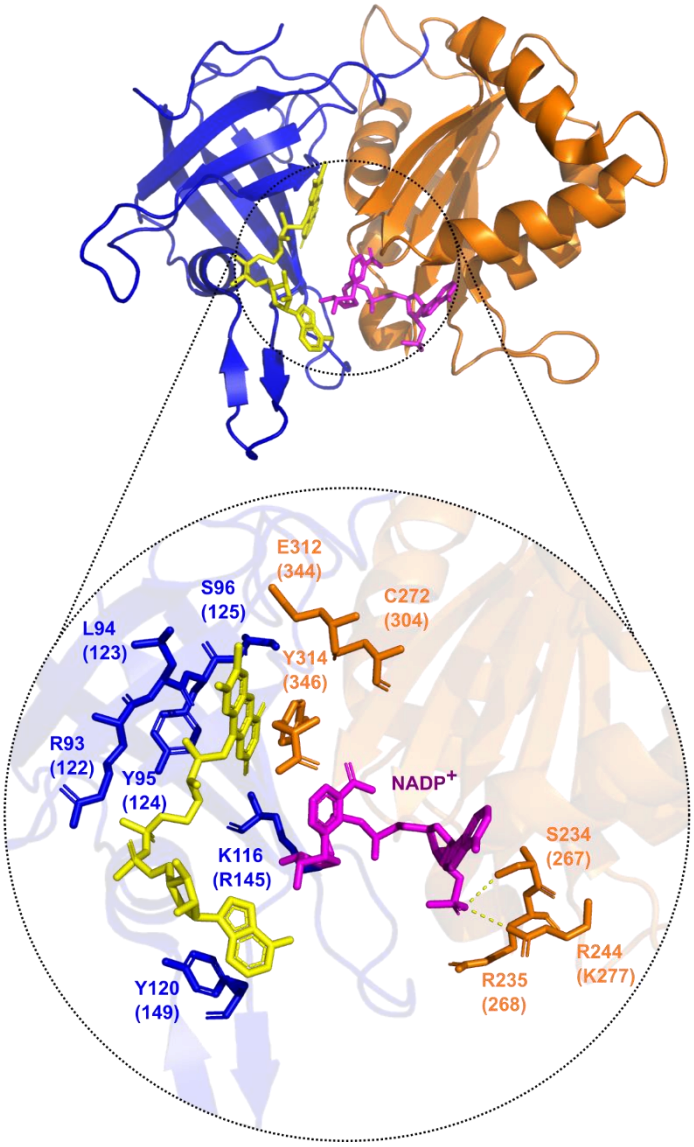


Figure I-9. FNR structure and its catalytic site. A. Structure of FNR (*pdb* 1GAQ from *Zea mais*). The N-terminus (blue) of the protein binds the FAD (yellow) while the C-terminus (orange) to $NADP^+$. $NADP^+$ was added to the structure by aligning *pdb* 1GJR. Structure from 1GJR was deleted. The close-up shows the residues involved in the active site and in brackets the corresponding residues from *C. reinhardtii* FNR. See text for explanation.

Figure I-9 shows other conserved residues involved in nicotinamide binding (C272, E312), in FAD binding (R93, Y95, S96, K116, Y120) and Fd interaction (L94; L76D variant from *Anabena* resulted in impaired electron transfer[140]).[131,132,135–137] The reaction mechanism has been investigated and the formation of a tertiary complex made of Fd, FNR and $NADP^+$ has been proposed.[131]

Surface charge analysis of FNR (*pdb* 1GAQ) and Fd shows that the interaction between FNR and Fd is electrostatic, as Fd is mainly negatively charged and the surface of FNR at the interface with Fd positively charged (**Figure I-10**).[134] The distance between the [2Fe-2S] cluster of Fd and FAD is within 6 Å, so that fast direct electron transfer can occur.[131] The FAD is accessible as electron transfer can be achieved with soluble redox mediators such as ferricyanide or benzyl viologen (BV).[137]

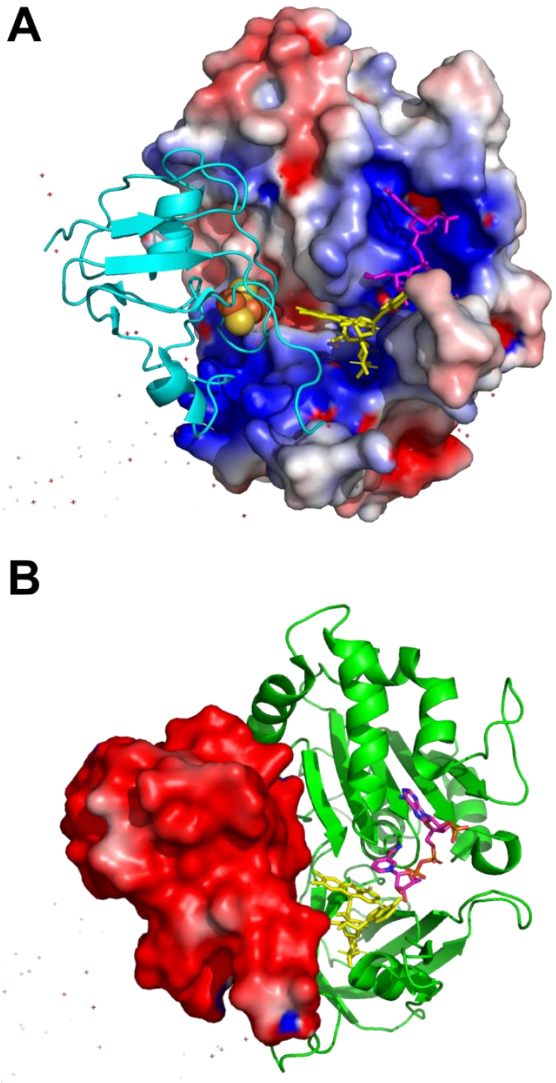


Figure I-10. Electrostatic interaction between FNR and Fd. A. Interaction of Fd (blue cartoon) and FNR (surface charge). The figure shows the position of the [2Fe-2S] cluster within Fd and FAD and $NADP^+$. Crystal structure from *pdb* 1GAQ. Structure of pdb 1GJR was aligned and removed as described in Figure I-9. **B.** Interaction of Fd (surface charge) with FNR (green cartoon). Adapted from Siritanaratkul *et al.*[134]

In 2016 it was discovered that it is possible to tightly bind FNR to a metal oxide (MO) electrode, mimicking the electrostatic interaction found in nature.[134,141] Metal oxide electrodes are very valuable candidates for this purpose: their isoelectric point (pI) is around 6,[142] so the material should be negatively charged at any pH value above the pI. Direct electron transfer between the electrode and the enzyme can be observed by simply dropping FNR on an indium tin oxide electrode. The resulting technology is called the "Electrochemical Leaf" and this forms the basis for the work carried out in this thesis.

1.6.2. Electrochemical results using the electrochemical leaf

In the electrochemical leaf system, the electrode support is made by electrophoretic deposition of nanoparticles (<50 nm) on a conductive support such as indium tin oxide (ITO) glass, titanium or graphite support, to form a mesoporous ITO layer (see Section 7.3.5.1.1.). **Figure I-11** shows the remarkable results that can be obtained using this system. A scanning electron microscopy (SEM) image of the resulting electrode (ITO glass) is shown in **Figure I-11-A**. The SEM data proved the pore size to be around 50 nm diameter (nanopores), and the layer thickness between 1 to 3 µm.[134]

When a concentrated solution of FNR (typically 5 µL from a 1.8 mM stock solution), from *C. reinhardtii* and overexpressed in *E. coli*, is dropped on the electrode, a very stable protein-electrode composite is achieved. The resulting material is denoted as FNR@ITO/Support.

Figure I-11-B shows the results in 50 mM borate (pH 8) of the cyclic voltammetry using FNR@ITO/Support as working electrode, Pt as CE and Ag/AgCl as RE (the technique measures the current as a function of the applied potential, see Section

7.1 for Electrochemical theory). The black trace shows the results obtained for an FNR@ITO/PGE electrode: as conventional for a cyclic voltammetry (CV) experiment, the resulting current is derived of both faradaic and non-faradaic contributions (see Section 7.1.). The red trace shows the same results after application of a baseline subtraction to eliminate the non-faradaic capacitive current (see Section 7.1.3.). The figure does not show the blank (before FNR absorption), which has the same shape of the black trace with no peaks.[134] The resulting peaks are called “non-turnover peaks” and correspond to the oxidation and reduction of the FAD centre of the protein-only since no substrate was present during the measurement. The half peak (δ) width for an ideal immobilized redox couple involving *z* electrons is 89/*z*. **Figure I-11**-**B** shows that the half peak width is 57–59 mV and this is consistent with a two electron reaction with good cooperativity (FAD/$FADH_2$ couple). [134] Moreover, the CV allows calculation of the FNR coverage, *i.e.* the amount of enzyme that is electroactive at the electrode, by integrating the non-turnover peaks, where the charge passed is proportional to the moles of FNR on the electrode (see Section 7.1.5.). **Figure I-11**-**C** shows background-subtracted current of several CV of FNR@ITO/Support electrode taken in buffers at different pH (5–9). At pH 9 (black trace) the enzyme coverage (area under the non-turnover peaks) is very high, around 500 pmol cm^{-2}, while it decreases towards more acidic pH (violet trace is at pH 5). The pH dependence of FNR coverage supports a scenario where the charge is crucial for the interaction between the electrode and the enzyme. At pH above its pI, ITO is negatively charged as Fd (see **Figure I-10** for FNR-Fd interaction). Moreover, the obtained coverage, such as 500 pmol cm^{-2}, is consistent with a multilayer electrode: the highest coverage on a monolayer electrode for FNR, based on a FNR diameter of

6 nm and tight packing, is 5 pmol cm^{-2}.[134] Hence, this data confirm that the electrode material used is (nano)porous as observed from SEM.[134,141]

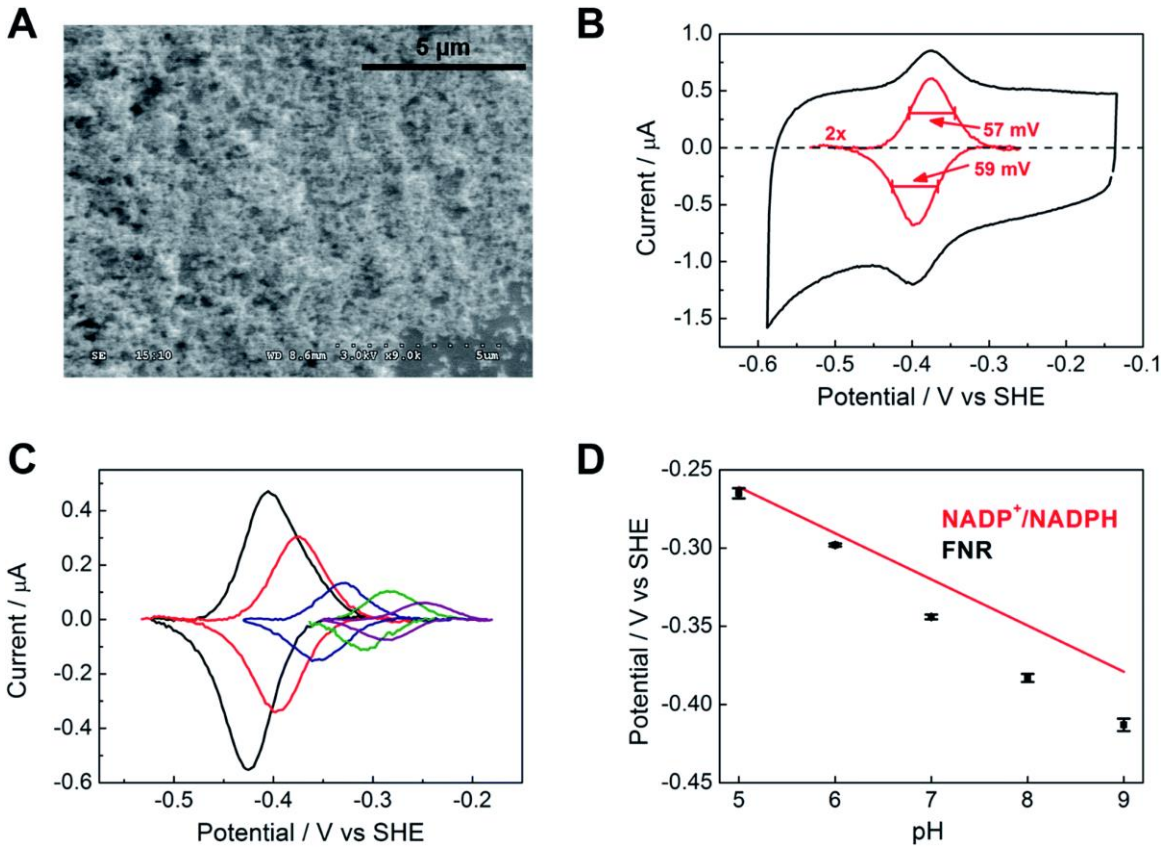


Figure I-11. The electrochemical leaf: the ITO layer, the non-turnover peaks and their pH dependence. A. SEM image of a cross section of an ITO electrode. **B**. Non-turnover peaks arising from FNR@ITO/PGE (raw data: black trace). Half peak width after background subtraction (red trace, magnified 2×). **C**. pH dependence of the non-turnover peaks from pH 9 (black trace) to 5 (violet trace). **D**. Comparison of FNR potential (FAD centre oxidation/reduction potential from non-turnover peaks at different pH) with the $NADP^+$/NADPH reduction potential (from Rodkrey *et al.*[143]) at different pH. Figure reprinted with permission from Siritanaratkul *et al*, [134] published by The Royal Society of Chemistry.

In order to confirm that FNR was indeed immobilized in the electrode nanopores, the authors studied the peak-current scan rate (volt/second, V/s) dependence. The peak current varies linearly with increasing of the scan rate for an immobilized species. A linear increase of the current up to 30 mVs^{-1} was

reported confirming the observation that FNR is indeed entrapped in the electrode nanopores.[134]

Figure I-11-D compares the reduction potential of FNR (calculated from the average potential of the oxidative and reductive non-turnover peaks from CV) with the $NADP^+$/NADPH couple at different pH values (–0.32 V vs. SHE at pH 7, varying −32 mV per pH unity[143]). The potential of the enzyme is always slightly more negative, especially at basic pH. Therefore, this enzyme slightly favours reduction of the cofactor as known from literature.[131]

The previous cyclic voltammetry experiments described were carried out in absence of the substrate ($NADP^+$). When $NADP^+$ is added to the electrochemical cell, upon application of small overpotential, FNR can reduce $NADP^+$ through its reduced FAD centre. **Figure I-12** shows the effect of adding $NADP^+$ (from 0 to 67 µM) in a CV experiment as described by Siritanaratkul *et al*.[134] (under stationary conditions, *i.e.* the experiment solution is not stirred). Note the change in shape of the CV after introduction of $NADP^+$ and the resulting catalytic peaks (peaks due to substrate depletion, see below). The peaks are defined as turnover-peaks as they result from catalytic interconversion of $NADP^+$/NADPH. $NADP^+$ is reduced to NADPH at the FNR@ITO/Support electrode surface and its reduction gives rise to a reduction current.[134] The shape of the current is a peak because, when going from an oxidative to a reductive potential, $NADP^+$ (under stationary conditions) is quickly consumed (depleted) at the electrode surface ([$NADP^+$] at the electrode surface = 0). Under stationary conditions movement of substrates and products is dictated by diffusion (see Section 7.1.6.): the produced NADPH slowly diffuses to the bulk solution. When the potential is scanned back towards oxidative values the reduced cofactor left at the electrode surface is oxidized to $NADP^+$.[134] This gives

rise to a (smaller) oxidative peak current, because of NADPH depletion. The average between oxidation and reduction potential at the peak current corresponds to the reduction potential of $NADP^+$/NADPH. Catalysis can be observed upon application of a very small overpotential and the reaction is *quasi*-reversible (by looking at the small peak separation *i.e.* difference between potential of reduction and oxidation peak).[134] By increasing substrate concentration, the K_M for the cofactor was calculated to be 39 μM at –0.37 V vs. SHE potential (pH 8).[134] This value was consistent with the value for K_M obtained using conventional biochemical assays using reduced ferredoxin.[131] The voltammetry result described by Siritanaratkul *et al.* proved that ITO replaces Fd, as the metal oxide is able to give or receive electron to and from FNR.

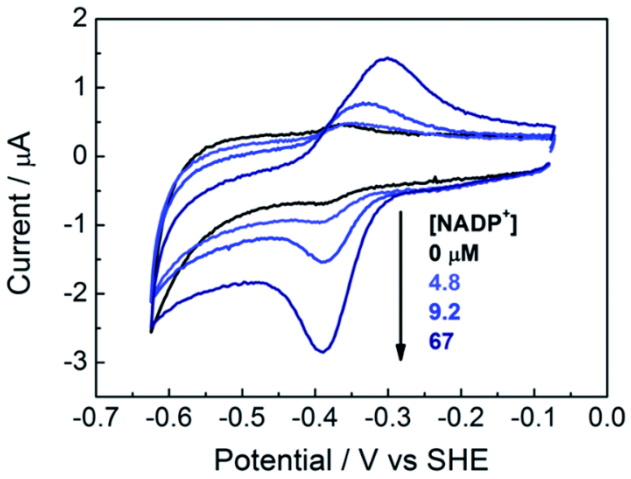


Figure I-12. Turnover peaks of the FNR@ITO electrode. Cyclic voltammetry (stationary, pH 8, 20°C) of an FNR@ITO/PGE electrode. The non-turnover peaks are shown in black. Addition of increasing concentration of $NADP^+$ causes the formation of catalytic peaks, demonstrating *quasi*-reversible cofactor oxidation and reduction. Figure reprinted with permission from Siritanaratkul *et al*,[134] published by The Royal Society of Chemistry.

The described electrochemical leaf system has the potential to be an extremely stable platform for organic synthesis and biocatalyst discovery. The

system can be coupled with any NADPH-dependent enzyme to perform organic synthesis via cofactor regeneration, with very small amounts of cofactor required (between 0.5 to 20 μM). As a proof of concept, the system was initially coupled to a glutamate dehydrogenase (GLDH). GLDH is a hexamer able to drive the reductive amination of α-ketoglutarate to L-glutamate in the presence of ammonium and NADPH. By using the FNR@ITO/Ti electrode and applying a small overpotential of 50–60 mV, it is possible to drive the reduction of $NADP^+$ while NADPH is re-oxidized by GLDH. The proposed new cofactor regeneration system can be driven electrochemically or by utilizing a hydrogen or air fuel cell, all methods provide very high turnover numbers of >10000 TTN.[134,139,144,145]

Part of the results of this thesis contributed to the discovery that not only FNR is entrapped within the electrode nanopore, but also the NADP(H)-dependent dehydrogenase. The co-localization of the two enzymes causes a massive increase in the reaction rate, which is measured directly as current. This is because the effective concentrations of the enzymes and cofactor massively increase so that diffusion distances are minimized. This principle is not unprecedented, for example in biology where co-operating catalysts are entrapped within tiny enclosure of membranes within organelles, such as the interspace membrane in chloroplast and mitochondria, to ensure fast and efficient catalysis. The notation used in this thesis to describe this confinement in the case of FNR and a secondary NADP(H)-dependent enzyme is (FNR+E2)@ITO/support.

1.6.3. The nanoconfinement effect

The nanoconfinement effect will be demonstrated in this thesis (see Section 2.4.2.5) and has been described in other publications from our group.[90,139,146] Nanoconfinement of FNR and E2 within the electrode nanopore gives crucial advantages to catalysis: (i) a much higher effective concentration of the enzymes is achieved and (ii) the diffusion distance of the cofactor becomes tiny. As a result, catalysis becomes very efficient. The only enzyme which needs direct electron transfer with the electrode is FNR, providing a report on the rate of catalysis at each time point of the reaction. **Figure I-13** explains the concept. Indium tin oxide nanoparticles can be electrophoretically deposited on a conducting support and FNR binds tightly to the electrode and establishes direct electron transfer. Cyclic voltammetry at this stage gives information on the FNR coverage by looking at the non-turnover peaks (as described for **Figure I-11**) and introduction of $NADP^+$ gives rise to the catalytic peaks observed in **Figure I-12**. Introduction of E2 in presence of a reactant causes a dramatic change in the electrochemistry (see below).

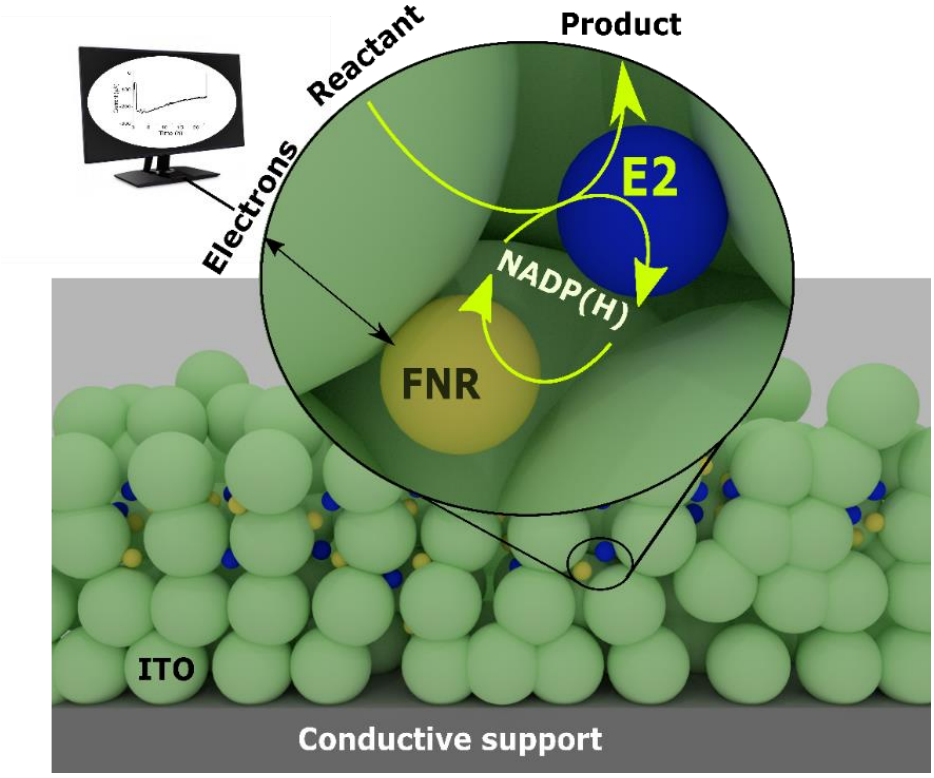
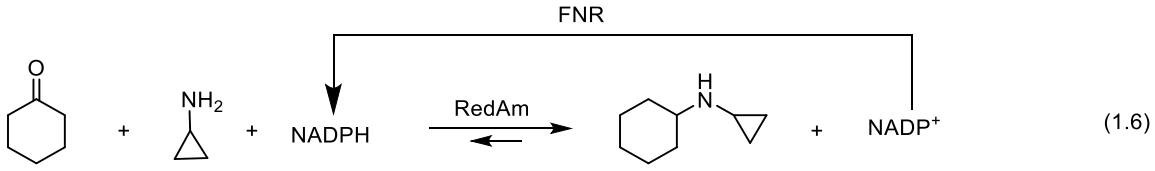


Figure I-13. A representation of the electrochemical leaf in action. An ITO nanoporous layer is made by electrophoretic deposition of ITO nanoparticles on a conductive support, such as ITO glass, titanium foil or PGE. FNR binds tightly to the electrode and establishes direct electron transfer with the electrode. By applying a potential, the enzyme can catalyse the oxidation or reduction of NADPH. When a secondary NADPH-dependent dehydrogenase (E2) is introduced, a massive enhancement of catalysis is obtained because of minimized diffusion distances and an increase of effective enzyme concentration. The rate of the reaction is read at each time point of the reaction as an electrical current.

One example of E2 used by Megarity *et al.*[139,146] was a reductive aminase (RedAm) from *Aspergillus oryzae*[147], an enzyme driving the reductive amination of cyclohexanone via NADPH in a solution containing cyclopropylamine. The resulting reaction (not showing the electron source or sink *i.e.* the ITO electrode) is described in the equation below (1.6):



(1.6)

Figure I-14 shows the effect of adding E2 (RedAm) in a CV experiment. Introduction of RedAm caused a large enhancement of reductive current: when a reductive potential is applied NADPH produced by FNR is immediately reoxidized by RedAm to drive the reductive amination of cyclohexanone. The black trace shows a CV (stationary conditions) in a buffer containing cofactor (5 µM NADPH), cyclohexanone and cyclopropylamine before introduction of RedAm. Injection of RedAm caused (after 3 minutes of purging the solution to remove O_2 introduced with enzyme injection) a massive catalytic enhancement and the shape of the voltammogram lost its peak-shape and became sigmoidal (red trace): due to RedAm activity $NADP^+$ is never depleted at the electrode (hence, the loss of peak-feature, for more information see Section 7.1.6.) The resulting CV shows the enhanced catalytic activity of the new catalyst (FNR+RedAm)@ITO/Support, driving the reductive amination of cyclohexanone. In electrochemistry current is proportional to the catalytic rate. During CV experiments it was observed upon introduction of E2 that the reductive current was increasing after each scan, suggesting that E2 was also binding to the electrode, increasing the rate of the reaction.

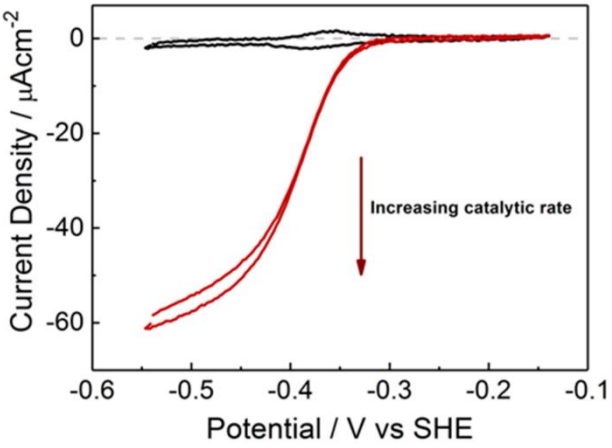


Figure I-14. Coupling of RedAm to the electrochemical leaf. Reductive amination driven by the (FNR+RedAm)@ITO/PGE electrode (0.03 cm^2) in buffer containing 5 µM $NADP^+$, 20 mM cyclohexanone, 0.2 M cyclopropylamine. Black trace: before addition of RedAm. Red trace: after addition of RedAm. After each scan the reductive current kept growing. Figure reprinted with permission from Megarity *et al*.[139]

Proof that E2 is binding to the ITO electrode was first confirmed with an alcohol dehydrogenase (ADH from *Thermoanaerobacter ethanolicus*)[148], driving the oxidation of (S)-(+)-4 phenyl-2-butanol using $NADP^+$. The complete coupled scheme with FNR is shown in equation 1.7:

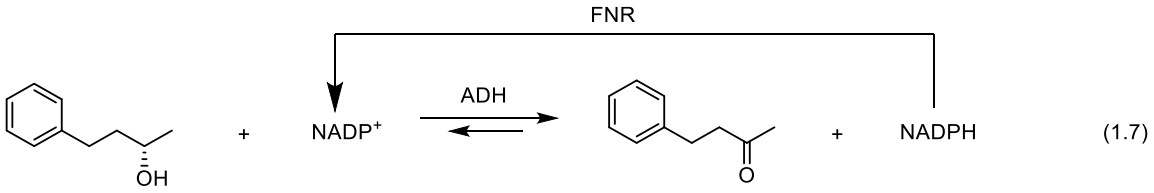


Figure I-15 shows the chronoamperometric experiment described by Megarity *et al*.[139,146] During a chronoamperometry experiment, the current (rate of the reaction) is monitored against time while the potential is held constant (in **Figure I-15**, +0.08 V vs. SHE). This potential applied is oxidative so that FNR can drive NADPH oxidation to $NADP^+$. Injection of ADH to the bulk solution enhances the rate as $NADP^+$ is now immediately converted back to the reduced cofactor, NADPH, which

is re-oxidized by FNR. It is important to notice here that injection of ADH causes a gradual growth of current, instead of a sharp increase of rate, suggesting that the enzyme was binding to the electrode over time (**Figure I-15**). The fact that the two enzymes (FNR and E2) were coming together in the electrode nanopores was increasing the overall rate. A buffer exchange experiment was carried out by Megarity *et al.* to prove that during the initial current growth ADH was binding within the electrode nanopores.[139,146]

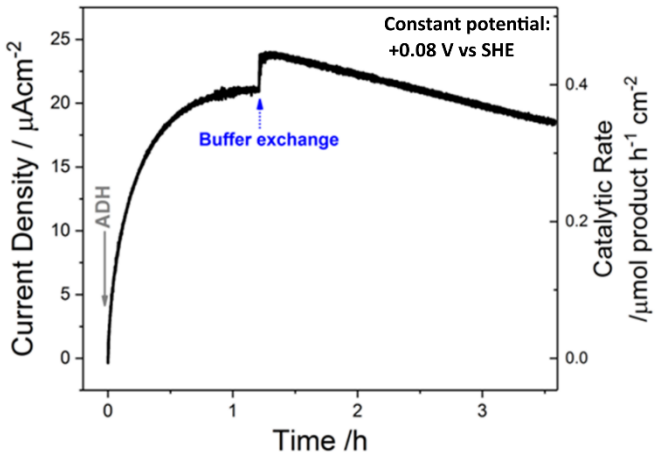


Figure I-15. The effect of nanoconfining E2. Chronoamperometry (+0.08 V vs. SHE, 20°C, 1000 rpm) for the oxidation of (*S*)-(+)-4 phenyl-2-butanol by a (FNR+ADH)@ITO/PGE electrode. Buffer containing 5 µM $NADP^+$ and 20 mM (*S*)-(+)-4 phenyl-2-butanol. ADH was injected to 0.3 µM (grey arrow). In blue a buffer exchange was performed to prove ADH binding. Figure reprinted with permission from Megarity *et al*.[139]

Briefly, after 1.5 hours (labelled as buffer exchange in **Figure I-15**) the experiment was paused, the experiment solution was discarded and the electrochemical cell was thoroughly washed. Then, fresh buffer with fresh substrate and cofactor at the same initial concentrations used, was added. Importantly no enzyme was re-injected. Nevertheless, the reaction rate was preserved, and the rate was higher than before buffer exchange, as indicated by the increase in current following buffer

exchange. Megarity *et al.* showed that the typical current enhancement upon E2 injection was not observed if E2 was injected in solution but entrapped within a tight membrane, preventing the enzyme from binding the nanopores.[146] These results therefore indicate that the only reaction that could be taking place and providing the current response observed, is derived from the interaction of FNR, E2, substrate and cofactor contained in the nanopores of the electrode (see **Figure I-13**).

1.7. Outline

A central aim of this Thesis is to further investigate the Electrochemical Leaf and to identify new applications and directions of the technology. The Electrochemical Leaf replaces part of photosynthesis and in Chapter II and III the overall mechanism of oxygenic photosynthesis was mimicked: the resulting system was able to oxidise water and reductively incorporate CO_2 into an organic precursor via NADPH cycling by using visible light. Chapter II describes the coupling of FNR to a new E2, the malic enzyme (MaeB), which drives the reductive carboxylation of pyruvate (C3) to malate (C4) via NADPH cycling. The Chapter includes cloning, electrochemical results and highlights the unprecedented power of monitoring the current (rate) to optimize a biochemical reaction. In Chapter III, the developed system was coupled to a PEC-PV system to drive light-only reductive carboxylation using water as electron donor. This Chapter also demonstrates an alternative direction for artificial photosynthesis to produce, rather than simple fuels as H_2 or CO, more complex chemicals that are more cost-effective and as such can eventually compete with fossil fuels.

Chapter IV shows that it is possible to “plug-and-play” any natural or artificial cascade within the electrode nanopore provided that one step is NADP(H)-dependent. The proof-of-concept will be demonstrated with a 5-enzyme cascade entrapped within the electrode nanopore to drive the reversible amination of pyruvate to aspartate. The applications of the Electrochemical Leaf can be extended to one-pot multi-enzyme biocatalysis, sensing and for the study of systems biocatalysis.

Chapter V introduces a new concept of using the Electrochemical Leaf as a high specific screening method for directed evolution of oxidoreductases: the nanoconfinement effect makes it possible to detect enzyme catalysis even from cell lysate eliminating the need of protein purification. This discovery can be helpful for the development of a biosensor for biocatalyst discovery and evolution.

Chapter VI contains the conclusions and future perspectives and Chapter VII the theory to understand this thesis and the material and methods section.

Chapter II

2. Introduction of the malic enzyme in the electrochemical leaf

2.1. Abstract

Reduction of CO_2 via a C3 to C4 reaction is achieved very efficiently by entrapping two enzymes within a nanoporous metal oxide electrode. The enzymes used are ferredoxin $NADP^+$ reductase (FNR) from *C. reinhardtii* and malic enzyme (ME) (MaeB from *E. coli*). The latter catalyses the NADPH-dependent reversible carboxylation of pyruvate (3 carbons) to malate (4 carbons), while the former establishes direct electron transfer with the electrode to drive $NADP^+$ reduction, thus regenerating NADPH. Entrapping the two catalysts is the key to ensure efficient catalysis as the distances between the two enzymes become so small (pore size ≈ 50 nm) that diffusion distances are minimised, and the effective concentration of enzymes is massively enhanced. The resulting electrocatalyst is able to drive efficient CO_2 reduction at a potential more positive than proton reduction even under low CO_2 atmosphere.

2.2. Introduction

Reduction of atmospheric CO_2 is of great interest, as it could promote the transition to a circular economy (zero net emitted carbon) where CO_2 can be re-used to supply the chemical industry with feedstocks and fuels.[149] This would have great advantages for environmental reasons and energy security. In nature, the circular economy is not a novel concept: every year 350 gigatons of CO_2 are fixed through the well-known Calvin cycle (90%) and the rest is handled by other autotrophic pathways.[150] Developing a more efficient process than photosynthesis could help towards building a sustainable society, not reliant on fossil fuels.

Ethylene, formate and carbon monoxide are examples of useful feedstocks for the chemical industries which could be produced directly from CO_2 reduction. However, its reduction is chemically extremely challenging, as a more reducing potential than H^+ reduction is required (–0.11 V vs. RHE for CO production).[151] Besides H_2 as the main product, a mixture of carbon compounds is often obtained which renders the faradaic efficiency (FE) very low (FE is the percentage of the total passed charge that is used to generate the desired product, see Section 7.1.8.).[152–154] Nevertheless, a mixture of CO and H_2 (called syngas) is of high interest because it can be used in several applications, for example as a feedstock for the production of alcohols and lubricants.[155]

In a hypothetical process the final product cost needs to be low to compete with fossil fuel-based systems. Therefore, the development of technologies and catalysts which are reasonably cheap is urgently needed.[156] Several materials have been studied for CO_2 reduction including Au-, Pd- and Pb-based catalysts.[156–158] A very promising candidate is based on Cu materials which have been reported to give a higher selectivity for the desired product. Encouragingly, promising FEs

have been reported for CO and formate (on average 79% and up to 90%) with high current densities (70–100 mA/cm^2).[159] According to economic analysis, electrocatalytic CO_2 reduction to 1 carbon (C1) and 2 carbons (C2) could soon be cost efficient with the continuous decrease in cost of electricity. However, longer and more complex chemicals are still challenging because of the catalysts' low selectivities.[160] In a system proposed by De Luna *et al.* renewable syngas could be used to feed a microbial factory to produce long-chain carbon products such as alcohols.[160]

Enzymes are efficient electrocatalysts and their use can lead to high FE. Moreover, enzymes offer a way to develop more effective synthetic catalysts for bioenergy production and high value products. Two enzymes – carbon monoxide dehydrogenase (CODH) and formate dehydrogenase (FDH) – are able to perform CO_2 reduction under mild conditions to give CO and formate, respectively. These enzymes have been interfaced with a conductor or a semiconductor material for electro- and photo-electrochemical studies.[59,89,161–163]

Generating longer carbon chains is of great interest, and for this purpose, another class of enzymes, carboxylases, can be used to build a biohybrid- or biotechnological- process to mimic photosynthesis: in photosynthesis in the light-independent reactions CO_2 is fixed through a cycle which results in reductive carboxylation of an organic precursor through NADPH cycling (see Section 1.2.). In nature the carboxylation step is performed by RubisCO, which is a slow enzyme and undergoes a side-reaction with oxygen. Phosphoenolpyruvate (PEP) carboxykinase and pyruvate carboxylase are more efficient carboxylases and could be used for designing new CO_2 fixation pathways. Phosphoenolpyruvate carboxykinase, for example, was overexpressed in *Synechocystis* PCC 6803 and

was demonstrated to support enhanced growth and production of ethylene.[164,165] Several other approaches have been under study, such as directed evolution of RubisCO and implanting a CO_2 reduction pathway in *E. coli.*[166–168] A notable study was published by Schwander *et al.*, who developed a synthetic CO_2 reduction cycle, called CETCH, which was more efficient than any natural one.[150] Crucial for this was the discovery of a new class of carboxylases, enoyl-CoA carboxylases/reductases (ERCs), which convert crotonyl-CoA to enoyl-CoA with a catalytic efficiency 2–4 times higher than RubisCO and no oxygen sensitivity. The synthetic cycle takes two CO_2 molecules and with propionyl-Coenzyme A (CoA) generates glyoxylate as a byproduct. The authors selected 17 enzymes (including those for cofactor regeneration), where selection was based solely on the desired biochemistry. Through cycles of evolution the selected enzymes were improved to optimize the flux through the cycle.[169]

In this Chapter, FNR was coupled to a NADPH-dependent carboxylase enzyme as E2. The goal (investigated in Chapter III) was to build a light-driven NADPH-dependent CO_2 reduction system using water as electron donor, mimicking oxygenic photosynthesis.

The first element to decide was which carboxylase enzyme to use. The best candidate was an ERC carboxylase (see above) but it was not used because of substrate availability and need for CoA. Phosphoenolpyruvate carboxykinase and pyruvate carboxylase were also avoided to decrease complexity given by the requirement to build a cascade reaction. PEP carboxykinase drives the carboxylation of phosphoenolpyruvate to oxaloacetate, while the nicotinamide cofactor is not a substrate. Hence, it would be necessary to add a NADPH-dependent dehydrogenase using oxaloacetate to detect a current with the

Electrochemical Leaf. Pyruvate carboxylase does not use NADPH either, as it drives the ATP-dependent carboxylation of pyruvate to oxaloacetate.

Malic enzyme (ME), a decarboxylating-malate dehydrogenase, was chosen to demonstrate the proof of concept. This is a ubiquitous class of enzymes capable of catalysing the reversible oxidative decarboxylation of malate to pyruvate using $NAD(P)^+$ as oxidant. By changing the assay conditions ME can also drive the reverse reaction, given the small $\Delta_r G$ (–7 $kJmol^{-1}$).[99,170–172] In prokaryota, this enzyme (among others) connects the glycolytic pathway to the tricarboxylic acid (TCA) cycle, allowing an organism to grow on media containing TCA intermediates or substrates metabolised to acetyl-CoA.[171] In plants and algae ME is involved in C4 photosynthesis.[26] The enzyme is reported to be more active in the oxidative direction, but its use for reductive carboxylation has also been investigated previously[171]: a common feature was multi-step electron transfer using several redox mediators such as methyl viologen.[56,173]

The best available ME variant to drive the reductive carboxylation system was found in *Thermococcus kodarensis*, as it was reported to catalyse either direction with no preference.[174] However, ME was eventually cloned from *E. coli* (DH5-α) due to the unavailability of the *T. kodarensis* strain. *E. coli* contains two MEs, an NAD^+-dependent ScfA, and an $NADP^+$-dependent MaeB; the former is faster in the carboxylation reaction but slower with $NADP^+$ (K_M for NAD^+ 68.8 µM and for $NADP^+$ 1 mM, k_{cat} with NAD^+ 82.7 s^{-1} and with $NADP^+$ 12.4 s^{-1})[171]. Thus, MaeB was selected instead (K_M for $NADP^+$ 41.5 µM and k_{cat} with $NADP^+$ 66.6 s^{-1}).[171]

This two-enzyme carboxylation system was driven within the electrode nanopores to catalyse the reductive carboxylation of pyruvate (3 carbons, C3) to malate (4 carbons, C4) as shown in **Figure II-1**. Briefly, FNR binds tightly within the

nanoporous indium tin oxide electrode. Upon application of a reducing potential FNR reduces the nicotinamide cofactor through its FAD centre (see Section 1.6). The goal of this project is to demonstrate the carboxylation of pyruvate to malate via NADPH cycling by using ME as E2.

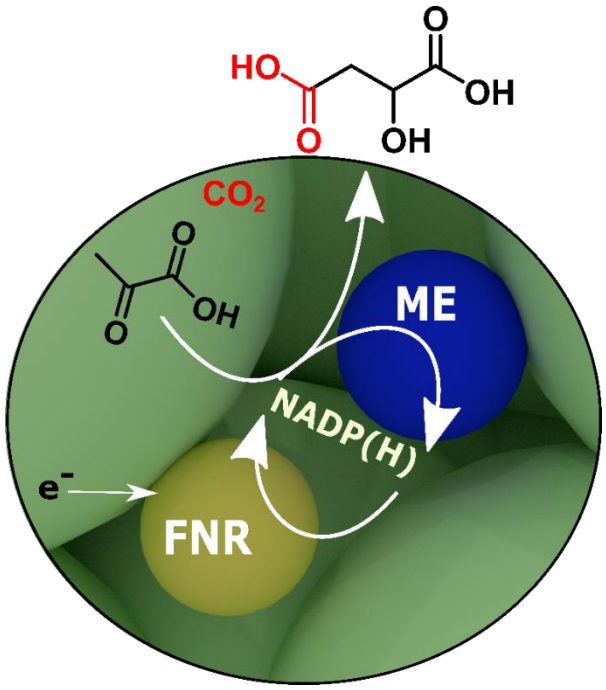


Figure II-1. The proposed nanoconfined electrode for the reductive carboxylation of pyruvate to malate. FNR binds tightly to a nanoporous ITO electrode and facilitates direct electron transfer, upon application of a potential, so that the nicotinamide cofactor can be reduced. FNR is coupled to the reversible decarboxylase, ME which can re-oxidize NADPH when it catalyses the reductive carboxylation of pyruvate to malate.

2.3. Aim of the Chapter

The aim of this Chapter is to introduce an NADPH-dependent reductive carboxylase, ME, within the electrode nanopores to drive the reductive carboxylation of pyruvate (C3) to malate (C4) via NADPH cycling. To achieve this aim, ME (MaeB from *E. coli*) was cloned, overexpressed and purified from *E. coli*. The purified protein was then coupled to FNR and the resulting electrochemistry investigated.

2.4. Results and Discussion

2.4.1. Cloning and expression of MaeB

Based on the DNA sequence of maeB (*E. coli*) reported in database (KEGG)[175], the following primers were designed to amplify the gene by colony PCR, using *E. coli* DH5-α cells:

Forward 5′-

GGTGATGATGATGACAAGATGGATGACCAGTTAAAACAAAGTGCA

C-3′

Reverse 5′-GGAGATGGGAAGTCATTATTACAGCGGTTGGGTTTGCGC-3′

Amplification was confirmed using electrophoresis by running the PCR sample on a 0.8% agarose gel. **Figure II-2** shows a band of the expected size (2.2 kb), which is absent in the control. The purified PCR product (see Section 7.3.1.1.) was inserted into a plasmid (pLATE51) by ligation-independent cloning and used to transform *E. coli* DH5-α cells (for more details see Section 7.3.1.4.). After plasmid purification, the correct DNA sequence was confirmed by SourceBioScience (Oxford).

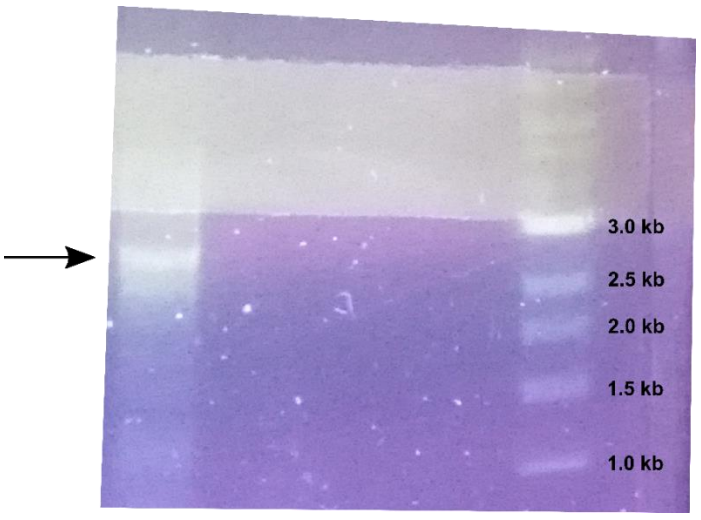


Figure II-2. **Amplification of MAEB by colony PCR.** 0.8% Agarose gel (100 V) loaded with the products of the colony PCR performed to amplify MaeB in *E. coli*.

The pLATE51 aLICator vector allows inducible expression by IPTG and insertion of an N-terminal His-tag for purification through a Ni^{2+}-column.

The first protocol used was similar to that used for FNR purification reported by Siritanaratkul *et al.* with the same vector (pLATE51).[134] However, the concentration of ME after eluting through a Ni^{2+} column was too low to proceed with the electrochemical experiments. As previously described, increasing induction time to 20 hours at 15°C enhanced the final yield.[171,172]

Figure II-3-A shows the result of an unoptimized elution trace using a linear imidazole gradient. A large contaminant peak was observed (Peak 1), and solution assay showed that the protein of interest was established to be present in elutions corresponding to the second peak (Peak 2).

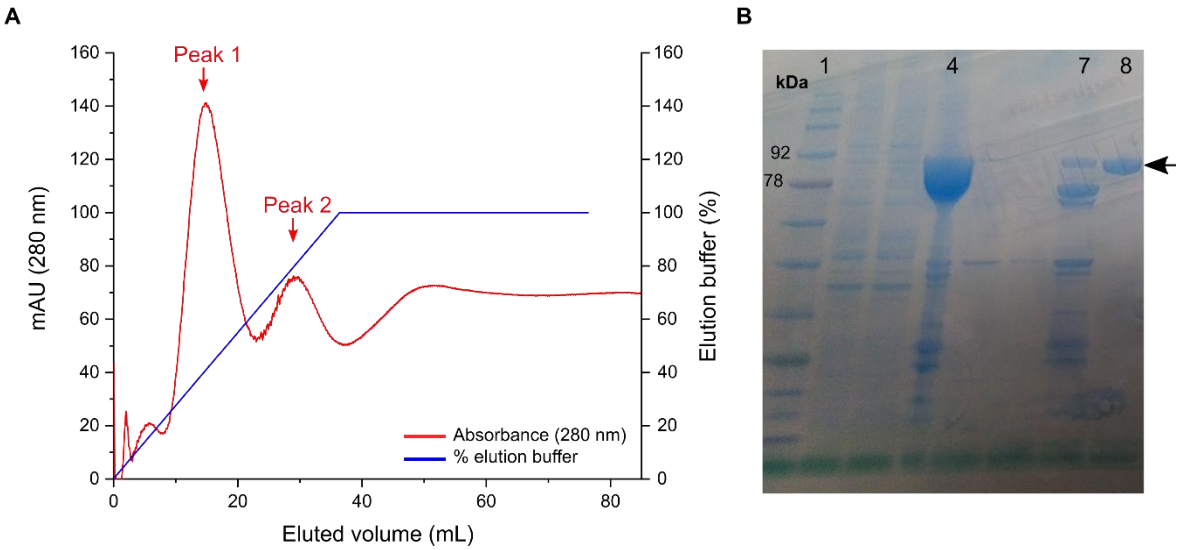


Figure II-3. Unoptimized ME purification by Ni^{2+} chromatography. A. Elution of ME from BL21 *E. coli* cells through a Ni^{2+} column. ME corresponds to the second peak (Peak 2) as confirmed by SDS-gel and solution assay. **B.** SDS-gel showing pooled and concentrated protein (lane 4) and fractions from the elution trace in Panel A (lane 7: elution corresponding to the maximum of peak 1, and lane 8: elution corresponding to the maximum of peak 2); MW of monomeric ME: 80 kDa.

Figure II-3-B shows the SDS-page of the protein eluted in **Figure II-3-A**: lane 4 shows the pooled samples after concentration to 1 mL (using a 50kDa cut-off

membrane), while lane 7 and 8 correspond to the protein fractions taken immediately after elution. Lane 7 contains the protein fraction at the absorbance maximum of peak 1 and lane 8 likewise for peak 2. The results show that a contaminant was eluted at lower imidazole concentration. The nature of the contaminant(s) is unknown, but it absorbed at 420 nm (data not shown). By adding 50 mM imidazole to the washing buffer the contaminant protein was removed. Moreover, to increase purity further, the IPTG concentration was decreased to 0.5 mM and the resuspension buffer was supplemented with protease inhibitors. The result is shown in **Figure II-4-A**: importantly a band at 420 nm was not visible. After concentrating the fractions (from 20 to 45 mL), the SDS-gel (**Figure II-4-B)** showed a significant increase in purity compared to that shown in **Figure II-3-B**. Moreover, elution of the contaminant during the washing step (prior to the elution) was visible on the chromatogram (data not shown).

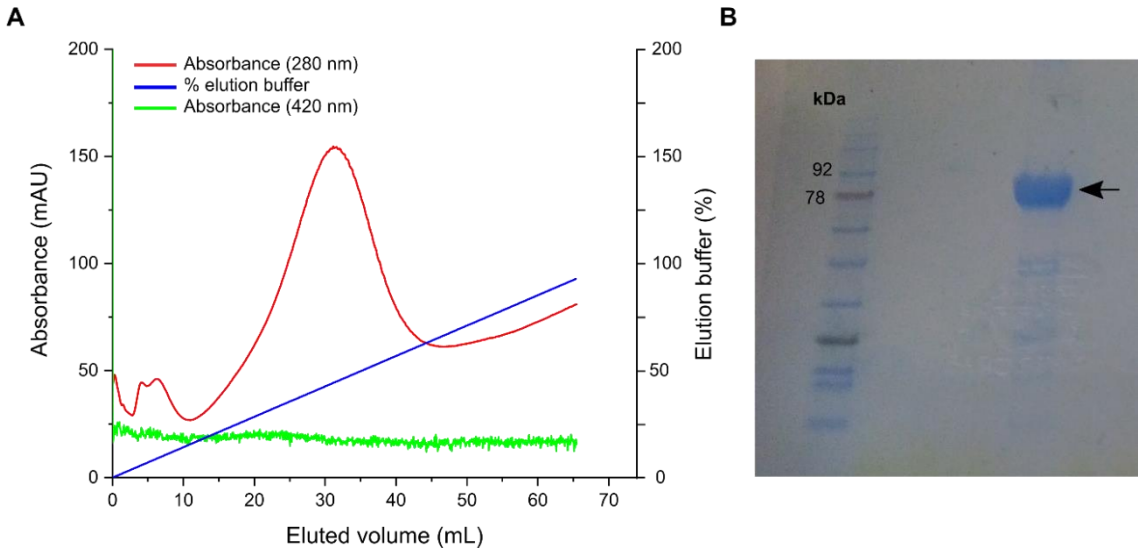


Figure II-4. Purification of ME by Ni^{2+} chromatography. A. Elution of ME from BL21 cells through a Ni^{2+} column. A single peak was obtained whereas no absorbance at 420 nm was observed. **B.** SDS-gel showing the concentrated ME (MW: 80 kDa).

Prior to use, desalting was performed to remove excess imidazole from the enzyme sample. Resulting fractions were confirmed to contain ME by an activity test using

a standard solution assay, which measures the change in absorbance at 340 nm, monitoring NADPH production; $NADP^+$ absorbs at 260 nm, while the reduced form has two absorption maxima, at 260 and 340 nm.[176] The buffer used for the solution assay, based on literature data, was 50 mM Tris, 4 mM $MgCl_2$, 50 mM malate, 1 mM $NADP^+$.[171] **Figure II-5** shows the results obtained with different fractions. The control (black trace) obtained after injection of buffer into the cuvette (at time t = 0) showed no change in absorbance. When an aliquot (5 µL) of fraction containing enzyme was injected into the cuvette, catalysis was observed (fractions 5,6 and 7), as the absorbance at 340 nm increased indicating NADPH production. The enzyme was not active when malate or dications (Mg^{2+} or Mn^{2+}) were not included. This result is important as it is known that ME requires these metal ions for catalysis.[171]

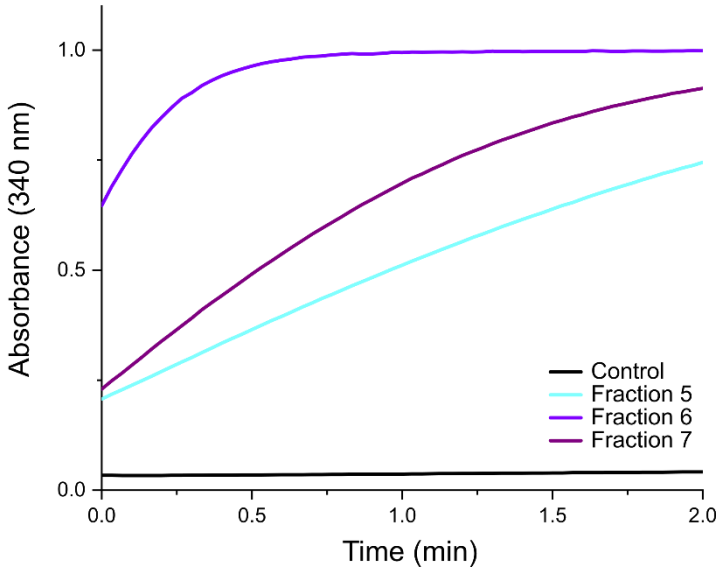


Figure II-5. Detection of ME activity in eluted fractions. Solution assay of ME by observation of NADPH production (malate oxidative-decarboxylation), monitoring absorbance at 340 nm. The assay was performed after a desalting step where the eluted volumes were manually collected into fractions. After improving the purity, the desalting step was replaced by dialysis for subsequent purifications.

2.4.2. Electrochemical results

2.4.2.1. Optimizing conditions

Cyclic voltammetry (1 mV/s, 25°C, stationary conditions, buffer containing 0.2 M HEPES, 0.1 M $NaHCO_3$, 4 mM $MgCl_2$, pH 7.5) was performed to confirm successful preliminary coupling of ME with FNR. Results are shown in **Figure II-6**. First, an ITO electrode was prepared by electrophoretic deposition (EPD, see Section 7.3.2.1.1.) of ITO nanoparticles on a conductive ITO glass slide. A small aliquot of FNR (5 µL, stock 1.8 mM) was dropped on the electrode and left to adsorb for 3 minutes at RT after which time, the electrode was rinsed with ultrapure (Milli-Q)-H_2O to remove unabsorbed enzyme. The black trace shows the peaks resulting solely from oxidation and reduction of the FAD centre of FNR (non-turnover peaks), hence confirming successful loading of FNR (**Figure II-6-A,** see Section 1.6). Then $NADP^+$ was added to a final concentration of 50 µM (**Figure II-6-B**) and the solution was bubbled for 1 minute with argon to remove introduced O_2. If present, oxygen gas will be reduced at the electrode convoluting the results. Note that the same procedure was carried out after each injection. Introduction of $NADP^+$ under stationary conditions caused the formation of catalytic peaks: when going from an oxidative to a reductive potential, at –0.35 V vs. SHE $NADP^+$ reduction occurs and gives rise to a reductive current. Under stationary conditions $NADP^+$ is quickly depleted at the electrode surface so a peak-signal is obtained (*i.e.* the process is diffusion-controlled). Moreover, reduced NADPH slowly diffuses from the electrode surface to the bulk solution. Reduced cofactor left at the electrode surface is reoxidised when the potential is swept back to an oxidative value. The oxidative current increases and quickly decays because of NADPH

depletion, hence an oxidative peak is observed (for a more detailed explanation see Section 1.6 and 7.1.6).

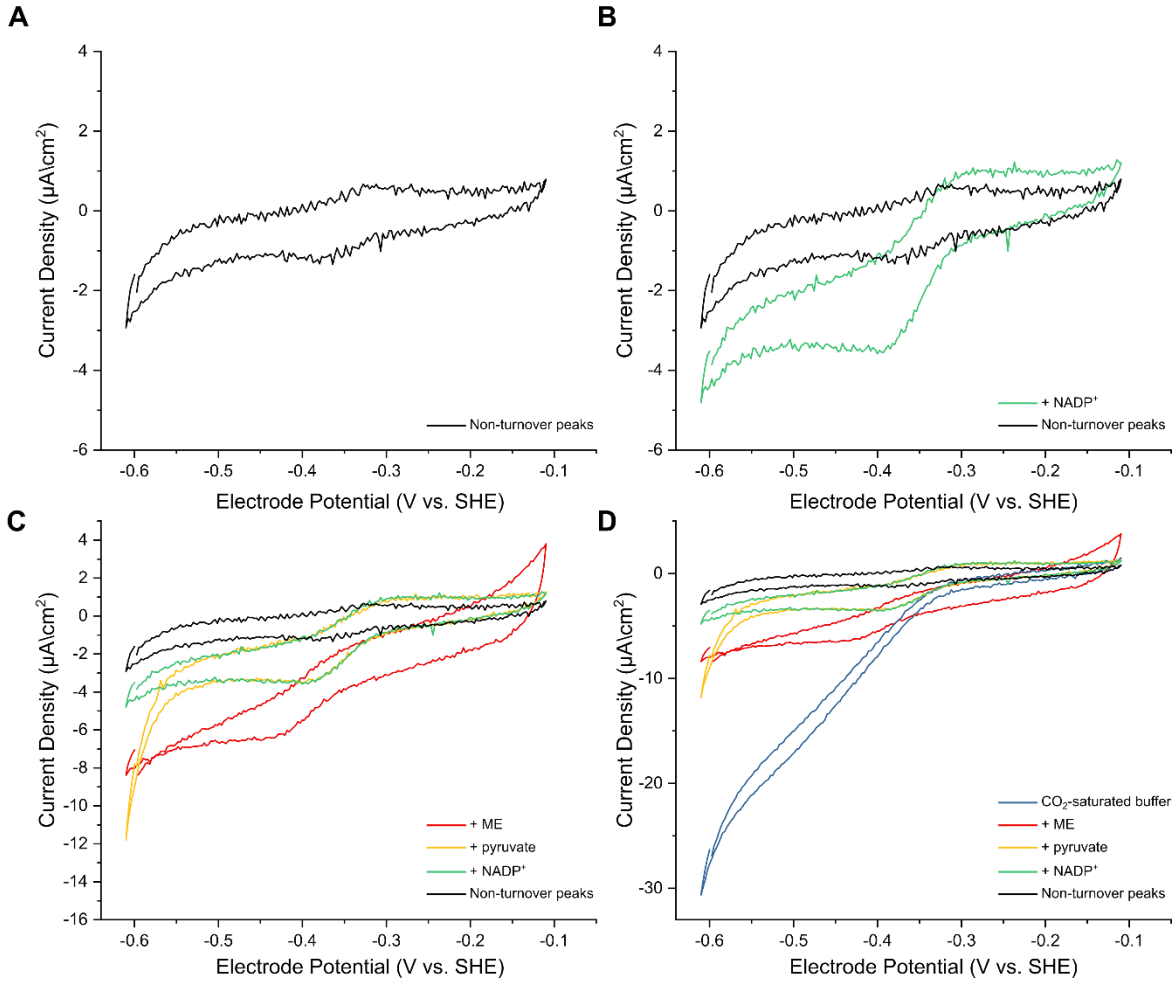


Figure II-6. Cyclic voltammetry: preliminary coupling of FNR@ITO/ITO glass with ME. Note that after each injection the solution was flushed for 3 minutes with Ar or CO_2. In chronological order: (**A**), black trace: non-turnover peaks; (**B**), green trace: injection of $NADP^+$ to a final concentration of 50 µM; (**C**), yellow trace, injection of pyruvate to a final concentration of 50 mM and red trace, ME to 2.5 µM; (**D**), blue trace: measured after saturating the buffer with 100% CO_2 for 10 minutes followed by maintaining a constant CO_2 atmosphere. CV (1 mV/s, 25°C) under an Ar-atmosphere of a (FNR+ME)@ITO electrode (1cm^2) in buffer (pH 7.5) containing 0.2 M HEPES, 0.1 M $NaHCO_3$,4 mM $MgCl_2$. CE: Pt; RE: Ag/AgCl.

Injection of pyruvate (to 50 mM) in the absence of ME did not affect the voltammetry except for the formation of a slight reduction tail commencing at -0.55 V vs. SHE (**Figure II-6-C,** yellow trace). This suggests that the substrate is non-catalytically electrochemically active at lower potentials, which therefore should be avoided if

possible. Although the observed reduction tail could be a problem, the high negative potentials at which this signal was observed are not necessary with the electrochemical leaf. Instead, at the potential required by the (FNR+ME)@ITO/Ti electrode (0.4-0.45 V vs. SHE at pH 7.5) side reactions do normally not occur. Nevertheless, it is important to first ensure whether the substrate of a reaction under investigation is electrochemically active at the electrode when investigating a new E2. An aliquot of ME was then injected to give a concentration of 2.5 µM and the corresponding trace is shown in the red trace: the voltammetry becomes slightly sigmoidal, showing very slow catalysis possibly due to CO_2 provided by $NaHCO_3$ slow dissociation (5 µA/cm^2, **Figure II-6-C,** red trace). Upon flushing the cell with 100% pure CO_2 for 10 minutes a sigmoidal voltammogram was obtained proving successful coupling between FNR and ME (**Figure II-6-D,** blue trace). The ME continuously re-oxidises NADPH to $NADP^+$, hence the cofactor is never depleted at the electrode. As a result, the voltammetry loses its peak-shape and becomes sigmoidal. The NADPH that is produced does not accumulate in the bulk solution because it is instantly reoxidised by ME, so the oxidative peak disappears. ME catalysis increases the concentration gradient (the flux) of $NADP^+$ towards the electrode and as a result the reductive current massively increases (**Figure II-6-D,** blue trace, see Section 7.1.6.). The large sigmoidal catalytic wave proves that there is efficient coupling between FNR and ME driving the reductive carboxylation of pyruvate to malate through NADPH recycling.

A chronoamperometry experiment was performed to gather information on the stability of the system and to generate detectable malate for product analysis. In a chronoamperometry experiment, the current is measured over time at a fixed potential. The current is proportional to turnover rate and the charge passed –

charge (C) = current (A) x time (s) – is proportional to the number of moles of formed product (see section 7.1.8.). A larger electrode surface area (14 cm^2) was used to ensure a higher conversion to malate, that would be analysable by ^{1}H-NMR. The electrode was prepared by incubation for 16 h in a stirred buffer (50 mM borate, pH 8, rt) containing FNR at a concentration of 7.2 µM. The electrode was rinsed and immersed in stirred, CO_2-saturated buffer (pH 7.5, 25°C, composition as for the CV) under an atmosphere of 100% CO_2. A potential of –0.45 V vs. SHE was applied, to drive the reduction reaction, based on the CV shown in **Figure II-6**. Results are shown in **Figure II-7**. Injection of $NADP^+$ (to 50 µM) gave rise to a reductive current attributable to the reduction of $NADP^+$ catalysed by FNR, while addition of ME caused a larger spike in current which corresponds to the reductive carboxylation of pyruvate to malate. Note again that each injection was followed by pausing the measurement and purging the solution with inert gas for 1 minute. ME catalysis increases the flux of the cofactor towards the electrode, hence, increasing the current several fold (here 10×). The current was unstable and the current trace reached the baseline level after 2.5 h. The high instability observed was an issue for product analysis, since the amount of malate produced was too low for product quantification by ^{1}H-NMR.

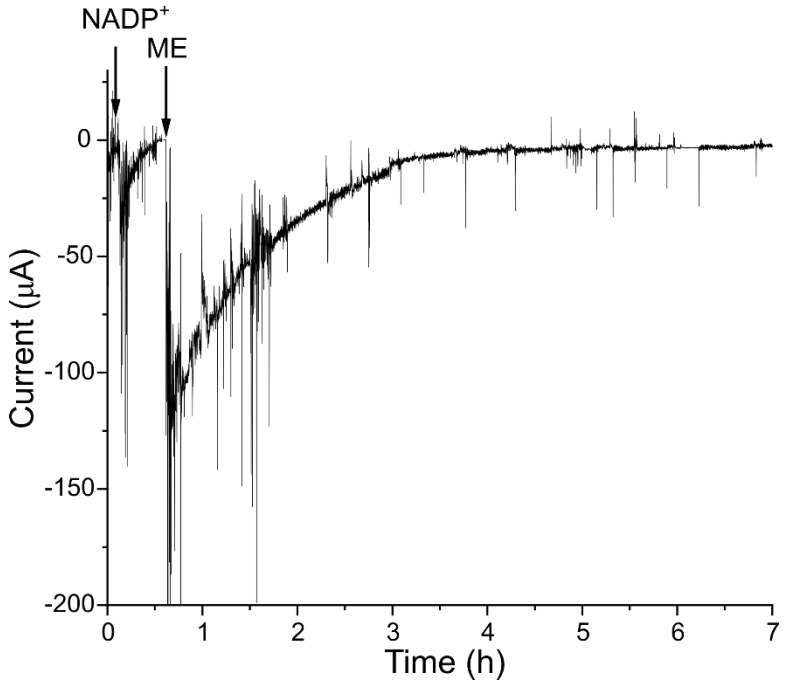


Figure II-7. Preliminary large-scale reductive carboxylation driven by the (FNR+ME)@ITO/Ti electrode and its instability. Arrows indicate the injection of $NADP^+$ to 50 μM and ME to 2.5 μM. Chronoamperometry (stirring, –0.45 V vs. SHE, 25°C, 2.5 mL) of a FNR@ITO/Ti electrode (12 cm^2) in 0.2 M HEPES, 0.1 M $NaHCO_3$,4 mM $MgCl_2$, 50 mM pyruvate.

The activity of ME is reported to be dependent on dications such as Mg^{2+} and Mn^{2+}. Chang *et al.* reported Mn^{2+} to be crucial not only for catalysis, but also to stabilise the tetrameric structure of the ME from pigeon liver.[177] It is known that Mn^{2+} precipitates quickly in a solution containing HCO_3^-, hence it was initially avoided.

Figure II-8 shows the difference in stability between chronoamperometries in a buffer containing Mn^{2+} compared to that containing Mg^{2+} (**Figure II-8** and **Figure II-7**, respectively). A chronoamperometry experiment was carried out as described for **Figure II-7**. After injection of ME, the reaction returned to the baseline just after 2.5 hours in the absence of Mn^{2+}. Reinjection of an equal concentration of ME after 11 h caused the same response: the rate obtained was similar to the first injection of ME and the reaction reached the baseline after a further 2.5 hours. This observation suggested that ME stability was the limiting factor rather than other

components of the system. When $MnCl_2$ was added to a final concentration of 4 mM after 16 h, the reductive current was not affected. Re-addition of ME after 19 h (same concentration as above and now in a buffer containing Mn^{2+}) caused a different response. The maximum current observed was similar to the value obtained after the first injection of ME, but the decay kinetics were considerably different in presence of Mn^{2+}: the reaction proceeded for 10 h instead of 2.5 h (**Figure II-8**). This observation suggests that ME unfolded irreversibly in absence of Mn^{2+} because the reaction rate was not restored after injection of Mn^{2+}.The results above proved that Mn^{2+} is required to ensure a higher stability of ME.

As expected, introduction of 4 mM $MnCl_2$ to a solution containing bicarbonate caused precipitation of highly insoluble manganese carbonate. This could cause problems over time in the electrochemistry or in the photoelectrochemistry, by accumulation of manganese carbonate, for example, between the working electrode (WE) and the counter electrode (CE) compartment or at the proton exchange membrane (PEM) used in the light-driven system (see Chapter VII for details of the setup used and Chapter III for the photoelectrochemical results).

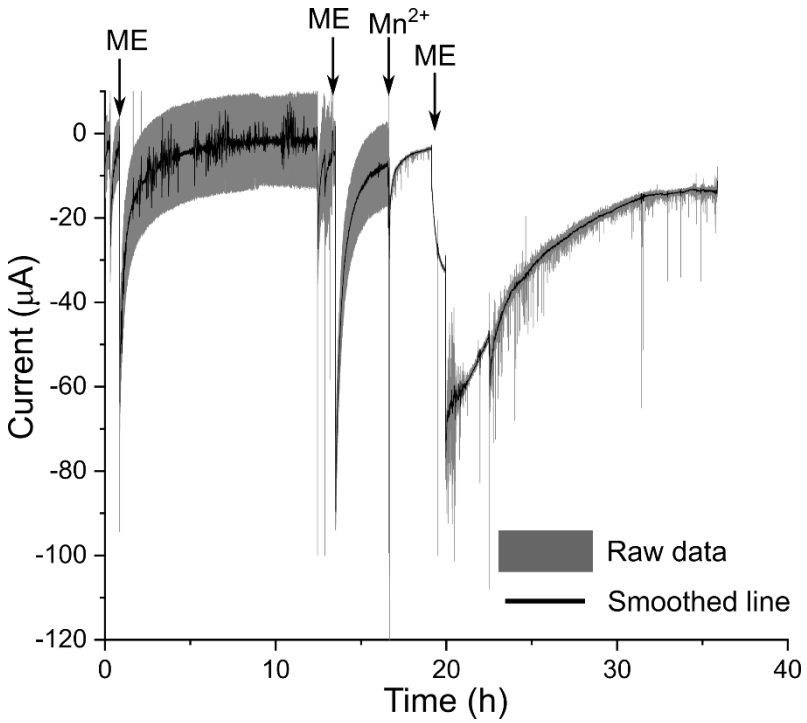


Figure II-8. The effect of introducing Mn^{2+} to a larger scale reductive carboxylation driven by the (FNR+ME)@ITO/Ti electrode. Electrode preloaded with FNR. After each injection the measurement was paused, cell solution flushed with CO_2 and measurement restarted after 1 minute. Injection of $NADP^+$ to 50 µM and ME to 2.5 µM. New enzyme was re-added in solution after 10 h. Injection of Mn^{2+} to 4 mM after 17 h. Reinjection of ME after 18 h causes formation of a new reduction current, this time stable for 10 h. Chronoamperometry (stirring, –0.45 V vs. SHE, 25°C, 2.5 mL) of an FNR@ITO electrode in 0.2 M HEPES, 0.1 M $NaHCO_3$, 4 mM $MgCl_2$, 50 mM pyruvate under 100% CO_2.

To optimise the conditions for stabilisation, smaller amounts of Mn^{2+} and different metal ions were tested in the buffer (data not shown). Ohno *et al*. reported that the carboxylation reaction is faster with potassium ions rather than sodium (5% and 2% of the forward reaction, respectively).[171,173] Hence, the effect of replacing $NaHCO_3$, with $KHCO_3$, in the presence of Mn^{2+} was investigated. Importantly, a Mn^{2+}-concentration of 1 mM did not lead to precipitation. **Figure II-9** shows that the reaction stability was greatly improved by comparing two parallel chronoamperometries: the buffer concentration in **Figure II-9-A** differs from the concentration in **Figure II-9-B** (**A**: CO_2-saturated buffer contained 0.2 M HEPES, 0.1 M $NaHCO_3$, 4 mM $MgCl_2$, 1 mM $MnCl_2$, 50 mM pyruvate, **B**: the sodium salt

was replaced by potassium bicarbonate). In **Figure II-9-A** the reaction proceeded for 3 hours and returned to the baseline, while in **Figure II-9-B** a very high current was obtained (≈ 350 µA) and in 20 h the current slowly approached 50 µA; currents of this magnitude would easily allow quantification by ^{1}H-NMR in future experiments. Additionally, the increase in current in **Figure II-9-A** is immediately followed by a rapid current decay, while in **Figure II-9-B** a growth is observed upon enzyme injection as the current keeps increasing for 2 h before slowly decreasing over the course of 20 h. The reason for this growth phase will be investigated later in this Chapter (see Section 2.4.2.5.).

Based on the previous results, all subsequent experiments were carried out in the presence of both $MnCl_2$ and $KHCO_3$. The enzyme buffer was supplemented with $MnCl_2$ (to 20 mM) and was added to the electrochemical cell upon each enzyme injection (resulting in a final concentration of 1 mM).

The electrochemical leaf appeared to offer an unprecedented way to monitor and optimize a multitude of biochemical reactions, showing how catalysis is affected at each timepoint by different conditions and interventions.

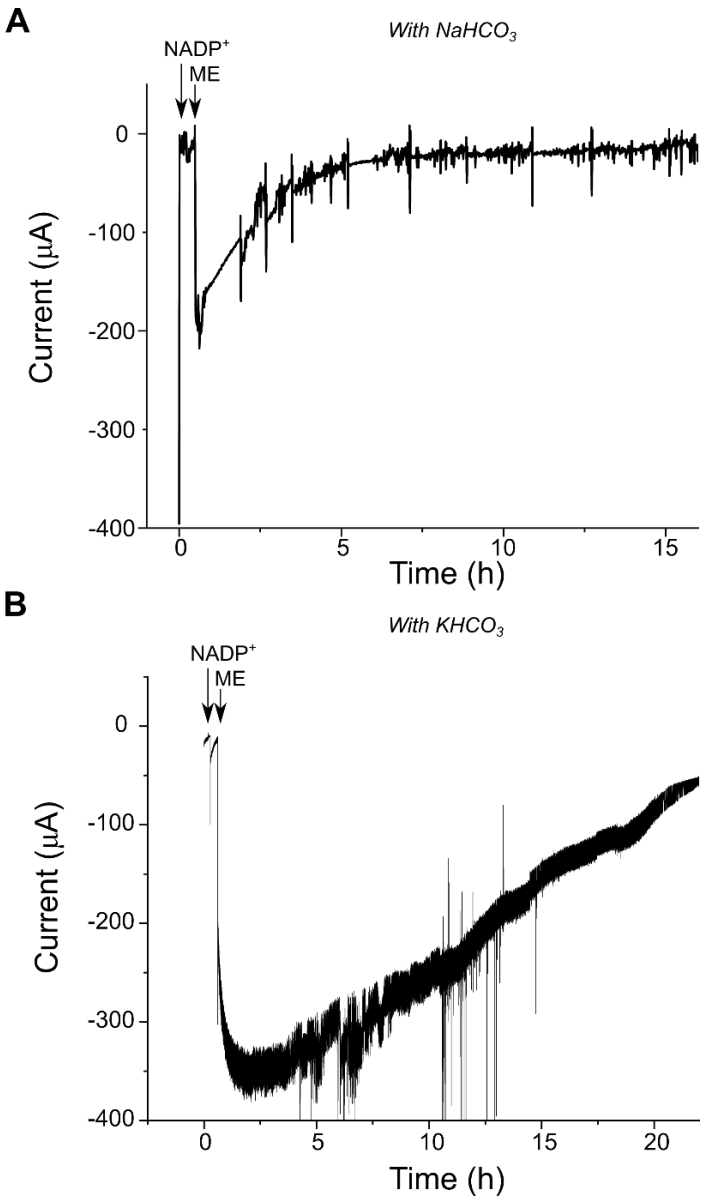


Figure II-9. Chronoamperometry showing the difference in stability with $NaHCO_3$ and $KHCO_3$. Injections of $NADP^+$ to a final concentration of 20 µM and ME to 2.5 µM. In both cases Mn^{2+} (to a final concentration 1 mM) is introduced along with the ME injection. **A. with NaHCO3:** chronoamperometry (–0.45 V vs. SHE, 25°C, surface area: 12 cm^2, 2.5 mL) of a FNR@ITO electrode in 0.2 M HEPES, 0.1 M $NaHCO_3$, 4 mM $MgCl_2$, 50 mM pyruvate under 100% CO_2. **B. with $KHCO_3$**: chronoamperometry as before in a buffer containing 0.2 M HEPES, 0.1 M $KHCO_3$, 4 mM $MgCl_2$, 50 mM pyruvate under 100% CO_2.

2.4.2.2. Reductive carboxylation

Figure II-10-A shows a CV for the (FNR+ME)@ITO/Ti electrode and the effect of product inhibition. The electrode was prepared as described previously, using titanium foil as a support. FNR was loaded by dropping 5 µL (1.8 mM stock) of enzyme solution on the electrode, and after thorough rinsing the electrode was immersed in a CO_2-saturated buffer (pH 7.5) containing 0.2 M HEPES, 0.1 M $KHCO_3$,4 mM $MgCl_2$, 50 mM pyruvate. The experiment was carried out under a 100% CO_2 atmosphere, at 25°C and at a scan rate of 1 mV/s. ME was then introduced to a final concentration of 2.5 µM (and with it, $MnCl_2$ to 1 mM). Since **Figure II-9-B** shows a lag phase upon enzyme injection, the first CV labelled as "pyruvate + CO_2" (black trace), was measured after 2 h to ensure recording the voltammetry at the current maximum. The resulting voltammogram shows a large reductive current when pyruvate (to 50 mM) was present in the solution, which corresponds to the reductive carboxylation of pyruvate to malate. Introduction of the product, malate (to 50 mM), shows the effect of product inhibition, because the reductive current is decreased to half of the original current (blue curve). The high reversibility of the system is clearly visible: only a small overpotential relative to the potential at zero current is needed to observe a reductive or oxidative current - the latter corresponding to malate oxidative decarboxylation (see section 7.1.7.). Furthermore, the point at zero current corresponds to the formal potential of the pyruvate (C3)/malate (C4) couple when equal concentrations of substrate and product are introduced. The resulting potential was –0.34 V vs. SHE, around 0.1 V more positive than proton reduction.[178]

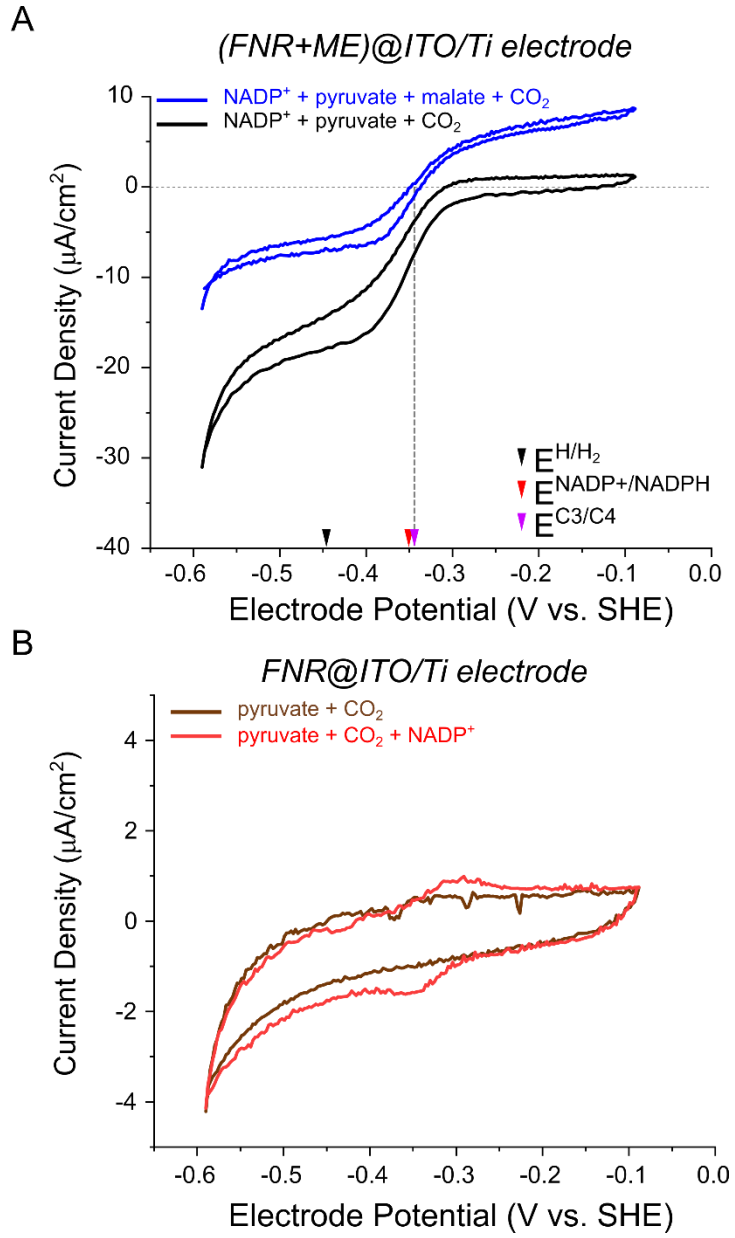


Figure II-10. Cyclic voltammetry of the (FNR+ME)@ITO/Ti electrode. A. Black trace: with pyruvate (to 50 mM). Blue trace: injection of equal concentration of malate (50 mM). CV (1 mV/s, 25°C) of a (FNR+ME)@ITO/Ti electrode (1 cm^2) in CO_2-saturated buffer (0.2 M HEPES, 0.1 M $KHCO_3$, 4 mM $MgCl_2$, 20 µM $NADP^+$, pH 7.5, under 100% CO_2). Prior to scans: injection of ME (to 2.5 µM). Triangles show potential for proton reduction, $NADP^+$ reduction and C3/C4 (the latter based on the potential at zero current from the blue trace). **B.** Control: CV (1 mV/s, 25°C) of a FNR@ITO/Ti electrode with no $NADP^+$ (purple trace), with 20 µM $NADP^+$ (red trace) in CO_2-saturated buffer containing 0.2 M HEPES, 0.1 M $KHCO_3$, 4 mM $MgCl_2$, 50 mM pyruvate (pH 7.5, under 100% CO_2). Figure adapted from Morello *et al.*[90]

The low potential for the C3/C4 reaction indicates the possibility of achieving high FE with this system. **Figure II-10-B** shows a control experiment to prove that no

catalysis is obtained if ME is not included in the system. The electrode was prepared as before and the experiment carried out under the same conditions as in **Figure II-10-A**. The purple trace is the scan for the FNR@ITO/Ti electrode in a buffer (as above) containing already 50 mM pyruvate under 100% CO_2. When $NADP^+$ was added to a final concentration of 20 µM, the voltammetry shows only the catalysis by FNR, the reduction of $NADP^+$ and on the return scan, the oxidation of NADP(H). Thus, ME is required to observe the sigmoidal wave attributed to the reductive carboxylation of pyruvate.

2.4.2.3. CO_2 titration

The following section investigates the affinity for CO_2 of the (FNR+ME)@ITO/Ti electrode, assessed both by chronoamperometry and cyclic voltammetry. Results are given in **Figure II-11**. **Figure II-11-A** shows a chronoamperometry (–0.45 V vs. SHE, 25°C, stirring, 2.5 mL) of a ITO/Ti electrode (1 cm^2) preloaded with FNR, then immersed in buffer (pH 7.5) containing 50 mM pyruvate. At the beginning of the experiment, oxygen was removed by continuously flushing Ar in the cell headspace. $NADP^+$ was added to a final concentration of 20 µM, giving rise to a reductive current corresponding to $NADP^+$ reduction. Then, ME was separately added to a final concentration of 2.5 µM. As expected, injection of ME, does not result in a current increase (as no CO_2 is present as a substrate) except for a small reductive signal due to O_2 introduction. After two hours, the CO_2 concentration was changed both in solution and in the headspace from 0.4% to 100%.

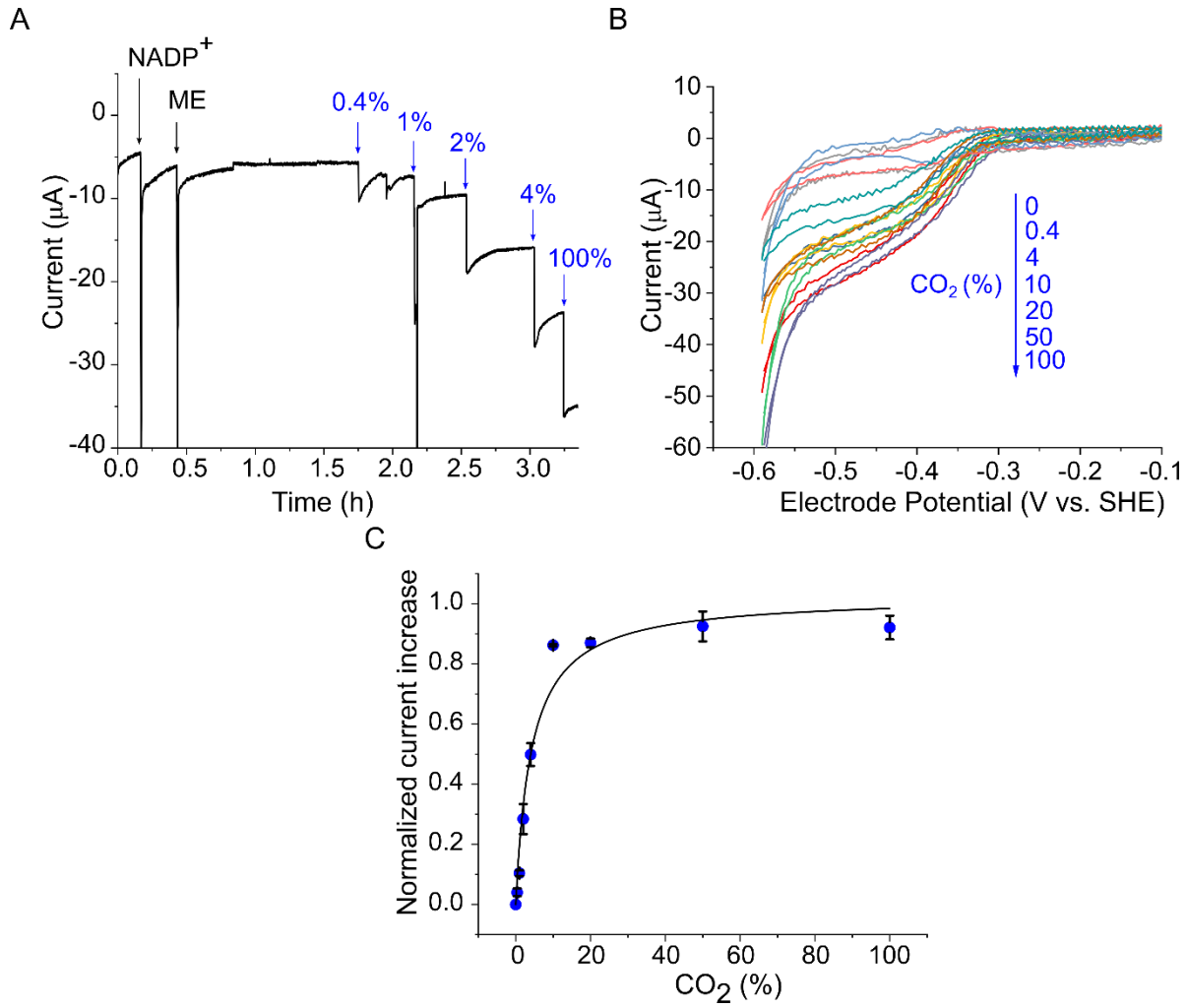


Figure II-11. The CO_2-dependence of the reductive carboxylation of pyruvate by the (FNR+ME)@ITO/Ti electrode. Aliquots of CO_2-saturated buffer were injected into the cell; at the same time the headspace composition was changed accordingly. Initially, the electrode (ITO/Ti) was loaded with FNR only. $NADP^+$ was injected to 20 µM and ME to 2.5 µM. **A.** Chronoamperometry (–0.45 V vs. SHE, 25°C, stirring) in buffer containing 0.2 M HEPES, 4 mM $MgCl_2$, 50 mM pyruvate (pH 7.5) of (FNR+ME)@ITO/Ti electrode (1 cm^2). **B.** experiment carried out as in A, but monitored as CV (1 mV/s; stationary). **C.** The normalized current increase (min of each run = 0 and max of each run = 1) from CV and chronoamerometries was plotted against CO_2 percentage. Error bars represent standard error (*N*=3). Figure adapted from Morello *et al.*[90]

Two mass flow controllers (MFCs) connected to an argon and CO_2 cylinder were used to vary the CO_2 percentage in the headspace. Aliquots of CO_2-saturated buffer were simultaneously injected to the desired CO_2 concentration. Each change in CO_2 concentration is indicated by an arrow. Moreover, each injection was followed by pausing the measurement for 1 minute and flushing the gas mixture

directly in solution to quickly remove traces of introduced oxygen present in the injected aliquot (O_2 gives rise to a reductive signal). A new injection was carried out after the signal levelled off and the current value was assigned to the corresponding CO_2 concentration. The current in the chronoamperometry shows that ½ of v_{max} is obtained at around 4% CO_2. The same setup and conditions were used in **Figure II-11-B** for a CV analysis (1 mV/s, 25°C, stationary) and the current at –0.45 V vs. SHE was compared between each CV at different CO_2 concentrations. **Figure II-11-C** shows the overall results (experiments carried out in triplicate): the current increase was normalized using the following equation (2.1):

$$\text{Normalized current } (i)\text{increase} = \frac{i - i(0\%\ CO_2)}{i(100\%\ CO_2)} \qquad (2.1)$$

The data points were plotted against CO_2 percentage and fitted to the Michaelis-Menten equation. The results show that the system is slightly active at 0.4% and reaches 50% of its activity at relatively low level of CO_2 equal to 4.0 ± 0.5%.

2.4.2.4. Product analysis

The chosen analytical method to quantify the product of the reductive carboxylation catalysed by ME (malate) was ^{1}H-NMR. This posed a problem with the buffer composition, especially for the traces of paramagnetic Mn^{2+} in the system, which would affect the signal. Malate is known to have the following chemical shifts, δ [4.2 ppm (dd, H-C-OH), 2.7 ppm (dd, HOOC-CH-H_1-CHOH-COOH), 2.35 ppm (HOOC-CH-H_2-CHOH-COOH)]. ^{1}H-NMR spectra of samples taken at the end of reductive carboxylation reactions were not resolved: the peaks related to malate were broad and small. The same result was obtained for a commercial sample of the product, by measuring the spectrum of 50 mM malate in a CO_2-saturated buffer containing 50 mM phosphate, 0.1 M $KHCO_3$, 4 mM $MgCl_2$, 1 mM $MnCl_2$ (pH 7.5). Results are shown in **Figure II-12**. **Figure II-12-A** shows the NMR spectrum (in 10% D_2O) of the commercial sample: the peaks are broad, small and no information on splitting is provided (even with such a high concentration of malate, 50 mM). Clearly, smaller concentrations would be almost or completely undetectable by this method. Treating the sample with concentrated HCl (5:1) prior to adding D_2O resolved the issue (**Figure II-12**). This is shown in **Figure II-12-B**, where large peaks related to malate are now visible (4.5 and 2.7 ppm). Malic acid is fully protonated upon acid-treatment, hence interactions with Mn^{2+} ions are prevented.

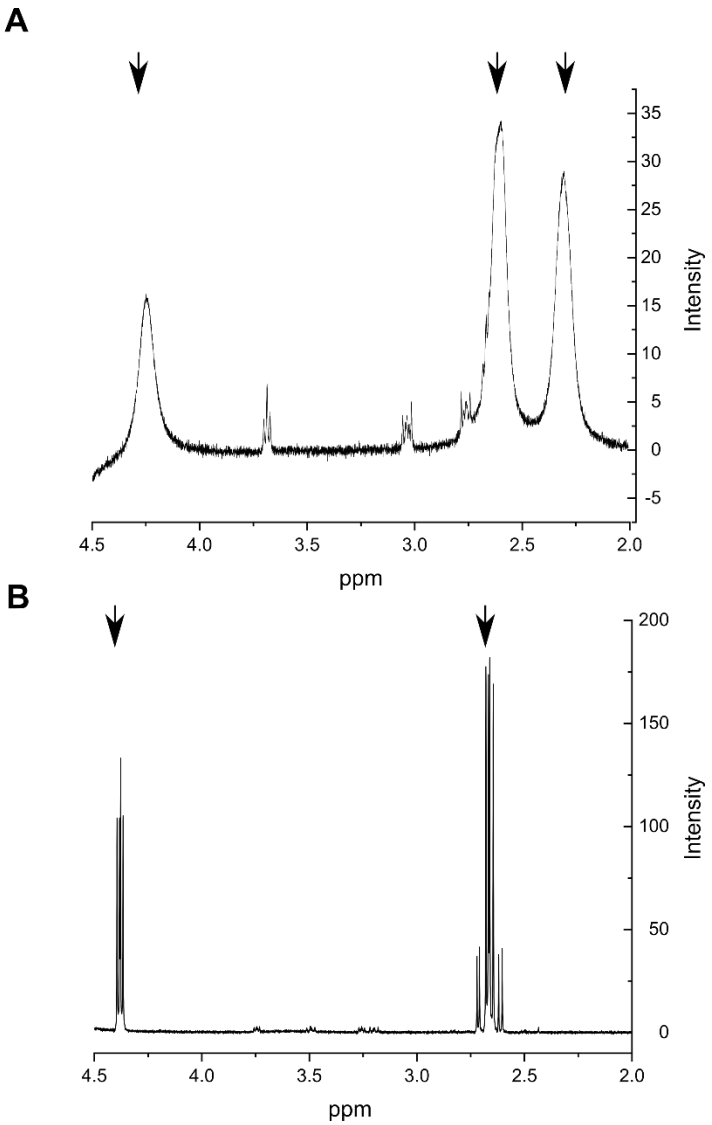


Figure II-12. ^{1}H-NMR of a standard sample of 50 mM malate in CO_2 saturated-buffer containing 50 mM phosphate, 0.1 M $KHCO_3$, 4 mM $MgCl_2$, 1 mM $MnCl_2$. A. 10% D_2O spectrum shows broad peaks at 4.2, 2.6 2.3 ppm **B**. The same sample of A. was treated with conc HCl (5:1) and then a 10% D_2O spectrum was measured. The resulting peaks become larger and resolved (4.4 ppm, dd and at 2.7 ppm).

When the same treatment was used for a sample taken from a typical reductive chronoamperometry experiment (as for **Figure II-9-B**) catalysed by a (FNR+ME)@ITO/Ti electrode after 24 h, the same effect was observed. **Figure II-13-A** shows the NMR analysis of the untreated sample. The two peaks for malate are visible with no information on splitting, as seen for the commercial sample of malate. **Figure II-13-B** shows the NMR of the same sample treated with HCl: the

peaks are now clear and visible, confirming that indeed the reaction observed electrochemically was the production of malate.

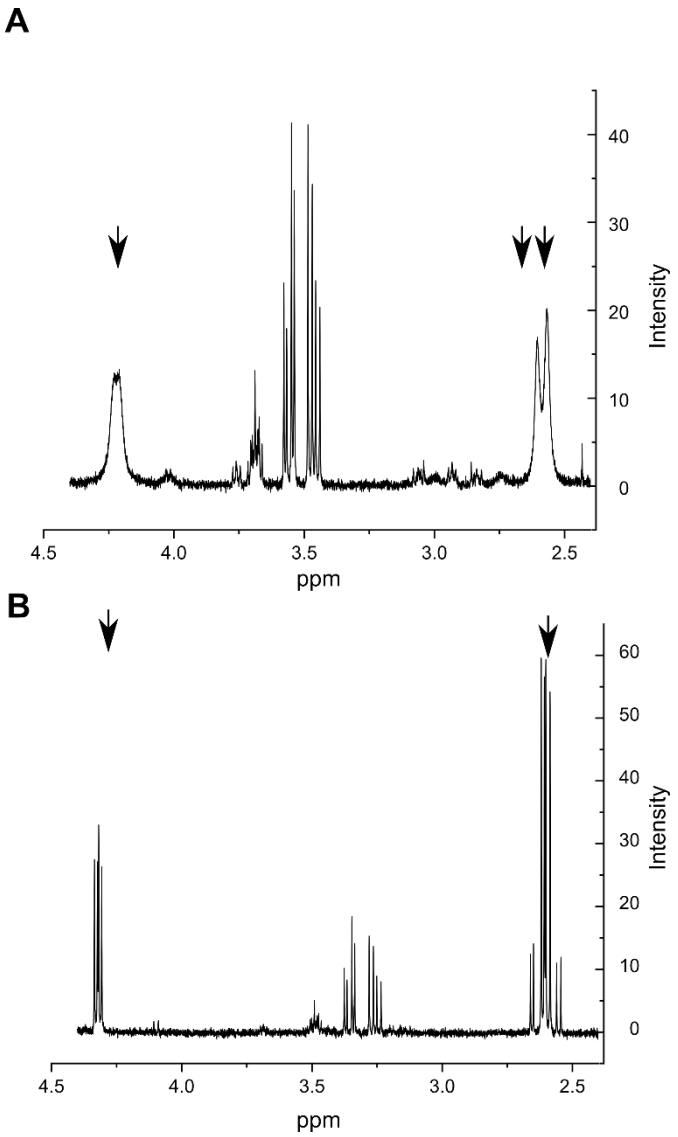


Figure II-13. A. ^{1}H-NMR of time point t = 24 h, for a typical reductive carboxylation of pyruvate catalysed by the (FNR+ME)@ITO/Ti electrode before and after acid treatment. Sample taken from a typical chronoamperometry carried out in CO_2 saturated buffer containing 50 mM phosphate, 0.1 M $KHCO_3$, 4 mM $MgCl_2$, 1 mM $MnCl_2$ (introduced after enzyme injection). **A** 10% D_2O solution was prepared for NMR with water suppression. **B**. The same sample from A. was first treated with conc HCl (5:1) and then a 10% D_2O solution was prepared for analysis. The malate peaks are clearly visible.

2.4.2.5. Bulk electrolysis and nanoconfinement of enzymes

This section describes the bulk electrosynthesis of malic acid, monitored through chronoamperometry. In the following experiments, phosphate buffer was

used to allow easier quantification of the product, since the buffer used in the previous electrochemical experiments contains peaks overlaying with the product peak. **Figure II-14** shows the results of the chronoamperometry for the bulk synthesis of malate from pyruvate. An FNR@ITO/Ti electrode (16 cm^2) was prepared by stirring in a dilute solution (7.2 µM) of FNR overnight. The experimental set-up was assembled in CO_2-saturated buffer (4 mL) containing 0.05 M phosphate, 0.1 M $KHCO_3$, 4 mM $MgCl_2$, 20 mM pyruvate (pH 7.5). **Figure II-14** shows the chronoamperometry (–0.45 V vs. SHE, 25°C, stirring). Addition of $NADP^+$ (to 20 µM) caused a small reductive current. The current returned to baseline after 1370 s, during which the charge passed (0.018 C) matched the conversion of 20 µM $NADP^+$. Injection of ME to a final concentration of 2.5 µM, initiated a large current growth lasting for 2 hours. The current reached a maximum after ca. 2 h (450 µA), and then slowly decreased, reaching 50 µA after 16 h (3.8× higher than baseline current). The current growth will be discussed further later in the chapter.

Calculation of the charge passed during the experiment equates to the amount of formed product. For instance, 17.6 mM malate (volume: 4 mL) was formed corresponding to 88% of conversion after 16 h (NMR in **Figure II-15**).

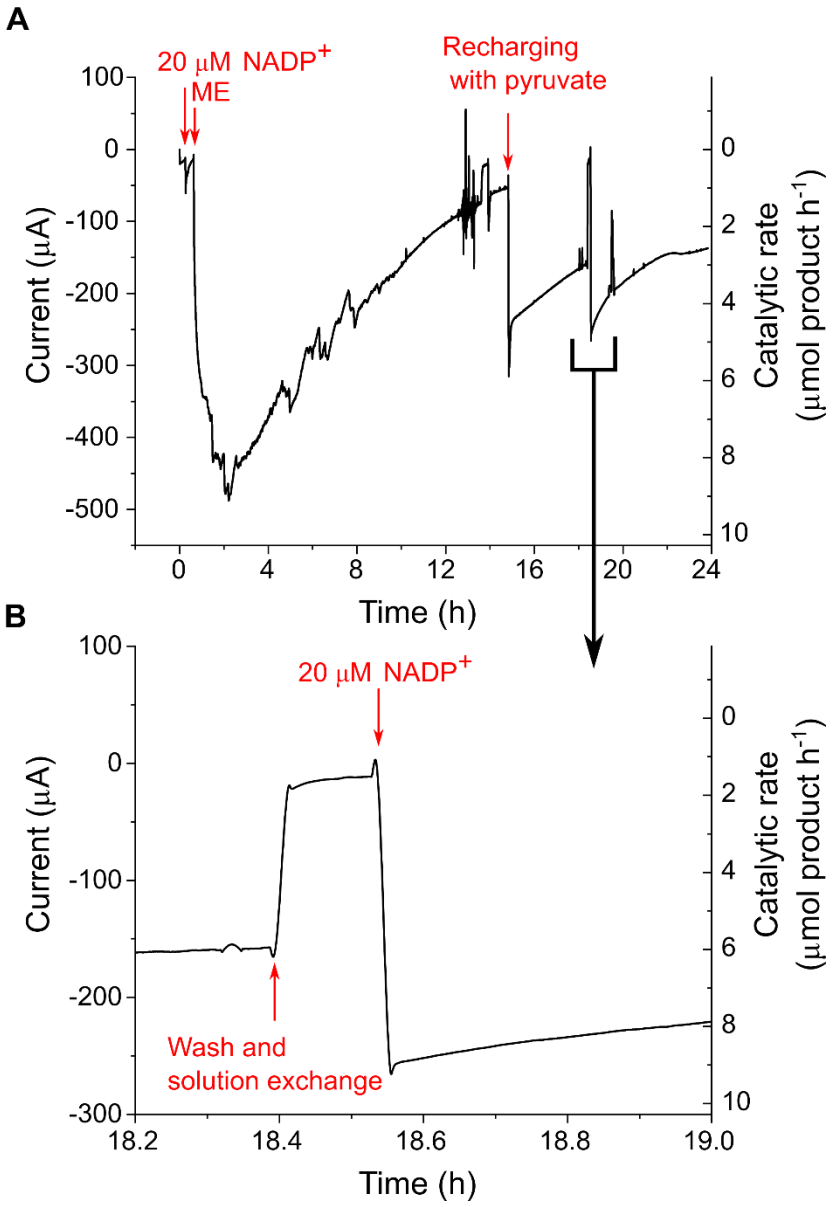


Figure II-14. A. Reductive carboxylation of pyruvate driven by a large surface area (FNR+ME)@ITO/Ti electrode. The electrode was preloaded with FNR only. **A.** Injection of $NADP^+$ to 20 µM and ME to 2.5 µM. The solution was recharged with 20 mM pyruvate after 15 h. A buffer exchange was performed after 18.5 h: solution was replenished with buffer containing no ME and no substrate. **B**. Enlargement of the wash and solution exchange. Reinjection of $NADP^+$ (to 20 µM) at 18.5 h. Chronoamperometry (–0.45 V vs. SHE, 25°C, stirring, 4 mL) with a (FNR+ME)@ITO/Ti (16 cm^2) in CO_2-saturated buffer containing 0.05 M phosphate, 0.1 M $KHCO_3$, 4 mM $MgCl_2$, 20 mM pyruvate (pH 7.5) under 100% CO_2. Figure adapted from Morello *et al.*[90]

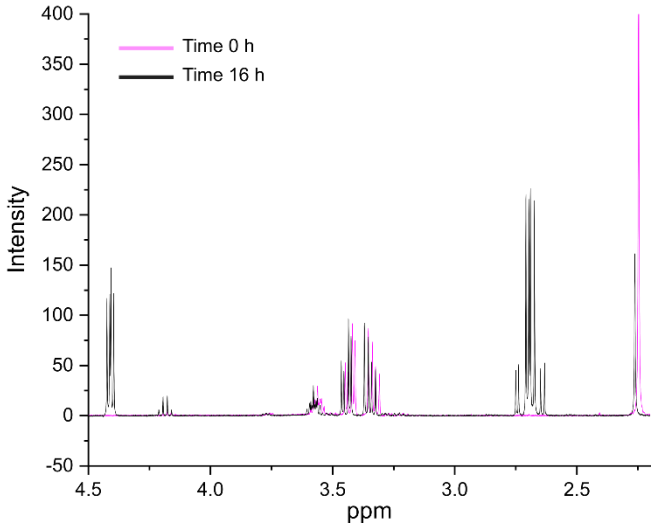


Figure II-15. ^{1}H-NMR of the reductive carboxylation at time t = 0 (magenta) and time t = 16 h (black) from Figure II-14-A. Sample treated with conc HCl (5:1) and 10% D_2O. Figure adapted from Morello *et al.*[90]

One of the most important indications of the performance of a cofactor regeneration system is the total turnover number (TTN, product concentration/$NADP^+$ concentration). In this experiment the TTN was 880. After 16 h, fresh substrate was re-added to a final concentration of 20 mM to restore the reaction rates (K_M, for pyruvate is 6.2 mM, hence the current decrease).[171] The rate was not restored to the original value, possibly due to product inhibition by malate and/or some degree of instability of one of the components. Product inhibition and other reasons for current decay will be discussed later.

The current growth observed upon enzyme injection can be interpreted as ME entering the electrode nanopores. Nanoconfinement of the two cooperating catalysts (ME and FNR) and $NADP^+$[146] minimises diffusion distances and maximises the effective concentrations of the enzymes. Hence, the rate of the reaction (current) is massively increased as catalysis becomes extremely efficient.

A buffer exchange was performed after 18 h to confirm the nanoconfinement of ME in the electrode pores as described in Megarity *et al.*[139,146] The original cell solution was removed and the cell was washed 10 times with MQ-H_2O and once with buffer. Fresh buffer without ME and $NADP^+$ was added to the cell. **Figure II-14-B** shows the enlargement of the buffer exchange. When the experiment was restarted (after initial bubbling of CO_2 to remove oxygen) the rate returned to the baseline, as no cofactor was present. Re-injection of $NADP^+$ (to 20 µM) caused a sudden increase in rate proving that ME is indeed adsorbed in the electrode pores since ME is no longer present in the bulk solution; the adsorption of ME must therefore have occurred during the initial phase of the experiment. Note that the increase of current upon $NADP^+$ injection is instantaneous, in contrast to the gradual observed upon enzyme injection. The current increase is instantaneous because now the enzymes are already absorbed on the electrode. Moreover, the current after buffer exchange is greater than right before (>100 µA), suggesting a contribution by product inhibition (**Figure II-14-B**). The effect of product inhibition is consistent also with the voltammetry shown in **Figure II-10-A**, where the reductive current was halved after malate (product) injection. After re-injecting $NADP^+$ the current did not come back to the original value of 450 µA probably because of disturbance to the electrode due to the solution exchange operation (such as excessive purging to remove O_2).

The buffer exchange result showed that ME entered the electrode nanopores. To confirm that ME binds to the ITO layer as well, an electrode was first pre-loaded with both FNR and ME and rinsed thoroughly prior to the experiment. Importantly FNR or ME will not be injected during the chronoamperometric experiment. **Figure II-16** shows the results of the co-loading experiment. An ITO/Ti electrode (1 cm^2)

was stirred overnight in a diluted solution of FNR (15.7 µM) and ME (7 µM) in borate buffer (pH 8). The electrode was rinsed thoroughly prior to the experiment to remove any unbound enzyme and immersed in the cell solution (a CO_2-saturated phosphate buffer containing 50 mM pyruvate, pH 7.5). Since all the substrates for ME catalysis were already present in the buffer, the addition of $NADP^+$ (to 20 µM) caused a large reductive current, which was stable for 24 h (current density: 20 µA/cm^2, similar to the rate of the coupled CV observed in **Figure II-10**). The large current enhancement confirms that ME (E2) was successfully entrapped within the electrode nanopores.

Figure II-16 shows that the average catalytic rate was 0.3 µmol product $h^{-1}cm^{-2}$. Based on the total amount of FNR adsorbed (in this experiment from non-turnover peaks, 9.9 pmol cm^{-2}) a rate per FNR of 8 s^{-1} (turnover frequency, TOF) was obtained. The obtained value is believed to be an underestimation of the true rate, as most of the FNR is redundant, as was observed by Siritanaratkul *et al*.[134,141] The authors studied $NADP^+$/NADPH interconversion by the FNR@ITO/Support electrode and observed (i) a TOF three orders of magnitude smaller (0.4 s^{-1}) than the value reported in the literature for FNR (40 s^{-1}) and (ii) the appearance of a non-turnover peak signal in CVs carried out in presence of $NADP^+$; the shoulder-signal was observed at a potential more negative than NADPH oxidation peak and corresponded to the FNR oxidative non-turnover peak. The shoulder-signal comes from FNR molecules which do not participate in the reaction. These results suggested that deeply buried FNR molecules are not active in catalysis. The TOF value increased to 40 s^{-1} if only the equivalent of one monolayer was participating in the reaction.[134] A similar observation was proposed by Megarity *et al.* using the (FNR+ADH)@ITO/support electrode to drive the oxidation of 4-phenyl-2-butanol

(see Section 1.6.3.).[146] Unfortunately it has not been possible to measure the moles of non-redundant FNR or the amount of adsorbed E2.[134,146,179]

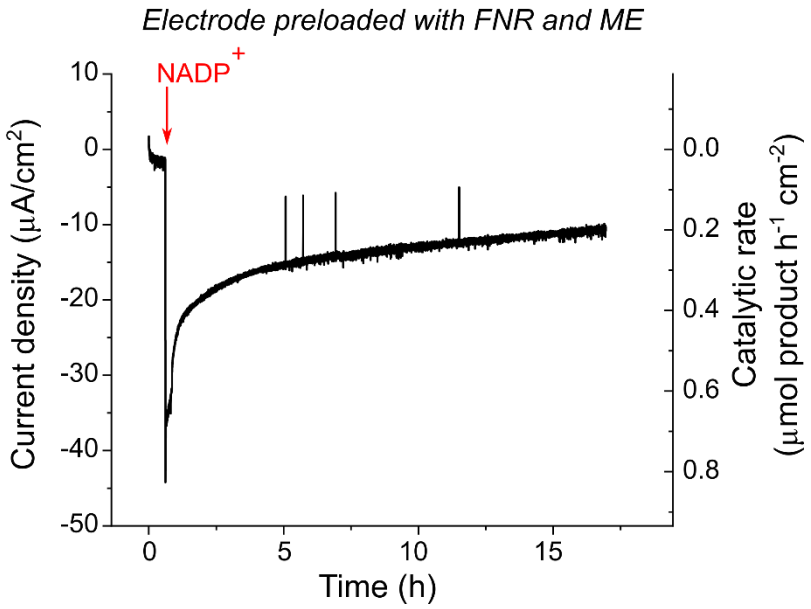


Figure II-16. Activity of a (FNR+ME)@ITO/Ti electrode in which the enzymes were co-loaded (no enzymes in solution). Chronoamperometry (–0.45 V vs. SHE, 25°C, stirring) in CO_2-saturated buffer containing 0.05 M phosphate, 0.1 M $KHCO_3$, 4 mM $MgCl_2$, 50 mM pyruvate (pH 7.5) under 100% CO_2 with an electrode preloaded with FNR and ME (1 cm^2). Reaction was initiated with $NADP^+$ (to 20 μM). Figure adapted from Morello *et al*.[90]

Previous experiments have shown that product inhibition is an important factor affecting the current. Hence the question arising here is how much of the observed current decay is due to product accumulation or to instability of the electrode. **Figure II-17** shows the results of comparing two chronoamperometries carried out with different $NADP^+$ concentration, in **Figure II-17-A** with 1 μM of $NADP^+$, while in **Figure II-17-B** the final concentration of cofactor was 20 μM (**Figure II-17-B** is the same experiment as in **Figure II-14**). By using 1 μM $NADP^+$ the rate of the reaction should be lower hence resulting in less product formed; the experiment compares the current decays between the two cases. The electrodes

were prepared as described for **Figure II-14** (buffer containing 20 mM pyruvate) and ME was injected to a final concentration of 2.5 µM after $NADP^+$ injection.

In the experiment with 20 µM $NADP^+$ (**Figure II-17-B)** the current reaches its maximum after 2 hours and then it starts decreasing, while with 1 µM (**Figure II-17-A**) the current increases for 4 hours before decreasing much less rapidly (> 50% of starting current after 24 hours). The main difference between the two experiments is the charge passed (current × time, *A* × *s*), which equates to the amount of product formed (see Section 7.1.8.). Hence, product accumulation influences the current growth related to enzyme binding to the electrode. While ME keeps binding to the electrode, product inhibition is already happening. The measured current is the result of a balance between current build-up and decay because of product inhibition. The result in **Figure II-17** is consistent with a scenario where an important factor for the current decrease is product formation, rather than instability of the electrode.

In **Figure II-17-A**, a conversion of 31% was obtained at the end of the experiment resulting in 6210 TTN based on coulometry. Such a high TTN shows the promising nature of this system for use in synthesis applications.[102]

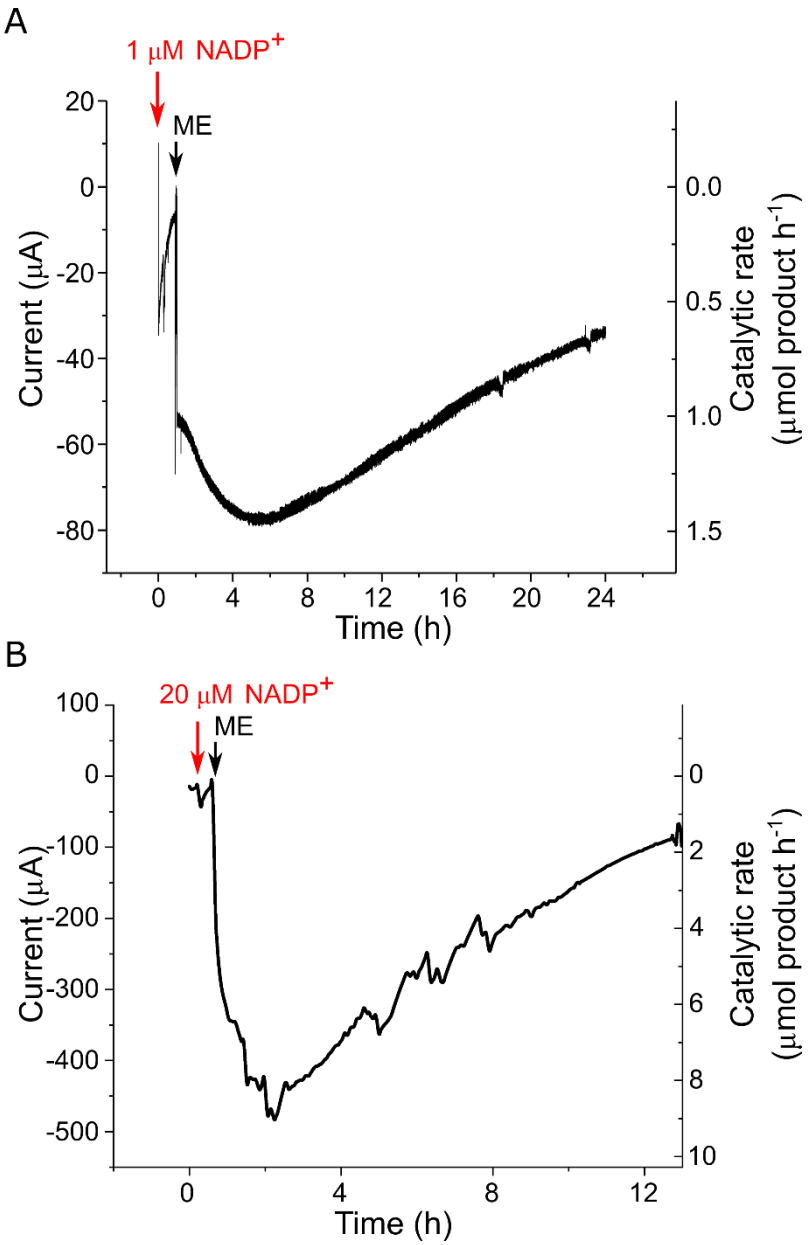


Figure II-17. Comparison of rate of current increase and decay between chronoamperometries carried out with 1 µM and 20 µM $NADP^+$. The electrode was preloaded with FNR only. **A**. $NADP^+$ was injected to 1 µM and ME to 2.5 µM. **B**. $NADP^+$ was injected to 20 µM and ME to 2.5 µM. Chronoamperometries (–0.45 V vs. SHE, 25°C, stirring) of a (FNR+ME)@ITO/Ti (16 cm^2) carried out in CO_2-saturated buffer containing 0.05 M phosphate, 0.1 M $KHCO_3$, 4 mM $MgCl_2$ (pH 7.5) under 100% CO_2 with 20 mM pyruvate. Figure adapted from Morello *et al*.[90]

Nanoconfinement of ME was demonstrated through buffer exchange as shown in **Figure II-14**. The current increase was attributed to ME binding to the electrode (related data from our group with other E2 enzymes is described by Megarity *et al*[139,146], see Section 1.6.3.). All the chronoamperometries shown so far

have been carried out on the bench, and removal of oxygen was ensured by continuously flushing the electrochemical cell with inert gas (either Ar or CO_2). Unless experiments were carried out in an anaerobic glove box, O_2 traces were always introduced into the cell upon injections, causing a spike in current: hence, after each injection, inert gas was flushed directly into the cell solution to accelerate removal of O_2.

In **Figure II-17-A** injection of ME causes first an immediate current increase and then a current growth. A new experiment was designed to make sure whether the first immediate current increase was a convolution given by O_2. To answer this question an experiment (performed by Dr. Clare Megarity) was setup in a glove box (N_2 atmosphere) to remove the O_2 convolution: no oxygen would be introduced during injections (**Figure II-18**). An ITO/PGE electrode (0.03 cm^2) was preloaded with FNR, rinsed thoroughly and immersed in a CO_2-saturated buffer containing 0.2 M HEPES, 0.1 M $KHCO_3$, 4 mM $MgCl_2$, 5 µM $NADP^+$. Then, ME was added "*live*" to a final concentration of 0.8 µM causing a slow growth in current with no current spike observed. Megarity *et al.* were able to conclude that catalysis only happens within the electrode nanopores from the results of enzyme "*live*" injection (ADH) in the glove box (as for **Figure II-18**) and from a solution exchange experiment carried out as in **Figure II-14**: the authors observed that even if E2 was completely removed from solution, catalytic rates were conserved when substrates were reintroduced.[139,146] Based on the results obtained in **Figure II-18** and **Figure II-14**, the same conclusion can be translated to ME: nanoconfinement of E1 (FNR) and E2 (ME) is essential for efficient catalysis.

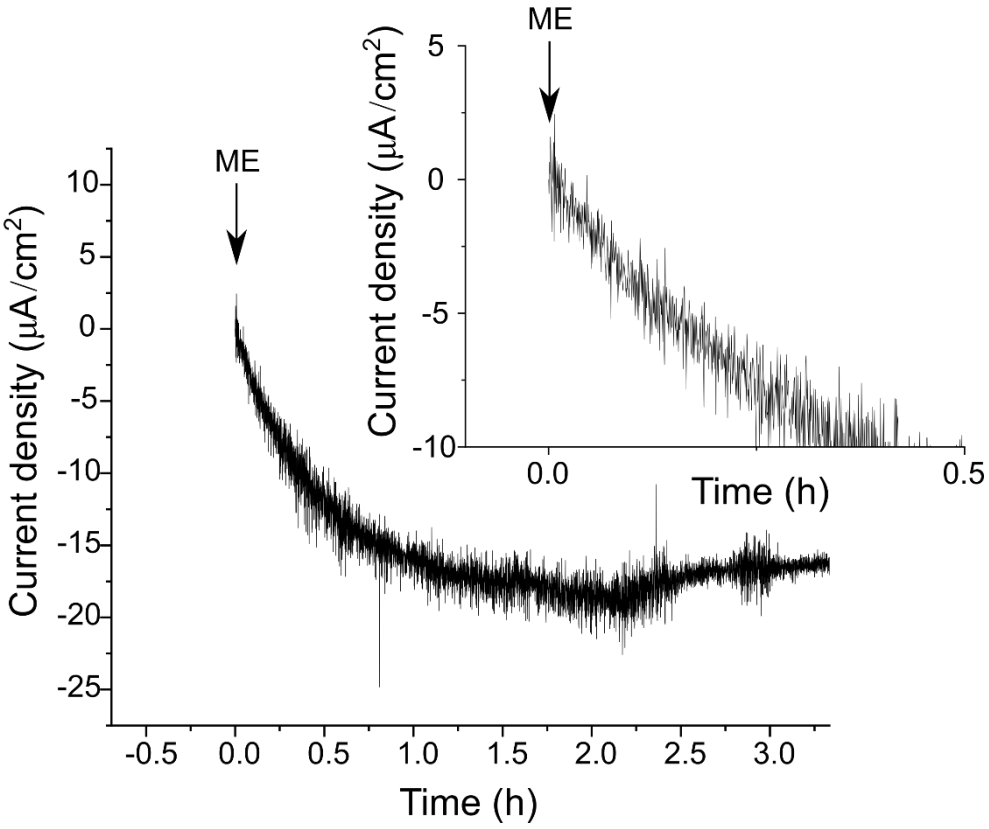


Figure II-18. Live injection of ME to show formation of an active (FNR+ME)@ITO/Ti electrode. The electrode was preloaded with FNR-only. Addition of ME to a final concentration of 0.8 µM. Chronoamperometry (–0.45 V vs. SHE, 20°C, in glove box, N_2 atmosphere, rotating electrode ω - angular velocity = 1000 rpm) obtained with a (FNR+ME)@ITO/PGE electrode (0.03 cm^2) in CO_2-saturated buffer containing 80 mM pyruvate, 0.2 M HEPES, 0.1 M $KHCO_3$, 4 mM $MgCl_2$, 5 µM $NADP^+$, under 100% CO_2. Experiment carried out by Dr. Clare Megarity. Figure adapted from Megarity *et al.*[146]

2.5. Conclusion

MaeB was successfully cloned from *E. coli* as confirmed by sequencing, SDS page and conventional solution assay. Preliminary coupling of ME with FNR to drive the reductive carboxylation of pyruvate to malate via NADPH cycling by the electrochemical leaf was successful when the buffer was saturated with 100% CO_2.

Preliminary conditions led to an unstable system and the current decreased to the baseline after just 2.5 hours. Optimization studies were performed to identify the ideal conditions for ensuring high and stable catalysis. These studies showed that Mn^{2+} ions were required for inherent stability of ME while potassium ions enhanced further the stability of the system. Further experiments could be performed to understand and investigate the reason for the enhanced stability with manganese and potassium.

Solution exchange experiments confirmed that ME binds to the electrode after injection and a current growth was observed as reported for other E2[90,139,144,146]. The “live” injection experiment in the glove box proved that a current growth is observed without the presence of O_2-spikes upon injection of enzyme E2.[146] The current growth reflects E2 entering the electrode nanopores, and the buffer exchange experiment (as also reported by Megarity *et al.*[139,146]) was crucial to confirm this for ME. Indeed, after replacing all the components in the buffer, the rates were re-established even if ME was not reintroduced into the solution. Nanoconfinement of FNR and ME makes the electrocatalyst extremely efficient as diffusion distances for NADP(H) are reduced and the concentration of enzymes within the nanopore are massively enhanced. The resulting electrocatalyst

(FNR+ME)@ITO, drives CO_2 reduction at a low potential, 0.1 V more positive than the hydrogen evolution potential, and even at low levels of CO_2, reaching 50% of the maximum rate at 4% CO_2.

One important factor affecting the current is product inhibition of ME. The extent of current decrease in chronoamperometry depends on the amount of product being formed, as shown in the comparison between the chronoamperometries with 1 and 20 µM $NADP^+$. In the latter, increased accumulation of product caused significant instability in current compared to the experiment with 1 µM $NADP^+$.

The unprecedent power of monitoring the rate of the reaction directly from the current was crucial to achieve a stable and efficient reductive carboxylation system. The electrochemical leaf offers a unique way to monitor, screen and optimise a biochemical reaction, which is not found in other methodologies.

Chapter III

3. Light-driven reductive carboxylation

3.1. Abstract

The very favourable conditions for the reductive carboxylation of pyruvate to malate achieved within the nanoconfined (FNR+ME)@ITO/support electrode were crucial for designing a photoelectrochemical (PEC) system which mimics oxygenic photosynthesis: visible light would thus be used to oxidise water to oxygen, reduce CO_2 and incorporate it into pyruvate to produce malate with high faradaic efficiency. To achieve this goal, two photoanode materials were tested: α-Fe_2O_3/CoB and 2%Mo:$BiVO_4$/FeOOH. Light-driven NADPH reduction was studied with the former where a large bias was required (0.9 to 1.2 V) and the cathode was light-sensitive in the PEC conditions. The material 2%Mo:$BiVO_4$/FeOOH was chosen for the complete light-driven reductive carboxylation because of its higher performance. To drive the system with visible light only, a hybrid PEC-PV system was developed by incorporating a 0.5 V Si solar cell. After 24 h, a conversion of 18.5% pyruvate to malate with 300 TTN was obtained and a FE for the C3/C4 reaction of 70%. The number of TTN obtained is 1–2 times higher than any other light-driven NADPH recycling system published so far.

3.2. Introduction

Artificial Photosynthesis aims at converting sunlight into chemical energy, using water and carbon dioxide as typical feedstock. This goal is particularly important for basic research, environmental reasons and energy security.[180]

A typical AP system mimics the fundamental aspects of photosynthesis (see Section 1.4.) and it typically contains one or two light absorber components and two catalysts. One catalyst drives the oxidation of an electron donor, typically water, and the other reduces an electron acceptor such as CO_2 or H^+.[44,50,181,182] Light absorber and catalyst components can be assembled in a PEC or a photocatalytic system. In the former, the materials are deposited on conducting supports and their performance can be monitored by measuring a current. In the latter, they are simply dispersed in suspension and their performance is analysed by measuring product formation, usually by gas chromatography (GC).[12,183]

The light absorber is typically a semiconductor material and its electronic band structure dictates whether the desired process can be driven solely with visible light. Briefly, the potential of the valence band (VB) must be more positive than the energy level of the redox couple to oxidise, while the potential of the conduction band (CB) must be more negative than the energy level of the redox couple to reduce. Moreover, the difference between CB and VB potential (band gap, E_g) needs to be below 2.8 eV so that visible light can drive the photochemistry. Most of the materials studied do not meet these conditions (see Section 1.4.).[46]

The materials investigated in this Chapter were hematite (α-Fe_2O_3) and bismuth vanadate ($BiVO_4$). Both can absorb visible light (E_g: 2.1 and 2.4 eV, respectively) and oxidise water. However, the position of their CB is not negative enough to drive H^+, $NADP^+$ or CO_2 reduction (see Section 1.4.). Therefore, an

additional applied bias, using a potentiostat, was required to perform the experiments.

The materials in PEC systems are assessed based on the photocurrent amplitude per surface area (mA/cm^2) and on the onset potential, the potential at which photocatalysis starts to occur. **Figure III-1** shows a current density-voltage (*J-V*) curve obtained for a photoanode (in this case 2%Mo:$BiVO_4$/FeOOH electrode). In the dark, water oxidation occurs only at potential above +1.6 V vs. RHE. If the photoanode is illuminated, this potential shifts to much lower values: in this case +0.4 V vs. RHE. Ideally, a very high current should be obtained at values close to the onset potential.

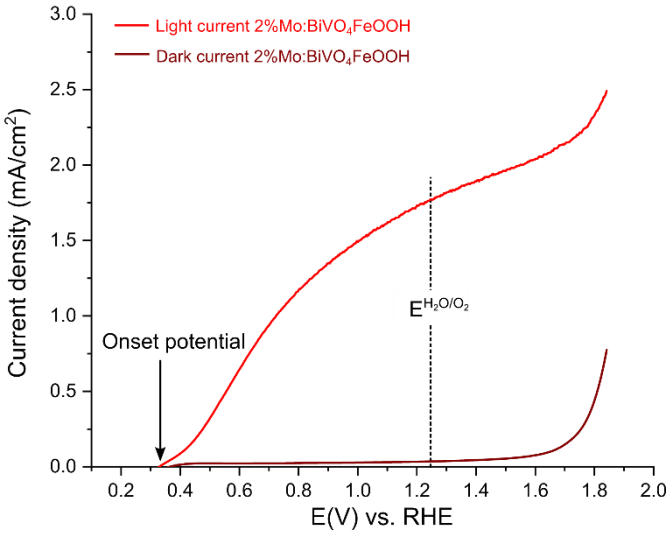


Figure III-1. *J-V* curve of a typical photoanode. Black curve: dark current; water oxidation is observed at very high potentials. When light is switched on, catalysis can occur at a lower potential (red trace). The onset potential is the *E* when photocatalysis begins to occur. A very steep rise in current is desirable. The highest photocurrent should be obtained at a potential close to the onset potential.

This Chapter describes the design and development of a PEC light-driven NADPH regeneration system for the reductive carboxylation of pyruvate to malate by the (FNR+ME)@ITO/support electrode (see Chapter II). Other light-driven

cofactor regeneration systems have been reported (see below). Most of the work published so far involved a mediator in solution, such as trisbipyridineruthenium ($Ru(bpy)_3^{2+}$) or methyl viologen (MV^{2+}), while to the best of my knowledge, only one other publication reported direct electron transfer from the electrode to the cofactor-regenerating enzyme.[184]

Brown *et al.* reported a biohybrid cofactor regeneration system consisting of CdSe-quantum dots (QD) particles using mercaptopropionic acid as capping agent and FNR.[185] Upon illumination – using a 405 nm light source – and in presence of an organic electron donor, such as ascorbate (to 100 mM), FNR was able to reduce the nicotinamide cofactor. The FNR-QD composite was coupled to the alcohol dehydrogenase (ADH)-catalysed reduction of isobutyraldehyde to isobutanol, to demonstrate the cofactor regeneration system. The product was quantified by GC. This reported system was active for 2–3 h with a TTN ([product]/[NADPH]) equal to 3.5, using 0.25 µM $NADP^+$. Similar values and stability were obtained when the reaction was extended to a two-step isobutanol production; the two-enzyme cascade was initiated by 2-ketoisovalerate, by integrating a keto-acid decarboxylase to the ADH-FNR-QD system. The instability of the QD and consequent leaching of Cd^{2+} in solution were considered the main reasons for the low stability observed.[184]

During the development of this thesis, other related publications were released. For example, Lee *et al*., reported a similar PEC-PV system (using $BiVO_4$/FeOOH-perovskite solar cell) to drive unassisted L-glutamate production through NADH cycling using glutamate dehydrogenase.[84] Perovskite solar cells are a promising new technology for the PV field. However, they suffer from instability – a problem which is under intense research.[186–188] Integrating a PV element allows the system

to be driven without the need of an additional bias, solving the issue of the photoanode thermodynamics. This approach has been reported in several publications and is a subject of this Chapter as well.[68,155,189] The cathode reaction was driven by a carbon nanotubes (CNT)-based electrode and a Rh-mediator in solution ($[Cp^*Rh(bpy)H_2O]^{2+}$; Cp = C_5Me_5, bpy = 2,2 bypiridine). The Rh-mediator is reported to reduce the cofactor to the active biological form (at –0.76 V vs. Ag/AgCl) preventing formation of NAD dimers, which would be otherwise produced by the CNT cathode alone at –1.2 V vs. Ag/AgCl. The authors reported high FE of 96.2% using a high NAD^+ concentration (to 2 mM) resulting in an impractical 20.3 TTN from 50 mM α-ketoglutarate.[84]

Willner *et al.* more than 30 years ago reported the light-driven reductive carboxylation of pyruvate to malate via NADPH cycling using the malic enzyme (ME). The light-driven system used $Ru(bpy)_3^{2+}$ as light absorber, MV^{2+} as mediator and mercaptoethanol as electron donor to drive NADPH regeneration. The authors reported a TTN of 64 using 180 µM $NADP^+$.[127] In another study, Inoue *et al.* assembled a biohybrid system with FNR and ME using TiO_2/clay or CdS as light absorber, MV^{2+} as mediator and lactic acid as organic donor. Oxidation of lactic acid generated pyruvic acid, the substrate of ME, while reduced MV^{2+} was able to reduce the FAD centre of FNR. The malic acid production was active for 1.5 and 5 hours, with TiO_2/clay and CdS, respectively. The authors used 100 mM lactic acid and 100 µM $NADP^+$, resulting in the formation of 300 µM malic acid (3 TTN) with CdS or 1 mM (10 TTN) with TiO_2/clay.[56]

This Chapter describes a PEC system to drive the reductive carboxylation of pyruvate to malate using the (FNR+ME)@ITO/support electrode. First a photoanode will be synthesised and coupled to the electrochemical leaf to test the

light-driven $NADP^+$ reduction. Then, the full light-driven reductive carboxylation reaction will be studied. The system is described in **Figure III-2**. Upon light illumination, charge separation occurs at the *n*-type semiconductor deposited on a conducting support (FTO glass). If thermodynamics allows it, the excited electron will be used by the cathode, the electrochemical leaf, to drive reductive carboxylation of pyruvate to malate via NADPH cycling.[90]

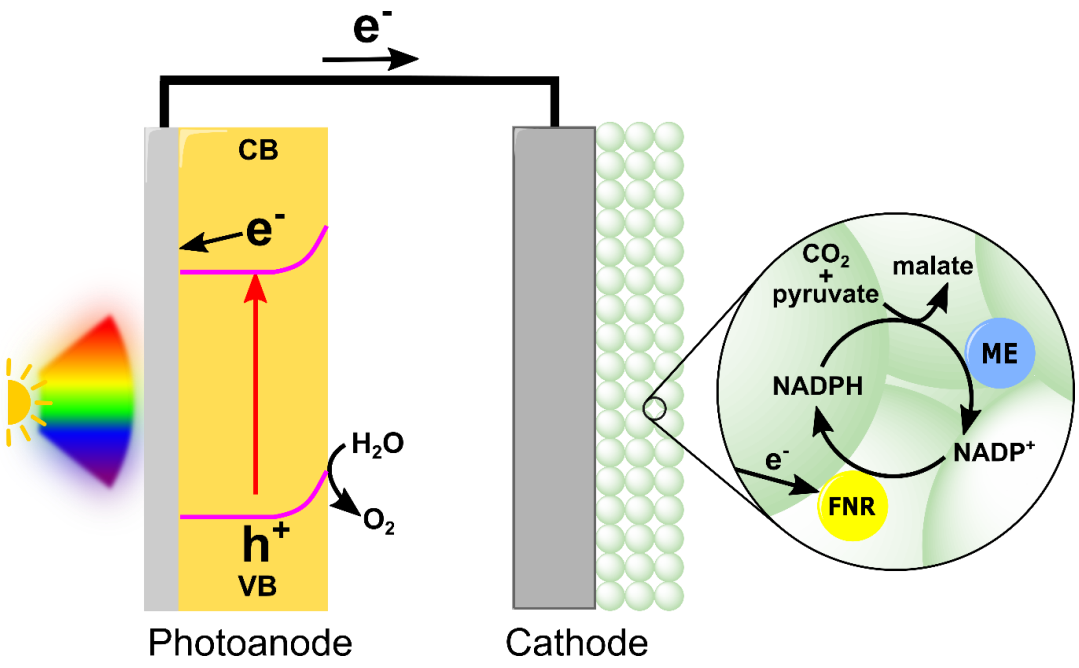


Figure III-2. Light driven reductive carboxylation of pyruvate (C3) to malate (C4) through NADP(H) cycling. The photoanode is an *n*-type semiconductor deposited on conducting FTO glass. Upon light illumination, charge separation occurs leaving a hole (h^+) in the VB. The h^+ can be quenched by an electron, resulting from water oxidation, to release O_2. The excited electron can be used by the cathode, the (FNR+ME)@ITO/support electrode to produce malate from CO_2 and pyruvate.

3.3. Aim of the Chapter

The aim of the Chapter is to demonstrate the possibility of driving the electrochemical leaf with visible light using water as electron donor. First, a light-driven $NADP^+$ reduction system was studied and characterised. After optimisation, the unassisted reductive carboxylation system driven by visible light was investigated.

3.4. Results and Discussion

3.4.1. Preparation of the photoanode and PEC results

Hematite is one of the most promising materials for water splitting because of its small band gap (2.1 eV), high abundance of iron and high theoretical photocurrent (12 mA/cm^2). However, there are limitations given by its low conductivity and small minority carriers diffusion distance (2–4 nm) resulting in high charge recombination and low current.[43,61]

Hematite (α-Fe_2O_3) was synthesized according to a protocol reported previously[190] and deposited on the electrode support using two techniques: (i) electrophoretic deposition (EPD, see Section 7.3.2.1.1. for further details) and (ii) direct growth of the precursor on the electrode.[190,191]

In the EPD method, a solution of 0.2 M $FeCl_3$ and 0.3 M urea was heated at 150°C in a Teflon-lined pressure vessel for 6 hours. After cleaning, washing and drying, the orange precipitate (FeOOH) was sintered at 550°C for 1.5 hours to produce the red oxide phase (α-Fe_2O_3). Electrophoretic deposition onto a clean FTO glass (1 cm^2) was performed at 10 V for 30 s using an ITO counter electrode (distance between electrodes, 1 cm) in a acetone suspension of synthesized α-Fe_2O_3 (10 mM) and I_2 (1.5 mM).[192]

In the direct growth method, a piece of FTO glass (typically 2 cm^2) was inserted in the Teflon-lined pressure vessel (containing 0.2 M $FeCl_3$ and 0.3 M urea) with the conductive side facing the Teflon wall and heated at 150°C for 6 hours. The resulting FTO glass was covered by a thin layer of FeOOH after 6 h, as the step induced the direct growth of FeOOH on the electrode. Then the electrode was rinsed and sintered at 550°C for 1.5 hours.

Both the electrodes from the electrophoretic deposition and from the direct growth were sintered at 800°C for 10 minutes. This ensures a better contact between the metal oxide and the FTO underneath and causes partial doping from tin to the oxide layer.[191] However, the heating treatment has to be quick, otherwise the conductivity of the FTO layer would be compromised.

The PEC performances are shown in **Figure III-3** using a Xe-lamp equipped with a UV cut-off filter (λ>420 nm), held at a distance of 6.5 cm: under this condition (used throughout the whole chapter), the light intensity was established by collaborators to be 0.92 sun (92 mW/cm^2). The experiment was conducted in a single compartment cell in 0.05 M borate, pH 8, using α-Fe_2O_3 (by EPD and direct growth method) as working electrode (WE), Pt as counter (CE) and Ag/AgCl as reference (RE). Typically, hematite electrodes are tested at a much higher ionic strength and higher pH (0.1–1 M NaOH, pH 13).[190] However, those conditions are not compatible with a protein system. **Figure III-3-A** shows that direct growth (dg) results in a higher photocurrent and an onset potential of ≈0.6 V vs. RHE, which is around 200 mV lower than the value obtained with the EPD electrode. Hematite electrodes synthesized in the same way but without the final heating step (800°C) showed no appreciable photocurrent (data not shown).

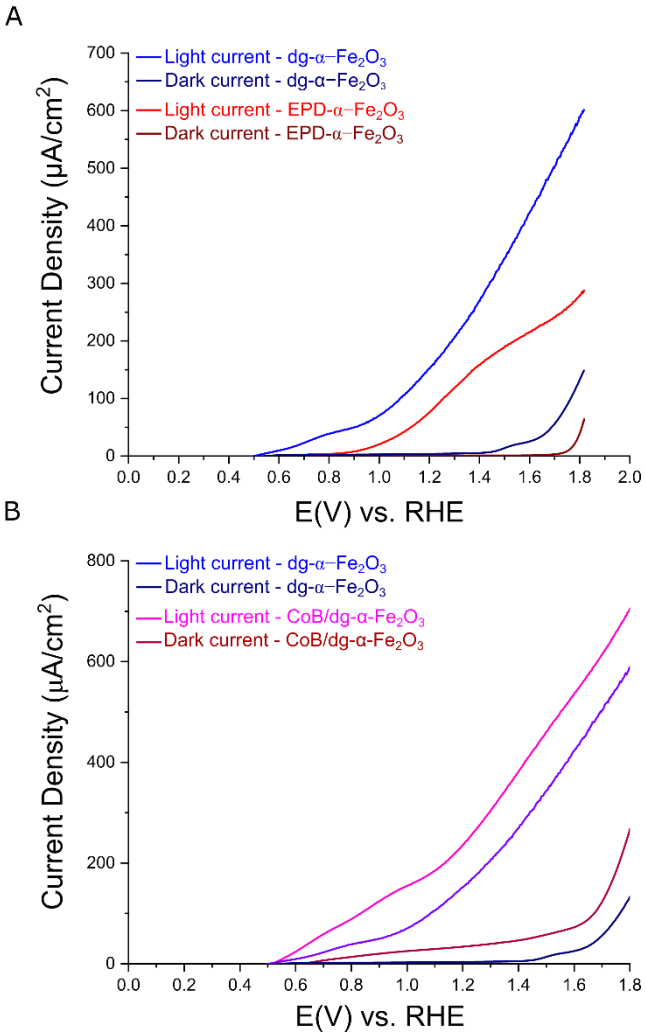


Figure III-3. PEC performance of hematite before and after catalyst deposition. A. Comparison between EPD and dg. Linear sweep voltammetry of α-Fe_2O_3 prepared by the direct growth method (blue) and electrophoretic deposition (red). Related dark currents (dark blue, dark red) **B.** Introduction of the OER catalyst. Experiments were carried out in 50 mM borate pH 8, using Pt as CE, Ag/AgCl as RE. Scan rate: 20 mV/s from 0.5 V vs. RHE to 1.8 V vs. RHE. Light intensity: 0.92 sun; λ>420 nm.

An oxygen evolution reaction (OER) catalyst was deposited on the photoanode to increase the rates of water oxidation and reduce recombination. Different catalysts for water oxidation have been reported in the literature, including IrO_2[193], NiOOH[85], nickel Borate (NiB)[83] and cobalt borate (CoB), the latter being the most promising in terms of cost-efficiency and performances.[50] CoB was deposited by an electrophoretic method, in a three-electrode system at 0.9 V vs. Ag/AgCl for three minutes.[82] The loading of the catalyst decreased the onset

potential of 80 mV and increased the photocurrent at lower potentials. The linear sweep voltammetry of the resulting photoanode (conditions as above) is shown in **Figure III-3-B:** the current density reaches higher values at lower potentials after catalyst deposition. Prolonged loading caused a very high dark current but almost no photocurrent (data not shown).

The material $BiVO_4$ is very promising for PEC applications. Even though its band gap is slightly larger (2.4 eV) than the hematite case, $BiVO_4$ has a bigger charge mobility (70–200 nm)[46] and a more negative CB than Fe_2O_3.[67] Synthesis of $BiVO_4$ and doping by Mo was carried out as described by Kim *et al*.[68] Briefly, three precursor solutions 0.2 M bismuth (III) nitrate, 0.03 M vanadium (III) acetylacetonate and 0.03 M bis(acetylacetonate) dioxomolybdenum (VI) were mixed in the following atomic ratio: Bi:(V + Mo) = 1. Different percentages of Mo doping were tested (from 0 to 20%). The resulting solutions were deposited on an FTO electrode (1 cm^2, 60 µL) by drop-casting, and after drying the electrodes were sintered at 550°C for 30 minutes.

Figure III-4 shows the results of the PEC experiments, carried out in 0.5 M borate (pH 9); a higher ionic strength and pH were used because this improves the PEC performance (data not shown). This photoanode was used later in a two-compartment cell, separated by the cathode (the Electrochemical Leaf). It is known that a too high ionic strength could harm the electrostatic interaction between FNR and the ITO layer.[141] Doping with 2% resulted in the highest photocurrent (2 mA/cm^2) and a small onset potential (0.42 V vs. RHE, **Figure III-4-A**). This result compares well with the 1% optimal doping reported in literature.[68] Doping generates a new energy level increasing the conductivity of the material. The

photocurrent and onset potential become worse at higher loading because high dopant levels can increase the chance of electron recombination.

Several OER catalysts were tested. Loading of CoB or NiB with the same protocol used for hematite caused suppression of the photocurrent (data not shown), by probably masking the underneath oxide layer. The best performance was obtained by using FeOOH as the OER catalyst, which resulted in the greatest combination in terms of onset potential, photocurrent and stability. FeOOH was electrodeposited by applying a constant potential of +0.2 V vs Ag/AgCl in a stirred 0.1 M Ar-purged $FeSO_4$ solution for 600 s under light, followed by +1.2 V vs Ag/AgCl for 60 s in the dark.[67,68] NiOOH alone and in combination with FeOOH were also tested: in both cases the achieved layers were less stable and the resulting photocurrent was lower. Therefore, FeOOH alone was used for this work. Note that this result is in contrast with literature reports where the photoanode $BiVO_4$/FeOOH/NiOOH was identified to be the most stable.[67]

PEC results are shown in **Figure III-4-B**. Loading of the catalyst caused a decrease of the onset potential of 100 mV: the resulting curve was now reaching higher currents at lower potentials. Beside improving the rates of water oxidation, the FeOOH layer provides a protection for the $BiVO_4$ layer increasing the stability of the photoanode.[69]

The synthesized photoanodes compare well with the literature even though some of the reports show electrodes with top record current reaching 4.52 mA/cm^2 and 6.56 mA/cm^2 at 1.23 V vs. RHE for α-Fe_2O_3 and $BiVO_4$- based electrodes, repsectively.[66–68,85,191,194–196]

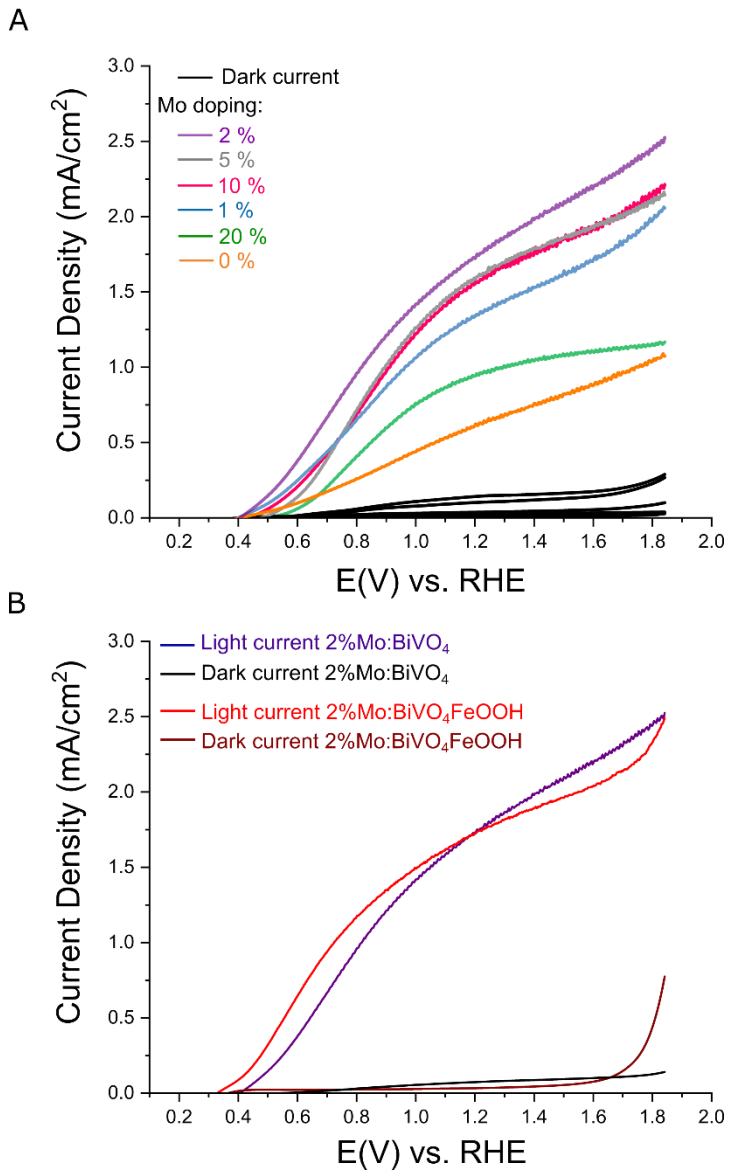


Figure III-4. PEC performances of $BiVO_4$ upon molybdenum doping and after catalyst deposition. A. Effect of Mo doping**.** Linear sweep voltammetry of $BiVO_4$ electrodes doped with different amounts of Mo. The electrodes were evaluated for their photocurrent and onset potential. **B.** Introduction of the OER catalyst**.** Loading of catalyst FeOOH determines a clear enhancement in the onset potential of the water oxidation reaction. Experiments were carried out in 0.5 M borate pH 9, using Pt as CE, Ag/AgCl as RE. Light intensity: 0.92 sun; λ>420 nm.

3.4.2. Light-driven $NADP^+$ reduction

The previous paragraph shows the synthesis of the photoanodes (α-Fe_2O_3 and 2%Mo:$BiVO_4$/FeOOH) and their PEC performances. The photoanode was then coupled to the electrochemical leaf to test the light-driven $NADP^+$ reduction.

The reactions were carried out in a one-cell compartment in 50 mM borate (pH 8) using a two-electrode setup: the ITO@FNR electrode was the working electrode (WE), while the photoanode (in this case α-Fe_2O_3/CoB) was both the counter and reference electrode (CE and RE, respectively). Different potentials and $NADP^+$ concentration were tested (data not shown) and no clear enhancement of current under light was observed until a large bias was applied (–1.2 V, using 100 µM $NADP^+$).

A chronoamperometric experiment (30°C, –1.2 V vs. CE) was set up under continuous Ar bubbling to ensure no mass transport limitation and to get rid of O_2. The result of the experiment is shown in **Figure III-5-A**. Almost no current was detected in the dark, while a big current enhancement was reported upon light illumination when $NADP^+$ was not present (0.92 sun, λ>420 nm). This current is related to H_2 production at the ITO electrode. After $NADP^+$ injection, the measurement was paused, the solution was flushed for 30 seconds to remove introduced oxygen and the current was then monitored again. Cofactor injection caused a current enhancement of ≈20 µA, which decreased over time and reached the same level of the background after 40 minutes. The current prior to $NADP^+$ injection and the current after reaching the baseline was fitted via a non-linear fitting procedure (Origin 2017): the resulting line (red dotted line, **Figure III-5-A**) represents the background current *i.e.* unrelated to $NADP^+$ reduction.

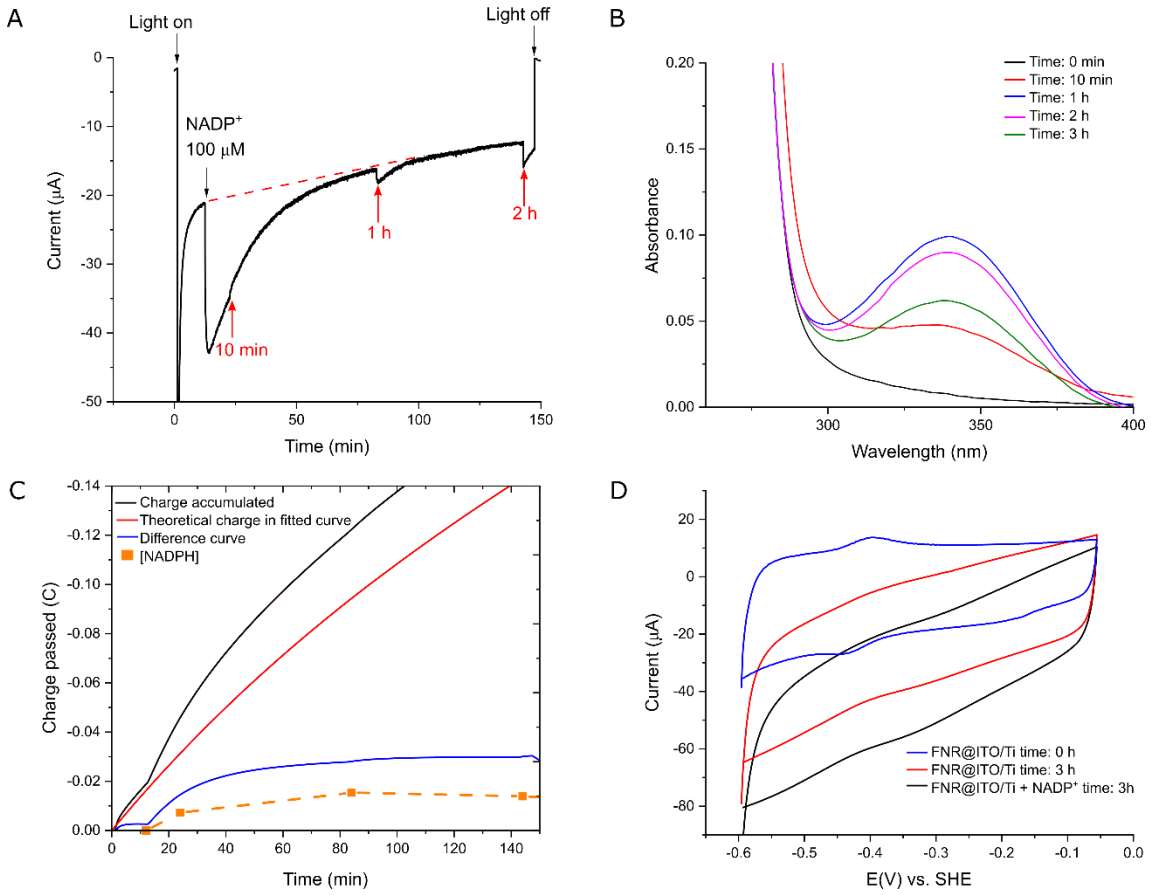


Figure III-5. Light driven NADP$^+$ reduction. **A.** Chronoamperometry. Photoanode: 1 cm^2 α-Fe_2O_3/CoB (CE and RE) and 2 cm^2 FNR@ITO/Ti electrode (WE) in a one-compartment cell containing 50 mM borate (5 mL, pH 8, 30°C). Light intensity: 0.92 sun; λ>420 nm. A bias of −1.2 V vs RE was used to drive the reaction. From left to right, black arrows indicate start of light illumination, injection of NADP$^+$ (to 100 µM) and light-switching off. Red arrows show time points of removal of 500 µL of the reaction buffer for NADPH quantification by UV-vis analysis. Dotted line represents fitted current curve predicting the trend with no cofactor injection **B.** UV-vis results. Absorption spectrum of the solution at time 0 (black), 10 minutes (red), 1 h (blue), 2 h (violet), 3 h (green). **C.** Charge passed. In black, total charge passed from trace in Panel A; in red, charge resulting from the fitted curve; in blue, the difference between black and red lines. Measured NADPH concentration (converted to charge) is plotted as orange squares. **D.** CV of the FNR@ITO/Ti electrode. CV in 50 mM borate pH 8 of the FNR@ITO/Ti electrode used in Panel A before the experiment (blue line). In red, CV (3 mV/s, 30°C) of the electrode after 3 h in the solution now containing 25 µM NADPH and ≈ 75 µM unreacted NADP$^+$. In black, after re-addition of NADP$^+$ to 100 µM.

Aliquots (500 µL) were removed at different time points as indicated in the graph to determine NADPH production by measuring UV-vis absorbance at 340 nm (A_{340}) using the literature extinction coefficient value (ε, literature value = 6.22 mM^{-1} cm^{-1}).[176] UV-vis results are shown in **Figure III-5-B**. After 10 minutes reduced cofactor

was detected (7.2 µM) and after 1 h it reached 15.4 µM (15% conversion). Surprisingly, after 2 h no increase in cofactor concentration was detected and the cofactor concentration decreased to 9.5 µM at the end of the experiment (3 h).

Results are clarified in **Figure III-5-C**. The current trace from **Figure III-5-A** was integrated (*charge* (C) = *current* (A) *x time*(s)) and resulted in the black trace (total charge accumulated, **Figure III-5-C**). The background current (red dotted line, **Figure III-5-A**) was integrated to model the charge passed if no $NADP^+$ was injected (red trace, **Figure III-5-C**). By subtracting the two traces (total current – background current) the blue line was obtained, which represents the charge related to $NADP^+$ reduction. The measured NADPH was plotted (as a charge using the empirical ε, orange squares) and the values are smaller than the charge difference calculated probably because of a small error derived from the fitting procedure (**Figure III-5-C)**.

The light driven $NADP^+$ reduction stopped working after 1 h. Further experiments showed that most of the cofactor is reduced within 30 minutes and plateaued after 1 h. Several reasons could be involved in the deactivation of the system. A CV of the FNR@ITO electrode was performed at the end of the experiment but $NADP^+$ reduction catalysis and non-turnover peaks (giving information on FNR coverage) were not visible (red line, **Figure III-5-D**). Re-addition of $NADP^+$ at that stage did not restore the current (black line, **Figure III-5-D**), suggesting that $NADP^+$ degradation was not the only reason for the system deactivation. The blue line shows the CV of the FNR@ITO/Ti electrode prior to the light-driven experiment.

Either FNR dissociated from the electrode or it denatured because of several reasons such as (i) high temperature, (ii) large negative potential, (iii) production

of toxic intermediates from the photoanode or (iv) light sensitivity of FNR. Below, each possibility was investigated and results are presented in **Figure III-6**, which shows the NADPH concentration measured by UV-vis spectrophotometry.

Siritanaratkul[141] reported an increased instability of the FNR@ITO/support electrode at a higher temperature (by observing the non-turnover peaks). The effect of changing the temperature was investigated and results are summarized in **Figure III-6-A**: a light-driven NADPH production experiment was carried out as described above at 20°C (black trace **,** using 200 µM $NADP^+$, **Figure III-6-A**) as opposed to the 30°C temperature used in **Figure III-5-A**. As for the 30°C case, the system stopped working after 60 minutes and achieved similar conversion (11%). Hence, the temperature does not affect massively the system, as also observed in related publication (**Figure III-6-A**).[90,139,144]

The large applied bias was reported by Siritanaratkul to affect FNR: the more negative the potential, the faster the decrease of the non-turnover peaks.[141] Here, smaller biases were then tested because the large applied bias could destabilise the electrode. The smallest potential still allowing for product detection with the α-Fe_2O_3/CoB photoanode was −0.6 V_{RHE} as established from LSV experiments (see **Figure III-3-B**). When the applied bias was decreased to −0.5 V bias and −0.8 V, NADPH was not detected (data not shown). When the applied bias was decreased only to −0.9 V, the NADPH concentration reached 12.4 µM and after 1 h the system reached inactivation (**Figure III-6-A,** red trace**).** Moreover, FNR non-turnover peaks and turnover peaks were not detected by CV at the end of the two experiments described above, as shown also for **Figure III-5** (data not shown).

During the PEC experiment the photoanode could generate detrimental compounds for the cathode (FNR@ITO/Ti electrode). For instance, it was reported

that partial oxidation of water to hydrogen peroxide could occur at the photoanode.[197] Thus, catalase was added in solution in two experiments carried out at 30°C and 20°C (catalase final concentration: 0.2 mg/ml, using −1.2 V applied bias). Catalase converts hydrogen peroxide to water and oxygen gas. Hence, it could improve the lifetime of the system by scavenging potentially generated H_2O_2. **Figure III-6-B** shows the resulting NADPH production at 20°C and 30°C when catalase was included: at 30°C NADPH production stopped after 60 minutes (green trace, **Figure III-6-B**). At 20°C, the NADPH concentration increased from 26.9 µM after 50 min to 32 µM after 180 min. However, this increase was not considered as significant given the small difference. **Figure III-6-C** confirmed that inclusion of catalase did not improve the stability of the FNR@ITO/Ti electrode in the PEC system: the final CV did not show non-turnover or turnover peaks. The blue trace shows the CV of the FNR@ITO/Ti electrode prior to introducing catalase (**Figure III-6-C** shows the example of the catalase experiment at 20°C). The red trace is the CV after $NADP^+$ injection with the resulting catalytic peaks before starting the light-driven experiment (see Sections 1.6 and 2.4.2.), hence proving the electrode was active (**Figure III-6-C**). At the end of the light driven experiment (after 3 h), a CV was carried out on the reaction solution, as described in **Figure III-5-D**.

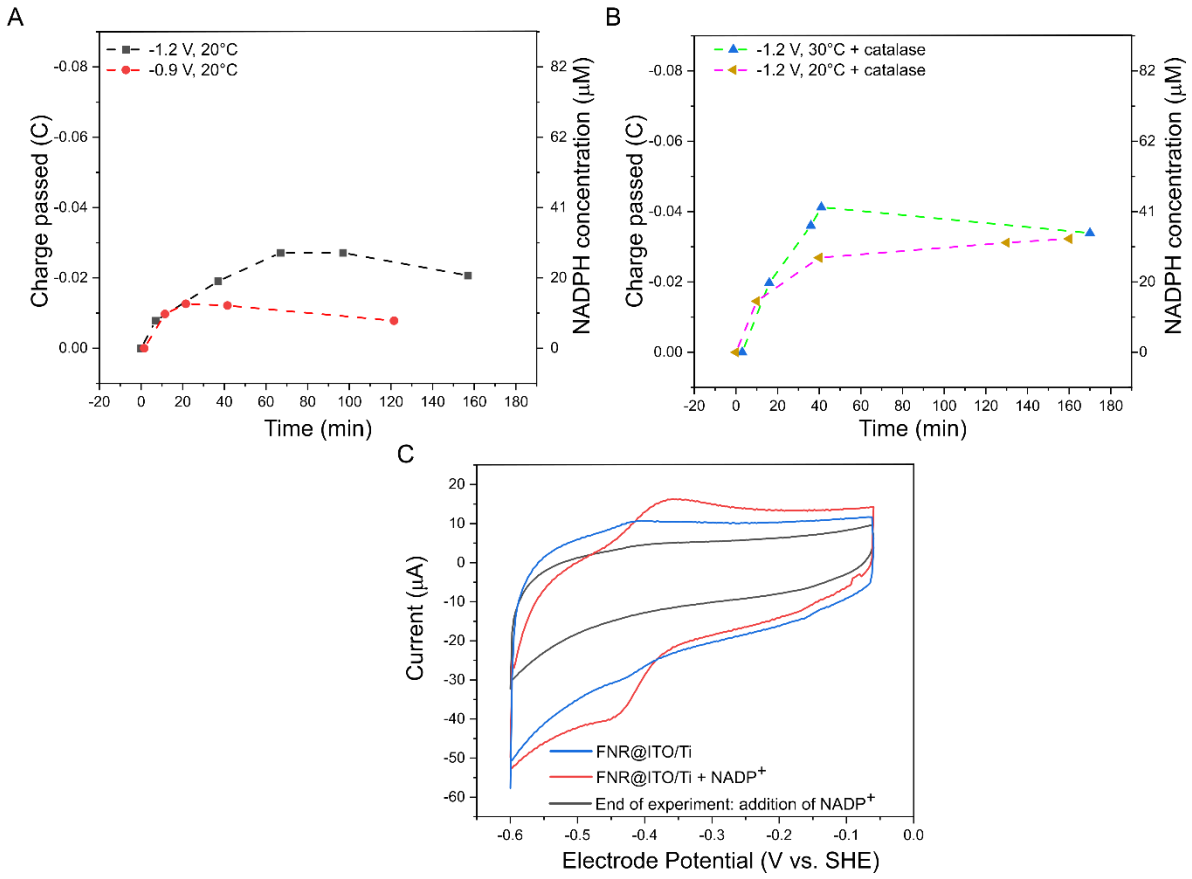


Figure III-6. Effect of decreasing temperature and applied bias and introduction of catalase to the system. A. Variation of temperature and bias**.** NADPH production measured by UV-vis (A_{340}) of light-driven $NADP^+$ reduction using the FNR@ITO/Ti electrode (2 cm^2) and as RE and CE α-Fe_2O_3/CoB (1 cm^2). Black trace: applied bias used –1.2 V and temperature 20°C; Red trace: applied bias used –0.9 V and temperature 20°C. **B.** Addition of catalase. NADPH production measured by UV-vis (A_{340}) of light-driven $NADP^+$ reduction using the FNR@ITO/Ti electrode (2 cm^2) and as RE and CE α-Fe_2O_3/CoB (1 cm^2). Catalase was injected in solution to 0.2 mg/mL. Green trace: applied bias used –1.2 V and temperature 30°C; Pink trace: applied bias used –1.2 V and temperature 20°C. **C.** CV of the FNR@ITO/Ti electrode from the catalase experiment. Blue: time 0 h (prior to catalase injection), non-turnover peaks; red: injection of $NADP^+$ (to 100 µM); black: in reaction solution after 3 h after injecting more $NADP^+$ (to 100 µM). Conditions: 3 mV/s, 20°C; Pt: CE; Ag/AgCl: RE; WE: FNR@ITO/Ti (2 cm^2) electrode supplemented with catalase. One-compartment cell.

The resulting CV showed neither non-turnover peaks nor catalytic peaks. Further injection of $NADP^+$ did not change the voltammetry (black trace, **Figure III-6-C**). Hence, even with the introduction of catalase the system showed the same pattern of deactivation. Note that when these experiments were carried out the nanoconfinement of E2 had not yet been discovered (see Section 1.6.3. and

Chapter II) and E2 (in this case, catalase) was predicted to work in solution. However, based on the results shown in Chapter II and by Megarity *et al*.[139,146] the success of the catalase-experiment depends on the ability of catalase to bind the electrode nanopores. The electrode was still defined here as FNR@ITO/Ti because experiments to determine whether catalase bound within the electrode had not been carried out.

The deactivation of the light-driven NADPH reduction system could be due to FNR or $NADP^+$ degradation. Instability of the FNR@ITO/Ti electrode was not due to a short inherent FNR half-life as it was known that the FNR@ITO/support electrode was stable for several days.[134,144] A one-cell compartment chronoamperometry experiment (α-Fe_2O_3/CoB: CE, RE, FNR@ITO/Ti, 2 cm^2, 30°C) was carried out to investigate the light sensitivity of the system. The FNR@ITO/Ti electrode was protected from the light by a black cylinder tube (**Figure III-7-A**). A bigger volume (8 mL) was used to accommodate the bulky setup within the electrochemical cell. The experiment was set up in 50 mM borate (pH 8) and $NADP^+$ was injected (to 100 µM) into the system after switching on the light. After taking the first aliquot at 1 h, the solution was discarded and exchanged with new buffer containing fresh $NADP^+$. The light was switched on again and the reaction was sustained for a further 90 minutes. **Figure III-7-B** shows that the current remained steady and did not come back to the baseline (red dotted line), in contrast to the current decay observed in **Figure III-5-A**. Results of the UV-vis experiments are shown in **Figure III-7-C**. After 45 minutes, NADPH was detected as in previous experiments. Successful washing of the cell is proven by looking at the aliquot taken directly after discarding the buffer trace (blue line, **Figure III-7-C**). Then, the NADPH concentration increased up to an unprecedented 90 minutes

(final concentration of the second experiment: 32 µM NADPH). Furthermore, by running a final CV it was clear that the electrode was still catalytically active, in contrast with the previous experiments (**Figure III-7-D,** red trace).

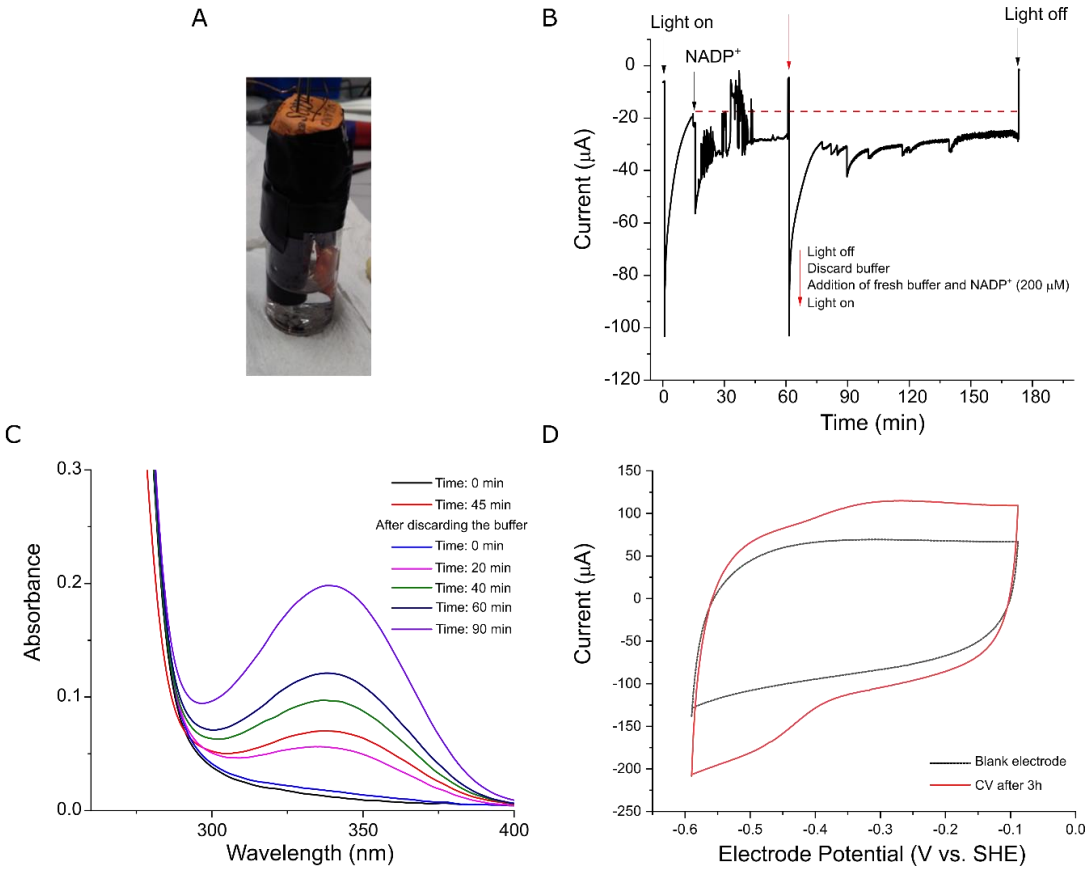


Figure III-7. Light-driven $NADP^+$ reduction using a light-protected electrochemical leaf. A. Setup used to protect FNR@ITO/Ti electrode from the light. **B.** Chronoamperometry**.** $NADP^+$ reduction in 50 mM borate (pH 8, 30°C) CE: 1 cm^2 α-Fe_2O_3/CoB photoanode; CE, RE: 2 cm^2 FNR@ITO/Ti protected from the light. Light intensity: 0.92 sun; λ>420 nm. Applied potential: –1.2 V. $NADP^+$ to 100 µM. Red arrow: switching-off illumination, discarding of buffer and reintroduction of buffer containing $NADP^+$ (200 µM) and switching on of the light. Red dotted line shows fitted line to the current with no $NADP^+$. **C.** UV-vis results**.** Spectra of samples taken at different time points before and after discarding and refreshing the buffer. **D.** CV of the FNR@ITO/Ti electrode**.** CV (3 mV/s, 30°C) using Pt as CE and Ag/AgCl as RE.

The experiment described above proved that intense light was destabilising the system. In order to discriminate between NADPH and FNR light sensitivity, a control was performed where solutions of 200 µM $NADP^+$/50 µM NADPH were prepared in 50 mM borate (pH 8). Two separate tubes were left at the same

temperature (25°C), one under light illumination (0.92 sun, λ>420 nm, **Figure III-8-A**) and the other in the dark, by completely covering with aluminium foil (**Figure III-8-B**). The experiment shows that no change was observed between the two cases, thus excluding significant NADPH degradation under light illumination.

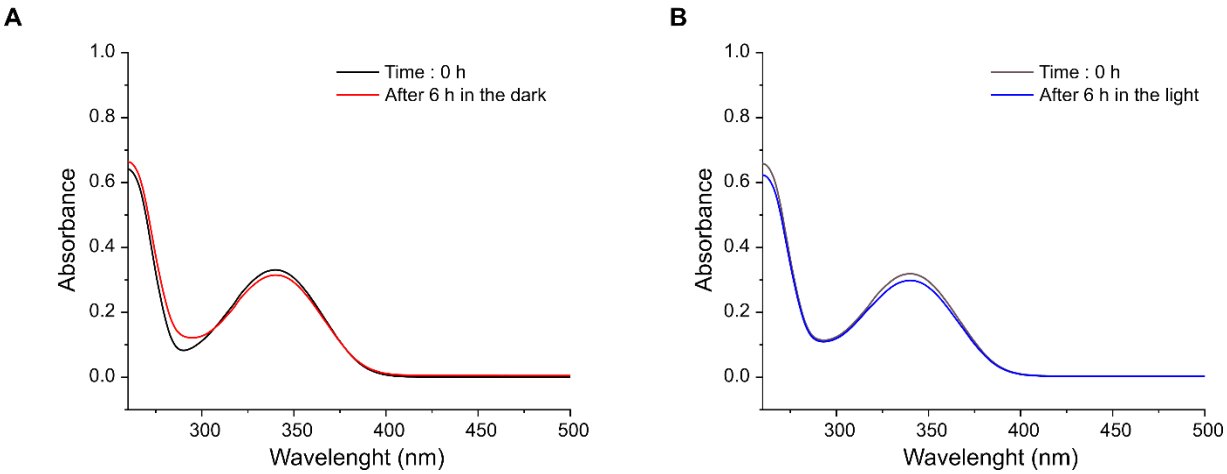


Figure III-8. NADPH light sensitivity. Two solutions of NADPH were prepared; one tube was left under light for 6 hours while the other was kept for 6 hours in the dark. Conditions: Ar purging, 25°C. **A.** Sample left in the dark. **B.** Sample under light illumination; light intensity: 0.92 sun; λ>420 nm.

The light sensitivity of FNR under intense light is likely due to the presence of the FAD in the catalytic cycle (see Section 1.6.1). The UV and blue light sensitivity of FAD and flavins has been long known.[198] Upon light illumination the excited state of the flavin can generate new chemistry. Sorigue *et al.* recently described an algal enzyme, a FAD-containing fatty acid photodecarboxylase (FAP) which is able to catalyse the generation of hydrocarbons from fatty acids upon blue light illumination.[199] The excited FAD* was proposed to be able to abstracts an electron from the fatty acid which triggers a decarboxylation to yield an alkyl radical. The alkyl radical can then receive the electron back from $FAD^{\bullet-}$ to form an hydrocarbon chain.[199] Lakavath *et al*. showed that FAP is irreversibly damaged by light exposure.[200] Briefly, the authors observed that purification under ambient light

yielded an inactive enzyme, while purification under red light and storage in the dark allowed obtaining an active enzyme. Furthermore, they reported a 60% decrease of the activity of FAP after 30 minutes of pre-illumination. Through Electron Paramagnetic Resonance (EPR) they were able to observe a strong radical signal in the light-inactivated enzyme. The authors reasoned that the inactivation is caused by the damage to the surrounding residues in the active site.[200] In this Thesis, although FNR was purified under ambient light illumination and its activity was not affected, the enzyme could be damaged in a similar way under intense light illumination, leading to the damage of the residues surrounding the FAD-centre (*eg.* C-terminal tyrosine). Methodologies, such as Tandem mass spectrometry (MS/MS) could be used to determine the chemical nature of potential damages.

3.4.3. Development of a *Z*-scheme without external bias

3.4.4. System with a single light absorber

The PEC results (see Section 3.4.1.) showed that both $BiVO_4$ and hematite electrodes required an applied bias to drive the NADPH regeneration. Because of the higher performances of the 2%Mo:$BiVO_4$/FeOOH photoanode, this was used for all following experiments in this Chapter, which describes the unassisted light-driven reductive carboxylation of pyruvate to malate using the (FNR+ME)@ITO/support electrode (see Chapter II).

Figure III-9 explains the thermodynamic limitation of the prepared photoanode to catalyse the cathodic reaction: it compares two separate voltammograms, in red the light-driven water oxidation by the photoanode (in 0.5 M borate, 4 mM $MgCl_2$, pH 9) and in blue the reductive carboxylation driven by the (FNR+ME)@ITO/Ti electrode (in a CO_2 saturated buffer containing 0.2 M HEPES, 0.1 M $KHCO_3$, 4 mM $MgCl_2$, 50 mM pyruvate, pH 7.5 under CO_2 atmosphere). In both voltammetries, Pt was the CE and Ag/AgCl the RE. **Figure III-9** shows that the onset potential for the light-driven water oxidation is more positive than the reduction potential of the pyruvate/malate couple (dotted line, $E^{C3/C4}$, see Chapter II), therefore, an applied bias of at least 0.4 V is needed. The problem resembles what naturally occurs in oxygenic photosynthesis. Nature solved the problem by adding another light absorber, PSI (see Section 1.2.).

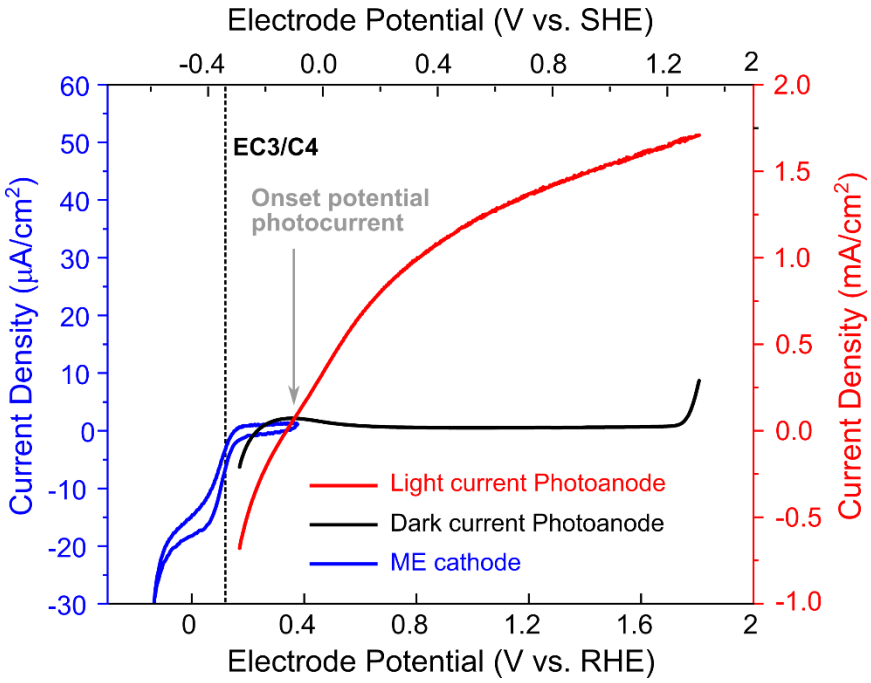


Figure III-9. Comparison between the light-driven water oxidation at the 2%Mo:BiVO$_4$FeOOH photoanode and the reductive carboxylation at the (FNR+ME)@ITO/Ti cathode. Photoanode: the voltammogram of the photoanode was measured using Pt as CE and Ag/AgCl as RE in 0.5 M borate, 4 mM $MgCl_2$ (pH 9). The current in the dark and under visible light are represented by the black and red line, respectively. Light intensity: 0.92 sun; λ>420 nm. Conditions: stationary electrode, 25°C. Cathode: the cathode CV was measured in a three-compartment cell using Pt as CE and Ag/AgCl as RE in a buffer containing 0.2 M HEPES, 0.1 M $KHCO_3$, 4 mM $MgCl_2$, 50 mM pyruvate under CO_2 atmosphere. The dotted line shows the potential for the C3/C4 reaction (pyruvate to malate through NADPH recycling) as shown in Section 2.4.2.2. Figure adapted from Morello *et al.*[90]

Several strategies can be pursued to design an unassisted light-driven AP system. One possibility is to choose a material able to drive both H_2O oxidation and the C3/C4 reactions. Example of these are TaON and *g*-C_3N_4. Both of them have the suitable energetics, but they have severe drawbacks (see Section 1.4).[46] Tantalum is a rare element and TaON synthesis and loading on the electrode is expensive and laborious. Moreover, the current is very low when no potential is applied, which is why the performance is usually reported for high potentials.[70,201–203] *g*-C_3N_4 is very promising, because it is metal-free, cheap and it could be used both as photoanode or as photocathode (the latter by doping to switch the

material's behaviour to *p*-type). However, *g*-C_3N_4 suffers from several problems, such as low conductivity and high recombination rate. Moreover, its use in a PEC system is underexplored, while most focus is given on particulate systems.[74,204]

Here, *g*-C_3N_4 was synthesized according to a protocol reported in the literature,[205] but no success was obtained for loading it on a conducting support such as FTO/ITO glass or Ti foil. The layer (loaded by EPD or drop-casting) was unstable so that no work could be pursued in that direction. However, it was successfully used in a particulate system, by using TEA as electron donor.

Figure III-10 shows the result of the experiment. *g*-C_3N_4 was sonicated for 2 h in 50 mM borate (pH 8), followed by stirring in buffer containing FNR (18 µM) for 2 h. Then, the suspension was centrifuged, the supernatant removed and the pellet was resuspended in borate buffer (pH 8, 8 mL) containing 0.1 M TEA as electron donor and $NADP^+$ (100 µM). NADPH production was monitored by UV-vis. Final concentration of 9.6 µM NADPH was obtained, but the production came to a halt after 2 hours, probably because of light sensitivity (**Figure III-10-A,B**). This preliminary experiment resulted in some initial data on the FNR-g-C_3N_4 composite for visible light-driven NADPH production. However, this direction was not followed by further experiments, as the main goal was to develop a PEC system. Results on light-driven particulate system for FNR-catalysed NADPH production were reported previously using dye-sensitised TiO_2.[141]

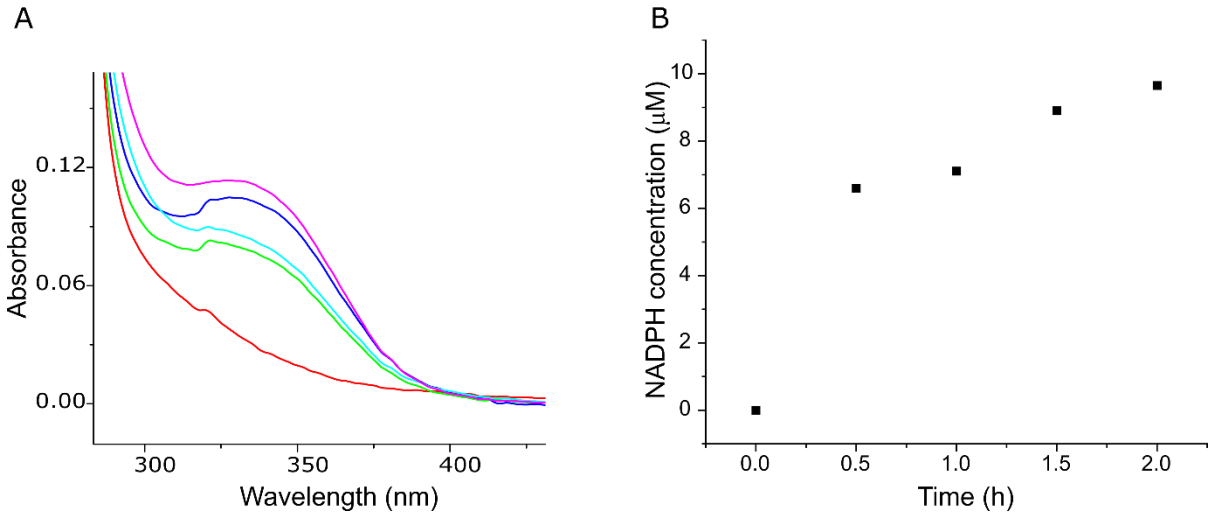


Figure III-10. Particulate light-driven NADPH reaction using a particulate FNR-*g*-C_3N_4 composite. *g*-C_3N_4 (0.2 g) was stirred for two hours with FNR. The reaction was carried out in 50 mM borate pH 8, supplemented with 0.1 M TEA and 100 µM $NADP^+$. Conditions: stirring, 25°C. At different time points aliquots (600 µL) were taken for UV-vis analysis (340 nm). Prior to measuring the spectra, samples were centrifuged to remove nanoparticles. **B.** NADPH production measured by absorption at 340 nm for 2 hours. No increase in concentration was detected afterwards. Light intensity: 0.92 sun; λ>420 nm.

3.4.4.1. Assembly of a Z-scheme

A *Z*-scheme as in oxygenic photosynthesis offers another solution to the thermodynamic issue described in the previous paragraph. For this purpose, a single junction solar cell was coupled to the 2%Mo:$BiVO_4$/FeOOH photoanode.

A commercially available 1 V Si-solar cell was first characterised to confirm its voltage. **Figure III-11-A** confirms the resulting voltage (around 1.1 V) through the *i*-V curve. The potential of the solar cell was halved through a set of constant resistors (equal resistance, **Figure III-11-B**) by developing a voltage-divider circuit. **Figure III-11-B** shows how the halved-solar cell circuit was connected to the photoanode, cathode and to the potentiostat for further experiments. A chrono-potentiometric experiment was carried out to determine the voltage of the “halved”

solar cell and **Figure III-11-C** confirms the halved voltage to be 0.5 V. Both solar cells (1 V and 0.5 V) were used in the following experiments.

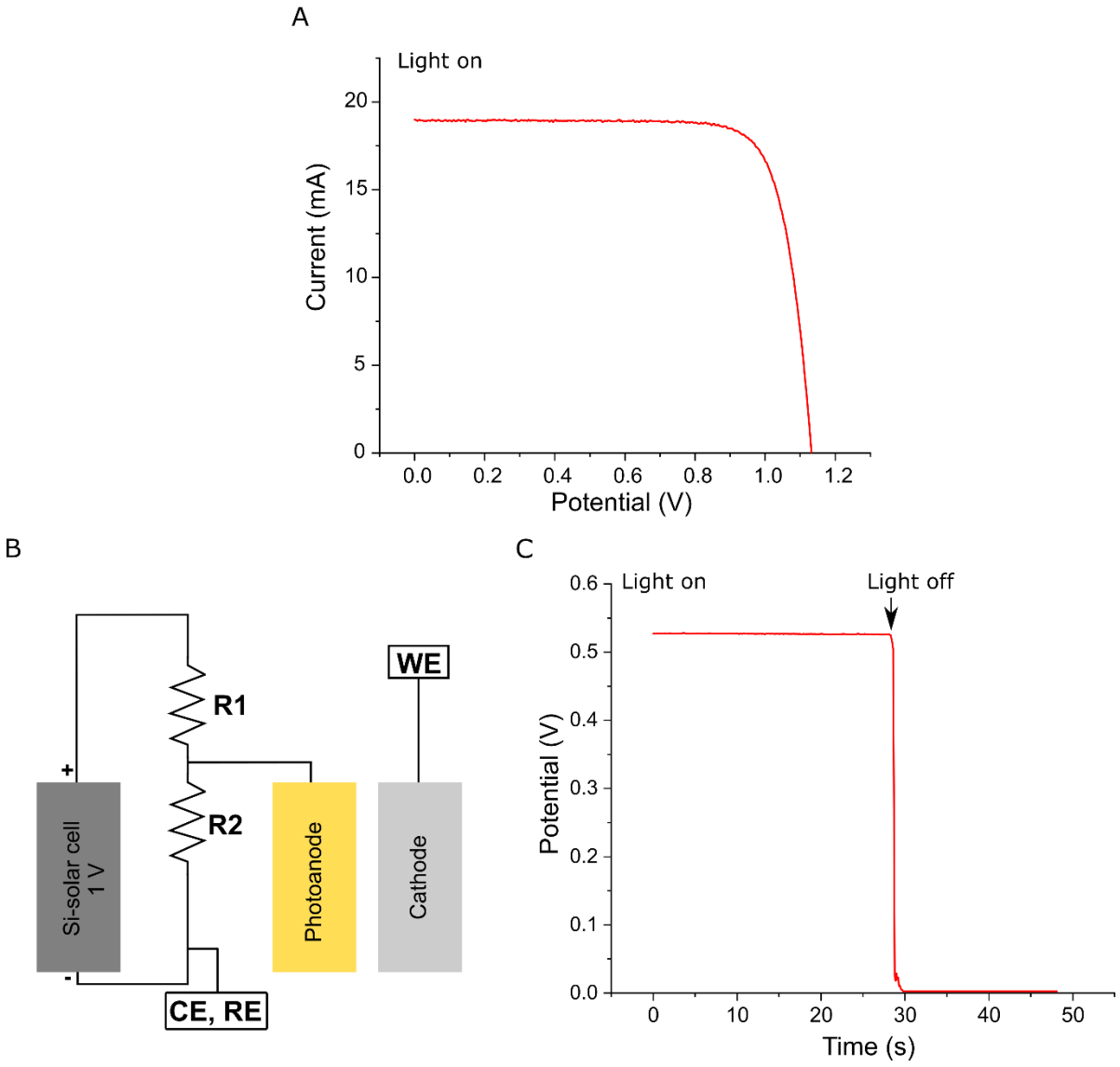


Figure III-11. Solar cell characterisation and scheme of experiment circuit. A. *i*/*V* curve of the commercial 1 V Si solar cell. **B.** Schematic representation of the circuit used to cut the voltage of the solar cell to 0.5 V and its connection to the AP system. WE, CE and RE are the connection points to the potentiostat circuit (see Section 7.1.2.) **C.** Chronopotentiometry of the 0.5 V solar cell (potential halved by using two set of resistors). Light intensity: 0.92 sun; λ>420 nm. Conditions: stationary, 25°C. Figure adapted from Morello *et al.*[90]

Figure III-12 shows the results of coupling the solar cell to the 2%Mo:$BiVO_4$/FeOOH photoanode using the circuit described in **Figure III-11-B**.

Linear sweep voltammetry was carried out using the same conditions as in the previous paragraph. When no solar cell was included (red trace, **Figure III-12**) the onset potential for light-driven water oxidation was more positive than the $E^{C3/C4}$ value. Addition of the solar cell (by wiring it to the CE) moves the onset potential by 1 V and by 0.5 V with the 1 V and 0.5 V Si-solar cell, respectively. In conclusion, addition of a 1 V or 0.5 V solar cell allowed the C3/C4 reaction to be driven only with visible light, as the onset potential of water oxidation became more negative than the potential of the C3/C4 reaction.

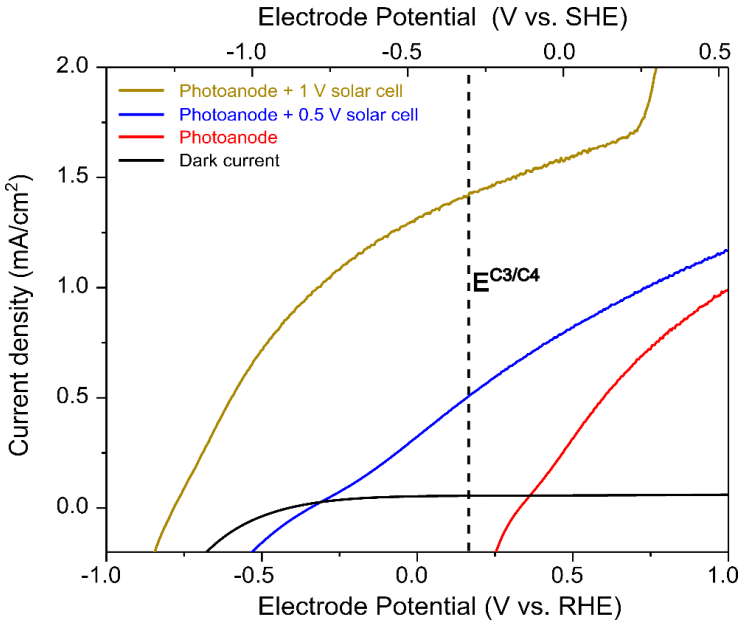


Figure III-12. Effect of coupling the photoanode to the Si-solar cell. Linear sweep voltammetry of the 2%Mo:$BiVO_4$/FeOOH photoanode coupled to a 1 V Si solar cell (yellow trace), 0.5 V Si solar cell (potential halved, blue trace), no solar cell (red trace, photoanode only). Circuit used is as in Figure III-11-B, but the photoanode was the WE, while the solar cell and Pt were wired together and connected to the CE and RE. Light intensity: 0.92 sun; λ>420 nm. Dotted line shows the potential of the C3/C4 reaction as shown in Chapter II and black line is the photoanode wired to the 1V Si solar cell dark current. Conditions: stationary electrode, 25°C. Figure adapted from Morello *et al.*[90]

3.4.5. Oxygen detection

Detection of O_2 is crucial to demonstrate that water is the electron donor in an AP system. The simplest method to measure oxygen production was to seal the anode compartment and take gas samples to be measured by GC. However, because of leakage of air into the electrochemical cell due to imperfect cell design and air contamination during sampling by syringe, a different analytical method was required. The collector-generator system, which was developed by Sherman *et al.* was better suited for this purpose. The system is based on O_2 electrochemical detection, allowing its *in-situ* sensing by using an FTO electrode held at a distance of 1–2 mm distance to the photoanode.[206] The FTO (collector) is held at a very reducing potential to drive reduction of O_2 produced at the photoanode (generator). Importantly, the collector and generator are not electrically connected.

Calibration of the collector-generator system was required to obtain the oxygen collection efficiency (see below). The calibration was performed by using a known oxygen producer (another FTO electrode) held at a very oxidative potential to catalyse water oxidation, while the collector is held at a reducing potential to reduce generated oxygen gas.

A linear sweep experiment was first carried out to determine the correct potential for the water oxidation and oxygen reduction using the FTO electrodes. **Figure III-13-A** shows the result of the generator experiment carried out in 0.5 M borate, 4 mM $MgCl_2$ (pH 9): the onset potential is above 2 V vs. Pt for the oxidation reaction. To determine the potential for the reduction reaction, the experiment was first carried out under an Ar atmosphere (blue trace) and then O_2 (red trace) was introduced: a potential of –1.8 V vs. Pt was used in the later experiments (**Figure III-13-B**).

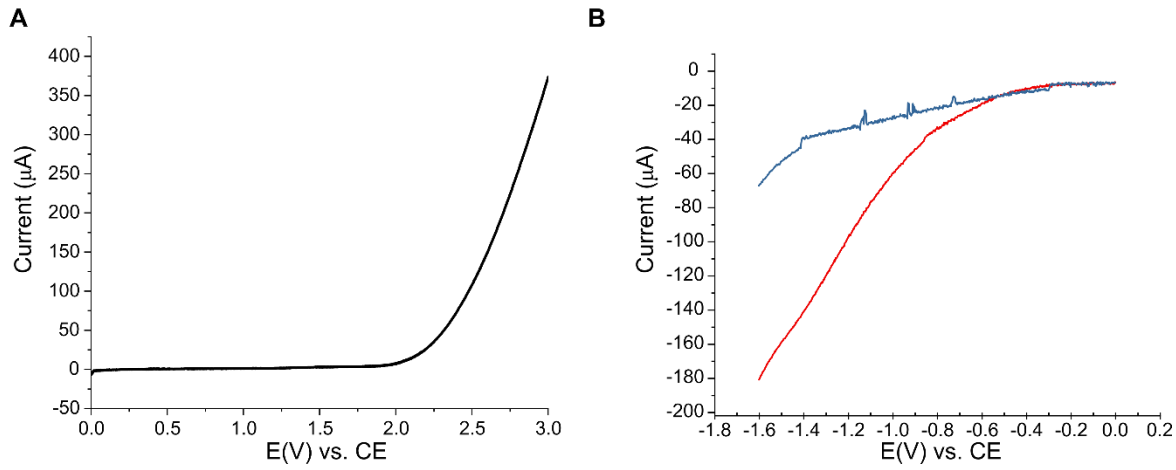


Figure III-13. Linear sweep voltammetry of FTO generator and FTO collector. A. Generator FTO electrode. Linear sweep voltammetry (stationary electrode, 25°C) in 0.5 M borate, 4 mM $MgCl_2$ (pH 9) using Pt as CE and RE. **B.** Collector FTO electrode. Linear sweep voltammetry (stationary electrode, 25°C) of a collector FTO electrode in 0.5 M borate, 4 mM $MgCl_2$ (pH 9) under Ar (blue) and after introduction of O_2 (red).

An example of a calibration experiment is shown in **Figure III-14**. A two-electrode system was used where the FTO collector electrode was the WE and its CE and RE (Pt wire) was held at the non-conductive side of the WE. Moreover, by using epoxy (to avoid short circuit) that setup was glued to the FTO generator electrode at a distance of 1–2 mm (**Figure III-14-A)**. The FTO generator (WE) was connected to a different Pt wire (CE, RE) via a second potentiostat. Two parallel chronoamperometries were carried out. **Figure III-14-B** shows the oxidation of H_2O and **Figure III-14-C** shows the reduction of generated O_2 (buffer as in **Figure III-13**). In **Figure III-14-B** the generator FTO electrode was kept at 0.5 V vs Pt when the system was off. Switching the potential to values above 2.0 V vs Pt. (3.0, 2.7 and 2.5 V vs. Pt) caused water oxidation to occur. At the same time, the collector FTO electrode was held at a constant potential of –1.8 V vs. Pt. Results are shown in **Figure III-14-C**. Switching on the generator caused the formation of a reductive current in all the three cases at the FTO collector. Equation 3.1 was used to calculate the collection efficiency ($FE_{col\ eff}$).

$$FE_{col\,eff} = {Q_{col}}/{Q_{gen}} \quad (3.1)$$

The charge passed at the collector (Q_{col}) was 4.36 C, 2.45 C, and 1.36 C, (**Figure III-14-C)**, while the charge passed at the generator (Q_{gen}) was 6.62 C, 3.79 C, and 1.97 C at 3.0, 2.7 and 2.5 V vs. Pt, respectively (**Figure III-14-B**). Note that the charge at the collector was corrected from the background to discard charge related to hydrogen production. The obtained average value was 65.4% ± 0.4. Similar values were obtained when a long single calibration experiment was conducted.

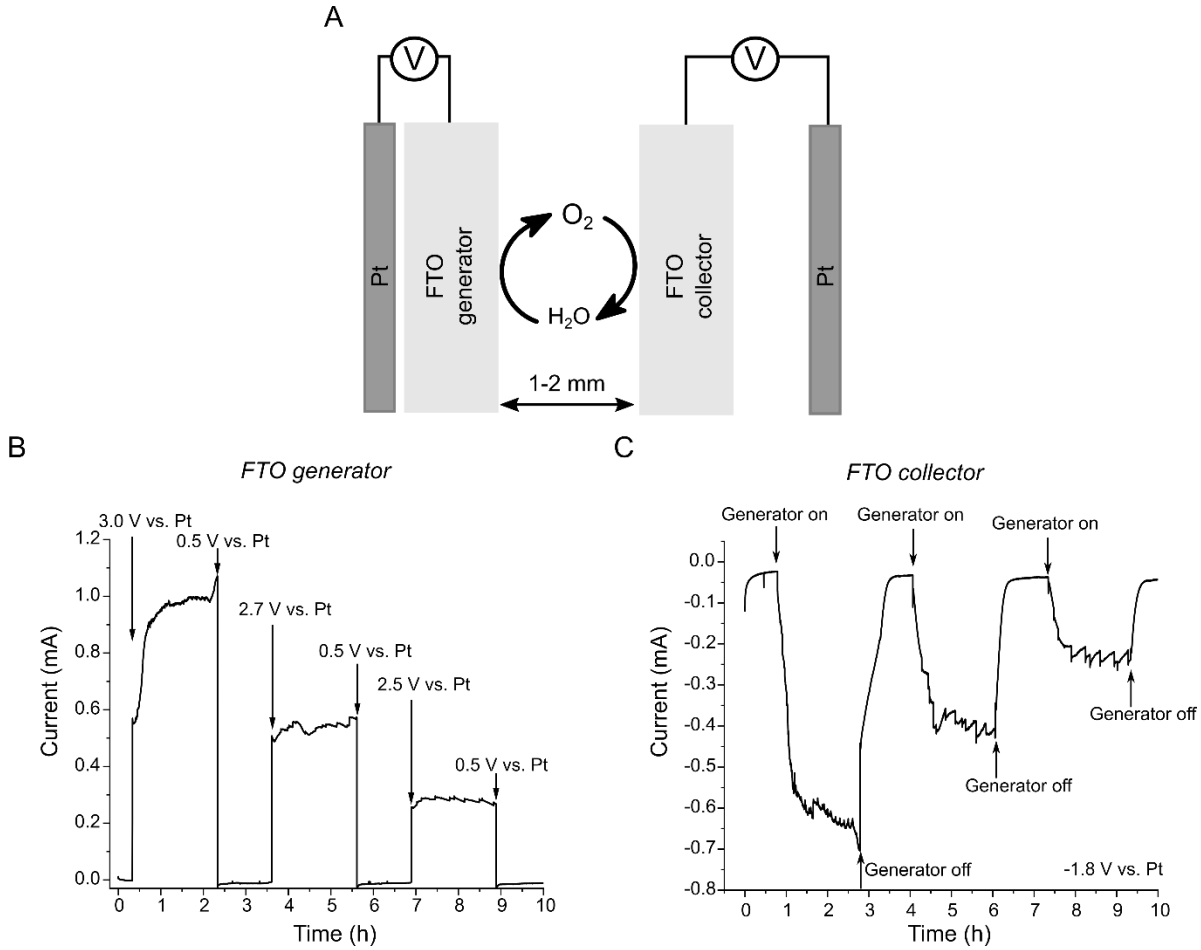


Figure III-14. Calibration of the collector electrode. A. Scheme of the experiment. Two potentiostats were used: The first potentiostat was connected to the FTO collector (WE, driving reduction of generated oxygen) and a Pt wire (CE, RE) was glued to the non-conductive side of the FTO. The second potentiostat was connected to another FTO electrode (generator, driving water oxidation) and to an additional Pt wire (CE, RE). The collector and generator electrodes were not in physical contact and were held at 1–2 mm distance. **B.** FTO generator. Chronoamperometry (stationary electrode, 25°C) of an FTO (generator, WE) electrode, using Pt as CE and RE in 0.5 M borate, 4 mM $MgCl_2$ (pH 9). At the beginning of the experiment, a potential of 0.5 V vs. CE was used (generator off). In order to allow water oxidation to occur, three different potential were tested (sequentially 3 V, 2.7 V, 2.5 V vs. Pt = generator on). **C.** FTO collector. Chronoamperometry (stationary electrode, 25°C) of an FTO (collector, WE), held at 1-2 mm from the generator and at -1.8 V vs. Pt. Switching on the generator (generator in Panel B) causes the formation of a reductive current.

3.4.6. Light-driven reductive carboxylation

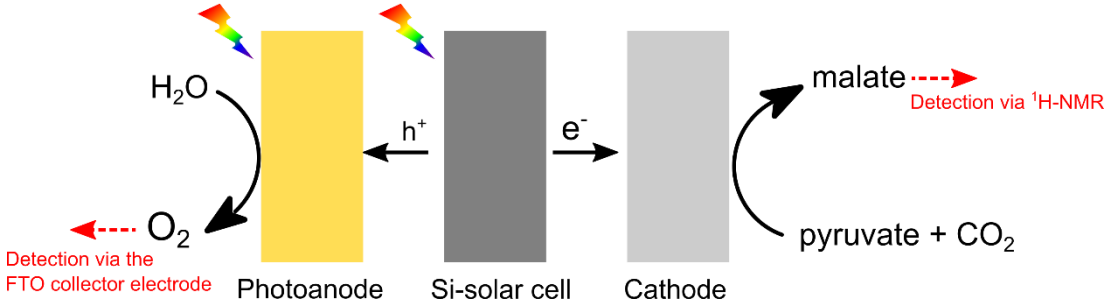


Figure III-15. Scheme of the reductive carboxylation. Visible light absorption triggers charge separation and water oxidation occurs at the photoanode. The excited electron reacts with the hole (h^+) produced at the Si solar cell (after charge separation). The electron from the silicon solar cell reaches the cathode where the enzyme can drive the reductive carboxylation of a carrier (pyruvate) to product (malate). The reaction was carried out in a two-compartment cell separated by a Nafion membrane. The electric circuit is shown in **Figure III-11-B.** Figure adapted from Morello *et al.*[90]

A light-driven reductive carboxylation experiment was set up in a two-compartment cell separated by a Nafion membrane with a 2%Mo:$BiVO_4$/FeOOH photoanode (1 cm^2), connected to an FNR@ITO/Ti electrode (12 cm^2) through a 0.5 V Si solar cell (unless stated otherwise). The potentiostat was used to monitor the current but no potential was applied (scheme in **Figure III-15,** circuit in **Figure III-11-B**). The anode compartment contained a solution of 0.5 M borate, 4 mM $MgCl_2$ (pH 9). Magnesium chloride was included to prevent migration of Mg^{2+} from the cathode to the anode compartment, which would result in a decrease of the cation concentration, which is important for ME activity.[171] In the anode compartment an FTO collector electrode for O_2 monitoring was held by epoxy to the photoanode at a distance of 1–2 mm. Care was used to prevent the collector from touching the photoanode, to avoid a short circuit. The FTO collector was connected to a secondary potentiostat and a potential of –1.8 V vs. Pt was applied to continuously reduce oxygen produced from the photoanode. The Pt (CE of the collector) was glued to the non-conductive side of the FTO collector electrode. The

compartment was flushed with Ar for 30 minutes and then sealed. The cathode compartment was filled with a buffer (4 mL) containing 0.05 M phosphate, 0.1 M $KHCO_3$, 4 mM $MgCl_2$, 80 mM pyruvate (pH 7.5). The cathode was prepared by immersing a piece of ITO/Ti (14 cm^2) in a stirred solution of FNR (18 µM, borate, pH 8) overnight. The electrode was rinsed and inserted into the two-compartment cell and the buffer was then flushed for 10 minutes with CO_2. Furthermore, the cathode compartment was protected from the light by using aluminium foil, continuously flushed with 100% CO_2 and stirred so that the system would not be limited by mass transport. Continuous flushing was performed because the electrochemical cell was not perfectly sealed and leakage of oxygen into the cell reduced the FE of the system. Note that when the cathode compartment was not flushed continuously but sealed instead, hydrogen gas was detected by GC (data not shown).

The pH difference between the two compartments (9 at the anode, and 7.5 at the cathode) can be a disadvantage as H^+ will migrate towards the anode compartment. However, it was observed that the photoanode would be more active at that pH.

Results of the chronoamperometric experiment are shown in **Figure III-16-A**. No current was detected in the dark. Switching on the light (0.92 sun, λ>420 nm) produced first a spike, which is a result of capacitive current; then a background current of 50 µA was observed.

Injection of $NADP^+$ (to 50 µM) produced a small increase in current, corresponding to $NADP^+$ reduction, and injection of ME (to 2.5 µM) caused the growth of a reductive current. The current growth signifies the entry of the enzyme within the electrode nanopores, as explained in Chapter II.

The response of the current upon injection of ME is different from the electrochemical data shown in Chapter II. Here it looks almost immediate instead of increasing for 2 hours. The reason for this difference is that catalysis of the light-driven system is limited by the photoanode and if not limited, a longer current growth would be observed. This was the case when a 1 V Si solar cell was used instead (see below).

The current persisted for 24 hours and decreased to around 50% of the original value, with an average catalytic rate of 2 µmol product h^{-1}. The current decrease throughout the experiment was not due to enzyme desorption or unfolding as re-addition of either ME or FNR did not restore the current. In separate experiments the cofactor and pyruvate were also re-injected after 24 h but the activity was not restored. No current was detected when the light was switched off.

In parallel, the result of the collector experiment is shown in **Figure III-16-B**. Switching on the light triggered a small increase in the reductive current, but the main factor affecting the current was the introduction of ME in the cathode compartment. Stopping light illumination at the end of the experiment caused a slow decrease of the current towards the baseline. By integrating the two traces the charge passed was 14.98 C for the reductive carboxylation in **Figure III-16-A** and 9.52 C for the oxygen reduction at the collector (after correcting for the background, **Figure III-16-B**).

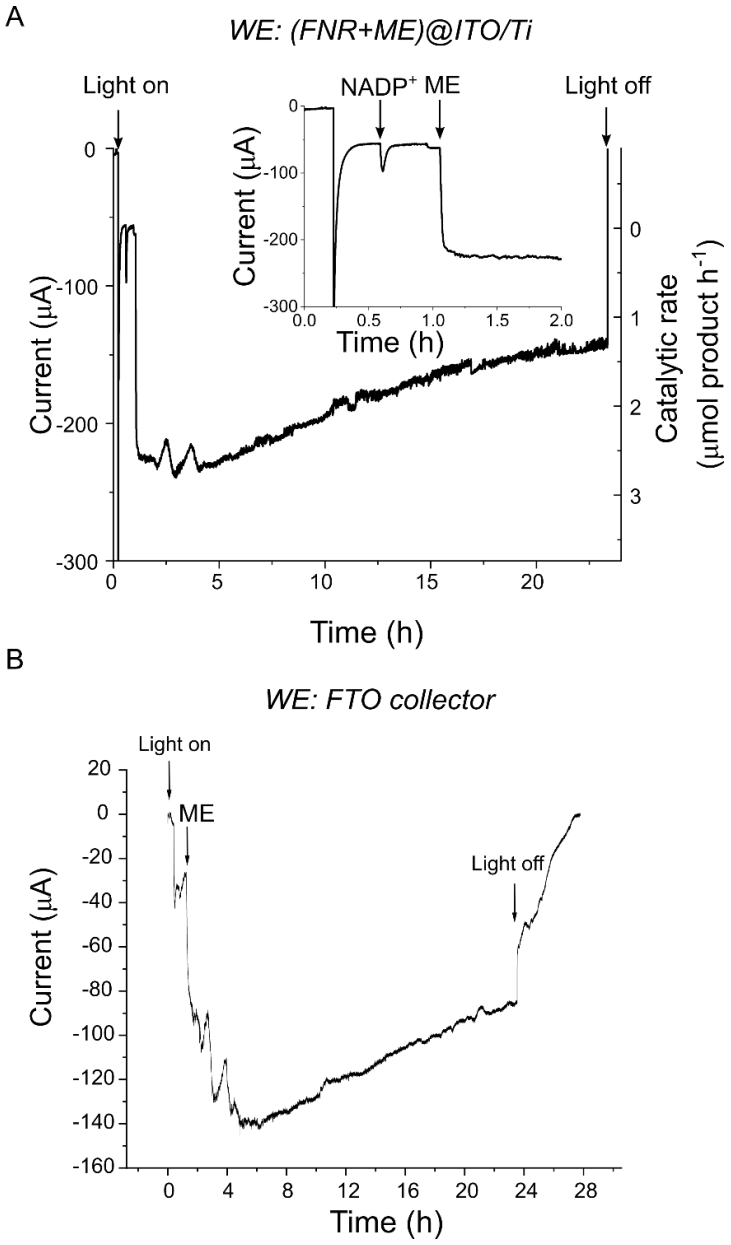


Figure III-16. Light-driven reductive carboxylation. A. The reductive carboxylation reaction. A 2%Mo:$BiVO_4$/FeOOH photoanode (1 cm^2) was connected to a 0.5 V Si-solar cell and a (FNR+ME)@ITO/Ti (14 cm^2) cathode. Anode compartment: 0.5 M borate, 4 mM $MgCl_2$ (pH 9) initially flushed with Ar and sealed. Cathode compartment: 0.05 M Phosphate, 0.1 M $KHCO_3$, 4 mM $MgCl_2$, under continuous flushing of 100% CO_2. Light intensity: 0.92 sun; λ>420 nm. $NADP^+$ was added to a final concentration of 50 µM, ME to a final concentration of 2.5 µM. Circuit as shown in Figure III-11-B. In the anode compartment an FTO collector was included at 1–2 mm from the photoanode to monitor oxygen production. Conditions: stirring, 25°C. **B.** Oxygen reduction. Electrochemical oxygen reduction from the FTO collector held at 1–2 mm from the photoanode at a potential of −1.8 V vs. Pt. Pt was both CE and RE. Figure adapted from Morello *et al.*[90]

Figure III-17 clarifies the results of the chronoamperometric experiment (**Figure III-16-A**), by comparing the quantified products (malate by ^{1}H NMR, spectrum shown in Panel **A**, and O_2 electrochemically) with the theoretical results assuming 100% FE. The red dotted line in **Figure III-17-B** represents the charge passed from the reductive carboxylation factored by 2 (*n*, number of electrons involved), while the blue dotted line is the same charge factored by four. They represent the theoretical charge for the C3/C4 reaction and the H_2O oxidation, respectively. Blue open circles represent the experimental data (charge passed) from the collector electrode driving oxygen reduction after correcting for the collection efficiency (65.4%). As is clear from the graph the theoretical trace (H_2O oxidation to O_2) and the experimental (O_2 reduction to H_2O) are in close correspondence, confirming that water was the electron donor in the system (**Figure III-17-B**). The FE for oxygen production calculated using equation 3.2 was 100 ± 1%.

$$FE_{O_2} = \left(Q_{col} \Big/ Q_{gen}\right) \times \left(\frac{1}{FE_{col\ eff}}\right) \qquad (3.2)$$

The reductive carboxylation reaction was monitored by taking aliquots (500 µL) for ^{1}H-NMR measurements, to measure malate production (red points). Malate concentrations were 0 mM (at 0 h), 3.4 mM (at 8 h) and 14.8 mM (at 24 h) as shown in **Figure III-17-B**. A high FE of 70% was obtained for the C3/C4 reaction by comparing the measured malate at 24 h with the theoretical red dotted trace

(**Figure III-17-B**). After 24 h a conversion of 18.5% was obtained which is equal to 300 TTN.

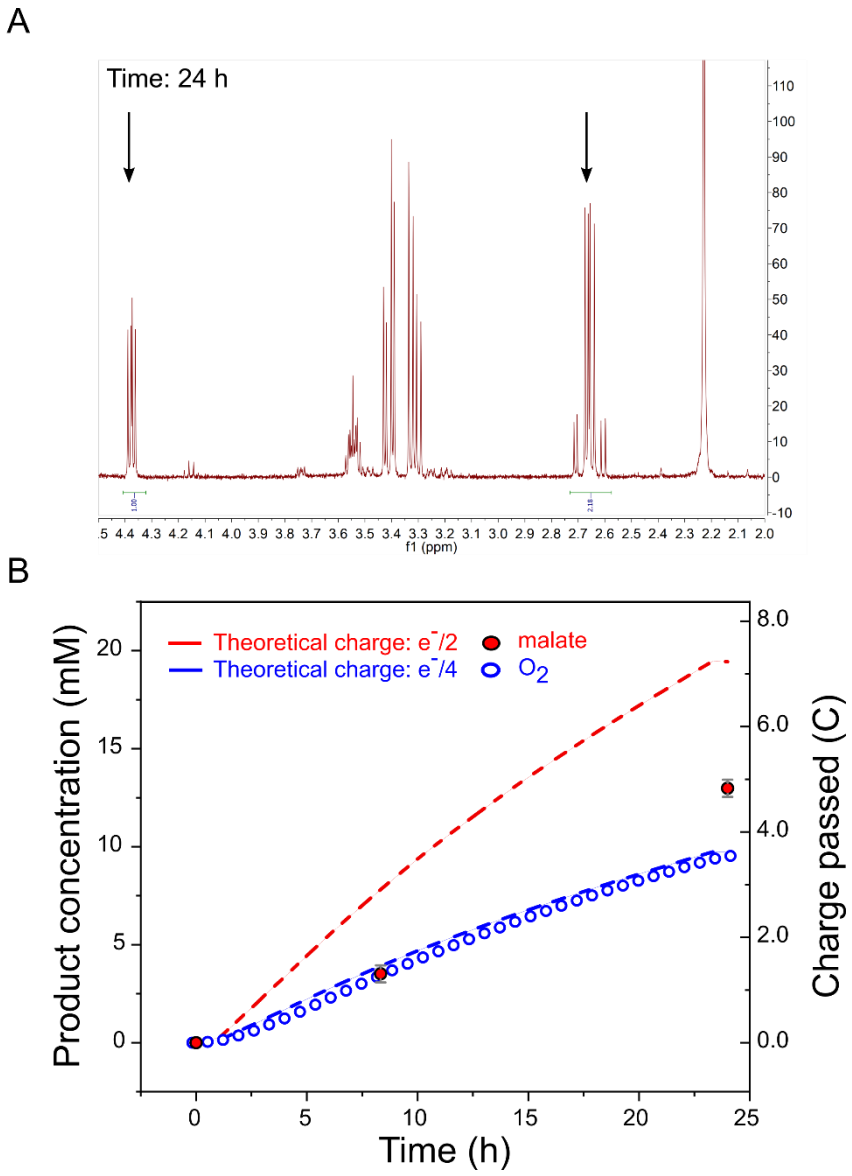


Figure III-17. Light-driven reductive carboxylation: product analysis. A. ^{1}H-NMR of the reaction in Figure III-16-A after 24 hours. The peaks of malate are detectable at 4.4 and 2.7 ppm. **B.** Analysis of the product from **A**. Dotted lines are the theoretical charges for reductive carboxylation (red, factored by 2) and water oxidation (blue, factored by four). Open circles are the data from the collector electrode corrected by the collection efficiency. Red dots are the malate detected by ^{1}H-NMR at three time points and related to the charge passed. Figure adapted from Morello *et al.*[90]

A much higher background photocurrent was obtained (600 µA) when a 1 V Silicon solar cell was used (total area: 10 cm^2; exposed area: 5 cm^2). Moreover, the current increased for 2 hours upon ME addition (**Figure III-18)**. This result confirms that in the previous experiment the system was limited by the photoanode performance. On average, a FE of 25% was obtained for the C3/C4 reaction when coupled to the solar cell at 1 V. A conversion of 34% was achieved, resulting in 544 TTN.

The value of 300 TTN (obtained for **Figure III-16**) is 1–2 times higher than any light-driven cofactor regeneration published so far. This is shown in **Table III-1** where the results obtained were compared with some light-driven cofactor regeneration systems discussed at the beginning of this Chapter (see Section 3.2). Several systems use a very high cofactor concentration compared to the work presented here. This high concentration is probably due to the usage of Rh/Ru-based catalyst, reported to have a FE for the biological active nicotinamide cofactor spanning from 89 to 99%. Even a 1% error would cause a dramatic decrease of the efficiency after several turnovers.

Based on total FNR coverage (101 pmol/cm^2), the TON ([product]/[catalyst]) was 4.89×10^4 and the TOF (rate of product formation 2.5 µmol product h^{-1}) 0.5 s^{-1}. These values represent the lower limit, as the amount of active FNR and ME on the electrode is unknown (see Section 2.4.2.5.). Thus, these values underestimate the real performance of the system.

The solar-to-malate efficiency was calculated with equation 3.3:[207]

$$\eta = \frac{J \times FE_{C3/C4} \times \left(V - V_{app}\right)}{Light\ intensity} \qquad (3.3)$$

where J is the maximum current density observed, $FE_{C3/C4}$ is the FE for the pyruvate/malate, V is the potential difference between $E^{H2O/O2}$ and $E^{C3/C4}$ reaction,

V_{app} was defined as the potential provided by the solar cell and the light intensity was expressed in W/cm^2. The value obtained was 0.027%.

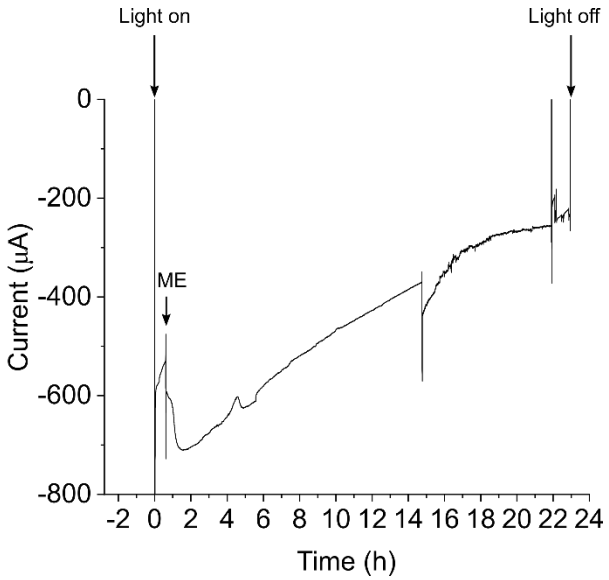


Figure III-18. Light-driven reductive carboxylation with a 1 V Si solar cell. Reaction in a two-compartment cell driven by a 2%Mo:$BiVO_4$/FeOOH photoanode (1 cm^2) connected to a 1 V Si-solar cell and a (FNR+ME)@ITO/Ti cathode (14 cm^2). Anode: 0.5 M borate, 4 mM $MgCl_2$. Cathode buffer: CO_2-saturated 0.05 M phosphate, 0.1 M KHCO3, 4 mM $MgCl_2$, 80 mM pyruvate, under CO_2 (pH 7.5). $NADP^+$ to 50 μM; ME to 2.5 μM. Light intensity: 0.92 sun; λ>420 nm. Conditions: stirring, 25°C. Figure adapted from Morello *et al*.[90]

Table III-1. Comparison of light-driven NADH/NADPH regeneration systems. The total turnover number (TTN) is defined as moles of products formed/moles of cofactor added at the beginning of the experiment. Table adapted from Morello *et al*.[90]

Substrate	Product	NAD(P)$^+$ (mM)	Absorber	Mediator	TTN
pyruvate	malate	0.18	$Ru(bpy)_3^{2+}$	MV^{2+}	64 [127]
α-ketoglutarate	glutamate	2	$BiVO_4$FeOOH - perovskite	$[Cp^*Rh(bpy)H_2O]^{2+}$	20.3 [84]
isobuthyraldehyde	isobutanol	0.25	CdS	No mediator	3.6 [184]
pyruvate	malate	0.05	2%Mo:$BiVO_4$FeOOH - Si solar cell	No mediator	300 [This work]

3.4.7. Faradaic efficiency-dependence on potential applied

This Section discusses the faradaic efficiency-dependence on the applied bias. In the experiment described below a solar cell was not used and a bias was applied through the potentiostat. Results are shown in **Figure III-19**.

The experiment was set up in a two-compartment cell, using the FNR@ITO/Ti cathode (2 cm^2) and the 2%Mo:$BiVO_4$/FeOOH photoanode (1 cm^2). The buffers in the anode and cathode compartments were used as in the previous paragraph.

A bias of 0.5 V was applied at the beginning of the experiment. No current was detected in the dark. Switching on the light (violet dotted arrow, **Figure III-19**) caused an increase of current even without cofactor: the new current value gives information on the *background current* related to the hydrogen production rates. Injection of the cofactor and ME was carried out to reach the final concentrations as in previous experiments (50 and 2.5 µM, respectively). The current grew as expected to a new value, defined as *total current*. After 2 h, the experiment was paused, cathode compartment emptied and washed 10 times with MQ-H_2O and once with buffer. Fresh buffer lacking cofactor, pyruvate and importantly enzyme, was re-added. The applied bias was increased from 0.5 to 0.8 V and the experiment restarted. All the steps described are represented in **Figure III-19** as a blue arrow. The *background-current* was higher when the light was restored after solution exchange. Injection of $NADP^+$ and pyruvate (marked as red arrow, **Figure III-19**, to a final concentration of 50 µM and 80 mM), induced a sudden increase of current revealing the *total current* at higher potential applied. The result of the buffer exchange gives two important information. First, it confirms that ME binds to the electrode during the first two hours of experiment (as discussed in Chapter II), because catalysis was observed after refreshing the buffer (and adding substrates)

even if ME was not present in solution. Second, by comparing the *total current* with the *background current* it is possible to calculate the FE for malate production at each potential. Results are shown in **Figure III-19-B**. In blue, the FE values are 75 ± 8 %, 50 ± 6 % and 33 ± 10 % at 0.5 V, 0.8 V and 1 V, respectively. The total current increases with potential as expected from the voltammograms shown in **Figure III-12**. The result from an applied bias of 0.4 V was not plotted as no significant photocurrent was observed (4 μA after injecting substrates of the reductive carboxylation and no background photocurrent observed).

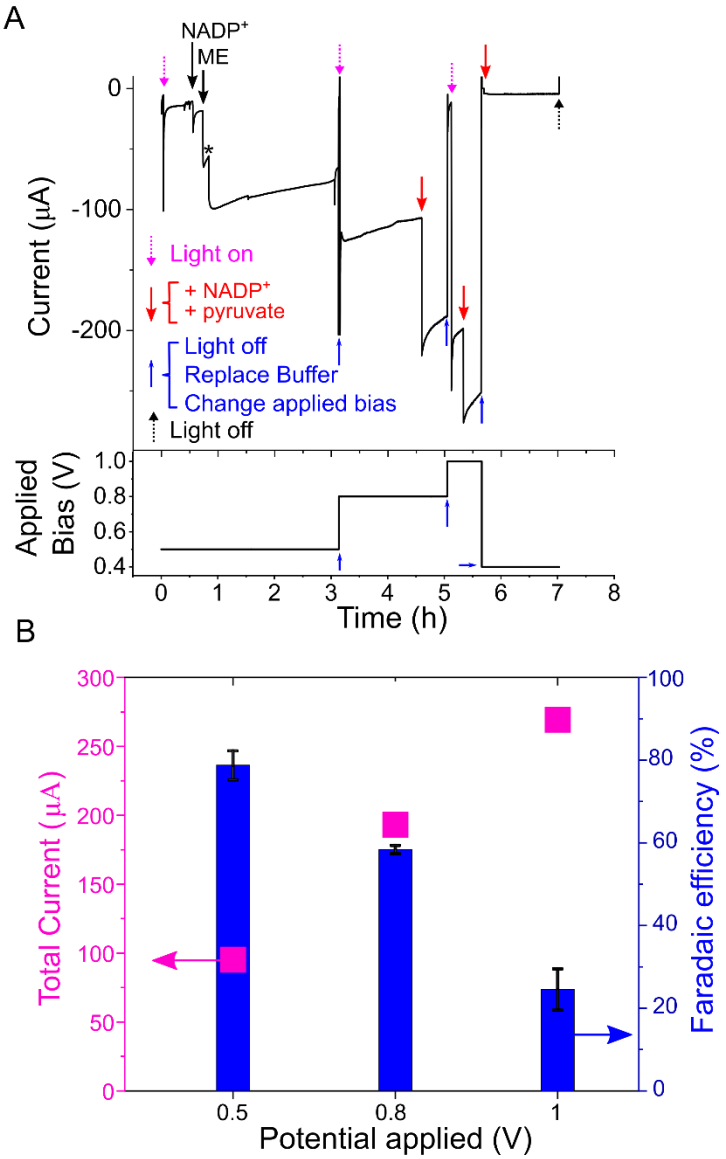


Figure III-19. Dependence of faradaic efficiency and potential applied. A. Light-driven reductive carboxylation. Chronoamperometry driven by a 2%Mo:$BiVO_4$/FeOOH photoanode (1 cm^2, CE, RE) connected to a (FNR+ME)@ITO/Ti cathode (2 cm^2, WE). A bias of 0.5 V was applied by the potentiostat. Black arrow signifies injection of $NADP^+$ (to 50 µM) and ME (to 2.5 µM). Blue arrow signifies: (i) switching off light, (ii) discarding buffer and refreshing it with fresh one without cofactor, pyruvate and enzyme and (iv) change applied bias. Bias was changed to 0.8, 1 V and 0.4 V. Magenta dotted arrows signifies light-switching on; black dotted arrow signifies switching off light. Light intensity: 0.92 sun; λ>420 nm. Conditions: stirring, 25°C. **B.** Result of experiment described in A. In blue, the FE at each investigated potential are shown with their standard errors (N = 3). The total current at each applied potential is shown in magenta. Figure adapted from Morello *et al.*[90]

3.5. Conclusion

α-Fe_2O_3/CoB and 2%Mo:$BiVO_4$/FeOOH electrodes were successfully synthesised with current densities of 200 μA/cm^2 and 2 mA/cm^2 at 1.23 V vs. RHE. Their onset potential was 0.6 and 0.4 V vs. RHE, respectively. The $BiVO_4$ and hematite electrodes compare well with what has been reported in the literature.[43,67,190] The synthesized photoanodes were then coupled to the Electrochemical Leaf.

Light driven $NADP^+$ reduction was first demonstrated with α-Fe_2O_3/CoB. A large applied bias was needed to obtain appreciable photocurrents (–0.9 to –1.2 V vs. CE). $NADP^+$ reduction was successfully detected. However, the system was stable for only 1 hour. Decreasing the potential to 0.9 V vs. CE or including catalase in the system did not affect the stability. Covering the cathode from the high light intensity allowed the system to be active for longer time. FNR was the light-sensitive component, as it was observed that NADPH was not affected by the intense light. Consequently, the cathode was always masked from the light in subsequent experiments. Achieving a stable system was crucial to investigate the carboxylation reaction with ME.

An unassisted light-driven system was developed through a PEC-PV design to eliminate the need of an additional applied bias: the 2%Mo:$BiVO_4$/FeOOH photoanode with a Si solar cell was able to provide a voltage of 1 and 0.5 V, building this way a *Z*-scheme. By doing so, the photocurrent onset potential for water oxidation shifted to potentials more negative than the potential for the C3/C4 reaction. This way the reaction could be driven with visible light-only. Another method to develop unassisted light-driven NADPH production is based on a particulate system and was demonstrated using a *g*-C_3N_4-FNR complex with TEA

as electron donor. More experiments are needed to compare the particulate system with the PEC developed. Surely, the high light sensitivity can limit the success of the particulate system. An alternative to protect FNR from intense light can be a wireless *Z*-scheme by designing an integrated device using *n*-type $BiVO_4$/FeOOH in contact with a *p*-Si/ITO blocking layer/ITO nanoporous structure via a similar concept to what Yang *et al* proposed.[208]

The light-driven reductive carboxylation experiment with a 2%Mo:$BIVO_4$/FeOOH photoanode coupled to a 0.5 V Si solar cell resulted in 18.5% conversion of pyruvate to malate by CO_2 fixation and a record 300 TTN with a high 70% FE for the C3/C4 reaction. Using a 1 V Si solar cell, the TTN increased slightly (544) but a dramatic decrease in FE to around 25% was observed. Solar to malate efficiency was 0.027% with the 2%Mo:$BiVO_4$/FeOOH-0.5 V Si solar cell. The applied bias strictly correlates with the FE. Increasing the applied bias allows achieving higher photocurrent, while decreasing the FE for the C3/C4 reaction. For instance, the FEs were 75 ± 8% at 0.5 V, 50 ± 6 at 0.8 V and 33 ± 10 at 1 V. These results stress the importance of choosing the correct light absorbers and (if necessary) mediators to achieve high FE in a AP system and to disrupt electron recombination as it occurs in oxygenic photosynthesis.[209]

Chapter IV

4. Wiring nanoconfined cascades: a five-enzyme cascade

4.1. Abstract

The nanoporous indium tin oxide (ITO) electrode offers a unique environment to drive and monitor extended and complex multi-enzyme cascades. Here the proof of concept is demonstrated by assembling an artificial five-enzyme cascade to drive the reversible reductive amination of pyruvate to aspartate, by integrating FNR, malic enzyme (ME), carbonic anhydrase (CA), fumarase (FumC) and aspartate-amino lyase (AspA). The FNR-ME couple converts the chemical flow into an electric signal through cofactor recycling. Importantly, the concepts described could be generalised to any cascade provided that FNR and any NADP(H)-dependent dehydrogenase are included. Cyclic voltammetry studies show the impressive reversibility of the cascade at each direction (reductive amination of pyruvate or oxidative deamination of aspartate). The direction of the rest of the cascade with respect to the FNR-ME couple (the E1-E2 pair) dictates the information that the current provides. Possible implications are extensive and include synthesis, biosensing and studies of systems catalysis.

4.2. Introduction

Nanoconfinement is crucial for efficient catalysis. This concept is true in biological systems where catalysts are confined within nanospaces like invaginations of organelle membranes so that diffusion distances between intermediates are minimised and effective enzyme concentrations massively increased. In living cells confining long metabolic pathways has ensured a high flow towards natural products by shifting reaction equilibriums and decreasing product inhibition.[210–213]

Industrial application of one-pot multi-step cascades for synthesis is extremely attractive as it would decrease the number of purification steps and avoid the formation of inhibitory or toxic compounds thus decreasing reaction waste. Biocatalysis is particularly suited for this purpose because enzymes function in mild and similar conditions so that it is easier to combine biocatalysts from different organisms or pathways.[214] Moreover, biocatalysts offer a unique platform to perform high stereo-control for the synthesis of novel targets for the pharmaceutical industry and as such they are under intense research.[215,216] Directed evolution, reported originally by Arnold *et al.*, has allowed the development of enzymes for novel or improved functions.[217,218] Thanks to this, the application of single enzymes is now a common strategy also outside academia.[217] However, use of combined enzymes in a cascade is still in its infancy in industry.[219] Cascades have been extensively exploited in whole-cell approaches, such as for the synthesis of the precursor for the antimalarial-drug artemisinin[112]; however, depending on the desired final product, flux-optimisation could be challenging.[106,220]

In vitro cascades have been under intense research.[105,221] One notable example was reported by Huffman *et al.* for the 9-step biocatalytic synthesis of the

HIV drug islatravir. Previous synthetic routes required between 12 and 18 steps and the use of several protecting groups.[219] Through the engineering of five enzymes and one auxiliary enzyme, the authors managed to achieve 51% yields in only 5 steps, with no need to isolate intermediates.[219]

Another example from Parmeggiani *et al.* reports the synthesis of the modified amino acid, D-tryptophan from indoles using a three-enzyme cascade, in high yield (91 to 99%) and high enantiomeric excess.[222]

Bio-derived production of cinnamyl alcohol was demonstrated by Klumbys *et al.* by combining three catalysts, phenyalanine aminolyase, carboxylic acid reductase and alcohol dehydrogenase (ADH) for the three-step conversion of L-phenylalanine into cynnamil alcohol, an important precursor for the fragrance, flavour and polymer industry. The final yield was 53%.[223]

Nanoconfining a whole cascade is expected to bring even greater benefits to catalysis and some publications have tried to achieve this goal by mimicking nature. The strategies for nanoconfinement of living cells are (i) confinement in an enclosed space such as an organelle (spatial confinement) or (ii) assembly of the cascade partners in a complex through the use of a protein scaffold (metabolon formation).[224] Typical examples are the entrapping of alcohol oxidase in the perixosomes in methylotrophic yeast[225] and the MAPK kinase pathway in yeast which is known to assemble into a complex through a protein scaffold, Ste5.[226] Thus, nature was used as inspiration for biocatalysis: the enzyme partners can be entrapped in an organelle-like structure or they can be bound to a DNA or protein scaffold (see below and **Figure IV-1**).[227]

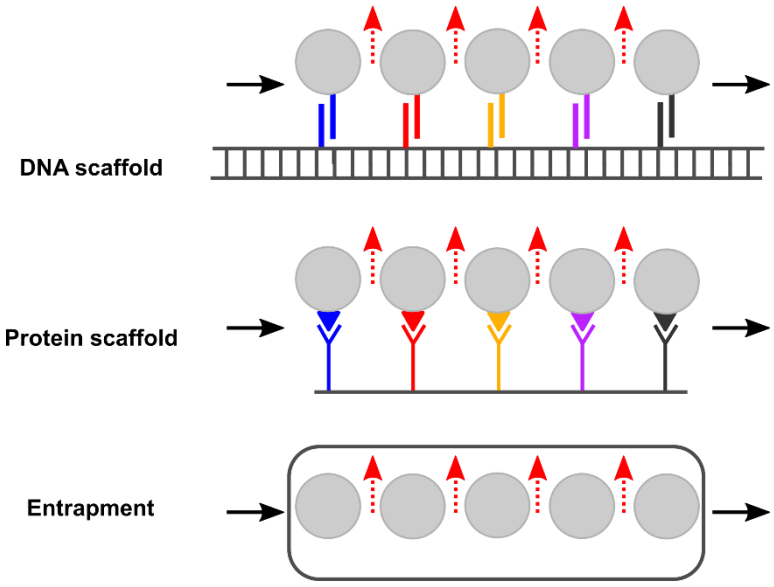


Figure IV-1. Strategies to nanoconfine a biocatalytic cascade. The cooperating enzymes working in a cascade can be bound at precise positions in DNA and protein scaffolds, using base-pairing and protein tags, respectively. Another strategy is based on physical entrapment of the enzymes in vescicles or nanoparticles. Black arrows represent the chemical flow, while red arrow the escape of the intermediates of the cascade in the bulk solution.

A metal organic framework (MOF) is an example of a platform used for spatial confinement. For instance, Chen *et al*. prepared[228] zeolitic imidazolate framework nanoparticles for two biocatalytic cascades. The first cascade used β-galactosidase, glucose oxidase (GOx) and horse radish peroxidase (HRP) entrapped by a co-precipitation method. In this way, lactose was hydrolysed to galactose and glucose and the latter was oxidised by GOx yielding gluconic acid and H_2O_2. By using peroxide, HRP would then drive oxidation of a dye to generate a fluorescent product, used to monitor the reaction. The authors reported an improvement of five-fold in the cascade performance compared to enzymes free in solution. A similar result was obtained when the MOF was combined with a NAD^+-dependent cascade. To achieve this goal, NAD^+ was bound to a polyallylamine scaffold further modified to bind the MOF. The resulting construct was adsorbed

together with ADH and lactate dehydrogenase (LDH) to drive NAD(H)-dependent oxidation of ethanol to acetaldehyde and reduction of pyruvate to lactate.[228]

Wang *et al.* reported a confined cascade for the reduction of CO_2 to methanol within microcapsules made of gelatin-modified Si, using formate dehydrogenase, formaldehyde dehydrogenase and alcohol dehydrogenase, to reduce CO_2 to methanol using 50 mM NADPH. Entrapping the catalysts by physical methods and covalent attachment caused a two-fold enhancement of the system efficiency compared to free enzymes.[229]

Another interesting concept is the use of macromolecules as scaffolds for providing a 3D nanoconfined environment.[227] For instance, DNA scaffolds (single strand (ss), double strand (ds) and DNA origami) have been used to confine biocatalytic cascades. Interestingly, DNA offers the possibility of switching on and off the cascade under specific triggers, such as pH or light.[230] Fu *et al*. tethered glucose dehydrogenase (GDH), NAD and malate dehydrogenase (MDH) to a ssDNA.[230] They found that a distance of 7 nm between cofactor and protein gave the best catalytic condition and observed a 90-fold increase in the activity of the system in the presence of only 100 nM cofactor.[230] In another work, DNA origami structures were used to confine two- and three-enzyme systems and the effect of substrate-channelling within a cascade was observed.[231,232] Binding of the enzyme to the DNA is based on chemically attached tether strands followed by hybridisation to the DNA scaffold. Other strategies to achieve a controlled spatial binding between enzymes in a cascade used DNA-binding motifs such as Zinc-fingers and CRISPR[228,233], however, the use of Zn-fingers (ZF) would require extensive engineering for each enzyme. Nguyen *et al.*, used molecular adaptors to bind ZF-fused enzymes in sequential order to a DNA origami.[234] They used xylose

reductase, xylitol dehydrogenase and xylulose kinase and proved that a cascade chip where the proteins were 10 nm apart, was more efficient than when this distance was 50 nm.[234] A CRISPR-based approach could be more versatile to achieve a similar goal. In the set-up used by Lim *et al.*, a catalytically inactive Cas9 was modified with a 12 kDa protein domain (SpyCatcher), able to bind a small 13-aa tag, called Spytag.[233,235] By expressing any enzyme with the Spytag and careful design of the single-guided RNA (sgRNA) it was possible to orientate each enzyme in specific positions on the DNA strand. The 4-enzyme synthesis of coloured violacein from L-tryptophan served as a model system and the authors observed a 3.2-fold enhancement in violacein production compared to a free enzyme system. However, comparison of rational and random enzyme order did not lead to different levels of violacein production.[233]

Using electricity to drive a biocatalyst could be of great interest to control biocatalytic reactions and Al-Shameri *et al*. published a work related to this purpose.[236] The system used two electrodes, one for the evolution of oxygen and the other for hydrogen evolution. The electrolysis reaction was carried out in a separate compartment (pH 1.3) and was initiated by applying a large voltage (3 V). The two gases produced by electrolysis were fed to a system where four enzymes were immobilised to catalyse the production of methylated *N*-heterocycles from diamines. The authors report a high conversion of 99% starting with 5 mM diamines and using a high concentration of NAD^+ (2 mM). This concentration is in the same range as the substrate concentration and 100–2000× higher than the typical concentrations used in this Thesis. Moreover, the system reported by Al-Shameri *et al*. cannot make use of the electrical current to monitor the reaction and the reported faradaic efficiency is 4 %.[236]

This Chapter reports for the first time the possibility to electrochemically drive, monitor and control nanoconfined multi-enzyme cascades. By loading a mixture of biocatalysts within the electrode nanopores we predict an extremely crowded environment where individual enzyme concentrations exceed the millimolar range. Such a crowded environment is considered to be a crucial factor to achieve efficient catalysis.[212] Moreover, we describe the unprecedented possibility of energising the cascade to drive it in either direction and to detect the overall rate at each time point. Importantly, the system is impressively easy as it is not necessary to carry out extensive engineering work to incorporate the enzymes within the nanopores. Any natural/artificial biocatalytic cascade could potentially be wired and studied with ease *in vitro*, provided that one step is nicotinamide cofactor dependent. While nanoconfinement and immobilisation of biocatalytic cascades are not novel concepts, the combination of these with the ability to energise and monitor a biochemical reaction is new and unprecedented. This system has enormous implications for catalysis, screening and synthesis.

As a proof of concept, a 5-enzyme cascade will be described using the developed reductive carboxylation described in Chapter II with the FNR-ME pair. To avoid the requirement for a continuous supply of CO_2, carbonic anhydrase (CA, from *B. taurus*, Sigma) was added to the system to convert bicarbonate to CO_2. Chapter II proved malate to be a product inhibitor. Therefore, fumarase was introduced to relieve malate-product inhibition on ME by converting malate to fumarate. There are three genes which encode for different fumarases in *E. coli*, fumA, fumB and fumC. The first two encode for oxygen sensitive-proteins, therefore it was decided to work with FumC (purification described in Section A.2.).[237] The product of FumC, fumarate, is also reported to be an inhibitor of ME, therefore the cascade was

further extended.[171] Aspartate amino-lyase (AspA, purification described in Section A.1) was included in the system to convert fumarate to aspartate. This enzyme is very active and is used industrially to produce L-aspartate.[238–240] Moreover, its activity is strictly dependent on cations such as Mg^{2+}, which is also required for ME. The cascade was investigated in both reductive and oxidative directions.

4.3. Aim of the Chapter

The overall aim was to investigate the possibility of 'electrically wiring' extended enzyme cascades to the nanoporous ITO electrode and to detect the overall rate as a form of electrical current. As a proof of concept, the reversible reductive amination of pyruvate to aspartate will be investigated by entrapping, driving and monitoring the overall activity of five enzymes, ferredoxin $NADP^+$ reductase (FNR), malic enzyme (ME), carbonic anhydrase (CA), fumarase (FumC) and aspartate amino-lyase (AspA), within the nanopores. This cascade will be investigated in both directions - oxidative and reductive - and it will be explained that the system can be used to drive and monitor any cascade provided that one step is a nicotinamide cofactor dependent step. The Chapter is divided in two parts, the first discussing the main findings, while the second showing further and preliminary results.

The first part will discuss the reversibility of the 5-enzyme system, the concepts of downstream and upstream reaction and the information that the current gives in these two situations. Rotation-dependent results will demonstrate that intermediates are retained in the pores and their escape in the upstream direction decreases the rate of the reaction.

In the second part of this chapter further results will be presented, including more details on the electrochemistry, the effect of changing the enzyme ratio, of omitting carbonic anhydrase, control experiments which confirm a lack of catalysis when the enzymes were not-confined together and details on steady-state kinetics of ME, FumC and AspA. Finally, an attempt to compare the nanoconfined cascade with a paraller cascade in solution will be described.

4.4. Part 1: Results and Discussion

4.4.1. The 5-enzyme cascade in action

The scheme of the 5-enzyme cascade, driving the reversible reductive amination of pyruvate (C3) to aspartate (C4) via cofactor regeneration, is shown in **Figure IV-2-A**. The cascade contains a linear set of enzymes, FNR, ME, FumC and AspA and carbonic anhydrase was provided at a branch point to avoid the need to supply gaseous CO_2 by using bicarbonate in the buffer mixture. It is relevant to point out that this is the first time that a non-dehydrogenase enzyme was indirectly coupled to the Electrochemical Leaf. Briefly, carbonic anhydrase drives the reversible dehydration of bicarbonate to CO_2 while ME catalyses the reversible reductive carboxylation of pyruvate to malate by using the produced CO_2 and NADPH. NADP(H) is continuously regenerated by FNR upon application of a potential and importantly, the cofactor dependent step (FNR-ME) gives rise to the electrochemical signal as shown in Section 2.4.2.1. Malate is then taken further by fumarase to fumarate and lastly AspA catalyses amination of fumarate to L-aspartate provided that an ammonium source is present. **Figure IV-2-B** investigates the cascade in both oxidative and reductive directions and proves the successful entrapment of the 5-enzyme cascade and its reversibility. An ITO/Ti foil (1.89 cm^2) was prepared by electrophoretically depositing ITO nanoparticles (< 50 nm) on a titanium foil and dropcasting and spreading a mixture (20 µL) containing all enzymes (pre-mixed in the following ratio 0.1 CA/1 FNR/5 ME/1 FumC/1 AspA) on the ITO layer. Herein 1 enzyme equivalent was defined as 2 nmol in a volume of 20 µL, thus the total amount of enzymes deposited on the electrode was equal to approximately 17 nmol. The electrode was covered and left for 20 minutes at room temperature (rt). Afterwards, the electrode was then washed thoroughly, to

remove unbound enzyme, and placed in an electrochemical cell in a buffer (pH 7.5) containing 0.05 M HEPES, 0.1 M $KHCO_3$, 0.1 M NH_4Cl, 4 mM $MgCl_2$, 1 mM $MnCl_2$, 20 mM pyruvate, under a continuous flow of argon. The pH was chosen as a compromise between the different pH optima for the enzymes. The cascade was investigated by cyclic voltammetry (1 mV/s, 25°C, stationary electrode) (**Figure IV-2-B**).

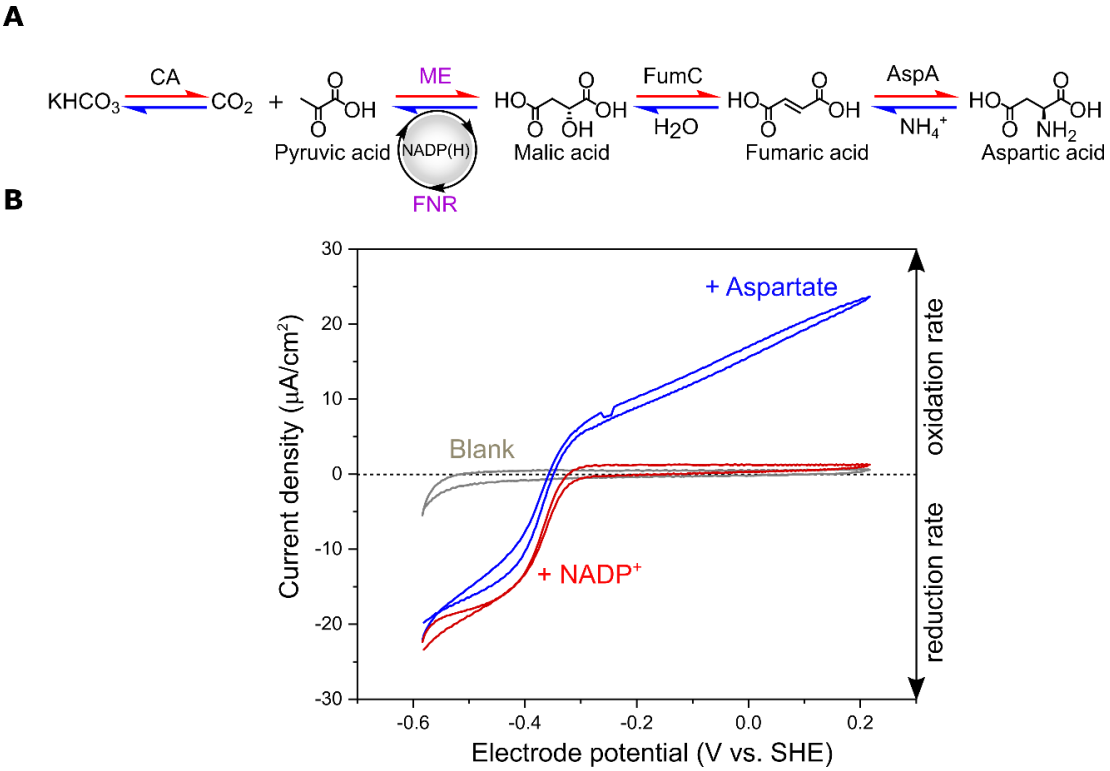


Figure IV-2. The five-enzyme nanoconfined cascade: scheme and cyclic voltammetry showing its activity. A. Scheme of the nanoconfined five-enzyme cascade driving the reversible amination of pyruvate to aspartate. Carbonic anhydrase (CA), catalyses the reversible hydration of bicarbonate to CO_2; FNR, catalyses NADP(H) interconversion and more specifically $NADP^+$ reduction at a cathodic potential and NADPH oxidation at an anodic potential. NADP(H) interconversion gives rise to the electrochemical signal as explained in Section 1.6.; ME, catalyses the cofactor-dependent reversible carboxylation of pyruvate to malate, while FumC the reversible dehydration of malate to fumarate and AspA the reversible amination of fumarate to aspartate. **B.** Cyclic voltammetry of the nanoconfined five-enzyme electrode proving successful entrapment of the five-enzyme cascade and its reversibility. Red trace: injection of $NADP^+$ (to 20 µM). Blue trace: subsequent injection of aspartate (to 20 mM). ITO/Ti electrode (WE, 1.89 cm^2) was preloaded with (enzyme equivalents) 0.1 CA/1 FNR/5 ME/1 FumC/1 AspA (1 enzyme equivalent = 2 nmol) and thoroughly rinsed prior to the experiment to remove unbound enzymes. Buffer (pH 7.5): 0.05 M HEPES, 0.1 M $KHCO_3$, 0.1 M NH_4Cl, 4 mM $MgCl_2$, 1 mM $MnCl_2$ containing 20 mM pyruvate under continuous flow of Ar. Figure adapted from Morello *et al.*[241]

The grey trace in **Figure IV-2-B** represents the electrode in the absence of a cofactor. Based on the non-turnover peak signals, the coverage of FNR was 64.5 pmol/cm^2, which would equate to a 1 µm layer having a protein concentration of 0.65 mM. This calculation assumes that the volume (1 cm × 1 cm × 1 µm = 1 × 10^{-7} L) comprises only reaction solution and does not consider the space taken by the ITO nanoparticles. Since only FNR is electroactive, a method to measure the coverage of the other enzymes is not yet available. However, based on the coverage of FNR, the total protein concentration is likely to exceed the millimolar range thus creating a crowded environment. When $NADP^+$ was included (to 20 µM) a large reductive current was observed (red trace, **Figure IV-2-B**) attributable to either the reductive carboxylation of pyruvate to malate (via the FNR-ME pair) or to the complete reductive amination of pyruvate to aspartate. More discussion on this will follow in the next Section (Section 4.4.2.). Introduction of aspartate (substrate of AspA, to 20 mM) generated a large oxidative current (blue trace, **Figure IV-2-B**): the enhanced oxidative current is proof of the successful entrapment of FumC and AspA, since the electrode was thoroughly rinsed prior to the start of the experiment *i.e.* the enzymes were not in solution. Hence, achieving an oxidative current upon introduction of aspartate (substrate of AspA) demonstrates that AspA and FumC are adsorbed in the electrode, because their presence was essential to produce malate (substrate of ME, aspartate → fumarate → malate). Only when malate is produced an electrochemical signal can arise: the FNR-ME pair catalyses the oxidative decarboxylation of malate to pyruvate via NADPH cycling (see Section 2.4.2.2.). Remarkably, the cyclic voltammetry result shows the first example of an extremely reversible reaction involving 5 enzymes entrapped, driven and controlled within the nanopores of an electrode. The point

at zero current approximates the thermodynamic potential of the whole cascade (**Figure IV-2-B**). More discussion on the cascade model and nanoconfinement of intermediates follows in the next paragraph (see Section 4.4.2.). The reaction could also be driven in an unbuffered system or in saturated CO_2 buffer bypassing the need for carbonic anhydrase (Part 2, Section 4.6.1.).

4.4.2. The cascade model and nanoconfinement of intermediates

The CV result shown above proved it was possible to drive the cascade in either direction simply by changing the applied potential (**Figure IV-2**). The information that the current provides changes depending on the chosen direction. The position of the FNR-ME pair, *i.e.* the cofactor-dependent step, is fundamental to the ability to monitor the reaction: it is the probe which allows for reception of an electrochemical signal.

Figure IV-3-A,B shows the cascade in a general form: FNR (E1), ME (E2), CA (E2A), FumC (E3) and AspA (E4). This model is valid for any cascade system provided that E1 is FNR and E2 any NADP(H)-dependent dehydrogenase. Note that their position can change in the cascade and that the E1-E2 pair converts the chemical flow to an electrical signal (violet arrow). The black arrows represent the chemical flow through the cascade and the green arrows the entry point of substrates and exit point of product. At each step the intermediate that is produced can be taken by the next enzyme or escape from the electrode nanopore (red dotted lines). In **Figure IV-3-A** the rest of the cascade (E3, E4) is downstream from the E1-E2 pair, while in **Figure IV-3-B** the rest of the cascade is upstream from the cofactor-dependent step.

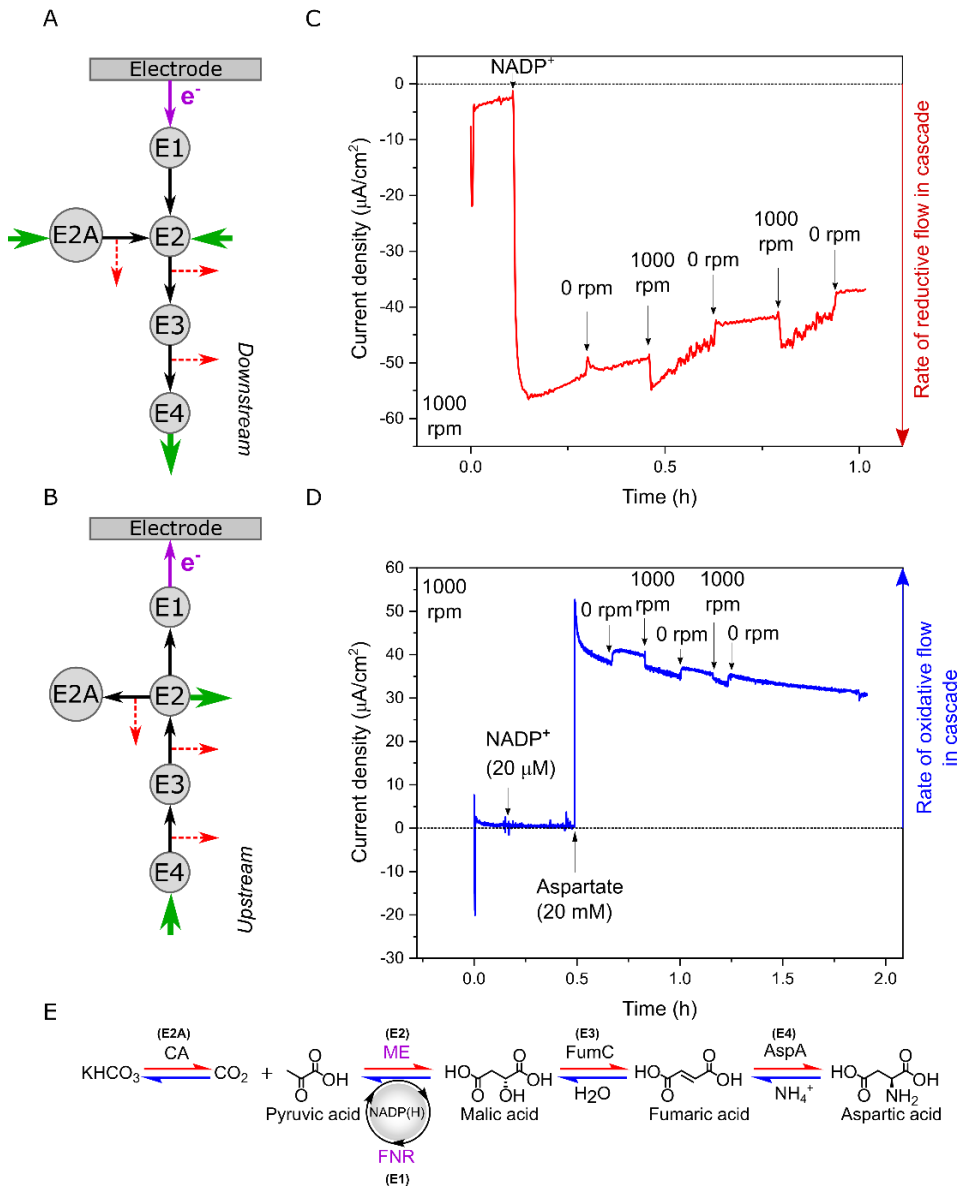


Figure IV-3. The downstream and upstream notation and the effect of electrode rotation on cascade activity in both directions. A. Downstream concept of the cascade. E1 is is FNR and E2 any NADPH-dependent dehydrogenase. The rest of the cascade is downstream with respect to the E1-E2 pair. **B.** Upstream concept. The rest of the cascade is now upstream with respect to the E1-E2 pair. Red dotted lines: escape of intermediates; green arrows: entry and exit points of substrates/product. **C.** Rotation dependence of the cascade rate. Chronoamperometry: −0.45 V vs. SHE, 25°C, rotation initially 1000 rpm. Injection of $NADP^+$ to 20 µM and aspartate to 20 mM. Rotation (angular velocity, ω) was varied between 0 rpm and 1000 rpm. WE: ITO/PGE (0.03 cm^2) preloaded with 10 µl of enzyme mixture (0.1 CA/1 FNR/5 ME/1 FumC/1 AspA, 1 = 1 nmol) and thoroughly rinsed prior to experiment. Buffer: 0.05 M HEPES, 0.1 M NH_4Cl, 0.1 M $KHCO_3$, 4 mM $MgCl_2$, 1 mM $MnCl_2$, 20 mM pyruvate (pH 7.5). **D.** Continuation of experiment in **C.** The cell was washed, fresh buffer (0.05 M MOPS, 4 mM $MgCl_2$, 1 mM $MnCl_2$) was supplied and a potential of +0.1 V vs. SHE was applied. Beginning of the experiment, ω = 1000 rpm and ω dependence was investigated as in **C**. Arrows signify injection of $NADP^+$ (to 20 µM) and aspartate (to 20 mM). **E.** Schematic representation of the 5-enzyme cascade. Figure adapted from Morello *et al.*[241]

In the downstream case (**Figure IV-3-A**) the electrochemistry is not necessarily informative of the overall rate of the cascade, as the current could arise even if the other enzymes were not included. This is because E1-E2 (in this case dependent on E2A) are the first catalysts acting in the cascade and their substrates are immediately provided. Thus, the system would generate an electrochemical signal regardless of the presence of the rest of the cascade. An example whereby a contribution to the current could be detected is if inhibitory intermediates accumulated, so that their removal would relieve the system from product inhibition.

In the upstream direction (**Figure IV-3-B**) the rest of the cascade, E4 and E3, are upstream with respect to the E1-E2 pair. Given that the substrate provided is the substrate of E4, the current signal gives information on the overall rate of the whole cascade. This is because the substrate of E2 (E2 is the NADP(H)-dependent dehydrogenase) must be present to convert the chemical flow to an electric signal and it can only be supplied if the cascade takes the substrate of E4 through each step producing the substrate of the NADP(H)-dependent dehydrogenase (E2).

The downstream direction in this Chapter is the reductive amination of pyruvate to aspartate, while the upstream direction is the oxidative deamination of aspartate to pyruvate. In the downstream direction, by introducing pyruvate (substrate of E2) and bicarbonate (substrate of E2A), the current provides information on the reductive carboxylation of pyruvate to malate catalysed by ME (see Chapter II) but it is less informative on the stages downstream from this. In the upstream direction – oxidative deamination – the current arises from the last step of the cascade, the oxidative decarboxylation of malate to pyruvate, and the charge passed (current × time) corresponds to the number of moles of pyruvate

produced. By injecting aspartate as the substrate of E4, any current in the oxidative direction is (i) a confirmation of the entrapment of the whole cascade within the electrode nanopores and (ii) informative on the rate of the whole cascade.

Rotation-dependence experiments are shown in **Figure IV-3-C**, **D** next to their respective schemes. The reductive amination (**Figure IV-3-C**) is downstream, while the oxidative deamination (**Figure IV-3-D**) is upstream. The experiment was carried out in a glove box under a N_2 atmosphere to eliminate any signal arising from oxygen reduction during injections of substrates in the downstream reaction. A pyrolytic graphitic electrode (PGE) was used in this case, onto which ITO was electrophoretically deposited (area: 0.03 cm^2). The enzymes were first mixed in the following ratio (0.1 CA/1 FNR/5 ME/1 FumC/1 AspA) and dropped on the surface of the electrode (10 µl per 0.03 cm^2) and left covered for 20 minutes at rt to adsorb. Afterwards, the electrode was washed thoroughly. A chronoamperometry experiment (−0.45 V vs. SHE) was set up to investigate the effect of rotation on the cascade rate. Rotation affects the diffusion layer at the electrode surface hence affecting the concentration gradient of reactant and intermediates between electrode surface and solution; hence, rotation increases the supply and escape of reactants and intermediates, respectively. The buffer (pH 7.5, as in **Figure IV-2**) contained all substrates ($KHCO_3$, NH_4Cl and pyruvate) except for $NADP^+$ and the initial electrode rotation was set at 1000 rpm. **Figure IV-3-C** shows the results. Injection of $NADP^+$ (to 20 µM) initiated a reductive current, current density around 50 µA/cm^2. The current is attributable to the reductive carboxylation of pyruvate to malate by the FNR-ME pair, while it provides no information on the stages downstream *i.e.* fumarate and aspartate production. The rotation was intermittently stopped and a sharp increase of the cascade reductive rate was observed upon

each resumption (ω, angular velocity, from 0 to 1000 rpm). Rotation ensures that the system is not limited by the mass transport of substrate (pyruvate) guaranteeing a constant supply to the electrode. After turning rotation off (ω from 1000 to 0 rpm) the current came back to the trend line.

At the end of the experiment in **Figure IV-3-C**, the electrochemical cell was disassembled and washed 10 times with MQ-H_2O and once with buffer. Fresh buffer (pH 7.5) containing 0.05 M MOPS, 4 mM $MgCl_2$, 1 mM $MnCl_2$ was added to the cell and a positive potential was applied (+0.1 V vs. SHE) to drive the upstream oxidative direction (**Figure IV-3-D**). Injection of $NADP^+$ (to 20 µM) did not have any effect as expected because of the oxidative potential applied; at the given potential, FNR cannot convert the cofactor unless the reduced form of the cofactor is present. Introduction of aspartate (to 20 mM) caused the immediate rise of an oxidative current. As mentioned earlier, this is proof that the whole cascade is working within the electrode nanopores.

Switching off rotation (ω to 0 rpm) caused the opposite effect of what was observed for the downstream direction: the oxidative current increased and when rotation was changed to 1000 rpm again, the current returned to its trend line. Rotation affects not only the supply of reactant but also increases the escape of intermediates (in this case fumarate and malate), because rotating the electrode increases the diffusion field hence the concentration gradient at the solution/electrode interface. This result confirms that intermediates are confined within the electrode nanopores and that they can partially escape. Their escape affects the rates of the reactions because the enzyme-catalysed rate is dependent on its substrate concentration, up to a certain point. Moreover, the experiment

proves that the enzymes remain adsorbed in the ITO pores because the current is retained upon high rotation.

4.4.3. Reversible reduction and oxidation: product analysis

The cascade performance was also analysed by ^{1}H-NMR. This procedure is particularly important for the reductive amination reaction to ensure that aspartate was being produced, because the interpretation of the current in the downstream direction is not straightforward, as mentioned in the previous section. Hence, product analysis is required to quantify how much of the observed current corresponds to the product aspartate or to the intermediates, malate and fumarate. A bigger electrode was used (12 cm^2 for the downstream and 3.6 cm^2 for the upstream reaction) to allow for the generation of substantial amounts of product such that quantification was possible. Results of the experiments are shown in **Figure IV-4** (**A** shows downstream and **B** upstream direction) and an example of NMR spectrum is given in **Figure IV-5**. The downstream experiments were carried out in a glove box to avoid a continuous Ar flush which would lead to the removal of CO_2 being produced by CA. This would otherwise decrease the CO_2 concentration which is the substrate of ME and thereby negatively affecting the cascade rate.

Figure IV-4-A shows a large-scale reductive amination/carboxylation of pyruvate to aspartate/malate. A mixture of the enzymes (0.1 CA/1 FNR/5 ME/2 FumC/1 AspA, 1 unit in 20 µL: 2 nmol) was dropped on the ITO/Ti foil (20 µL per 1.6±0.3 cm^2, total area: 12 cm^2) and left to adsorb for 20 minutes. Importantly, the electrodes were washed thoroughly to remove unbound enzyme before insertion into the electrochemical cell.

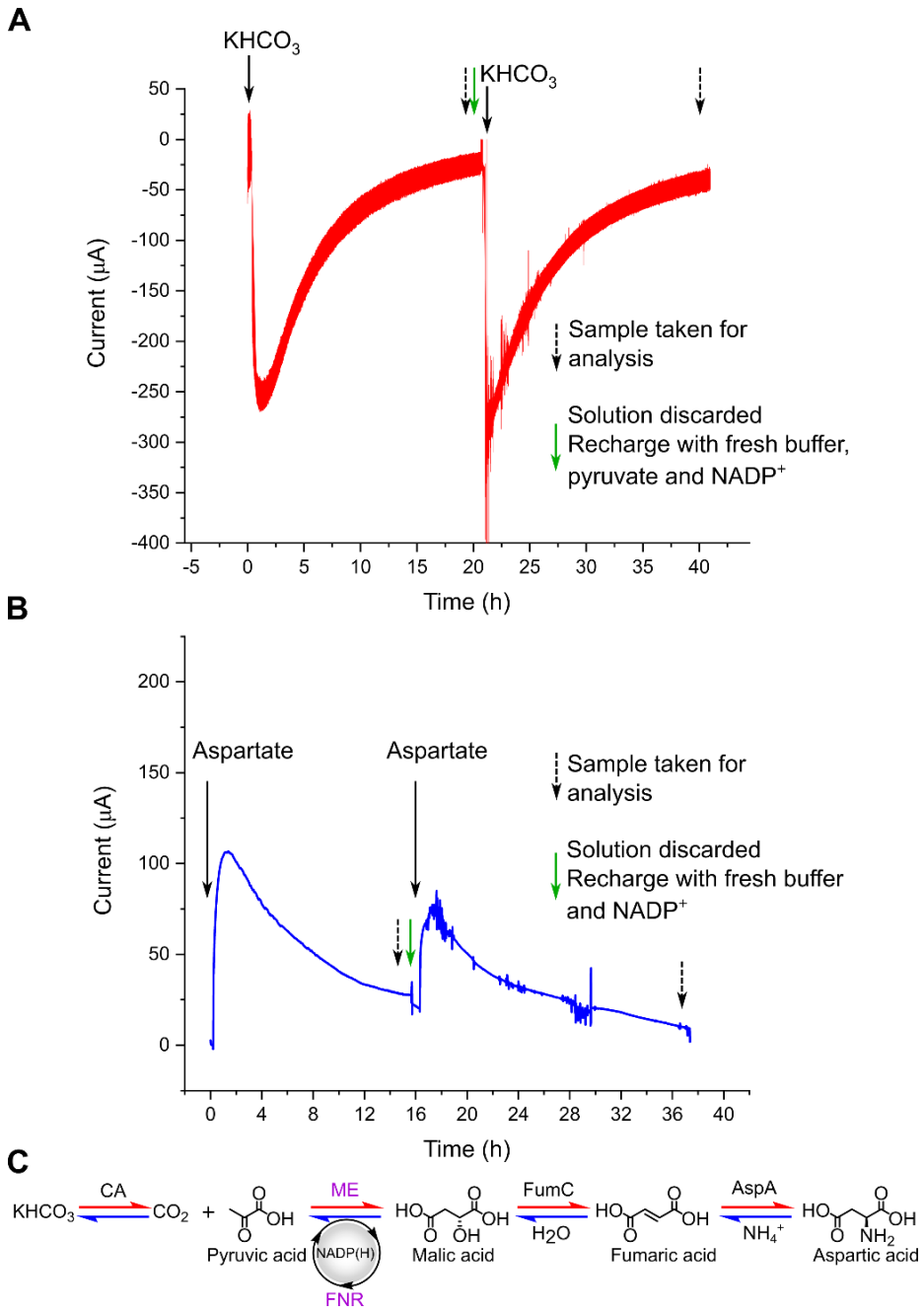


Figure IV-4. Chronoamperograms for the downstream and upstream cascade reaction. A. Reductive amination of pyruvate. Conditions: −0.45 V vs. SHE, 25°C, stirring. Buffer (pH 7.5): 0.05 M HEPES, 0.1 M NH_4Cl, 4 mM $MgCl_2$, 1 mM $MnCl_2$, 20 mM pyruvate, 20 µM $NADP^+$ (pH 7.5) under a N_2 atmosphere. An ITO/Ti electrode (12 cm^2) was loaded with the 5-enzyme mixture (0.1 CA/1 FNR/5 ME/2 FumC/1 AspA; 1 = 2 nmol in 20 µL of enzyme solution; 20 µL were used per 1.6±0.3 cm^2). Black arrows show injection of $KHCO_3$ to a final concentration of 0.1 M. After 20 hours, the solution was discarded and replaced with fresh buffer and substrate but without bicarbonate. Bicarbonate was then added (to 0.1 M) after 21 h. **B.** Oxidative deamination of aspartate to pyruvate. Conditions: +0.1 V vs. SHE, 25°C, stirring. Electrode area: 3.5 cm^2. Ratio: 0.1 CA/1 FNR/1ME/1 FumC/1 AspA. Buffer (pH 7.5): 0.05 M MOPS, 4 mM $MgCl_2$, 1 mM $MnCl_2$, 20 µM $NADP^+$. Injection of aspartate to 20 mM. After 16 h the solution was discarded and replaced with fresh buffer. After 17 h aspartate was re-injected to 20 mM. **C.** Schematic representation of the 5-enzyme cascade. Figure adapted from Morello *et al.*[241]

The chronoamperometry experiment (−0.45 V_{SHE}) was carried out in buffer (pH 7.5, 25°C, stirring) containing all the substrates required except for bicarbonate (0.1 M NH_4Cl, 20 mM pyruvate and 20 µM $NADP^+$). Introduction of $KHCO_3$ (to 0.1 M) triggered the start of the cascade reaction, as CO_2 – now supplied *in situ* via CA – is needed by the cofactor dependent step (FNR-ME, **Figure IV-4-C** shows the overall scheme of the cascade). Injection of $KHCO_3$ caused first an immediate increase in current and then a gradual current growth, which was never observed when FNR and ME were coloaded together in Chapter II. The current was stable for the first 3 h and after 20 h it stabilised at lower rates. In similar experiments, reintroduction of pyruvate, $NADP^+$ or bicarbonate did not cause an increase of current. However, after exchanging the solution with fresh buffer and substrates, re-addition of $KHCO_3$ (to 0.1 M, t = 21 h) initiated catalysis with the same trajectory of decay for another 20 h (**Figure IV-4-A**). Achieving the same maximum rate and trajectory of decay underlines the stability of the electrode and suggests that the decrease in rate may be due to product/intermediates inhibition and decrease of pyruvate concentration to values close to K_M (K_M of ME for pyruvate = 8.6 mM, see Part 2, Section 4.6.6.).

A similar pattern of stability was obtained for an upstream oxidative deamination (**Figure IV-4-B**). This experiment was carried out on the bench under a continuous flow of argon. An ITO/Ti electrode (3.5 cm^2) was prepared and loaded with the enzyme mixture (0.1 CA/1 FNR/1 ME/1 FumC/1 AspA; 1 unit in 20 µl: 2 nmol) by dropping 20 µl of this mixture per 1.6±0.3 cm^2. After rinsing thoroughly, the electrode was inserted into buffer (pH 7.5, as in **Figure IV-3-D**) containing 20 µM $NADP^+$. Injection of aspartate initiated catalysis as indicated by the occurrence of an oxidative current. After 16 h the solution was taken for NMR analysis and

replaced with fresh buffer without aspartate. Reinjection of aspartate (to 20 mM, t = 17 h) re-initiated catalysis with a similar maximum current and decay-trajectory. This result shows the stability of the enzymes and suggests the involvement of product/intermediates inhibition and a high K_M of AspA for aspartate (9 mM) to explain the decay trajectory (Part 2, Section 4.6.6. for steady state kinetics analysis). In the upstream direction, injection of substrate also triggered first an immediate increase in current followed by a growth which, in contrast to the downstream reaction, was also observed with initiation after solution exchange. The gradual growth in current observed in the upstream direction will be discussed in Section 4.6.4.

The reactions were monitored by ^{1}H-NMR and an example of an NMR spectrum obtained for the downstream (**A**) is shown in **Figure IV-5**. The samples were first treated with EDTA (final concentration 10 mM) to chelate paramagnetic Mn^{2+} and then ^{1}H-NMR with water suppression (90% H_2O, 10% D_2O) was performed. Note that this is a different approach of treating the sample than in Chapter II; this is because acidifying the sample (using conc. aq HCl) caused the complete overlap of the peak at 3.8 ppm (H-C_α of aspartate) with the buffer peak at 3.7 ppm. **Figure IV-5** shows that all three intermediates are visible [δ 6.4 ppm (s, H-C=C-H, *fumarate*); 4.2 ppm (dd, H-C-OH, *malate*); 3.8 ppm (dd, H-C_α, *aspartate*)]. The remaining proton resonances for malate and aspartate overlap with the buffer peaks. The results of quantitative NMR for the downstream reaction measured before buffer exchange (after 20 h for downstream) and after 40 h (20 h after buffer exchange) in **Figure IV-4-A** were as follows (using TMSP as a reference): 6.80/4.8 mM aspartic acid, 0.06/0.02 mM fumarate and 1.4/1.26 mM malate (before solution exchange/after solution exchange). A conversion of

pyruvate to aspartate of 34%/24% was obtained corresponding to a TTN ([aspartate]/[$NADP^+$], [$NADP^+$] = 20 µM) of 340/240 and 420/304 considering the total amount of product formed ([malate+fumarate+aspartate]/[$NADP^+$]). Moreover, the relative ratio of the product/intermediates achieved in the first 20 h was maintained after solution exchange and, in both cases, the main product was aspartate. In the case of the upstream reaction a conversion of 24% was obtained, equal to 220 TTN.

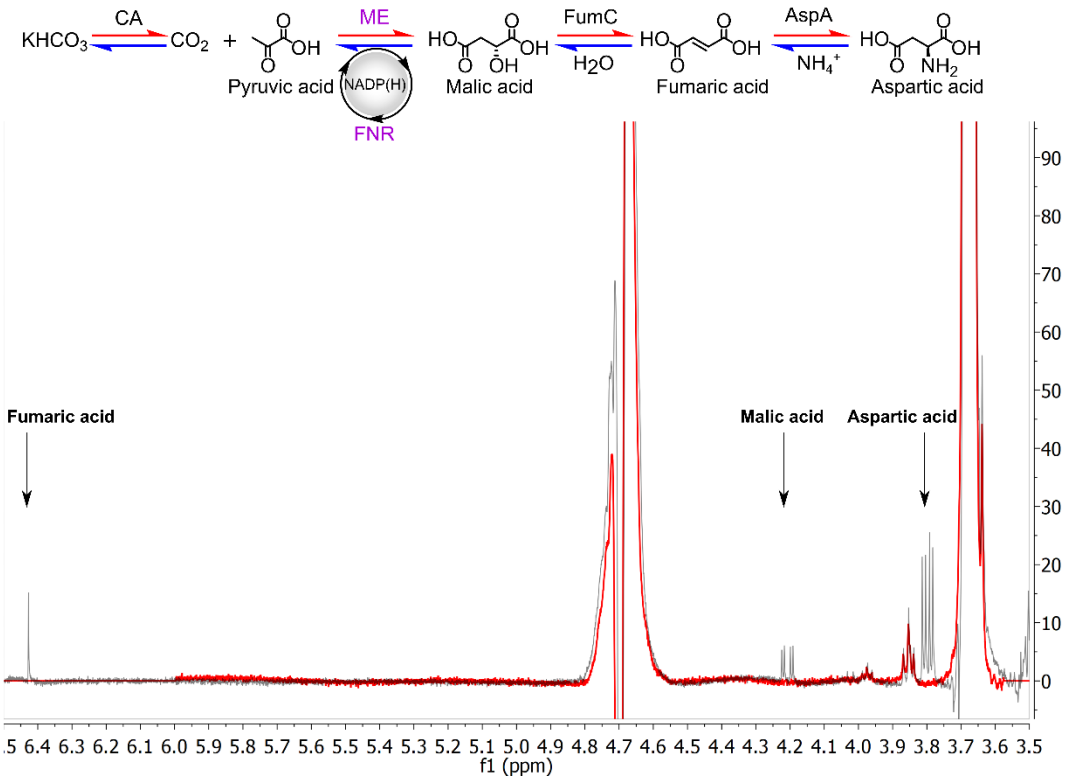


Figure IV-5. ^{1}H NMR of the downstream and upstream reactions. A. Downstream reaction: ^{1}H-NMR at 20 h (grey) and time 0 h (red). Prior to analysis, samples were treated with EDTA (final concentration 10 mM) and 10% D_2O. Peaks: δ 6.4, s, fumarate, δ 4.2, dd, malate; δ 3.8, dd, aspartate. Figure adapted from Morello *et al.*[241]

Figure IV-6 shows the average relative product/intermediates distribution resulting from ^{1}H-NMR analysis of a set of chronoamperometries carried out as in **Figure IV-4** (for more details Part 2, Section 4.6.5.). The relative amounts of intermediates and products were plotted, while the sum of the intermediates and

product was arbitrarily set to 1. Importantly, after recharging the solution in both the downstream and upstream experiments, the relative product distribution was maintained, suggesting a high stability of the nanoconfined enzymes inside the ITO layer. In the downstream direction (**Figure IV-6-A**) aspartate corresponds to 80% of the total product and a small leakage of malate occurred. Increasing the amount of FumC should increase the flux of malate to fumarate, decreasing the chance of losing the intermediate (malate) to the bulk solution. To increase the rate of the malate → fumarate step, the enzyme mixture relative composition was changed: FumC was varied between 0.1 to 2 equivalents, where 1 equivalent is defined as 2 nmol (see Section 4.6.6.). However, the resulting relative products/intermediate distributions were not affected (average in **Figure IV-6-A** and further details in Part 2, Section 4.6.5., **Figure IV-15)**. In the upstream direction (**Figure IV-6-B**) malate is the main product accounting for around 60%, while fumarate and the final product pyruvate only account for 15% and 20%, respectively. FumC and AspA were varied over a factor of 50 to decrease the flux of aspartate to malate, but the relative product/intermediate distributions were not affected (average in **Figure IV-6-B** and further details in Section 4.6.5). The same result was achieved when FNR and ME were increased to 5 units (Part 2, Section 4.6.5: **Figure IV-12-14**).

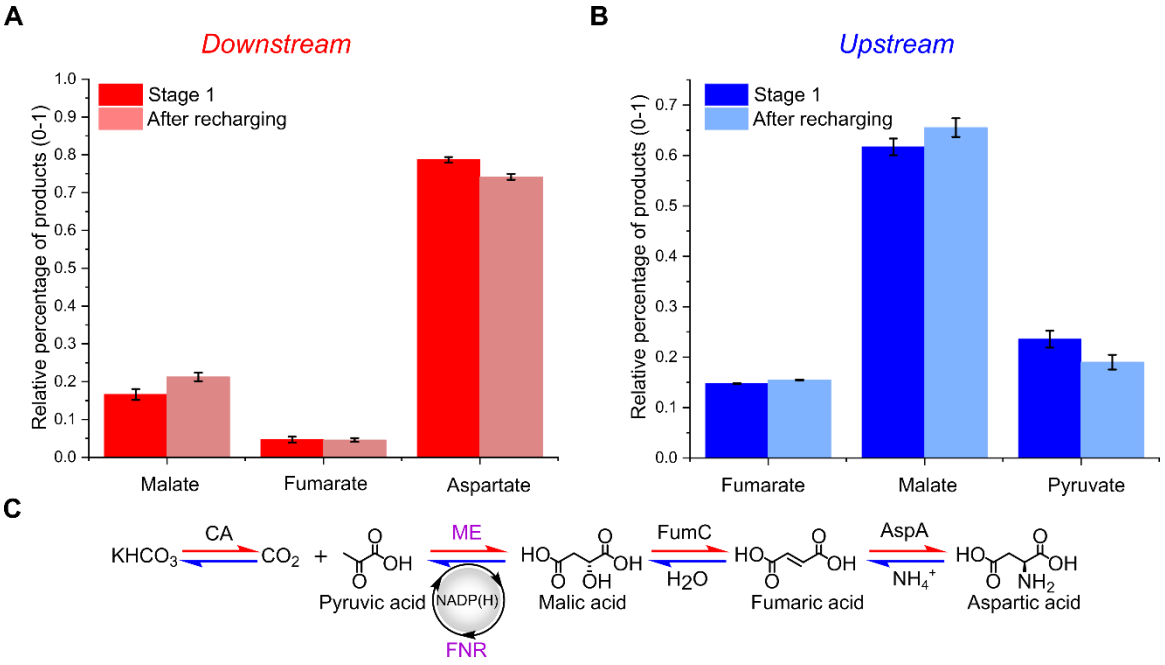


Figure IV-6. Product distribution in the downstream and upstream directions, before and after buffer exchange. A. Downstream direction: sample taken after 24 h and after 48 h. **B.** Upstream direction: after 16 h and 32 h. **C.** Schematic view of the cascade. Figure adapted from Morello *et al.*[241]

Variation of the enzyme mixture relative composition did not change the product/intermediates distribution: as a summary, it was observed that FumC and AspA are not needed in high amounts (for both downstream and upstream), and that CA is essential for the downstream reaction but not for the upstream (see above and Section 4.6.3. for more details). Note that a method to confirm whether the ratio applied to the electrode translates to the effective ratio in the pores is not yet available, because E2 to E4 are not redox active.

In order to clarify and explain the relative product/intermediates distribution results steady-state kinetic experiments for ME, FumC and AspA were carried out by solution assay in the same buffer conditions as used in the electrochemistry experiments; for the downstream reaction, 0.05 M HEPES, 4 mM $MgCl_2$, 1 mM $MnCl_2$ (pH 7.5), while for the upstream 0.05 M MOPS, 4 mM $MgCl_2$, 1 mM $MnCl_2$ (pH 7.5). Note that for ME carboxylation activity the buffer was first saturated with

CO_2. The results ($K_{M(app)}$ and $k_{cat(app)}$) are summarised in **Table IV-I** (see section 4.6.6. for the steady-stake kinetics experiments). The specificity constant ($k_{cat(app)}/K_{M(app)}$, M^{-1} s^{-1}) gives an indication of the catalytic efficiency of each enzyme. The most active enzyme is AspA with a specificity constant of 2.65×10^6 M^{-1} s^{-1} and 4.0×10^5 M^{-1} s^{-1} for the downstream and upstream reaction, respectively; the slowest enzyme is ME with values of 2.0×10^3 M^{-1} s^{-1} and 4.86×10^4 M^{-1} s^{-1} for the downstream and upstream reaction, respectively (**Table IV-I**). Based on these values, malate (the product of ME) is assumed to be immediately taken forward in the downstream reaction due to the high efficiency of E4 (AspA). In the upstream direction, malate is produced at high rates but is caused to accumulate inside the pores and diffuse (escape) to the bulk solution due to the slower activity of ME [$k_{cat(app)}$(ME) < $k_{cat(app)}$ (E4) and $k_{cat(app)}$ (E3)].

The data summarised in **Table IV-I** can be used to calculate τ-values ($1/k_{cat\ app}$). These values are only relevant at high intermediate concentrations, but they can still provide a useful model to understand the system. The calculated τ-values were compared with an assumed diffusion constant of a small molecule (10^{-5} cm s^{-1}, assuming a planar layer) formed at 1–2 µm depth (defined as δ).[242] The value, δ, represents the thickness of the ITO layer. By using the relationship for the calculation of the thickness of the diffusion layer, $t = (\delta / D_0^2)^{1/2}$ the time of escape of a solute in water would be 1–2 ms but probably slower in a crowded environment.[211,242] The times of escape obtained are on the same time-scale as the values obtained for FumC and AspA (downstream/upstream 4.5/4.5 ms and 2/2.7 ms for FumC and AspA, respectively, **Table IV-I**). Interestingly, the higher τ-value of FumC (in comparison to AspA and the time of escape of a solute) supports the higher leakage of malate compared to fumarate in the downstream reaction.

Clearly, ME is the limiting factor as its τ-value is much higher (average 40 ms). This supports the result mentioned above where a five-fold increase in the amount of ME did not affect the product/intermediates distribution in the upstream direction (see Part 2, Section 4.6.5.). To increase the flux towards the product in the upstream direction, it is likely that the concentration of ME should be much higher (> 20×) so that the rate of conversion of malate to pyruvate could compete with the rate of escape of malate (provided that all the other variables remain constant). The high *τ*-values of ME (29 ms) and the time of escape of the intermediate (1–2 ms) emphasises the importance of crowding the enzymes to increase the chance of the catalytic step to compete with the escape of the intermediate.

Table IV-I. Kinetic data for the enzymes (ME - E2, FumC - E3 and AspA - E4) measured in steady-state solution assay experiments for the downstream and upstream directions. Errors represent standard error (N = 3). Results shown in section 4.6.6.

	Aspartate synthesis (downstream)			**Aspartate oxidation (upstream)**		
	ME	FumC	AspA	ME	FumC	AspA
$k_{cat(app)}$ (s^{-1})	17 ± 1.1	220 ± 54	503 ± 33	34 ± 3.1	220 ± 29	359 ± 15
$K_{M(app)}$ (mM)	8.6 ± 2.2	1.5 ± 0.11	0.19 ± 0.03	0.7 ± 0.22	0.6 ± 0.2	9 ± 1.6
$k_{cat(app)}/K_{m(app)}$ (M^{-1}/s^{-1})	2.0×10^3	1.47×10^5	2.65×10^6	4.86×10^4	3.67×10^5	4.0×10^5
τ ($1/k_{cat(app)}$, ms)	**58**	4.5	2	**29**	4.5	2.7

4.5. Part 1: Conclusion

The work described in this chapter demonstrated the possibility to drive complex biocatalytic cascades within the nanopores of an electrode and importantly to energise, control and monitor the cascade in an unprecedented way. Cyclic voltammetry studies proved that the 5-enzyme cascade reaction is reversible, and that it can be driven in either direction by simply changing the electrode's potential. Moreover, an oxidative current in the upstream direction is a proof of successful entrapment of E3 and E4 within the electrode nanopores.

Rotation-dependence experiments showed that intermediates are produced and confined inside the pores. Rotation affects the supply of reactants and intermediates to the electrode and stopping rotation affects catalytic rates: in the upstream reaction the rate increased by 5% when rotation was switched-off, as intermediates are no longer spun away into the bulk solution. The rate in the upstream direction is proportional to the rate of the overall cascade and the charge passed proportional to the moles of the final product.

The stability of the reaction and product analysis was studied by electrochemistry and ^{1}H-NMR, respectively. A general decrease in rate was not only due to the decrease of substrate concentrations because reinjection of the substrate did not restore the rates. Instability of the electrode was also ruled out, as recharging the reactions with fresh buffer and substrates did restore the rates. Thus, product/intermediates inhibition was established as an important factor affecting the current. In the downstream reaction, most of the product was aspartate (80%) while in the upstream direction, the majority was the intermediate malate (60%). The poor catalytic efficiency of ME compared to AspA (AspA: 1000× higher efficiency) explains why the flow is mostly directed towards the product in the

downstream reaction. On the contrary, ME cannot compete with the faster FumC and AspA and a high escape of malate occurs in the upstream direction. Comparison of the estimated escape time for a small organic molecule (1–2 ms) with the *τ*-values for E2, E3 and E4 shows that ME catalysis does not compete with the time of escape as τ-values for ME are on average 40 ms. This also suggests that crowding and nanoconfinement is likely to be crucial to observe a signal at all.

This work demonstrates the proof-of-concept for a new and unprecedented way of energising and driving biocatalytic cascades for one-pot synthesis via cofactor regeneration. Importantly, this technology does not need complex treatment of the enzymes for immobilisation. Further possible developments of the cascade for biosensing applications could emphasise the power of this system: by building an artificial cascade, any relevant metabolite could be connected to a cofactor-dependent step for diagnostics. Connecting and energising the cascade can be important for systems catalysis to quickly investigate, evolve and optimise cascade reactions. The system requires only catalytic amounts of $NADP^+$ and allows the detection and monitoring of the rate of any multi-enzyme system provided that one step is cofactor-dependent.

4.6. Part 2: The 5-enzyme cascade, further results

The following section shows further preliminary results of the 5-enzyme cascade. It investigates the possibility to drive the cascade reaction in a different reaction solution, such as an unbuffered system or with CO_2 bypassing CA in the downstream reaction. The possibility of using a catalytic amount of $NADP^+$ is demonstrated in the downstream direction, showing the potential of this technology to be used as a platform for synthesis. Furthermore, the role of Mn^{2+} in the stability of the cascade will be investigated.

The previous section discussed the effect of changing the relative enzyme ratios. Here, further and more detailed results are discussed on this subject. In the upstream direction, upon substrate injection, a gradual current growth was observed after an immediate spike in current (see Section 4.4.3., **Figure IV-4**). The gradual growth will be discussed and investigated further. The last section shows steady-state solution assay of ME, FumC and AspA and an attempt to compare the electrified nanoconfined cascade with the cascade working in solution. Cloning and purification results for FumC and AspA were not included in this Chapter but can be found in the Appendix section of this Thesis.

4.6.1. 5-enzyme cascade in the unbuffered condition and the role of CA in the downstream direction.

It was unclear whether the 5-enzyme cascade could be driven in an unbuffered solution. To address this question, an ITO/Ti electrode (2 cm^2) was loaded with the enzyme mixture (0.1 CA/1 FNR/5 ME/1 FumC/1 AspA, 1 = 2 nmol), washed thoroughly and then inserted into an electrochemical cell containing 0.1 M ammonium carbonate, 4 mM $MgCl_2$, 1 mM $MnCl_2$, 20 mM pyruvate (initial pH 7.5). Results are shown in **Figure IV-7-A.** Addition of $NADP^+$ to 20 µM gave rise to a large reductive current, corresponding to the reductive amination/carboxylation reaction (red trace) and injection of aspartate to 20 mM is shown in the blue trace, where a large oxidative current is immediately detected upon its injection (**Figure IV-7-A**). However, this condition in a chronoamperometric experiment was highly unstable as the pH of the solution changed from 7.5 to 8.1 over 20 h.

Carbonic anhydrase was essential for the downstream reaction in a solution containing bicarbonate. If the buffer was saturated with CO_2, the reaction could proceed even without CA. An ITO/Ti electrode (1.9 cm^2) was loaded with a 4-enzyme cascade (1 FNR/5 ME/1 FumC/1 AspA, 1 = 2 nmol), washed thoroughly and inserted into a CO_2-saturated buffer (initial pH 7.5) containing 0.2 M MOPS, 0.1 M $KHCO_3$, 0.1 M NH_4Cl, 4 mM $MgCl_2$, 1 mM $MnCl_2$, 20 mM pyruvate. The system was maintained under a continuous flow of 100% CO_2 and results are shown in **Figure IV-7-B**. Injection of $NADP^+$ to 20 µM gave rise to a reductive current (red trace) and addition of aspartate (to 20 mM) produced a small oxidative current (blue trace). Flushing of CO_2 out of the system caused an increase of the oxidative current and a decrease of the reduction rate: this is likely because CO_2 suppresses the oxidative decarboxylation driven by ME (see Appendix, A.3).

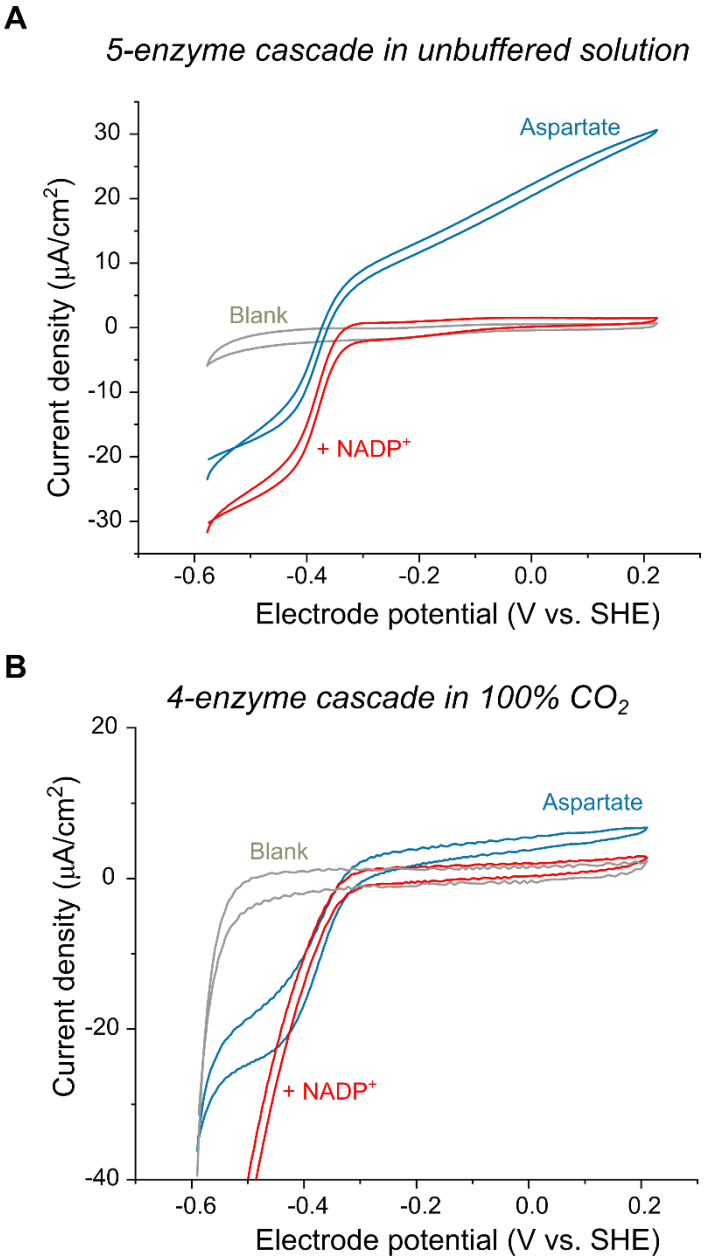


Figure IV-7. Cyclic voltammograms showing the activity of the cascade in unbuffered solution and in 100% CO_2 atmosphere. A. Unbuffered solution. CV for the 5-enzyme cascade (0.1 CA/1 FNR/5 ME/1 FumC/1 AspA) in 0.1 M ammonium carbonate, 4 mM $MgCl_2$, 1 mM $MnCl_2$, 20 mM pyruvate (pH 7.5), 1 mV/s, 25°C, stationary electrode. Addition of $NADP^+$ to 20 µM (red) and aspartate to 20 mM (blue). **B.** 100% CO_2. CV for the 4-enzyme nanoconfined cascade. CA was not included (enzyme mixture: 1 FNR/5 ME/ 1 FumC/1 AspA). CO_2-saturated buffer used: 0.2 M MOPS, 0.1 M $KHCO_3$, 0.1 M NH_4Cl, 4 mM $MgCl_2$,1 mM $MnCl_2$, 20 mM pyruvate (initial pH 7.5) (1 mV/s, 25°C, stationary). Blank CV (grey); Injection of $NADP^+$ to 20 µM (red). Injection of aspartate (to 20 mM) (blue). Figure adapted from Morello *et al.*[241]

4.6.2. Reductive amination catalysed by the 5-enzyme cascade using smaller, catalytic amounts of $NADP^+$.

The nicotinamide cofactor must be regenerated to decrease the costs of an industrial process (see Section 1.5.). In the experiments from the previous Section (Section 4.4.) a low concentration of 20 µM $NADP^+$ was used. This value was decreased even further and similar conversions were achieved.

In the experiment shown in **Figure IV-8** a concentration of 5 µM was used to drive the reductive amination of pyruvate to aspartate. An ITO/Ti electrode (12 cm^2) was prepared by electrophoretic deposition and loaded with the cascade mixture (0.1 CA/1 FNR/5 ME/1 FumC/1 AspA; 1 unit: 2 nmol per 20 µL of enzyme solution). Then, the electrode was washed thoroughly to remove unbound proteins and added to an electrochemical cell in a buffer (pH 7.5, 4 mL) containing all the required component except for $NADP^+$ (0.05 M HEPES, 0.1 M $KHCO_3$, 4 mM $MgCl_2$, 1 mM $MnCl_2$, 20 mM pyruvate). A potential of −0.45 V vs. SHE was applied and the current monitored over time (stirring, 25°C) in an anaerobic glove box (mBraun, O_2 < 2 ppm; N_2 atmosphere). The reaction was initiated by injecting $NADP^+$ to a final concentration of 5 µM. The current trajectory after 24 h reached 40% of the maximum current. The experiment with 5 µM $NADP^+$ shows a higher current stability if compared with the chronoamperometry carried out with 20 µM (see previous **Figure IV-4**, Part 1, Section 4.4.3.); with 20 µM $NADP^+$ 16% of the maximum current is retained after 24 h. This result supports the notion that product/intermediates inhibition is an important factor affecting the current as the maximum current achieved with 5 µM cofactor is 2.5× smaller than in the experiment with 20 µM $NADP^+$. Hence, after 24 h, less product/intermediates are produced. In the experiment with 5 µM $NADP^+$ after 40 h the retained current was

16% of the maximum current and a total conversion (pyruvate to intermediates, from ^{1}H-NMR) of 28.9% was achieved (23.5% to aspartate). More specifically, the final concentrations (4 mL) were 4.68 mM for aspartate, 0.86 mM for malate and 0.28 mM for fumarate. These ratios result in the following relative product/intermediates distribution: aspartate 80%, malate 14.7% and fumarate 4.8%. This is in line with the product/intermediates distribution of previous results (**Figure IV-6**, Part 1, Section 4.4.3.). After 40 h, the TTNs were 960 or 1156 based on aspartate or on the total amount of products, respectively. The TTN of 960 is 197× to 387× higher than recent biocatalytic cascades using different cofactor regeneration methods such as the hydrogenase-based systems.[124,236]

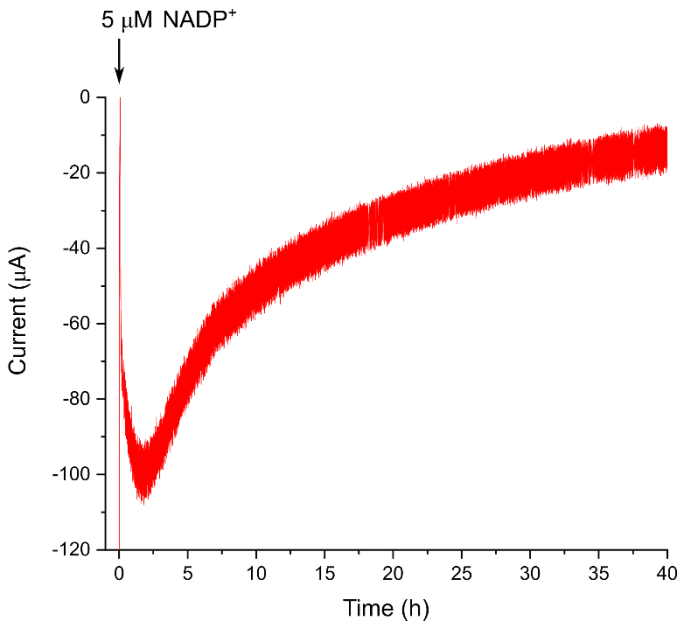


Figure IV-8. Chronoamperogram showing the reductive amination of pyruvate with 5 µM NADP^{+}. Conditions: −0.45 V vs. SHE, 25°C, stirring, under N_2. WE: ITO/Ti (12 cm^2). A volume of 20 µL per 1.6±0.3 cm^2 was used to load the 5-enzyme cascade (0.1 CA/1 FNR/5 ME/1 FumC/1AspA; 1 unit, in 20 µL: 2 nmol) and thoroughly rinsed prior to the experiment. Buffer (pH 7.5): 0.05 M HEPES, 0.1 M $KHCO_3$, 0.1 M NH_4Cl, 4 mM $MgCl_2$, 1 mM $MnCl_2$, 20 mM pyruvate. Injection of NADP^{+} to 5 µM as indicated. Figure adapted from Morello *et al.*[241]

4.6.3. The role of CA and nanoconfinement in the upstream direction

Carbonic anhydrase was essential for the downstream reaction, as it provides CO_2 *in situ*, eliminating the need for a continuous flush of CO_2 into the system. In this paragraph the role of CA in the upstream direction was studied, and to investigate this, two parallel experiments were setup. The same surface area electrode (ITO/Ti, 2.9 cm^2) was used in both cases. In the first experiment, a mixture of enzymes (1 FNR/1 ME/1 FumC/1 AspA) with no CA was dropped onto the electrode, while in the second set up, the full cascade was used (0.1 CA/1 FNR/1 ME/1 FumC/1 AspA). **Figure IV-9** shows the results from the reactions in MOPS buffer (pH 7.5) containing 20 µM $NADP^+$. To initiate the reaction, aspartate was injected to a final concentration of 20 mM and a first current increase was observed followed by a slow growth in current (see Section 4.6.4 for the current growth). The chronoamperograms of the electrode with and without CA are represented in orange and blue, respectively (**Figure IV-9**). Note that the current values are similar in both cases, thus they can be compared to each other because product formation/inhibition is similar (see Section 4.4.3. for the discussion of the current decay). The experiment showed that CA did not drastically affect the upstream reaction and the trace with CA tends to be less stable. Although there was no change of pH in the bulk solution, a possible explanation for the observed instability is that CA could slightly affect the local pH inside the pores by bicarbonate formation.

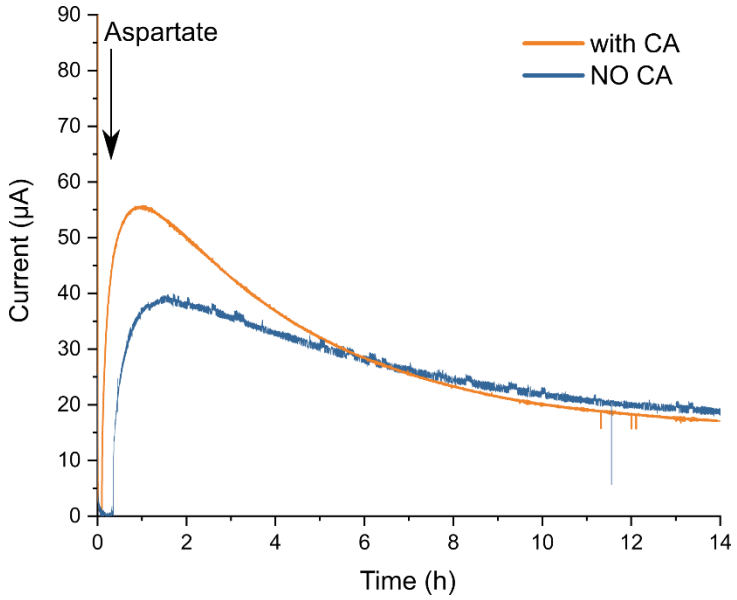


Figure IV-9. The role of CA in the upstream direction. Chronoamperograms showing a comparison of stability of the oxidative deamination reaction (upstream direction) with (orange trace) and without (blue trace) CA. Injection of aspartate to 20 mM to initiate reaction. Conditions: +0.1 V vs. SHE, 25°C, stirring. Buffer: 0.05 M MOPS, 4 mM $MgCl_2$, 1 mM $MnCl_2$, 20 µM $NADP^+$. Ratio: 0.1 CA/1 FNR/1 ME/1 FumC/1 AspA (orange trace) and 1 FNR/1 ME/1 FumC/1 AspA (blue trace). Figure reprinted from Morello *et al.*[241]

The enzymes operating in the cascade should be physically located in the same pore to detect an activity. To confirm this hypothesis, an experiment in which the 4-enzymes (no CA) were dropped onto different areas of the electrode, was carried out (**Figure IV-10**). The 4 enzymes (no CA) were dropped onto different areas of the electrode ensuring that the enzyme solution spots were not in contact. A chronoamperometry experiment (+0.1 V vs. SHE, 25°C, stirring) was carried out in the same MOPS buffer (pH 7.5) lacking cofactor (**Figure IV-10**). Injection of NADPH (to 20 µM) caused formation of an oxidative current, corresponding to the oxidation of NADPH to $NADP^+$ by FNR. Addition of aspartate (to 20 mM) did not affect catalysis but caused a small increase in current. This response is probably due to the increase of the volume of the cell solution upon substrate injection, which increases the exposed electrode area, affecting the current. Note that injection of

the same volume of buffer caused the same effect. The increase in current is therefore likely to be attributable to an increase in electrode surface coming in contact with the solution. This control experiment supports the hypothesis that all enzymes must be nanoconfined together within the pores.

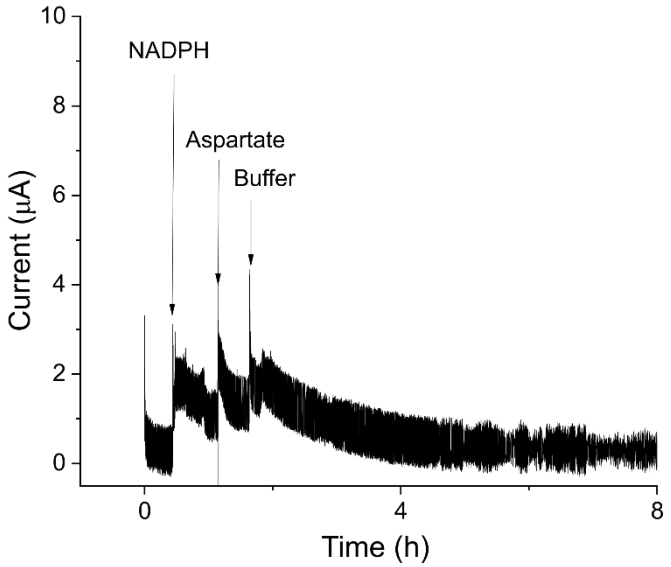


Figure IV-10. The requirement for nanoconfinement of the enzymes. Control experiment: an ITO/Ti electrode (1 cm^2) was prepared and four enzymes (FNR, ME, FumC, AspA) were dropped separately onto the surface, making sure there was no contact between the enzyme solution spots. Chronoamperometry experiment (+0.1 V vs. SHE, stirring) carried out in buffer (pH 7.5) containing 0.05 M MOPS, 4 mM $MgCl_2$, 1 mM $MnCl_2$. Buffer was reinjected to show that injection of aspartate (to 20 mM) did not cause any catalytic effect. Figure reprinted from Morello *et al*.[241]

4.6.4. The gradual current growth in the upstream direction

Upon substrate injection an immediate increase in current was followed by a gradual growth during the chronoamperometric experiments (see **Figure IV-4**, Section 4.4.3.). In Chapters II and III the growth in current was observed upon enzyme (E2) injection in solution, while substrate injection caused an immediate increase of current when FNR and E2 were coloaded together (see Section 2.4.2.5.). It was rationalised that, for the former, the current growth was due to

enzyme molecules adsorbing into the electrode surface. However, in the experiments carried out in this Chapter the enzymes were already preloaded and the electrodes were then rinsed thoroughly before introducing them into the electrochemical cell. Hence, the enzymes were not present in solution. The following section aims to shed light on the gradual current growth observed upon aspartate injection in the upstream reaction. Aspartate amino-lyase has been reported through conventional solution assay (absorbance vs. time) to have a lag phase in the amination reaction, where the extent of this lag phase decreased with higher concentration of aspartate.[243] However, a lag phase has not been reported in the literature for the de-amination reaction (corresponding to the upstream direction).

In the 5-enzyme cascade, the gradual current growth was observed upon substrate injection both at the beginning of a typical oxidative deamination and after solution exchange (≈ 20 h, see **Figure IV-4**). There are two possible explanations: the gradual growth represents the accumulation within the pores of malate through the flux across the cascade which increases the rate of E2 to reach steady-state over time. The growth could also be due to a substrate-induced activation and assembly of a metabolon.[212]

Figure IV-11 investigates the gradual growth in current. In **Figure IV-11-A**, an ITO/Ti electrode (2.9 cm^2) was prepared as described for **Figure IV-4-B**. In this experiment, the system was initiated with malate (to 20 mM, substrate of ME - E2), instead of using aspartate, thereby bypassing the need for the rest of the cascade. If the growth is related to malate accumulation through the flux over the cascade, injection of malate to a high concentration should produce only an immediate increase in the rate. However, a growth in current was observed as in the typical

case where the reaction was initiated with aspartate. Initially, the rate reached a high value, but the current rapidly decreased. The result suggests that malate accumulation to reach steady-state is not the reason for the growth in current.

Figure IV-11-A at 22 h shows a solution exchange: the cell solution was discarded and exchanged with fresh buffer containing $NADP^+$ and injection of aspartate induced after an immediate spike a growth in current, reaching a lower maximum than the one obtained upon malate injection (**Figure IV-11-A**). The growth after buffer exchange - and not only at the beginning of an experiment - precludes that the gradual current growth is due to experimental errors *i.e.* inadequate rinsing of the electrode may cause some enzyme to get in solution.

In **Figure IV-11-B** the upstream reaction was initiated by addition of aspartate and after 20 h a solution exchange was carried out as described for **Figure IV-11-A**. In this case however, all the intermediates (the substrates of E4, E3, E2, aspartate, fumarate and malate) were injected to a final concentration of 20 mM, causing only an immediate increase in current. The comparison of the current growth obtained from these three events (injection of aspartate, injection of malate and injection of all the intermediates) is shown in **Figure IV-11-C**, where the current was normalised (min = 0, max = 1). The growth of current is similar for the injection of aspartate and malate but considerably faster when all the intermediates were injected together. The result supports a substrates/intermediates induced activation of the cascade. This is either due to a build-up of all intermediates to reach a steady-state (in some cases reported to take up to hours)[244] or a substrate-induced metabolon assembly, that is the formation of an enzyme cluster, which increases the rates either by substrate channelling or by a probabilistic effect (a metabolite has a higher chance of encounter another enzyme in an assembly

compared to free enzymes).[212] The metabolon formation is an intense area of research and one example by Zhao *et al*. is the substrate-induced chemotactic assembly of the first four enzymes in glycolysis.[212,245]

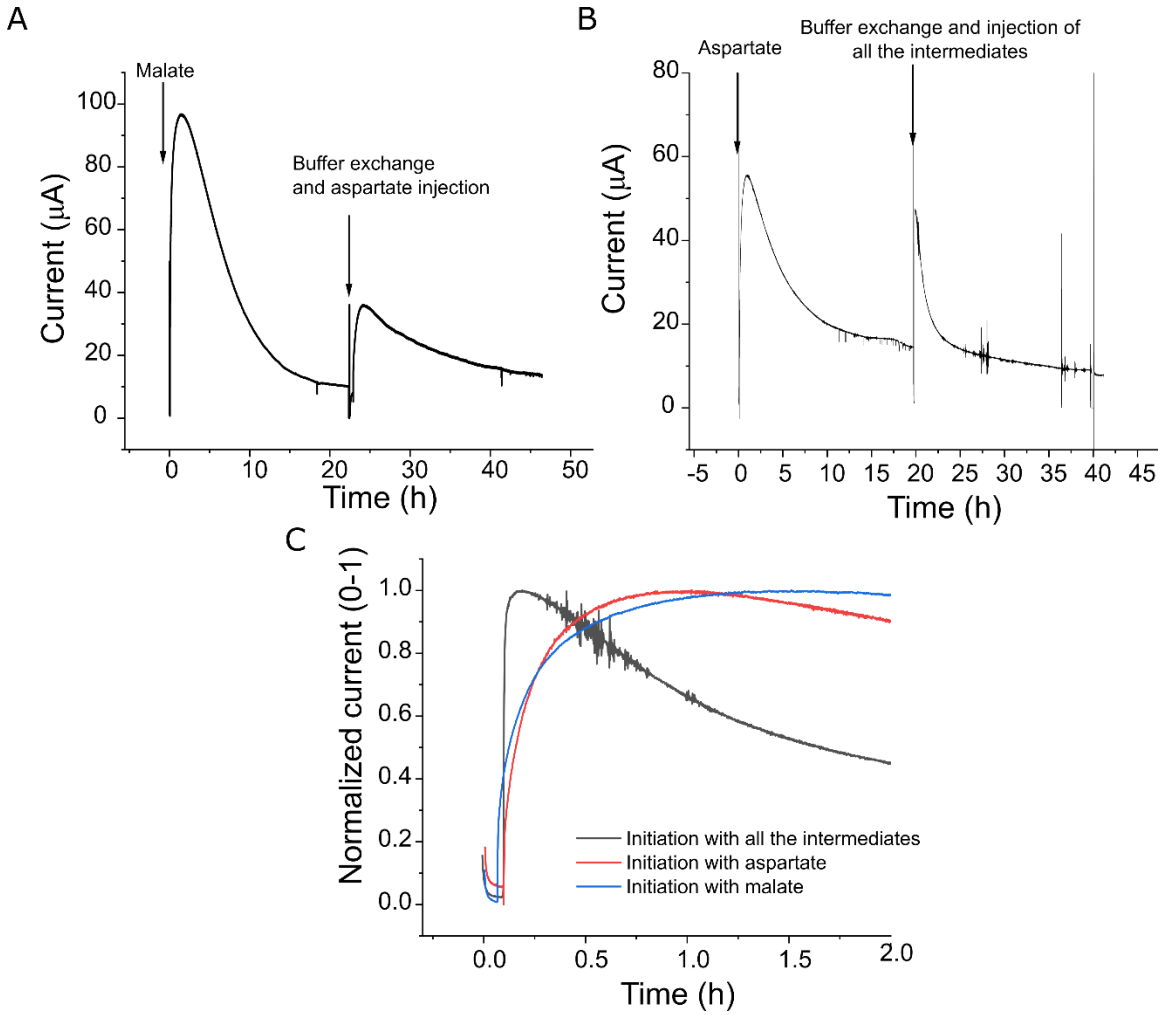


Figure IV-11. Gradual current growth in the upstream direction. A. Reaction was initiated with malate (to 20 mM, substrate of E2), bypassing the whole cascade. After 20 h, the solution was discarded and new buffer was introduced. The reaction was then initiated with aspartate (to 20 mM, substrate of E4). **B.** Reaction was initiated with aspartate (to 20 mM, substrate of E4). After 20 h the solution was discarded as in A. In this case, the reaction was initiated by injection of all the intermediates (aspartate, fumarate and malate, substrates of E4, E3 and E2 to a final concentration of 20 mM). **C.** Overlay of A, B and C. Currents were normalised by fixing minimum to 0 and maximum to 1. Grey: injection of all intermediates; red: injection of aspartate; blue: injection of malate. Chronoamperometry: +0.1 V vs. SHE, 25°C, stirring. 0.05 M MOPS, 4 mM $MgCl_2$, 1 mM $MnCl_2$, 20 µM $NADP^+$. Electrode (2.9 cm^2) prepared as in Figure IV-4-B.

4.6.5. Varying enzyme ratios

NMR analysis of the upstream reaction showed that the main intermediate was malate, accounting for 60% of the products, while in the downstream reaction aspartate was the main product and only a small leakage of malate was detected (20%, Section 4.4.3., **Figure IV-6**). In this paragraph, the relative enzyme ratio was varied to change the product/intermediates distribution both in the downstream and the upstream direction. Note that the enzyme ratios (*e.g.* 0.1 CA/1 FNR/5 ME/1 FumC/1 AspA), are described in relation to 1 enzyme equivalent = 2 nmol in 20 µL of enzyme solution used to prepare the electrode of typically 1.6±0.3 cm^2.

One possible strategy to change the product distribution for the upstream direction is to slow down the steps catalysed by E4 and E3, by decreasing the amount of E4 and E3. Alternatively, increasing the amount of E1 or E2 could both enhance the rate of the malate-to-pyruvate step, thus affecting the product distribution. CA was not varied since it did not significantly affect the upstream reaction in previous experiments (see Section 4.6.3.).

Figure IV-12 shows the results of four chronoamperometry experiments where each enzyme was in excess (5 × 1 equivalents = 10 nmol/1.6±0.3 cm^2) relative to the others (except for CA, fixed at 0.1 unit = 0.2 nmol/1.8 cm^2). The ITO/Ti electrodes (2.89 cm^2) were prepared as before and loaded with the different enzyme mixtures, then washed thoroughly and inserted into a buffer (pH 7.5, 4 mL) containing 20 µM $NADP^+$.

The rate of the cascade over time was monitored to identify the best reaction conditions: the ideal situation for optimal conversion would be to obtain a high current (rate) and maintain the high rates for a long period of time (high stability). **Figure IV-12** shows that the best combination occurs when FNR is in excess (blue

trace, charge passed: 3.8 C; equating to 4.93 mM of pyruvate formed). The most unstable trace is when FumC is in excess (yellow trace, charge passed: 1.6 C; 2.2 mM of product), while the traces corresponding to an excess of AspA and ME show similar behaviour (green and red trace, respectively; charge passed for both: 2.7 C; equal to 3.5 mM of product formed). Comparison of the four experiments suggests that an excess of FumC is detrimental to the system, probably because of accumulation of malate, which is inhibiting the system. The stability for the other traces is similar, except for that in which FNR is in excess (blue trace, **Figure IV-12**). This trace is more unstable than the traces corresponding to an excess of ME and AspA (red and green trace, **Figure IV-12**). However, given the higher rates (hence higher conversion) this is less comparable (**Figure IV-12**).

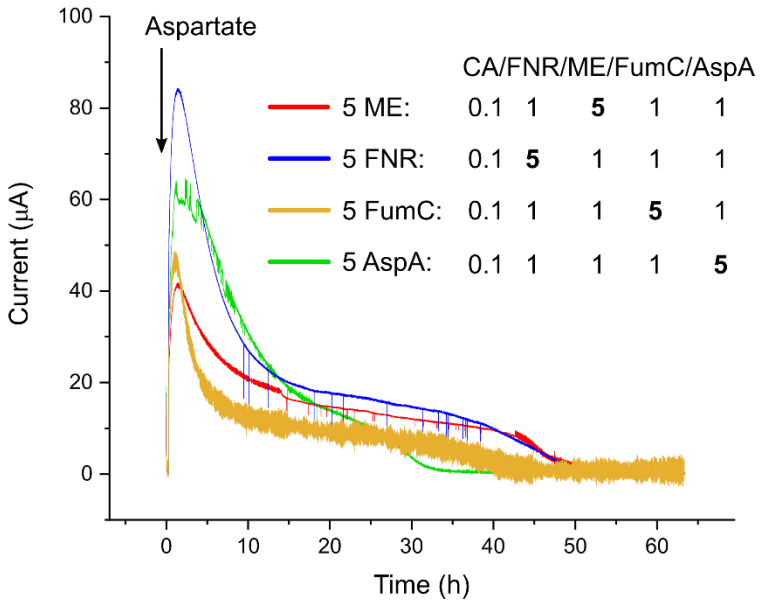


Figure IV-12. Variation of enzyme ratios in the upstream direction. Chronoamperograms for the oxidative deamination of aspartate (20 mM) in a buffer containing 0.05 M MOPS, 4 mM $MgCl_2$, 1 mM $MnCl_2$ at 25°C, +0.1 V vs. SHE (stirring) with an ITO/Ti electrodes (2.89 cm^2). The traces show different experiments where the relative ratio of the enzymes was varied. CA was constant in each experiment. Red: ME in excess (5 times more); blue: FNR in excess; yellow: FumC in excess; green: AspA in excess. 1 enzyme equivalent is defined as 2 nmol/1.6±0.3 cm^2. Figure adapted from Morello *et al.*[241]

As suggested from **Table IV-I** (see Section 4.4.3.), the slow rate of ME explained the high leakage of malate (60% of the total products) in the upstream direction. Therefore, the amount of E3 and in E4 (FumC and AspA) deposited on the electrode was decreased. For this purpose, the best ratio (in terms of conversion) from the previous experiments was chosen and modified to decrease FumC and AspA to 0.1 equivalents (0.2 nmol). Hence the ratio, 0.1 CA/1 FNR/1 ME/0.1 FumC/ 0.1 AspA, was investigated. Results are shown in **Figure IV-13** (violet trace; in **B** current and in **A** and **C** normalised current). Note that in **Figure IV-13-A** the violet trace was not compared with the 'parent' enzyme ratio (5 FNR = 0.1 CA/5 FNR/1 ME/1 FumC/1 AspA), because the current (rate) in the 5 FNR experiment was more than two times higher, equating to more product formed. Thus, product inhibition may convolute any claim in stability. The 5 ME trace (red trace, 5 ME = 0.1 CA/1 FNR/5 ME/1 FumC/1 AspA, **Figure IV-13-A**) was chosen for the comparison because it reached the same highest current (40 µA see **Figure IV-12**) and both traces also exhibited similar maximum current densities (19 and 17 µA/cm^2 for the 5 ME and the violet trace, respectively). The trajectory of current decay was investigated after normalising the current. Injection of aspartate (to 20 mM) initiated the current growth with the same growth and decay trajectory as observed for the precedent results (current growth ≈40 min). **Figure IV-13-A** shows the comparison of the violet trace (0.1 CA/5 FNR/1 ME/0.1 FumC/0.1 AspA) with the 5 ME trace (0.1 CA/1 FNR/5 ME/1 FumC/1 AspA). Both the red trace and violet trace reached the maximum current at the same time (≈40 min) but the red trace (5 ME) reached 30% of the maximum current in 8 h, while after 24 h the violet trace (0.1 FumC, 0.1 AspA) showed still 60% of the current (**Figure IV-13-B**). By decreasing FumC and AspA to 0.1 equivalents the rate of formation of malate is

decreased, so that the slow kinetics of ME compete with E3 and E4. As a result, it is likely that less malate diffuses to the bulk solution resulting in diminished inhibition of the cascade reaction.

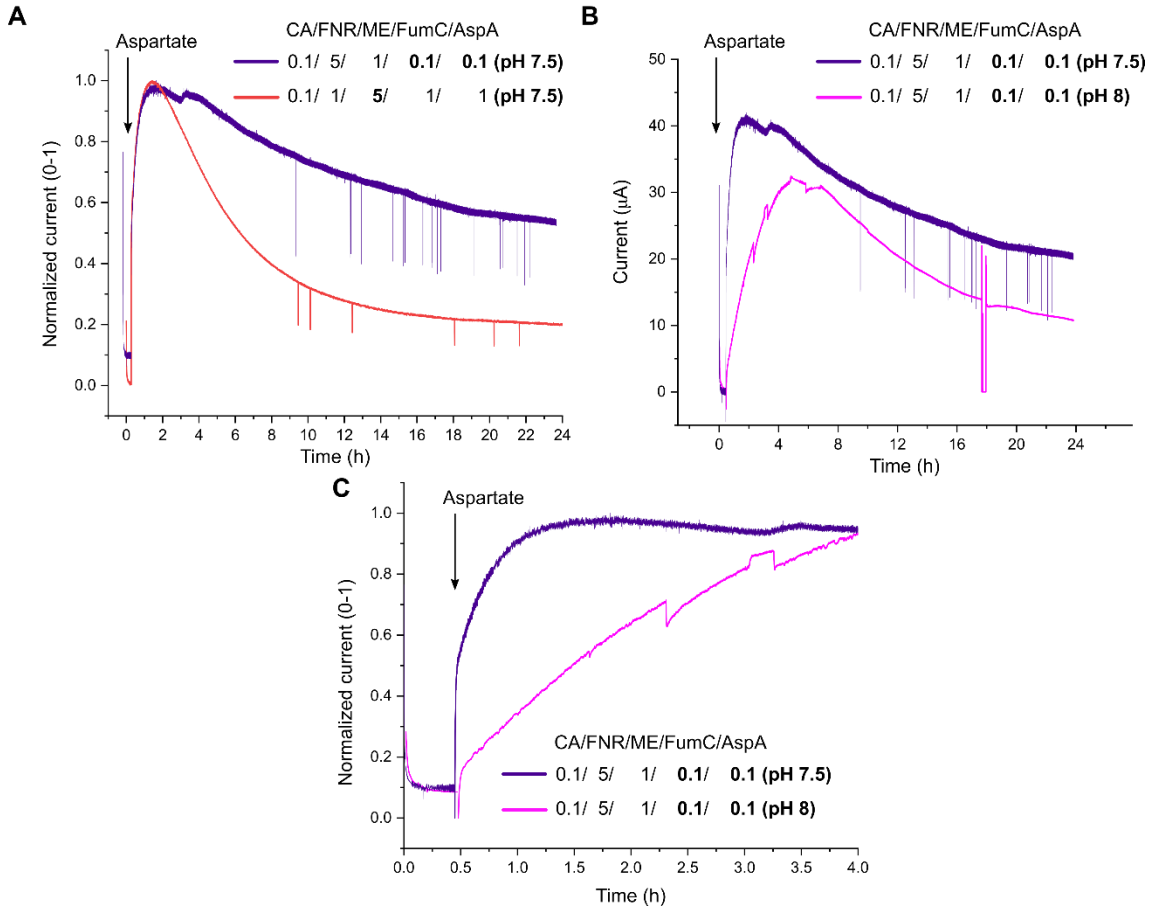


Figure IV-13. The effect of decreasing E3 and E4. A. Chronoamperogram for an ITO/TI electrode (3 cm^2) loaded with enzyme ratio (0.1 CA/5 FNR/1 ME/0.1 FumC/0.1 AspA) in buffer containing 0.05 M MOPS, 4 mM $MgCl_2$, 1 mM $MnCl_2$. $NADP^+$ injected to a final concentration of 20 µM and aspartate to 20 mM. In red, same conditions but with enzyme ratio: 0.1 CA/1 FNR/5 ME/1 FumC/1 AspA. Current was normalised to minimum = 0 and maximum = 1. **B.** Chronoamperogram for an ITO/TI electrode (3 cm^2) loaded with enzyme ratio (0.1 CA/5 FNR/1 ME/0.1 FumC/0.1 AspA) in buffer as in A (violet trace) and in 0.05 M borate, 4 mM $MgCl_2$, 1 mM $MnCl_2$ (pH 8). $NADP^+$ injected to 20 µM; aspartate injected to 20 mM. **C.** For comparison, gradual current growth of traces shown in B after normalisation.

Figure IV-13-B (in **C** normalised current) shows a preliminary result using the enzyme ratio (0.1 CA/5 FNR/1 ME/0.1 FumC/0.1 AspA) at two different pH values, pH 7.5 and pH 8 (the latter in 0.05 M borate buffer). The difference in the current

growth was remarkable (**Figure IV-13-C**). The rate reached a maximum after 4 h at pH 8 (magenta trace, **Figure IV-13-C**) while the maximum was reached after 40 min at pH 7.5 (violet trace, **Figure IV-13-C**). There are several potential explanations, such as a slow change of local pH within the nanopore or the varying pH optimum for different enzymes (*e.g.* the optimum for AspA is pH 8.5).[246] This is a very interesting preliminary result which requires further investigation.

The relative product/intermediates distributions obtained upon varying the enzyme ratio in the upstream direction are shown in **Figure IV-14** and plotted by setting the sum of product and intermediates to 1. **Figure IV-14** shows that changing the ratios did not affect the final product distribution. The discrepancy in k_{cat}/K_M and τ-values between ME and FumC/AspA (see **Table IV-I**) and the assumed time of escape of a typical intermediate (see Section 4.4.3.) provide a possible explanation.

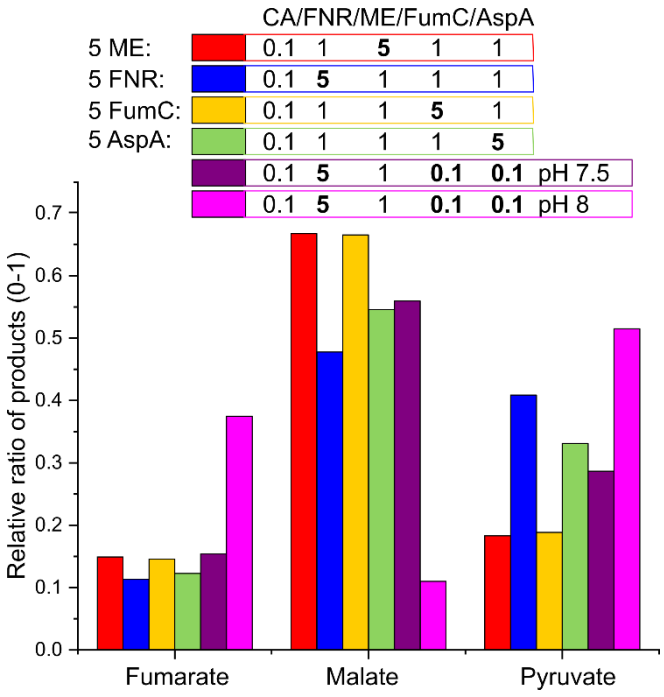


Figure IV-14. The relative ratio of products in the upstream direction. Relative percentage of products from ^{1}H-NMR analysis for various combinations of enzyme ratios from experiments in Figure IV-12 and Figure IV-13. Figure adapted from Morello *et al.*[241]

Apart from the experiment at pH 8, the relative product/intermediates distribution is consistent with the observation in **Figure IV-6** (pyruvate ≈20% and malate ≈60%). Increasing FumC and ME caused an increase of malate accumulation which was lower in the 5 FNR experiment. The situation with borate pH 8 (magenta bars, **Figure IV-14**) shows a much different result (fumarate leakage increases and malate becomes the least intermediate), but further experiments are required to reproduce and interpret the result. Additional experiments at different pH will also help to explain the current growth in the upstream direction (see Section 4.6.4.).

In the downstream direction, FumC was varied (from 0.1 to 2 equivalents) to decrease the accumulation of malate, but it did not cause a definite change in the product/intermediates distribution (**Figure IV-15**).

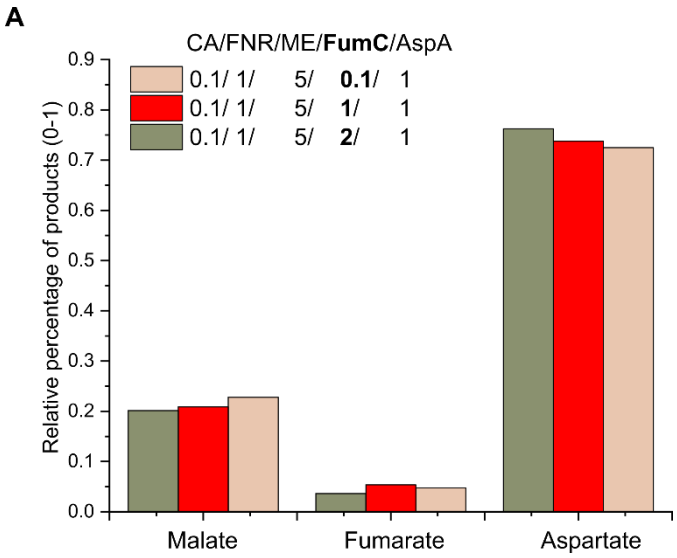


Figure IV-15. The effect on product distribution by changing enzyme ratios in the downstream direction. Change of relative percentage of products from varying FumC between 0.1 to 2 enzyme equivalents relative to FNR (1 enzyme equivalent in 20 µL = 2 nmol dropped on 1.6±0.3 cm^2). Figure adapted from Morello *et al.*[241]

Upon decreasing FumC to 0.1 a strong increase of malate leakage was expected. One possible explanation for the different result can be that the effective

enzyme ratio within the electrode does not reflect the enzyme ratio loaded on the electrode. Different affinities of the enzymes loaded onto the electrode could affect the loading efficiency in an unpredictable way. This means that a lower affinity could lead to a lower effective loading even though a higher concentration of that enzyme was applied during electrode preparation. Therefore, the different affinity for the ITO layer can result in different effective ratios between the enzymes in the cascade. The interaction between FNR and ferredoxin (Fd) is based on charge: ferredoxin is negatively charged and FNR has a distinct positively charged area to interact with Fd. Charge is an important element also for the interaction between FNR and ITO (see Section 1.6).[134,146] Megarity *et al*. started to investigate the reasons for different binding of E2, but a clear picture has not been established yet. The authors reasoned that interaction does not depend on the oligomeric state of the protein, while the isoelectric point could give a hint of the enzyme affinity for the ITO layer.[146] The enzymes varied in this paragraph were FNR (monomer), ME (dimer-> octamer), FumC (tetramer), AspA (tetramer). Analysis of the surface charge of the enzymes above did not give a clear picture as for FNR: a specific positive charged area on E2, E3 and E4 was not observed (data not shown). The isoelectric point (pI) was predicted by using ExPASy, from which FNR has a pI of 6.54, ME 5.34, FumC, 6.12 and AspA 5.19. The predicted pI for FNR and ME compare well with the experimental values reported by Megarity *et al*.[146] Based on the isoelectric points FumC could have a higher affinity for the ITO layer than ME and AspA, possibly resulting in a higher relative amount of FumC. However, this observation requires further experiments, but it reveals one crucial point. A method to quantify the loading of each enzyme onto the electrode is required in order to interpret and control the product/intermediates distribution in a cascade. Once the

loading efficiency of the other enzymes is known a tailored protocol for electrode preparation can be established.

4.6.6. Steady state kinetic data for ME, FumC and AspA

Solution assays monitoring the activity of ME, FumC and AspA were carried out and the resulting data (**Table IV-I** ;**Figure IV-16**) were used to interpret the results from varying the enzyme ratio. The buffer used for the downstream direction was 0.05 M HEPES, 4 mM $MgCl_2$, 1 mM $MnCl_2$, pH 7.5 (in the case of ME this was first saturated with CO_2 for 2 hours), while in the upstream direction the buffer used was 0.05 M MOPS, 4 mM $MgCl_2$, 1 mM $MnCl_2$, pH 7.5. For ME, A_{340} was used to monitor NADPH consumption and production (downstream and upstream, respectively). FumC and AspA catalysis was monitored looking at 250 nm (A_{250}) for fumarate formation (ε = 1.45 mM^{-1} cm^{-1}). In case of its consumption A_{250} was used for concentrations lower than 1 mM while for concentrations above 1 mM, A_{293} was used instead (ε = 0.082 mM^{-1} cm^{-1}).[243] The values $k_{cat(app)}$ and $K_{M(app)}$ were then used to calculate the specificity constant of each catalyst ($k_{cat(app)}/K_{M(app)}$) and their τ-values (1/ $k_{cat(app)}$) at high substrate concentration. The slower kinetic values of ME are detrimental for the upstream direction, because it does not compete with the fast kinetics of FumC and AspA. In the downstream direction most of the product of ME (malate) is directed to the final product (aspartate) because of the faster kinetics of FumC and AspA. For more discussion see Section 4.4.3.

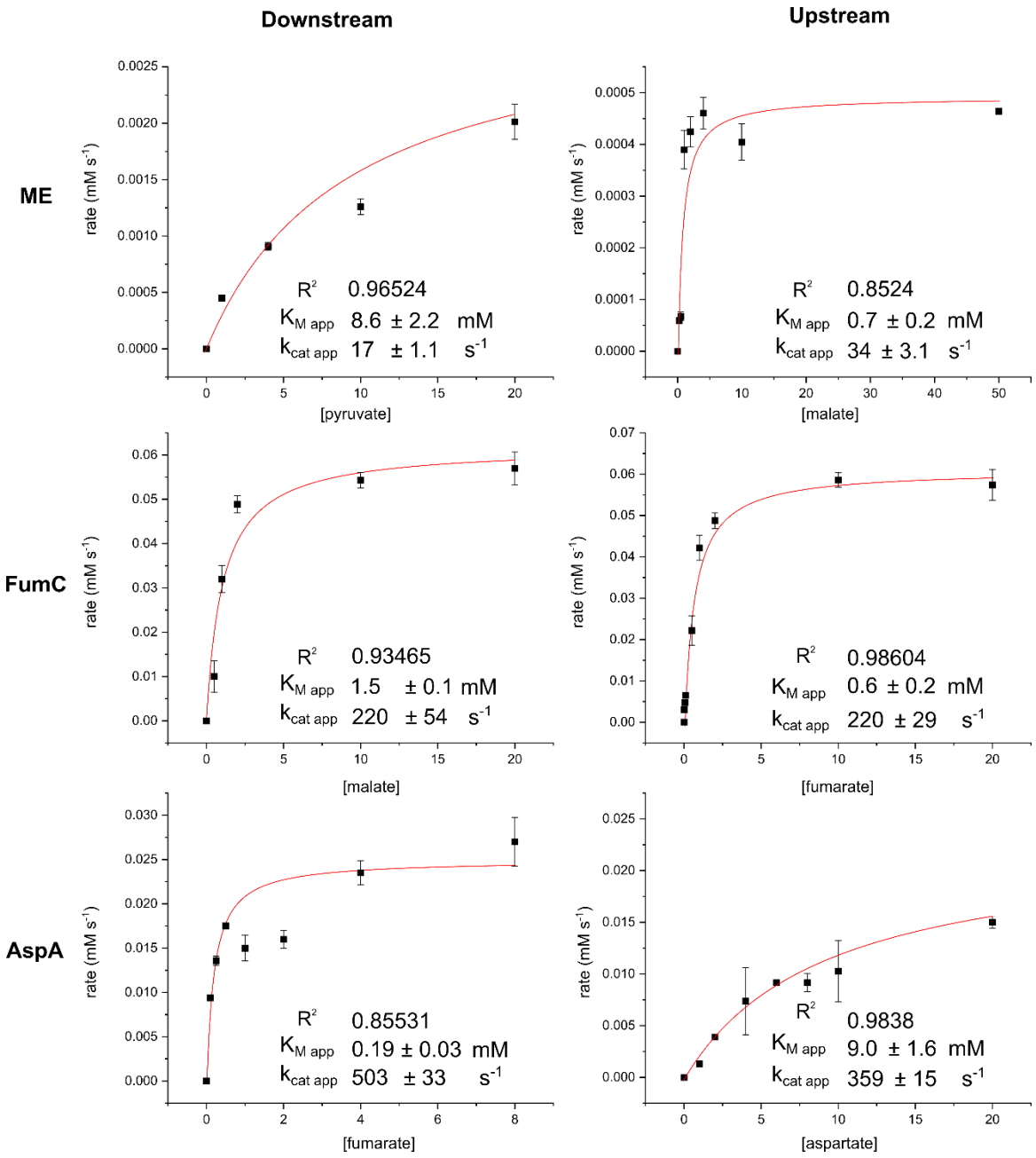


Figure IV-16. Steady state kinetic analysis of ME, FumC and AspA. Results of downstream and upstream directions by monitoring absorbance (340 nm for ME and 290/250 nm for FumC). [E] = ME, 0.1155 µM (downstream) and 0.01155 µM (upstream); FumC, 0.409 µM; AspA, 0.0584 µM. Substrate concentration in mM. Non-linear fitting of the data points (black points) was executed using the Michaelis-Menten equation and the Levenberg Marquardt iteration algorithm in Origin (software). The resulting curve is shown in red with the corresponding R^2 values.

4.6.7. Comparison between the electrified nanoconfined cascade and the cascade in solution

Comparison of the nanoconfined cascade with the same reaction in solution would be ideal to prove the advantage of confining cooperating enzymes together. A cascade composed of GOx and HRP (see Section 4.2) has been extensively exploited to design nanoconfined cascade systems. However, it is still under debate whether proximity of enzymes improves the catalytic rates. For instance, recently, Hess and co-workers challenged the main view that proximity enhances the rate of the short two-enzyme cascade system composed of GOx and HRP when entrapped on DNA scaffolds.[247,248] Establishing the advantage (if any) of nanoconfinement is normally straight forward when the scaffold serves solely as a support.

Comparison of the electrified nanoconfined cascade with the same cascade in solution is more complicated in this work, as the support does not only serve a purpose of confining the enzymes, but it is also the electron sink and acceptor for FNR. The ideal comparison would be to keep every parameter the same while masking either the electrode or the enzymes to prevent their binding to the nanopores. Our previous publication already proved nanoconfinement to be essential for our system: current was not observed when an E2, an alcohol dehydrogenase (ADH), was injected inside a dialysis membrane preventing it from binding to the FNR@ITO/Support electrode.[146] A slow growth in current was detected when the membrane was sliced open as the enzyme could then bind to the nanopores where FNR was entrapped.[146] Moreover, this Chapter proved that the cooperating enzymes have to be nanoconfined together to obtain a current (see **Figure IV-10**). Hence, nanoconfinement is crucial for this system.

Comparison of the electrified nanoconfined cascade with the same reaction carried out in solution *i.e.* without electrode, would be very interesting but challenging. The main problem is that we are not currently able to know the amount of enzymes that are actually absorbed on the electrode and more importantly how much of them are actively contributing to the current. In collaboration with Dr. Clare F. Megarity we attempted to draw a comparison. The upstream aspartate deaminative oxidation was monitored by looking at the absorbance at 600 nm in a cuvette (1 mL) containing 20 µM $NADP^+$, 0.05 M Benzyl viologen, 4 mM $MgCl_2$, 1 mM $MnCl_2$ and 0.05 M MOPS buffer (pH 7.5). Benzyl viologen (BV) reduction catalysed by FNR is necessary to regenerate the cofactor $NADP^+$ and reduced BV absorbs at 600 nm (in **Figure IV-17-A** the reaction scheme). The question arising was how much moles of enzymes to use in the solution assay. It is useful to remind the reader of the protocol for the preparation of the (FNR+E_n)@ITO electrode. A concentrated enzymes solution droplet (1 enzyme equivalent = 0.1 mM final concentration) was dropped on titanium or graphite and left at RT for 20 minutes. Note that the volume used for the titanium electrode was 20 µL while for graphite was 10 µL, hence 1 enzyme equivalent was defined as 2 nmol and 1 nmol was used for the graphite electrode. Thus, based on a 5/1/1/1 ratio (FNR/ME/FumC/AspA) a total number of moles of 16 nmol and 8 nmol was used on titanium and graphite, respectively. After 20 minutes the electrodes were thoroughly rinsed discarding most of the enzymes used. The same number of moles was used in the following solution assays in a volume of 1 mL. Upon injection of aspartate (to 20 mM) the rate of the reaction was extremely fast (data not shown). Dilution of the enzymes was then necessary to be able to obtain a rate from the experiments.

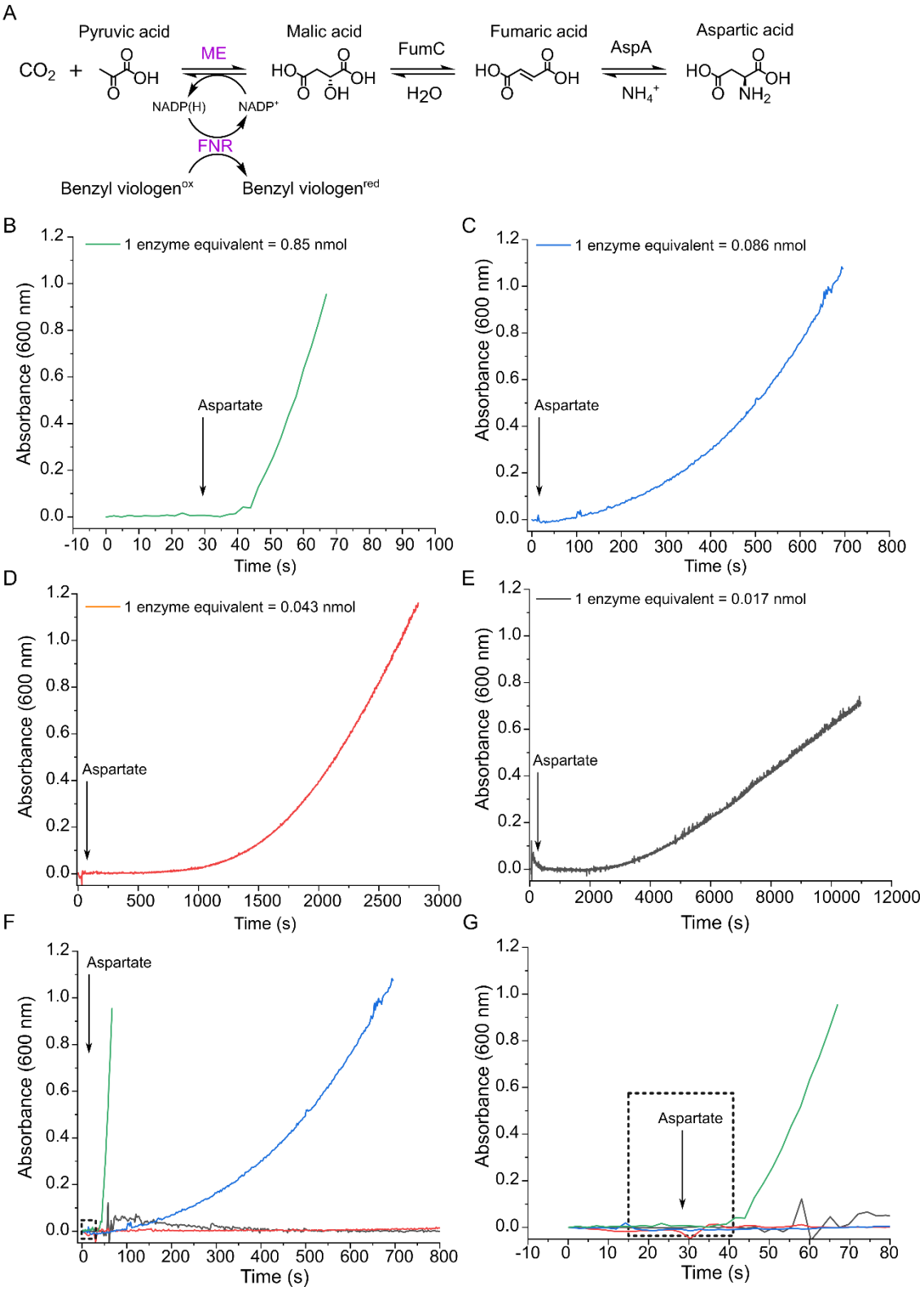


Figure IV-17. Solution assay of the 4-enzyme cascade monitoring the reduction of benzyl viologen and appearance of a lag. A. Scheme of the cascade in solution. Buffer (1 mL): 0.05 M MOPS, 4 mM $MgCl_2$, 1 mM $MnCl_2$, 20 µM $NADP^+$, 0.05 M BV. Aspartate injected to 20 mM. Ratio: 5/1/1/1 ratio FNR, ME, FumC, AspA. **B**. 1 enzyme equivalent: 0.86 nmol. **C.** 1: 0.085 nmol **D.** 1: 0.043. **E.** 1: 0.017 nmol. **F.** Comparison of the lag after injection of aspartate. **G.** Inset of Panel F. Figure adapted from Morello *et al.*[241]

Table IV-2. Comparison of the cascade performance with the enzymes free in solution.

		Total moles in droplet (nmol)	Rate (nmol cm^{-2} s^{-1})	Rate/total moles in droplet (s^{-1})	[Cascade] assuming 100% absorption (mM)	Rate molecules of product/minimal catalytic unity (s^{-1})	Length of lag after aspartate injection (s)
Echem	Figure IV-12	16	0.15	0.004	53.3	90	0*
	Figure IV-3-C	8	0.21	0.026	26.7	126	0*
		Total moles in 1 mL cuvette (nmol)	Rate (nmol s^{-1})	Rate/total moles (s^{-1})	[Cascade] (mM)		Length of lag after aspartate injection (s)
Solution assay	Figure IV-17-B	6.72	5.98	0.89	22.4	-	≈10 s
	Figure IV-17-C	0.672	0.421	0.67	2.24	-	≈75 s
	Figure IV-17-D	0.336	0.138	0.41	1.12	-	≈800 s
	Figure IV-17-E	0.134	0.0135	0.10	0.45	-	≈2200 s

Figure IV-12 refers to the blue trace (ratio 0.1/5/1/1/1): current density 28.3 µA/cm^2; in Figure IV-3-C an average current density of 40 µA/cm^2 was obtained (ratio 0.1/1/5/1/1). Total moles in droplet were calculate from 20 µL and 10 µL volumes containing FNR/ME/FumC/AspA where 1 = final concentration in droplet 0.1 mM and 5 = final concentration in droplet 0.5 mM. The rates (nmol cm^{-2} s^{-1}) were calculated by dividing the current density by 2*F* (Faraday constant). The rates in solution were calculated using the literature known ε at 600 nm of reduced BV (7.2 mM^{-1} cm^{-1})[249]. Minimal catalytic unity calculated from an assumed flat area of 10 nm x 10 nm which result in 10^{12} number of minimal unities in a 1 cm^2 electrode. Molecules of product (rate x Avogadro's number) were divided by the number of catalytic unities to obtain the rate based on molecules of product/minimal catalytic unity. *See Figure IV-18 for more details.

Figure IV-17 (**B to G**) shows the result of the experiment (designed by Dr. Clare F. Megarity and I, and carried out by Dr. Clare F. Megarity) and **Table IV-2** summarises the results. The experiments were carried out by diluting the enzyme stock solutions to decrease the 1 enzyme equivalent to 0.85, 0.086, 0.043 and 0.017 nmol, while maintaining the ratio 5/1/1/1 (FNR/ME/FumC/AspA). The enzymes were then injected into a volume of 1 mL. **Figure IV-17 (B to G)** shows the result of the experiment upon addition of aspartic acid. After a variable lag

period (dependent on the enzymes concentration) the rates observed were very high. For instance, the rates in the solution assays are between 100x to 4x higher than in the nanoconfined situation, by using as a comparison a current density of 40 μA/cm^2 (obtained with the graphite electrode) or 28.3 μA/cm^2 (obtained with the titanium electrode), after normalising the rates for the total moles of enzymes used (**Table IV-2**). However, this comparison is not realistic as it is impossible that all the enzymes dropped on the electrodes absorb in the ITO layer. If we consider an electrode of 1 cm x 1 cm x 3 μm, the volume, assuming that ITO is not occupying any space, would be 0.3 μL. Absorption of an undiluted droplet (total moles = 16 nmol) would result into a protein concentration of 53 mM or 160 mM (the latter assuming 1 μm thickness). Hence, the former solution would weigh 18 kg/L, which is an impossibility. Based on the moles of enzymes used in **Figure IV-17-B, to F** assuming a perfect absorption into an ITO layer of 3 μm, a concentrations of 22, 2.2, 1.4 and 0.45 mM would be obtained (**Table IV-2**).

It is important to point out that electro-catalysis occurs mostly in regions which are close to the electrode/solution interface. Hence, if we divide the electrode in catalytic units, only the units closest to the surface will actually participate to catalysis, while everything which is buried will be redundant.[250,251] An alternative calculation on the rate of the nanoconfined cascade is based on the target area model described in our previous publication.[146] If we describe our electrode as a collection of microelectrodes where the minimal unitiy is a flat surface of 10 nm x 10 nm (10^{12} minimal unities/cm^2) the electrochemical rate per minimal unities drastically changes (90 – 126 s^{-1}, as opposed to ≈ 1 s^{-1} for the fastest solution assay) and approaches 90x - 127x faster than the rates/moles of cascade in the solution assay (details in **Table IV-2**). Obviously, the calculation described above

is an assumption. However, an empirical data support that the nanoconfined cascade is actually behaving more efficiently than the cascade with enzymes free in solution.

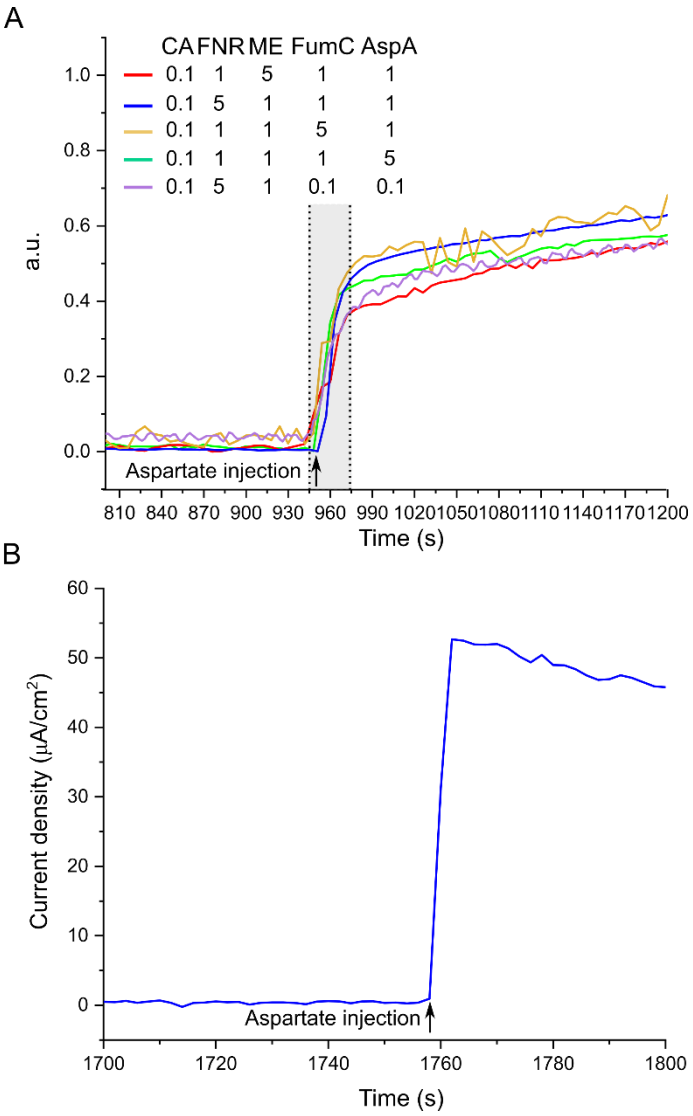


Figure IV-18. Effect of adding aspartate by using the electrified nanoconfined cascade: a lag period is not observed in the electrochemical experiments as opposed to the solution assays. A. Addition of aspartate (20 mM) in chronoamperometric experiments carried out with a titanium support as shown in **Figure IV-12**. Addition of aspartate causes an immediate spike (within seconds, grey area) reaching 40-60% of the maximum current, followed by a current growth (see Section 4.6.4.). The current was normalised (min = 0, max = 1). **B.** Addition of aspartate (20 mM) in chronoamperometric experiments carried out with a rotating graphite electrode (same experiment as **Figure IV-3-D**). Substrate injection causes an immediate increase in current. See original figures for the experimental conditions (**Figure IV-12** and **Figure IV-3-D**).

Figure IV-17 shows the appearance of a lag in the reaction rate upon injection of aspartic acid and the length increases with decreasing the enzyme concentration, as expected for an enzymatic cascade in solution (**Table IV-2**).[252] This situation is different from the electrochemical experiments where injection of aspartic acid causes an immediate response in the reaction rate, which accounts for ≈40-60% of the maximum current when using a titanium electrode, while for 100% for a graphite electrode (**Figure IV-18**). Hence, the lack of a lag period suggests that the nanoconfined cascade is effectively working extremely efficient, suggesting a high enzyme concentration and importantly proving the high retain of the intermediates within the nanopores.

4.7. Part 2: Conclusions

The second section of this Chapter sheds further light on the multi-step enzymatic cascade. Moreover, it emphasises the power of live monitoring. For instance, the role of CA was investigated: carbonic anhydrase was shown to be essential in the downstream reaction unless bypassed by using CO_2, while it did not influence the upstream reaction. The proposed technology is also very valuable for synthetic applications because of the tiny amounts of cofactor needed, resulting in high TTNs of ≈1000. Crucial for the catalytic efficiency of the system is the possibility to easily nanoconfine the enzymes within the electrode nanopores. No catalysis was observed if the enzymes were not deposited together in the same spot on the electrode. Hence, nanoconfinement of all enzymes in a single pore is crucial for activity.

A gradual current growth, after an immediate increase of current, was observed upon substrate addition in the upstream reaction. This growth did not occur when all the intermediates (aspartate, fumarate and malate) where injected to initiate the reaction. This may signify a substrate-induced activation and assembly of the metabolon, or the accumulation of the intermediates to achieve steady-state. It is still to verify why this gradual current growth was not observed in the rotation dependence experiments upon aspartate injection (Section 4.4.2., **Figure IV-3**) and why changing the pH to 8 increased the growth of current time more than three fold (to 4 h). Further experiments are needed to investigate the current growth in the downstream direction and the difference with the growth in the upstream direction *i.e.* why the current increase after buffer exchange in the downstream direction was instantaneous.

Changing the ratio of the enzymes had no effect on product distribution. The main information obtained was that FumC and AspA were not required in high amounts. For instance, in the upstream reaction E3 and E4 could be reduced by a factor of ten and still achieve similar conversions. More experiments could be envisaged to explain the unusual result obtained at pH 8. For instance, it will be required to study steady-state kinetics of all the enzymes at different pH values. Importantly the development of a method to quantify the loading of each enzyme loading is crucial for full interpretation of the data and for rational manipulation of the enzyme ratio in the electrode.

Quantification of the advantage of nanoconfining the enzymes was challenging because we cannot measure the amount of enzymes absorbed on the electrode (other than FNR) and because the scaffold (the electrode) acts also as an electrode sink. Hence, simply comparing the cascade in solution is not possible. We already proved nanoconfinement to be crucial for the catalysis observed with the Electrochemical Leaf.[146] The cascade with the enzymes free in solution appears to have superior rates by dividing the rates with the total moles of enzymes used. However, most of the enzyme used to prepare the electrode cannot absorb and it is mostly discarded. The increase of the lag time upon aspartate injection with decreasing the enzyme concentration in the solution assay is the strongest result to prove the advantage of nanoconfinement. In the nanoconfined electrified cascade a lag is not observed demonstrating that the cascade is effectively working very efficiently. However, the analysis above shows the importance of developing more efficient ways of loading the enzymes on the electrode. This issue is particularly important for the scaling-up of the Electrochemical Leaf.

The results of this Chapter show an unprecedented way of monitoring and energising any multi-step biocatalytic cascades for applications spanning from synthesis, biosensing and system catalysis. Studying a secondary model cascade in combination with the proof-of-concept described here will help in obtaining more information to explain observations such as the growth in current and the results of the variation of enzyme ratio. Any biocatalytic cascade could be connected to the Electrochemical Leaf provided that at least one step is NAD(P)(H)-dependent. As reported by Vidal *et al.* oxidoreductases constitute the largest class of enzyme and 50% of the oxidoreductases use NAD^+ and $NADP^+$. Hence, it is likely that any pathway under investigation could be connected to a cofactor-dependent step.[253]

Chapter V

5. Exploitation of the electrochemical leaf as a sensor for biocatalyst discovery and evolution

5.1. Abstract

The Electrochemical Leaf was exploited for a further application: developing a biosensor platform to screen biocatalysts for discovery and evolution. The results show that it is possible to use the nanoporous indium tin oxide (ITO) electrode loaded with ferredoxin $NADP^+$ reductase (FNR) to detect oxidoreductase enzyme catalysis from cell lysate with high specificity in the presence of low levels of $NADP^+$. The direct use of cell lysate avoids resources-consuming protein purification. As a proof of concept, *E. coli* BL21 was transformed with an inducible plasmid to overexpress the $NADP^+$-dependent malic enzyme (ME). This enzyme drives the reductive carboxylation of pyruvate to malate by using NADPH. By comparing induced and non-induced cell lysate it was observed that the proposed screening method detects ME activity from cell lysate with low background interference.

5.2. Introduction

Biocatalysis holds an immense potential for modern chemistry. Compared to traditional catalysis, the use of enzymes makes it possible to drive synthetically challenging reactions under mild conditions with high stereo- and regioselectivity and to perform one-pot multi-step catalysis.[254,255] A well-known example where biocatalysis had a beneficial impact for the pharmaceutical industry was the production of Stagliptin, for which an evolved biocatalyst achieved a final yield of 200 g L^{-1}, in 50% DMSO with an enantiomeric excess (*ee*) of 99.95%.[256] Oxidoreductases need a stochiometric amount of expensive nicotinamide cofactor (NAD(P)H) as electron donor and acceptor for catalysis. Hence, a cofactor regeneration method is required (see Section 1.5.).[104] Several oxidoreductases are already involved in the synthesis of various drugs in industry. For example, ketoreductase (KRED) has replaced its traditional catalysis counterpart for the synthesis of the cholesterol-related drug Lipitor. Furthermore, KRED has been used for the synthesis of intermediates in drug production by companies like Codexis and Pfizer.[101] Biocatalyst discovery and evolution is a crucial step to tailor these enzymes for industrial applications.

Directed evolution was developed by Nobel Laureate Frances Arnold and has had a huge impact on biocatalysis, as it facilitates the discovery and design of customized enzymes. Certain enzyme properties such as thermostability, enantioselectivity and cofactor specificity can be changed and improved through protein engineering.[95,97,170] Directed evolution – just like natural evolution – is based on many cycles of random mutations to be introduced into the open reading frame (ORF) of a gene coding for the desired protein. Error-prone PCR[257] (epPCR) or DNA shuffling[258] are examples of how to introduce mutations. In epPCR, the

mutation rate of a low fidelity DNA polymerase, such as Taq polymerase, can be increased by using Mn^{2+}, imbalanced amounts of Mg^{2+}, or by introducing modified deoxynucleotide triphosphates (dNTPs) which all decrease the base-pairing fidelity.[96,257] DNA shuffling is based on fragmenting the ORF with DNase and using the generated fragments as primers in a standard PCR reaction: it was the first method to be developed for directed evolution based on large DNA recombination.[96,258] Currently, generation of large mutant libraries is not the bottleneck, because the required elements to introduce mutations such as synthetic primers are all readily available.[94,259] Several methodologies for library generation have been reported and can be tailored for each individual project.[96] The mutated sequence is normally introduced into an organism, typically a bacterium, for expression.[94] Methods to perform bacterial expression-free evolution are also under investigation.[260,261] Regardless of the chosen method, the introduced random mutations generate a very high number of protein variants and the key for successful evolution is having a quick way to discriminate each variant. The challenge is then to pick the improved version for a specific trait from a plethora of inactive and unaffected protein variants (the number of possible combinations are 20^{100} for a small protein containing 100 amino acids).[94] Therefore, the success of such experiments highly depends on the availability of a fast and efficient screening method.[218]

Several screening technologies have been proposed. The simplest screening is based on picking single colonies (*e.g.* directly on an agar plate). However, this screening method is limited to the necessity of directly linking the protein variant's properties to the survival of the organism used for expression.[96,262] Fluorescence-activated-cell-sorting (FACS) is usually the method of choice where a fluorophore

is the substrate of a mutated protein variant: in this case, the use of cell-display technologies such as yeast display (fusing the mutated protein variants to the C-terminal of *S. cerevisiae*-mating adhesion receptor, Aga2) allows for high throughput screening.[96,263] However, this method is very challenging when applied to enzyme catalysis which does not involve fluorophores.

Bornscheuer *et al.* discussed in a review from 2019 that "*For enzyme catalysis, the challenge of high-throughput screening to efficiently explore the natural protein sequence is still unsolved today*."[94] Despite the development of methods to reduce the size of the mutant library (by designing a "rationalized" evolution), the potential of improvement is not fully explored.[94] Oxidoreductases are of great interest for industrial purposes.[264] However, a screening method to rapidly detect their activity is lacking and mainly depends on tracking changes in absorbance of their cofactor at 340 nm, which provides a measure of NAD(P)H production or consumption. This process is time consuming and requires high amounts of protein and expensive cofactor.[265] Moreover, a high background is usually obtained if protein purification is not performed after each expression step during directed evolution. Note that protein purification after each step should be avoided because it would make the screening unfeasible. Therefore, cell lysate should be used instead. Another screening strategy for oxidoreductases is based on the reaction of NADPH with nitroblue tetrazonium and phenazine methosulfate to generate a blue-product, formazan, detectable at 580 nm.[266–268] This protocol was first reported by Mayer and Arnold in 2002. However, this methodology has not been widely used, either in the industrial or academic world. Another possible screening method is based on product detection using HPLC/MS or GC. These methods are very sensitive, but the major drawbacks are (i) small library size and (ii) long time for each

evolution cycle (1.5 to 16 h to assess each clone by measuring the product at each stage of evolution). Nevertheless, cytochrome P450 has been successfully evolved with HPLC/GC-based methods to catalyse enantioselective cyclopropenation of internal alkynes, carbene chemistry and oxidation of silanes to silanols.[269–272] A screening platform for almost instantaneous detection of the reaction rate would make it possible to select from a much larger number of mutants.

Oboyiki *et al*. developed an electrochemical system for the detection of NAD(P)H using a boron-doped diamond (BDD) electrode, to drive the oxidation of the reduced cofactor upon application of a large applied potential (+0.6 V vs. Ag/AgCl).[265] The same group extended the concept in 2020 to develop a microfluidic directed evolution method, using the BDD electrode. A microfluidic device made it possible to reduce the volume of the sample to 30 nL. As a proof of concept, they applied their method to the directed evolution of dehydrogenases, such as alcohol dehydrogenases (ADH) and isocitrate dehydrogenases (IDH).[260] The authors did not mention the possibility of studying the reverse reaction (reduction direction).[260,265] A probable explanation could be that the large overpotential required would generate mainly the inactive form of the reduced cofactor (see Section 1.5.4.).

In this Chapter, I am proposing a new application for the electrochemical leaf to detect the activity of any NAD(P)H dependent enzyme for oxidation and reduction with extreme specificity and minimal background signals. The Electrochemical Leaf is an electrochemical technology based on a nanoporous indium tin oxide (ITO) electrode within which the enzyme ferredoxin $NADP^+$ reductase (FNR) is entrapped (see Section 1.6.1.).[90,134,139,144–146,179] This enzyme catalyses NADPH interconversion when a potential is applied (see Section 1.6.2.).

When a second NADP(H)-dependent oxidoreductase (E2) is added to the system, it also enters the pores of the electrode and a large catalytic enhancement occurs because diffusion distances of substrates are minimised and the effective concentration of each enzyme may be massively increased (see Section 1.6.3.). In this Chapter, I have investigated whether it is possible to use cell lysate to detect the rate of an overexpressed oxidoreductase (E2) directly as electrical current without too much background noise. Thanks to the high reversibility of the system it should will be possible to investigate the dehydrogenase reaction in either direction, in contrast to the systems reported above.

5.3. Aim of the Chapter

This chapter describes a novel application for the Electrochemical Leaf as a platform for enzyme screening. As a proof of concept, untreated cell-lysate containing malic enzyme (ME) (see Chapter II) was injected directly to the electrochemical cell. The system was studied in the reductive direction (reductive carboxylation of pyruvate to malate using NADPH). The chapter discusses the sensitivity of the system and future perspectives.

5.4. Results and Discussion

The Electrochemical Leaf makes it possible to detect the rate of any oxidoreductase as an electrical current as shown in Section 1.6, Chapters II and IV. As such, it holds great promise to be exploited as a sensor for biocatalysts discovery; several reaction conditions can be changed and the difference in catalysis immediately detected on screen. The results shown in this paragraph investigate whether cell-lysate from bacteria overexpressing a certain dehydrogenase can be used directly instead of injecting pure enzyme.

To demonstrate the proof of concept, *E. coli* BL21 cells were transformed with *pLATE51:maeB* (plasmid encoding for ME, see Section 2.4.1). Single colonies were grown in LB media (20 mL) supplemented with ampicillin. Isopropyl-β-D-1-thiogalactopyranoside (IPTG) was added (to 0.5 mM) to induce expression of ME. A parallel control flask was not induced. Cells were then harvested, resuspended in cell lysis buffer (1 mL, pH 7.5, see Chapter VII) and lysed by sonication. The lysates were then frozen at -80°C and used in the next experiments. As a result, one lysate was obtained containing overexpressed ME (from the IPTG-induced cells), and another lysate was obtained without overexpressed ME. **Figure V-1** summarizes the protocol.

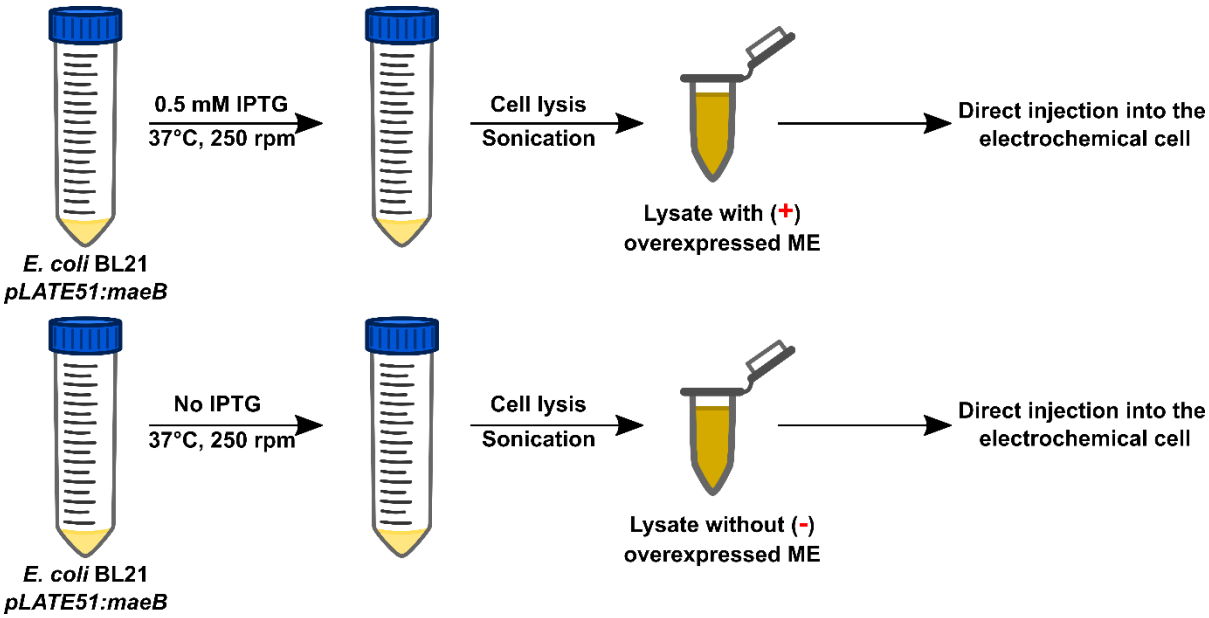


Figure V-1. Preparation of enzyme lysates for use in the electrochemical screens. *E. coli* BL21 transformed with *pLATE51:maeb* to overexpress the malic enzyme (ME) was grown in 20 mL LB supplemented with ampicillin (to 100 µg mL^{-1}). After 3 h of growth (37°C, 250 rpm) IPTG (to 0.5 mM) was added to one test tube. Another tube was left growing in the same conditions for a further 3 h (37 °C, 250 rpm). Cells were harvested (3000 rpm), resuspended in lysis buffer (1 mL), disrupted by sonication and the lysates (with overexpressed, + ME, without overexpressed, –ME) were then frozen at –80°C.

Figure V-2 shows the result of the chronoamperometry experiment (–0.45 V vs. SHE, 25°C, stirring, under continuous flow of CO_2) carried out in a three-compartment cell. The FNR@ITO/Ti electrode (1 cm^2) was prepared by dropping 5 µL of FNR (1.8 mM) on the nanoporous ITO electrode: it was then inserted into a CO_2-saturated buffer (pH 7.5, 2.5 mL) containing 0.2 M HEPES, 0.1 M $KHCO_3$, 4 mM $MgCl_2$, 1 mM $MnCl_2$, 80 mM pyruvate and 20 µM $NADP^+$. Initially a background current, related to $NADP^+$ reduction was observed, then an increasing prominent response was observed upon each injection of the cell lysate from induced cells (thus containing overexpressed ME). The initial current spike due to O_2 is followed by a slow increase in current that is attributed to ME entering the pores of the electrode (see Section 2.4.2.5). A large reductive current of 22 µA/cm^2 was finally obtained after having injected a total of 100 µL of induced-cell lysate.

That current corresponds to the rate of the reductive carboxylation of pyruvate to malate driven by ME that has entered the pores (see Chapter II).

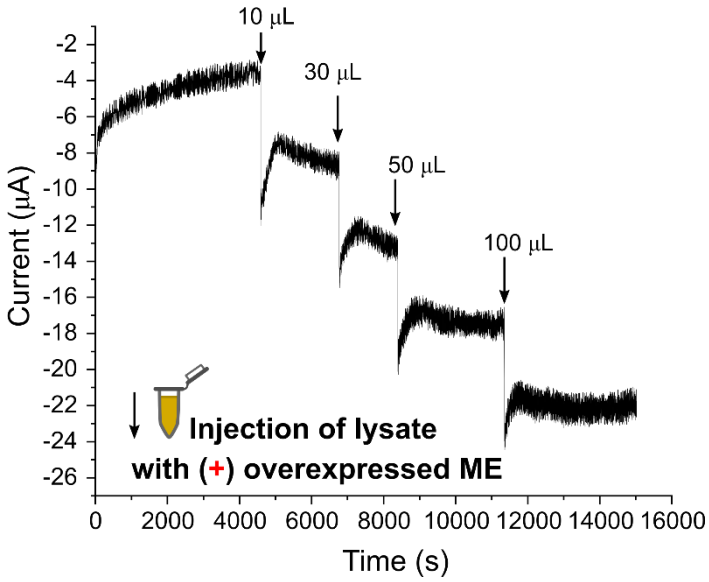


Figure V-2. Detection of ME activity from cell lysate. Chronoamperometry (–0.45 V vs. SHE, 25°C, stirring, under CO_2 purging) carried out with a FNR@ITO/Ti foil electrode (1 cm^2) in a CO_2 saturated buffer (2.5 mL, pH 7.5) containing 0.2 M HEPES, 0.1 M $KHCO_3$, 4 mM $MgCl_2$, 1 mM $MnCl_2$, 20 µM $NADP^+$, 80 mM pyruvate. Arrows signify injection of different volumes of lysate containing overexpressed ME (+). Three-compartment cell; RE: Ag/AgCl; CE: Pt.

The cell lysate contains a multitude of other metabolites, proteins and nucleic acids that could contribute to the electrochemical signal. Thus, further experiments were required to ensure that the signal was due to the reactions under investigation. In the first control, the experiment described above was repeated using lysate obtained from non-induced cells (ME not overexpressed). Results are shown in **Figure V-3**. A chronoamperometry experiment was carried out and non-induced cell lysate was injected as before. The electrochemical response in **Figure V-3** is very different to that shown in **Figure V-2**, most obviously because no reductive current is observed upon lysate injections apart from the spikes due to oxygen.

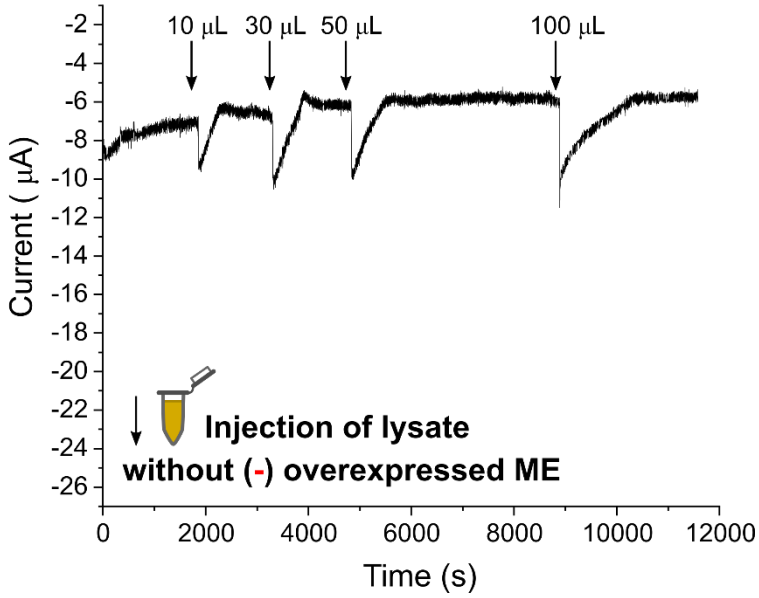


Figure V-3. Control: injection of cell lysate without overexpressed ME. Chronoamperometry (–0.45 V vs. SHE, 25°C, stirring, under CO_2 purging) of a FNR@ITO/Ti foil electrode (1 cm^2) in a CO_2 saturated buffer (2.5 mL, pH 7.5) containing 0.2 M HEPES, 0.1 M $KHCO_3$, 4 mM $MgCl_2$, 1 mM $MnCl_2$, 20 µM $NADP^+$, 80 mM pyruvate. Arrows signify injection of different volumes of lysate without overexpressed ME (-). Three-compartment cell; RE: Ag/AgCl; CE: Pt.

Another control was carried out to ensure the current was related to the reductive carboxylation reaction: induced lysate (with overexpressed ME) was used in a buffer without the substrate of the reductive carboxylation reaction (pyruvate). Results are shown in **Figure V-4**. The induced cell lysate (with overexpressed ME) was used in a new chronoamperometric experiment (–0.45 V vs. SHE, 25 °C, stirring, under continuous flow of CO_2) in a buffer containing 0.2 M HEPES, 0.1 M $KHCO_3$, 4 mM $MgCl_2$, 1 mM $MnCl_2$, 20 µM $NADP^+$. Note that pyruvate was *not* included. Injections of cell lysate did not cause any increase in current, in contrast to what was observed in **Figure V-2**. The slow decrease in current is likely due to $NADP^+$ reduction at the FNR@ITO/Ti electrode. Finally, addition of the substrate of the reaction (pyruvate, to 80 mM) initiated a large

reductive current (current density, as before ≈ 22 µA/cm^2). The three experiments together prove that (i) the current enhancement observed was related to ME activity detected from cell lysate and (ii) background current related to unspecific oxidoreductases or metabolites from cell lysate was not present at this stage.

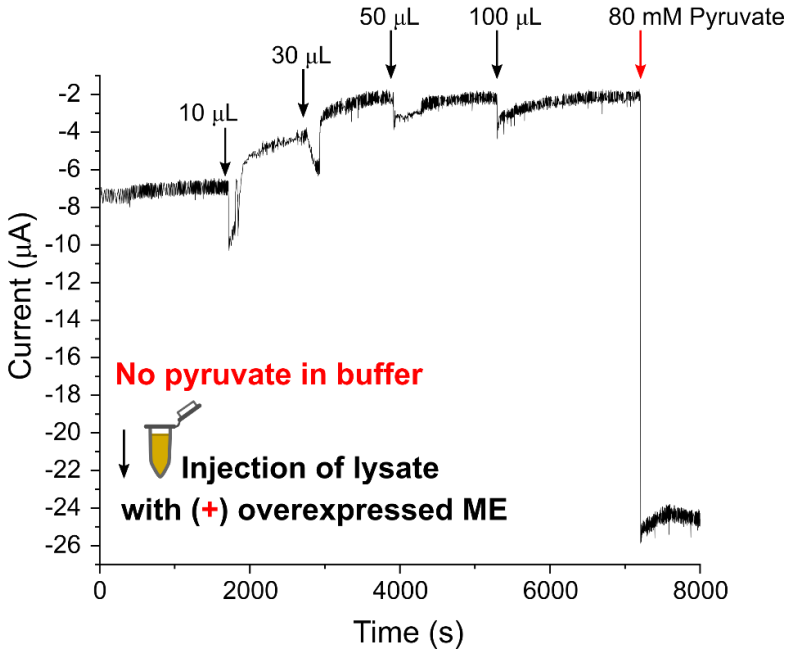


Figure V-4. Control: injection of cell lysate with overexpressed ME in a buffer lacking pyruvate. Chronoamperometry (–0.45 V vs. SHE, 25 °C, stirring, under CO_2 purging) of a FNR@ITO/Ti foil electrode (1 cm^2) in a CO_2 saturated buffer (2.5 mL, pH 7.5) containing 0.2 M HEPES, 0.1 M $KHCO_3$, 4 mM $MgCl_2$, 1 mM $MnCl_2$, 20 µM $NADP^+$. Arrows signify injection of different volumes of lysate with overexpressed ME (+). Injection of pyruvate (to 80 mM). Three-compartment cell; RE: Ag/AgCl; CE: Pt.

5.4.1. Further results

The paragraph above shows that it is possible to detect an overexpressed oxidoreductase of interest from cell lysate. In all the experiments described, cell lysates were obtained by growing *E. coli* in a 20 mL test tube. Ideally, the volume of 20 mL should be decreased for screening experiments. For this purpose, preliminary work was carried out to decrease the culture volume used to generate cell lysates. Cells were grown as in **Figure V-1** and the cell culture volume was decreased to 10, 5, 2 and 1 mL. **Figure V-5** shows the results of using induced-cell lysate (containing overexpressed ME) obtained from 10 mL of culture. The chronoamperometry (–0.45 V vs. SHE, 25 °C, stirring, under continuous flow of CO_2) was carried out in CO_2-saturated buffer containing 0.2 M HEPES, 0.1 M $KHCO_3$, 4 mM $MgCl_2$, 1 mM $MnCl_2$, 80 mM pyruvate and $NADP^+$ was added to reach a final concentration of 20 µM. Injection of 160 µL of induced-lysate initiated a reduction reaction, proving that growing 10 mL of cell culture is enough to detect a large catalytic signal. Preliminary results with lower volumes did not give positive results, but the experiments were only performed once so further experiments are needed. Obviously, the volume required for the signal depends also on the expression levels of the enzyme under investigation. Hence, it is not a generalizable concept. Moreover, it is important to notice that the volume used for the experiment (2.5 mL) is large for screening experiment as upon injection, the cell lysate was diluted 26X.

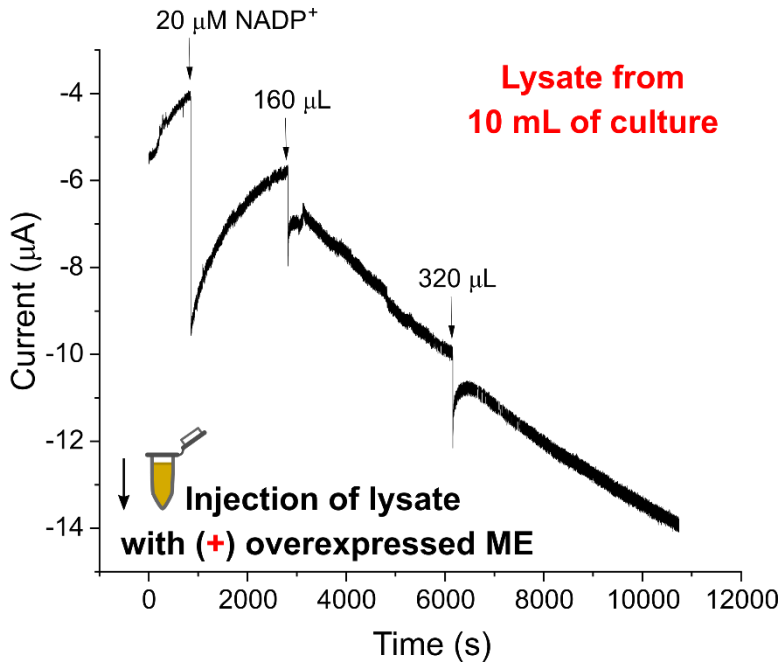


Figure V-5. Detection of ME activity from cell lysate (10 mL culture). Chronoamperometry (–0.45 V vs. SHE, 25 °C, stirring, under CO_2 continuous flow) of a FNR@ITO/Ti foil electrode (1 cm^2) in a CO_2 saturated buffer (2.5 mL, pH 7.5) containing 0.2 M HEPES, 0.1 M $KHCO_3$, 4 mM $MgCl_2$, 1 mM $MnCl_2$, 80 mM pyruvate. Inection of $NADP^+$ to 20 µM. Arrows signify injection of induced-lysate with overexpressed ME (+). Lysate was obtained from 10 mL culture of *E. coli* BL21 (*pLATE51:maeB*). Three-compartment cell; RE: Ag/AgCl; CE: Pt.

Another useful application would be to use the Electrochemical Leaf-based sensor to screen metabolites. **Figure V-6** shows the related experiment. An FNR@ITO/Ti electrode (1 cm^2) was prepared and inserted into a CO_2-saturated buffer containing 0.2 M HEPES, 0.1 M $KHCO_3$, 4 mM $MgCl_2$, 1 mM $MnCl_2$. Then $NADP^+$ was injected to a final concentration of 20 µM and *purified* ME to a final concentration of 2.5 µM. After 2 hours, non-induced cell lysate (from 20 mL of cell culture) was injected into the electrochemical cell (note that 2 h is the optimal binding time of ME under these conditions, as discussed in Section 2.4.2.5.). The experiment shows that upon injection (i) there is a very small and stable increase of current (after injection of 300 µL), which suggests a catalytic response even if

pyruvate was not included, (ii) the response is very low, but the reaction volume used (2.5 mL) was too large to draw any conclusion. It is important to repeat that the cell lysate was diluted 26X upon injection of 100 µL and 9.3X after 300 µL. Therefore, it is necessary to dramatically decrease the reaction volume to < 100 µL.

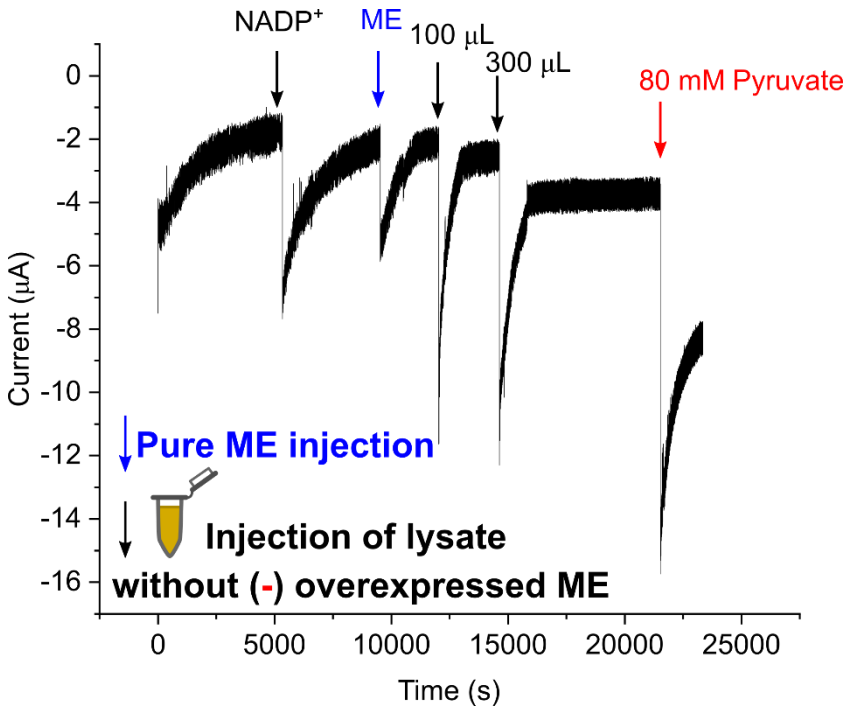


Figure V-6. Detection of metabolite (pyruvate) from cell lysate (20 mL culture). Chronoamperometry (-0.45 V vs. SHE, 25 °C, stirring, under CO_2 continuous flow) of a (FNR+ME)@ITO/Ti foil electrode (1 cm^2) in a CO_2 saturated buffer (2.5 mL, pH 7.5) containing 0.2 M HEPES, 0.1 M $KHCO_3$, 4 mM $MgCl_2$, 1 mM $MnCl_2$, 20 µM $NADP^+$. Arrows signify injection of $NADP^+$ to 20 µM, of pure ME (to 2.5 µM) and of non-induced lysate (20 mL cell culture, without overexpressed ME). Final injection of pyruvate (to 80 mM). Three-compartment cell; RE: Ag/AgCl; CE: Pt.

A preliminary attempt to develop a miniaturized sensor, using another dehydrogenase (ADH, W110A variant)[148], is shown in **Figure V-7**. This time the ITO was electrophoretically deposited on a screen-printed carbon working electrode (PalmSens), then, FNR was introduced by dropcasting a concentrated enzyme solution (10 µL, 1.8 mM), incubating for 3 minutes and rinsing with MQ-H_2O. The chronoamperometric experiment (+0.1 V vs. SHE, air, stationary) was carried out in a buffer (pH 8, 100 µL) containing 0.2 M TAPS, 10 mM S-(+)-4-phenylbutanol. After injecting NADPH to a final concentration of 20 µM, addition of ADH (to 0.3 µM) initiated the growth of an oxidative current. The signal was unstable over time, possibly due to evaporation, and this and other factors will need further investigation.

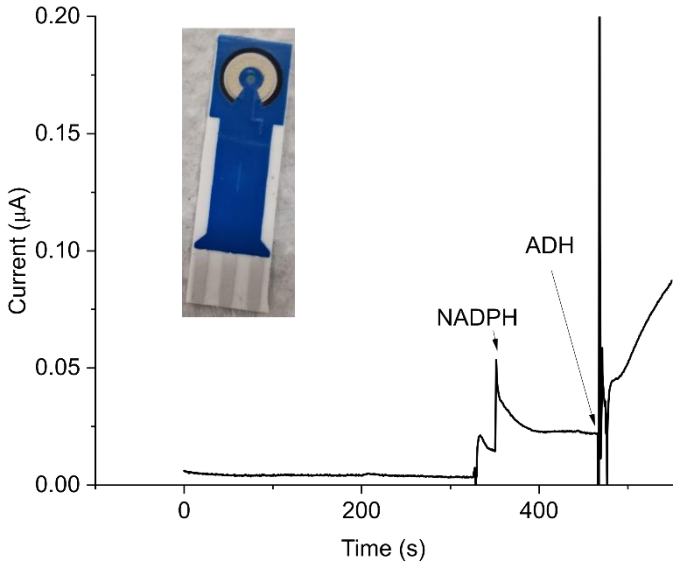


Figure V-7. Trial experiment to examine feasibility of producing a miniaturized sensor: ADH-driven oxidation of S-(+)-4-phenylbutanol by using a screen-printed electrode loaded with FNR. Chronoamperometry: +0.1 V vs. SHE, RT, air, stationary. Buffer: 0.2 M TAPS (pH 8), 10 mM S-(+)-4-phenylbutanol. NADPH injected to 20 µM; ADH to 0.3 µM. WE: (FNR+ADH)@ITO/carbon; RE: Ag/AgCl; CE: Pt.

5.5. Conclusion and future perspective

The results shown in this chapter demonstrate for the first time the possibility of using cell lysates to detect enzyme activity with the Electrochemical Leaf. There are interesting implications for designing a sensor platform for biocatalyst discovery. Using cell lysate can be very valuable, to avoid time- and resources-consuming protein purification. Given the complexity of the injected solution it was necessary to demonstrate the specificity of the signal. Encouragingly, it was shown that the catalytic enhancement observed was due to the oxidoreductase under investigation (ME) and unspecific signals with the current experiment conditions were not detected.

It might now be possible to design high-throughput arrays for sensing enzymes and metabolites that are more efficient and quantitative than those currently used. Such an array (scalable to any size of multi-well array) could be used for screening both cell lysate and pure enzymes. Each well volume would need to be relatively small (< 100 µL) and contain a three-electrode system: as WE, ITO/support such as Ti or carbon, as RE, Ag/AgCl and as CE, Pt or carbon. Once the system has been miniaturized, the specificity of the system will have to be re-investigated (*i.e.* background current upon lysate injection ≈ 0). Importantly, it will be necessary to investigate whether quantitative or semi-quantitative information can be obtained. **Figure V-8** explains the concept of a multi-well array to monitor enzyme activities live with high throughput screening of enzyme variants. Preliminary results on miniaturization showed that ITO can be easily electrophoretically deposited on the WE of a screen-printed electrode (PalmSens). With the resulting device, (*purified*) ADH-driven oxidation of *S*-(+)-4-phenylbutanol

was successfully detected by chronoamperometry (+0.1 V vs. SHE, air) in a total volume of 100 µL.

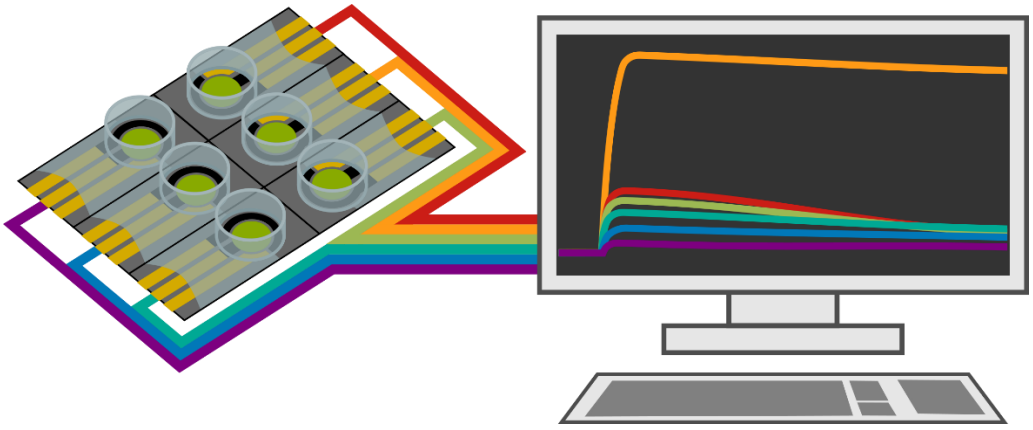


Figure V-8. Concept of high-throughput screening based on the electrochemical leaf. The development of a scalable multi-array of electrodes with a small volume (20–100 µL) would make it possible to build an extremely sensitive system for enzyme and metabolite screening. The ability to monitor the rate of the reactions live on screen would allow optimization in seconds/minutes, rather than within the current timescale of hours.

The results obtained for cell lysate are not only relevant for biosensing purposes. Usage of lysate for synthesis purposes would also dramatically decrease the cost of a hypothetical process, as purification is normally expensive and time consuming. This advantage could facilitate the implementation of the technology outside academia, because use of lysate for biocatalytic reactions is a common practice in industry.[273] The data shown here are encouraging but further experiments in big scale are required for deeper studies.

Chapter VI

6.1 Conclusions

The Electrochemical leaf was first developed in 2016 in the Armstrong group in Oxford. Since then, it was clear that the technology based on the nanoporous ITO electrode with ferredoxin $NADP^+$ reductase (see Section 1.6), could serve as a powerful platform to perform organic synthesis by coupling FNR with a secondary dehydrogenase (E2).[134,141] The system's high efficiency and total turnover number was demonstrated electrochemically (in this work and in other publications by our group)[134,139,146], by using hydrogen/air[144,145] and light (in this work)[90] by using a variety of E2 such as glutamate dehydrogenase (GLDH)[134,139,144], alcohol dehydrogenase (ADH)[145,146], reductive aminase (RedAm)[146], imine reductases (IRED)[146] and malic enzyme (this work)[90]. When large scale experiments were performed with GLDH[134,139,144], ADH[145], RedAm (not published) and ME (this work)[90] the total turnover number ([product]/[$NADP^+$], TTN) was between 10^3 - 10^4. The high TTN demonstrates the applicability of the system to drive biocatalysis via cofactor regeneration. Compared to most reported cofactor regeneration systems, the Electrochemical Leaf needs a very small amount of cofactor (typically between 1 to 20 µM) and no co-substrate (see Section 1.5.3.).

Results of this thesis and of Megarity *et al.*[146] showed that nanoconfinement of FNR and E2 is the crucial element which ensures the high catalytic efficiency of the electrode-protein composite. Through nanoconfinement, a principle crucial in Biology, diffusion distances of cofactor are minimized and enzyme concentrations massively increased. The favourable conditions offered by the electrode were then crucial in this thesis to construct a light-driven system with high-faradaic efficiency (using H_2O as electron donor) for the reductive carboxylation of pyruvate to malate to mimic oxygenic photosynthesis.

This thesis also demonstrated for the first time, the extension of the biocatalytic reactions coupled to FNR. A five-enzyme cascade was successfully nanoconfined, driven and controlled using the Electrochemical Leaf proving that it should now be possible to drive and monitor any natural or artificial cascade within the electrode nanopores provided that one step is NADP(H)-dependent. FNR becomes the “device” which translates the chemical flow of long cascades into an electrochemical flow. Any cascade could then be monitored live on screen, by observing the electrical current, which corresponds to the rate of the reaction. Obviously, crowding of the enzymes in the pores becomes even more important in a long cascade: diffusion of intermediates is minimized and enzyme concentration approaches millimolar. Hence slow kinetic steps can be compensated, as happens in biology, by increasing the amount of enzyme; then, the enzymatic rate could compete with the rate of escape of the intermediate needed from a slow reaction (large τ-value, see Section 4.4.3). The applications go beyond one-pot synthesis via cofactor regeneration technology; the Electrochemical Leaf can be a platform for single biocatalyst discovery and evolution if miniaturized (from pure enzyme or from cell lysate), for the optimization of system catalysis and for its fundamental investigation.

6.1.1 Introduction of the malic enzyme in the electrochemical leaf

In Chapter II a NADPH-dependent reductive carboxylase, malic enzyme (ME) from *E. coli,* was coupled with FNR within the nanopores of the ITO electrode to drive the reductive carboxylation of pyruvate to malate. Very efficient catalysis occurred as a result of ME nanoconfinement. The thermodynamics to drive the process was very favorable as CO_2 reduction occurred at a potential 0.1 V more

positive than H^+ reduction and catalysis was observed even at low CO_2 levels (half of V_{max} observed at 4% CO_2). High TTN were obtained with the (FNR+ME)@ITO/Ti electrode: 880 (with 20 μM $NADP^+$) and 6210 (with 1 μM $NADP^+$). Importantly, Chapter II shows a unique way of optimizing the reaction conditions to achieve stability of the system (see Section 2.4.2.1.) via live monitoring of the rates, which was the key to obtain the results described above.

6.1.2 The light driven reductive carboxylation

In Chapter III the reductive carboxylation via cofactor recycling was driven with light and water by using as photoanode 2%Mo:$BiVO_4$/FeOOH. The results of the Chapter point out the importance of developing a material with the energetics straddling the potential of the C3/C4 couple (pyruvate/malate) to achieve high faradaic efficiency (FE). A high FE of 70% for the C3/C4 reaction and 300 TTN were obtained by connecting the photoanode to a 0.5 V Si solar cell and to the (FNR+ME)@ITO/Ti cathode. The TTN value is 1-2 times higher than any light-driven cofactor regeneration reported to date. There is an inverse relation between applied potential and faradaic efficiency (75 ± 8%, 50 ± 6 and 33 ± 10 at 0.5 V, 0.8 V and 1 V applied bias). Hence, provided that the photoanode could generate photocurrent at smaller applied potential (< 0.5 V) it is predictable that the smaller the potential applied, the more the FE value would increase.

6.1.3 Wiring nanoconfined cascades: a five-enzyme cascade

Chapter IV shows that the nanoporous ITO electrode is suitable to drive multi-step cascade reactions. The possibility of monitoring given by the direct electron transfer between ITO and FNR allows for the detection of the rate of such multi-step reactions at each time point in a reaction. As a proof of concept, the

reversible amination of pyruvate to aspartate using a mixture of five enzymes was investigated. The position of FNR and E2 (*E1-E2 pair*) influences the information the cascade provides. Downstream and upstream terminologies were used to describe two extreme situations; where downstream, the E1-E2 pair is the first component of the cascade while upstream the last. Obviously, several other possibilities can exist for other cascade possibilities. It was observed that downstream the final product aspartate was the main product (accounting for 80%), while upstream this was not the case and a large escape of malate occurred (final product, pyruvate, was only 20%). By entrapping all the catalysts within the electrode nanopore, the result is the formation of a crowded environment which likely decreases the chance of escape of an intermediate. Attempts to change the product distribution were not successful as it was rationalized that the concentration of ME should be at least > 20X to compete with the rate of escape of malate. The discrepancy of the τ-values ($1/k_{cat}$) for ME with the assumed rate of escape of an intermediate of the reaction suggests the importance of crowding. Importantly, any natural or artificial cascade reaction can be directly “plugged in” to the ITO electrode for synthesis, biosensing and the study of system catalysis.

6.1.4 Exploitation of the electrochemical leaf as a sensor for biocatalyst discovery and evolution

Chapter V showed that the electrochemical leaf can detect enzyme catalysis from cell lysate with very low background signal: a specific and high response was obtained when all the components for the reaction under investigation (the reductive carboxylation of pyruvate to malate driven by ME) were present, while

the signal was negligible when the reaction mixture was lacking one component needed for ME catalysis. Thus, this platform could be very useful for rapid and high-throughput screening of enzyme variants for discovery and directed evolution. The use of cell lysate can be very valuable also for synthesis as it could decrease drastically the cost of a hypothetical process.

6.2 Future perspectives

6.2.1 Concentration of E2, E3 and product inhibition

In this thesis it was observed that a mixture of enzymes, not only FNR, can be entrapped within the electrode nanopore. While we can measure the amount of adsorbed FNR (see Sections 1.6 and 7.1.5.), the amount of adsorbed coupled enzymes (E2, E3, *etc.*) is currently not known. Developing a method for calculating the amount of adsorbed coupled enzymes, could be very valuable for kinetic measurements, for simulations and for controlling the effective ratios in a cascade reaction (see Section 4.6.6.). Moreover, availability of a method could also help to study the binding of the coupled enzyme to the ITO layer and the reasons why some enzymes bind better than others. In an hypothetical protocol, after incubating the electrode with the enzyme/s mixture and subsequent rinsing, the recovered solution could be analysed by Bradford method or fluorescence methods; the latter offer higher sensitivity (from 10 ng/mL[274], while Bradford from 1 µg/mL[275]) hence fluorescence is more suitable for this work.[274] The challenge is technical rather than intellectual to ensure reproducibility of the results; the loading of the enzyme will be influenced by several factors such as (i) the volume of enzyme mixture dropped/surface of electrode ratio, (ii) method (and time needed) of spreading the

volume on the surface, (iii) volume (and method) to rinse the electrode after incubation with the enzyme. Alternatively, stirring the electrode in a diluted solution of the enzyme mixture could decrease these variables; importantly, the volume of the solution should be reduced as much as possible while the electrode area used should be as large as possible. Direct detection of the enzymes within the nanopores could provide further evidences for nanoconfinement. Several techniques could be used for this purpose: (i) Förster resonance energy transfer (FRET) – a method to measure the distance of two fluorescently tagged proteins by energy transfer between the fluorophores in close proximity as described for example by Lim et al[276]; (ii) addition of a chemical cross-linking agent (after preparing the electrode) and subsequent analysis by SDS-page and MS. Chemical cross-linking would occur only if the proteins were in close proximity. These approaches would not give information on the amount of active enzymes in the electrode nanopores.

The results in Chapter II and IV suggest that both the reductive carboxylation and the amination are product inhibited. For instance, in Chapter IV (see Section 4.4.3.) after buffer exchange, the rates of the reaction were restored to the original value and the relative product ratio, measured by ^{1}H-NMR, was maintained. Hence, the decrease in current was mostly due to product inhibition. Product inhibition is expected when electrodes with a large surface area are used because of the large product formation. However, the current decrease has been observed (in the Armstrong group) also with small electrodes, probably because the pores are also entrapping and concentrating the product, increasing its effective concentration. Strategies to remove the product such as development of cascade reactions or electrochemical methods can be useful to investigate the

matter. I originally designed the cascade reaction in Chapter IV to relieve the product (malate) inhibition of ME (Chapter II). Success of this approach depends on ensuring that the escape of intermediate into the bulk solution is minimized. Development of new cascade reactions will be important to investigate the contribution of product inhibition to the current decrease and to generalise the observations in Chapter IV.

6.2.2 Generation of pores of controlled size

As discussed throughout this thesis, catalysis occurs within the nanopores of the ITO electrode and crowding of the enzyme is crucial to achieve the results obtained. The nanopores are generated by simply electrophoretically depositing ITO nanoparticles (< 50 nm) on a support and their random assembly generates nanocavities. It would be interesting to study (i) whether, by increasing the number of nanopores, the current density of a coupled reaction (FNR+E2) increases and (ii) the nanopore size required for the observed catalytical enhancement. For this purpose, it is possible to create pores by mixing ITO and polystyrene beads (PS beads) of a uniform and specific size. Upon calcination (450°C) the ITO layer is left with pores of the same size as the PS beads used (for more details see Section 7.3.2.1.3.).

Prior to this work, Dr Bhavin Siritanaratkul (DPhil thesis) investigated how both FNR coverage (monitored by non-turnover peaks) and $NADP^+$ catalysis by FNR (see Section 1.6), were affected by an increased porosity achieved by the formation of uniform 1 µm pores within the ITO layer using the PS bead approach. The porosity was increased since the ITO particles were smaller than the spaces between the PS beads.[141] The conclusion of that work was that no significant difference was observed. Here, I started to investigate how the introduction of

smaller PS beads (size: 0.5 µm and 0.1 µm) affected the (FNR+ADH)@ITO/Support electrode. The catalytic enhancement was tested by driving the oxidation of S-(+)-4-phenyl-2-butanol, catalysed by the (FNR+ADH)@ITO/Ti, with and without PS bead treatment (data not shown). **Figure VI-1** shows scanning electron microscopy (SEM) characterization of the calcined resulting electrodes using 0.5 µm and 0.1 µm PS beads (in collaboration with Alexander Robertson, University of Oxford). At this stage no significant difference between templated (with PS beads) and untemplated electrode (no PS beads) was observed (data not shown). In future work, decreasing the size of the pores to 0.05 µm could induce an enhancement of the rate and help finding the "sweet spot" in term of nanopore size.

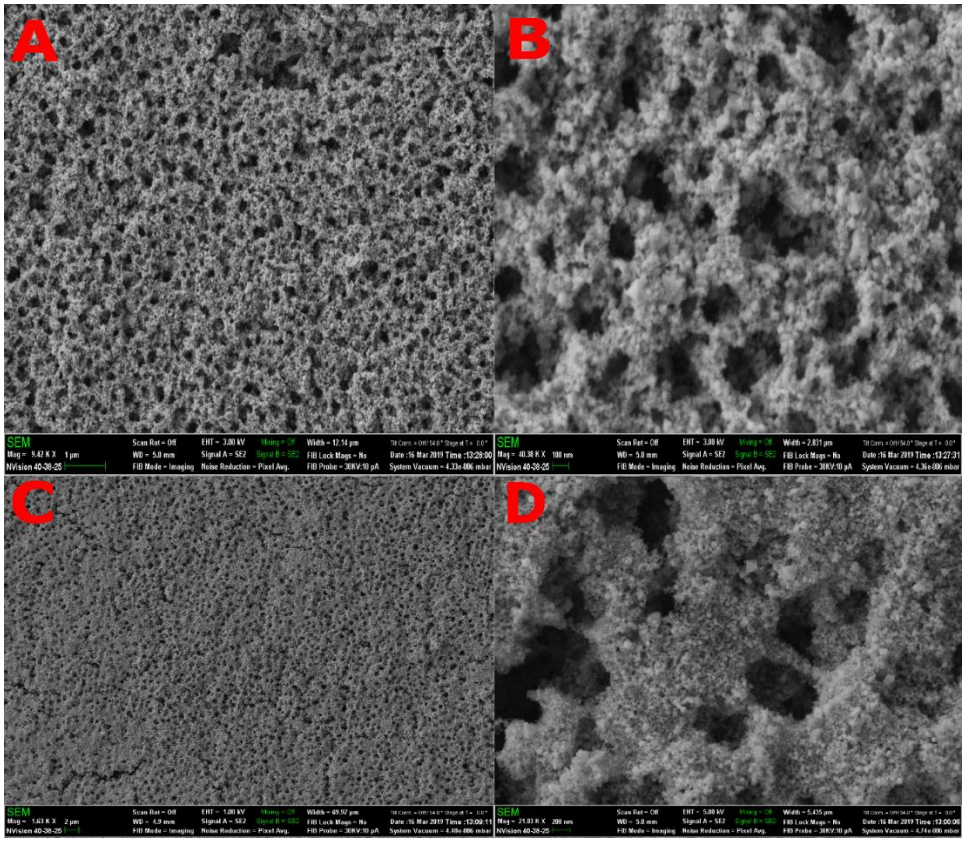


Figure VI-1. Scanning electron microscopy of ITO/ITO glass upon the creation of pores of known size by using PS beads. PS beads: 0.1 µm (**A**, **B**) and 0.5 µm (**C**,**D**) through pre-mixing ITO with PS beads and subsequent calcination at 450°C (see Section 7.3.2.1.3.). Data obtained in collaboration with Alexander Robertson, University of Oxford.

6.2.3 Scale-up of the system and use of cell lysate to drive synthesis

Scaling-up of the system is crucial for its adoption by industry. A relatively large-scale experiment using L-glutamate dehydrogenase was recently published (scale-up carried out by DPhil student Beichen Cheng).[139] For industrial purposes it could be interesting to test the possibility of using a two-electrode system instead of the classical three-electrode system, by using Pt as CE and RE. The disadvantage would be that the applied potential will change because of the high current passing through the RE (see Section 7.1.2.), but ease of the system would be improved (the RE should be close to the WE so designing an optimally large-volume electrochemical cell could be challenging).

A large-scale experiment as performed with GLDH (500 mL, 192 cm^2) should be carried out to compare reactions of industrial interest carried out by conventional methods with the Electrochemical Leaf. For instance, it would be very interesting to replicate the biocatalytic synthesis of the cholesterol-lowering drug, atorvastatin precursor as published by Luo *et al*.[277] Eventual improvement in several aspects such as time, [enzyme], TTN, conversion and temperature should be investigated. Importantly, the preparation of the electrode should be drastically optimised to decrease the moles of enzyme dropped on the surface while maintaining similar current densities. Similar rates could be achieved by simply increasing the incubation time of the diluted enzyme mixture on the electrode. Variation of the thickness of the ITO layer should also be investigated in relation to a coupled reaction (FNR+E2). Previous studies focused simply on the effect on FNR binding alone.[141]

The possibility of using cell lysate (lyophilized or not) instead of purified enzymes is very valuable not only for screening but also for synthesis. Testing lysates will be invaluable for the adoption of this technology outside the laboratory. For instance, how stability and rates would change in the reductive carboxylation of pyruvate (Chapter II) and in the five-enzymes cascade (Chapter IV) by using lysate instead of purified enzymes, could be investigated.

For further biocatalytic applications an ATP recycling system, using adenylate kinase and polyphosphate kinase, could be integrated in the Electrochemical Leaf. The nanoporous system could be compared with the results published by Strohmeier *et al*.[278] Development of an effective ATP/NADPH recycling system, in addition to mimicking photosynthesis, will make the use of carboxylic acid reductases (CAR) *in vitro* more accessible. This class of enzymes drives the chemically-challenging reduction of carboxylic acid to aldehydes and is of great importance for industry.[279–281]

6.2.4 Development of a directed evolution system

Miniaturizing the electrochemical leaf is crucial to design a powerful biosensor for biocatalyst discovery and evolution. The concept of a multi-well array was shown in Chapter V (see Section 5.5). If developed, a proof-of-concept directed evolution experiment could be carried out in a similar approach as in Goto *et al*.[260] An example of an enzyme to evolve is ferredoxin $NADP^+$ reductase Y346S.[139] This variant can use NAD^+ but not $NADP^+$ and it was developed by Dr. Clare Megarity (see Section 1.6) and tested by Part II students (one of which Sacha Tchen under the guidance of myself, Dr. Clare Megarity and Dr. Bhavin Siritanaratkul). The NAD^+ variant was active but not stable as the activity decayed

quickly in chronoamperometry experiments when coupled to a NAD^+-dependent E2 (J. Dunn Part II thesis 2017; S. Tchen Part II thesis 2019). Evolution and screening for stability would be possible with the proposed system by using a stable NAD^+-dependent dehydrogenase such as extensively used glucose dehydrogenase. Furthermore, optimizing the NAD^+-FNR variant is crucial to widen the collection of enzymes accessible to the electrochemical leaf.

6.2.5 Using the sensor for metabolite detection

Development of a biosensor for the detection of metabolites in fluids, can be important for early-stage detection of diseases such as cancer. Cancer cells display an aberrant metabolism and leave a metabolic fingerprint which is released into the blood stream/urine by excretion or uncontrolled cell death.[282] Specific metabolites have been identified as potential cancer biomarkers and can be detected by NMR and MS analysis (technologies which so far are not suitable for regular *on-chip* diagnosis).[283] Loading of a cascade on the ITO electrode could allow for the detection of metabolites, by using an *upstream* cascade, where the first substrate is the metabolite to sense and FNR-E2 is the last step of the cascade (for upstream terminology see Section 4.4.2.). In this instance the current would be related to the amount of metabolite in the fluid under investigation allowing possibly for quantitative analysis. **Figure VI-2** explains the concept. The levels of the metabolite *O*-acetyl-L-carnitine were reported to be affected in early-stage cancer.[282] In the cascade shown in **Figure VI-2**, the reaction is upstream to the E1-E2 pair (in this figure FNR and carnitine-3-dehydrogenase). Hence, the current reflects the rate of the overall cascade, which would be dependent on the availability of the first substrate (*O*-acetyl-L-carnitine), provided that coenzyme A is

available. It could be envisaged that by designing an array based on this technology, the monitoring of the metabolic fingerprint of a patient could be made possible. Measurement of the amount of coupled enzyme adsorbed could be very important for this application to facilitate obtaining quantitative data.

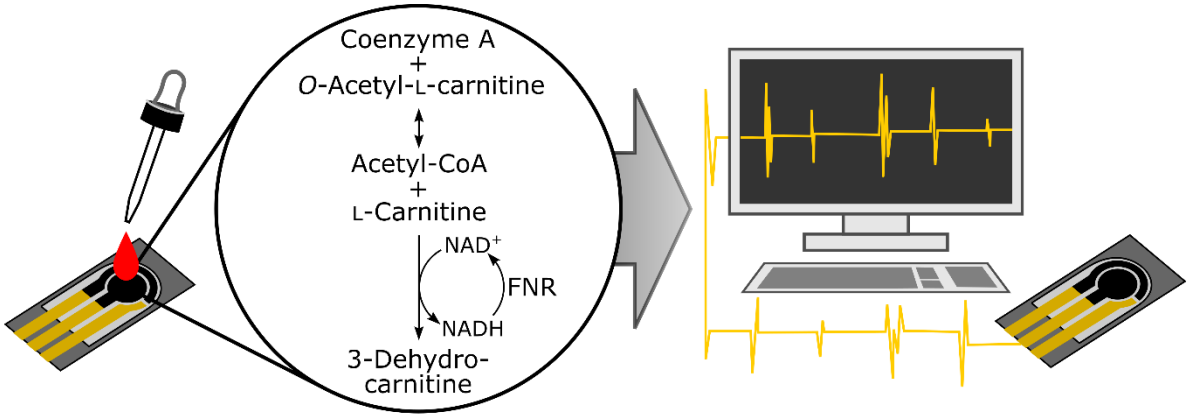


Figure VI-2. Scheme of the diagnostic biosensor device for the detection of *O*-acetyl-L-carnitine

Chapter VII

7 Electrochemical theory

7.1.1 Protein film electrochemistry

Protein film electrochemistry (PFE) is a technique which studies redox enzymes deposited on conducting surfaces. The resulting protein film can be used for several applications, such as mechanistic study of enzymes, or biocatalytic applications.[134,178,179,284,285] The technique offers several advantages, such as (i) need of very small amounts of protein, (ii) possibility of reusing the same protein film to test quickly and reliably several conditions (simply by moving the protein film into a new condition such as a buffer with a different pH or temperature), (iii) it is a quick technique, as it immediately gives information on the rate of catalysis. Unfortunately this method does not give structural information.[286] In PFE current is proportional to rate: current arises from three elements and **Figure VII-1** helps with understanding the concept:[178,286]

- Electron transfer between electrode and enzyme (blue arrow).
- Intramolecular electron transfer within the enzyme (not represented, but it can be important for enzymes containing relay centers such as Fe–S clusters in [NiFe]-hydrogenases).
- Availability of substrate (black arrow).
- Inherent catalytical activity (red arrow).

Electron transfer between electrode and enzyme, availability of substrate and interfacial electron transfer need to be optimal, to ensure that the current reflects the inherent catalytical activity of an enzyme. For instance, if the contact between the electrode and the enzyme is sluggish the measured current would not be

necessarily linked to the enzyme properties, because the current reflects the rate determining step of the process.

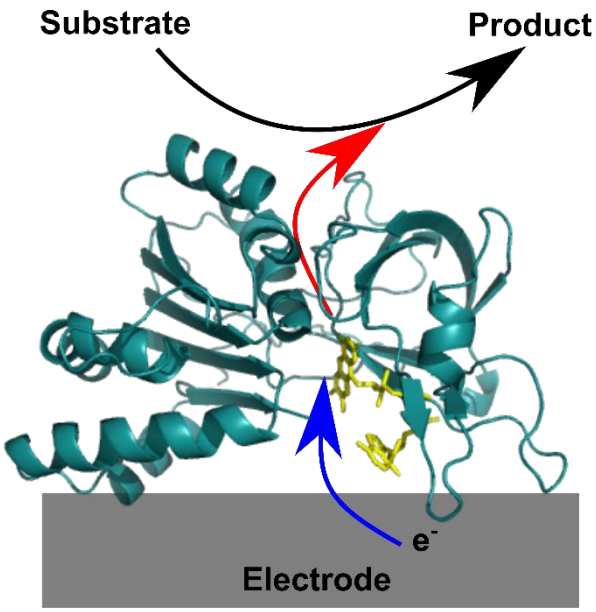


Figure VII-1. Protein film voltammetry. This technique studies enzymes through direct contact with an electrode. The electrode becomes an electron source and sink and fundamental kinetic activity of an enzyme can be investigated. First, some conditions must be fulfilled: (i) the electron transfer between the electrode and the enzyme is not limiting (blue arrow), (ii) there is a continuous supply of substrate to the enzyme-electrode composite (black arrow). The enzyme shown is ferredoxin $NADP^+$ reductase (*pdb*: 1FUC) and in yellow its FAD centre.

Figure VII-1 shows ferredoxin $NADP^+$ reductase (FNR), from Spinach, (*pdb* 1FUC) and its FAD centre, shown in yellow, which can be oxidized or reduced upon interaction with the electrode (see Section 1.6.). Typically, common conducting materials are pyrolytic carbon or indium tin oxide (ITO).[59,86,287] Intramolecular electron transfer depends on the relay centers within some proteins.[288] In FNR no relay centers are present (see Section 1.6) so this element will not be discussed. Constant availability of substrate at the electrode is important to avoid mass transport limitation; hence, the electrode can be rotated (see Section 4.4.2.) or the

solution can be stirred by using a stir bar (Chapter II, III and IV) or by purging inert gas directly into the cell solution (see Section 3.4.2.). Moreover, by rotating the electrode or stirring, the product is constantly removed from the electrode/solution interface.

7.1.2 Electrochemical setup

In a PFE experiment three components are usually necessary, a working electrode (WE), a counter electrode (CE) and a reference electrode (RE). A potential is applied to the WE electrode where an enzyme or protein is absorbed. The electrode become this way an electron source or sink for the redox enzyme and, if its substrate is present in solution, catalysis can occur. For instance, in this thesis, upon application of a potential, the oxidation or reduction of the FAD centre is visible when FNR is absorbed on the electrode (non-turnover current). Eventually in the presence of $NADP^+$ (substrate) catalytic current is detected (turnover current, see Section 1.6). The CE drives the opposite reaction of the WE, *i.e*. in this thesis during $NADP^+$ reduction, it typically drives water oxidation, and during NADPH oxidation, H^+ reduction. The CE must be in excess compared to the WE surface area to sustain catalysis.[242] The potential applied depends on the equation below.

$$E = \Delta\Phi_{e/sWE} + iR + \Delta\Phi_{e/sRE} \quad (7.1)$$

In equation 7.1, $\Delta\boldsymbol{\Phi}_{e/s}$ is the potential difference across the electrode/solution interface for the WE and RE ($\Delta\boldsymbol{\Phi}_{e/s\ WE}$, $\Delta\boldsymbol{\Phi}_{e/s\ RE}$, respectively). Passage of a large current through the RE electrode would result into a change in the applied potential, hence a three-electrode system is used which ensures that no or little current passes through the RE (in this thesis a Ag/AgCl electrode).[289] The term *R* in

equation 7.1. reflects the resistance of the solution between WE and CE, while *iR* is the change in voltage caused by the passage of current between the two electrodes. To reduce *R*, the solution's conductivity can be increased and the WE can be positioned as close as possible to the RE. **Figure VII-2** shows the circuit of a typical potentiostat.

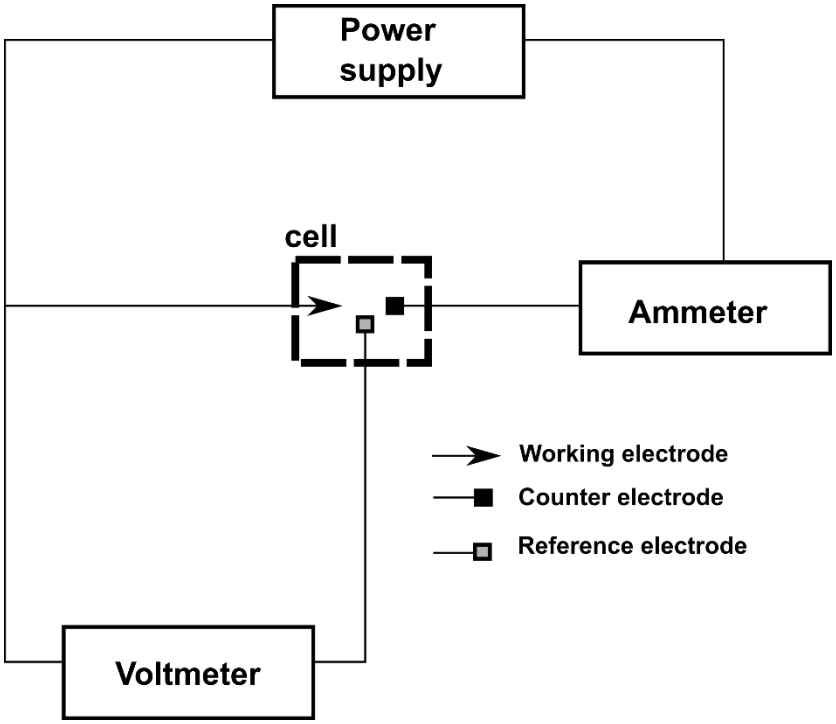


Figure VII-2. Scheme of the circuit of a typical potentiostat. An electrochemical setup contains a working electrode (WE), a counter electrode and a reference electrode. A voltmeter is used to apply a potential and an ammeter to read the current at the WE.

Note that in some experiments described, a two-electrode system was used instead, where the CE was used both as reference and counter to drive the reaction with visible light (see Chapter III). Typically, the electrochemical experiments are referenced to the standard hydrogen electrode (SHE) or to the reversible hydrogen electrode (RHE, details for conversion in Section 7.1.5.).

In this thesis electrochemical experiments were usually carried out in a three-compartment cell or in a two-compartment cell (unless specified otherwise). In the three-compartment cell WE, CE and RE were all separated by each other and housed in different compartments connected through a glass frit. The RE was held as close as possible to the WE via a Luggin-Hubber capillary, hereafter referred as Luggin-capillary.[242] In the two-compartment cell (see Section 4.4.2.) the WE and CE were housed together while the RE was separated via a Luggin- capillary. Throughout this thesis the main techniques used were cyclic voltammetry and chronoamperometry: in these techniques, current is recorded against potential and time, respectively (see Sections 7.1.5. and 7.1.8). The current contribution comes from a non-faradaic and a faradaic element. Moreover, the current can be negative in case of a reduction- or positive for an oxidation-reaction.

7.1.3 Nonfaradaic current

When a potential is applied to an electrode, opposite charges are typically drawn at the surface. Moreover, every time a potential is changed the amount of charge on the electrode varies (**Figure VII-3**). As a result, an electrical double layer builds up on the electrode surface. The model resembles a capacitor, according to the equation below:

$$C = \frac{q}{E} \tag{7.2}$$

In equation 7.2. *C* is capacitance, *q* is the accumulated charge and *E* is the potential applied. By knowing that the current is the variation of charge over time (*dq/dt*) equation 7.2 can be rewritten to

$$I = \frac{dq}{dt} = C\,\frac{dE}{dt} = C\,v \tag{7.3}$$

Equation 7.3 shows that the capacitive current varies linearly with the change of potential over time *i.e.* scan rate ν (unit: *V/s*). The non-faradaic current is important in techniques such as cyclic voltammetry (see Section 7.1.5.), where the contribution of the non-faradaic current can be removed by comparing the scan of a protein film with a blank scan (with no protein).

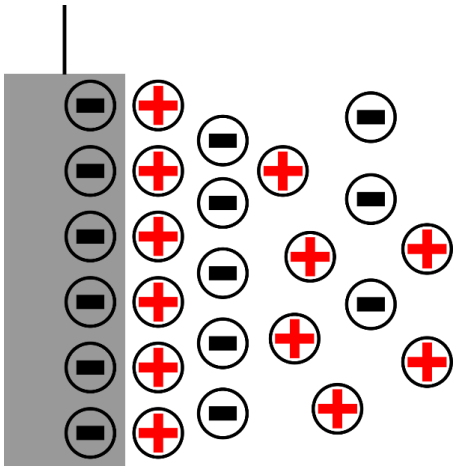


Figure VII-3. Double layer formation. Upon applying a potential to an electrode, opposite charges build up at the electrode surface, forming an electrical double layer.

7.1.4 Faradaic current

Faradaic processes involve oxidation and reduction of a certain species and they are governed by Faraday's law. Assuming a redox process, equation 7.4. can be used to describe the reaction, where an oxidized species (*Ox*) is reduced by receiving *z* electrons (e^-) with a kinetic constant, k_{red} and a reduced species (*Red*) can be oxidized with kinetic constant k_{ox}:

$$Ox + ze^- \underset{k_{ox}}{\overset{k_{red}}{\rightleftarrows}} Red \qquad (7.4)$$

The current from the resulting electrochemical process (i_{tot}) is the sum between an oxidation and reduction current (i_{ox} and i_{red}, respectively) as shown in the equation below:

$$i_{tot} = i_{ox} - i_{red} \tag{7.5}$$

Thus, at equilibrium (rate of oxidation = rate of reduction) the total current (i_{tot}) is equal to zero. In CV experiments, the potential of the redox couple (E^0) can be obtained by looking at the E at current equal to zero (i_{tot} = 0). The Nernst equation (see equation 7.6) shows that when the concentration of substrates and products is the same ([Ox]/[Red] = 1), then E^0 = E.

$$E = E^0 + \frac{RT}{zF}\ln\frac{[Ox]}{[Red]} \tag{7.6}$$

In equation 7.6 the potential of the redox couple under investigation is E^0, R is the gas constant, T is temperature, z is the number of electrons involved and F is the faradaic constant.

Equation (7.5) can be rewritten in terms of the rate constants k_{ox} and k_{red} and results in the following equation,

$$i_{tot} = zFAk_{ox}\Gamma_{red} - zFAk_{red}\Gamma_{ox} \tag{7.7}$$

In equation 7.7, z is the number of electrons involved, F the faraday constant, A is the electrode area, k_{ox} and k_{red} are the rate constants and Γ is the coverage of the electroactive species.

Equation 7.7 can be used to obtain the Butler-Volmer equation which shows how the current varies with the applied potential. This equation (7.8), uses Transition

State Theory (TST), which states that before formation of products an activated complex is in equilibrium with the reagents and products.[242]

$$i = i_{ox} - i_{red} = i_0 \left(\Gamma_{red} \exp\left(\frac{(1-\alpha)zF}{RT} (E - E^0) \right) - (\Gamma_{OX} \exp\left(\frac{-\alpha zF}{RT} (E - E^0) \right)) \right) \quad (7.8)$$

In the equation above a dimensionless term, α, the transfer coefficient, is used to describe the transition state. The value ranges from 0 to 1 and specifically if α → 0, the transition state resembles more the reagents, while if α → 1 more the products.

The Butler-Volmer equation is also known in a more compact form, which expresses the term *(E-E⁰)* as η, the overpotential of the reaction (equation 7.9).[242]

$$i = i_0 \left(e^{\frac{\alpha z F \eta}{RT}} - e^{\frac{(\alpha-1) z F \eta}{RT}} \right) \quad (7.9)$$

In this thesis, faradaic processes are observed both in turnover and non-turnover conditions. In the former the substrate of the FNR@ITO/Ti electrode is present in solution ($NADP^+$), while in the non-turnover condition is missing. In the latter case, the signal corresponds to the oxidation and reduction of the FAD group of FNR (see Section 1.6.).

7.1.5 Cyclic voltammetry

In cyclic voltammetry (CV) the potential is swept from a starting value (E1) to an end value (E2) and back to E1 for N number of scans. The time needed to perform the cycle depends on the scan rate (*v*, V/s). **Figure VII-4** shows the typical "V" shape of a potential vs time (*E vs. t*) plot in a CV experiment, where the slope is equal to the scan rate (**Figure VII-4**-**A**). When the potential is swept only from

E1 to E2 (*i.e.* without going back to E1) the resulting technique is called linear sweep voltammetry (LSV, see Section 3.4.1 for relative experiments). During a measurement (for both CV and LSV) the current at the WE is measured and plotted against the applied potential (**Figure VII-4**-**B**). Panel B shows a current vs. potential (*i vs. E*) plot of a CV (in the example of the FNR@ITO/Ti electrode, see Section 1.6.). From the voltammetry the faradaic contribution is visible (peaks at -0.59 V vs. Ag/AgCl from FAD oxidation and reduction, see Sections 1.6.2. and 2.4.2.1. for more details). Moreover, the current in the forward direction is not the same of the reverse direction. In the region where no redox reactions are occurring, this difference is the result of the non-faradaic-current (see Section 7.1.3.), while when redox reactions are occurring, the direction of the sweep determines the initial state of the species.

The strategy for CV and LSV is to first start from a potential where no catalysis happens and then sweep potential until current arises. The onset potential is defined as the potential at which catalysis starts to occur. Throughout the whole thesis the potential was always converted to either SHE or RHE, by using the following equations:

$$E_{SHE} = E_{Ag/AgCl} + 0.19 \qquad 7.10$$

$$E_{RHE} = E_{SHE} + 0.059 * pH \qquad 7.11$$

The CV provides also useful information of the amount of the electroactive species absorbed which is important in this thesis for the calculation of the coverage of FNR. **Figure VII-4-B** shows the non-turnover peaks due to oxidation and reduction of the FAD centre within FNR (see Section 1.6). Integration of the

current under the peak (after baseline correction) is helpful to know the amount of electroactive species on the electrode, using equation 7.12.

$$Q = \int i\, dE = \int i\, dt \left(\frac{dE}{dt}\right) = zFA\,\Gamma\,\mathrm{v} \qquad (7.12)$$

In equation 7.13, *i* is the current, z is the number of electrons involved, *F* is the faradaic constant, *A* is the area, Γ is the coverage (mol cm^{-2}), *E* is the potential and *v* is the scan rate. The coverage of the electroactive species can be calculated if area (*A*) and scan rate (*v*) are known.

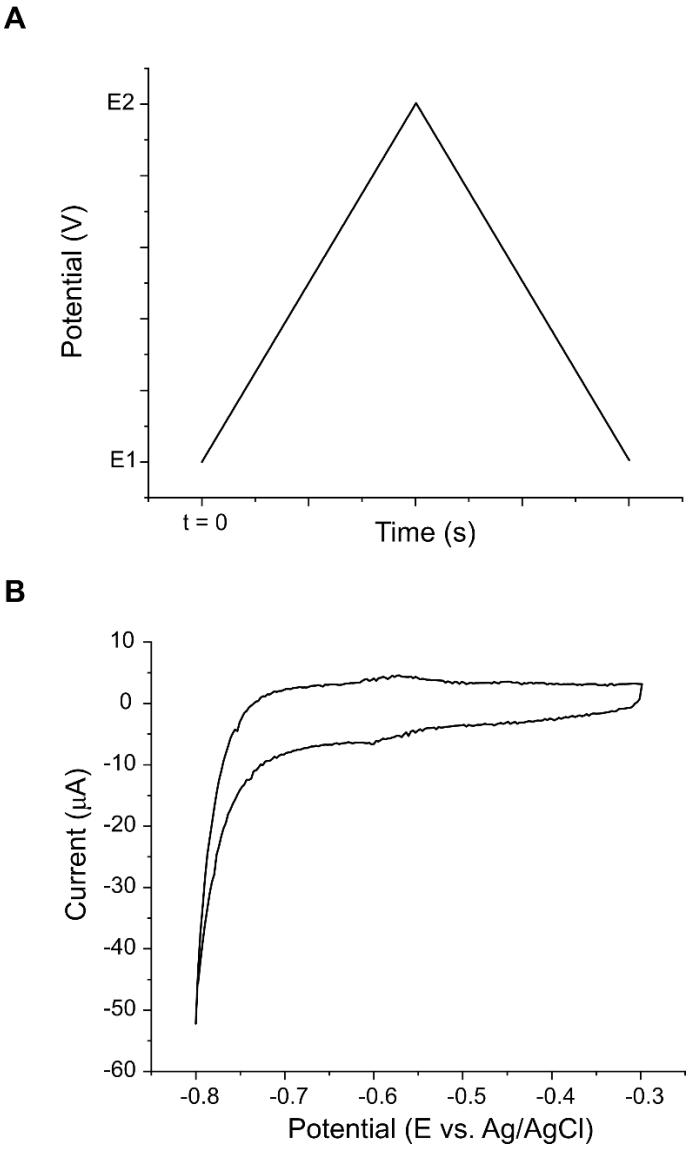


Figure VII-4. The two-plots of cyclic voltammetry. A. Potential vs. time plot. The potential is swept back and forth between two limiting values (from E1 to E2 and back to E1). The time required depends on the scan rate (*V/s*). **B.** Current vs. potential plot.

7.1.6 Catalytic current

This paragraph is relevant for explaining some results in this thesis (Sections 2.4.2.1, 2.4.2.2. and 4.4.1.) which describe the coupling between FNR and a secondary dehydrogenase. The overall mechanism is given by the equations below:

$$Ox + ze^- \underset{k_{ox}}{\overset{k_{red}}{\rightleftarrows}} Red \tag{7.13}$$

$$Red + X \rightleftarrows Ox + Y \tag{7.14}$$

In equation 7.13 an oxidized species (*Ox*) receives *z* number of electrons (e^-) upon interaction with the electrode: a reduced product (*Red*) is formed. In equation 7.14 the reduced products can react further with an electro-silent molecule (*X*) to regenerate the oxidized species (*Ox*) and produce a new molecule called (*Y*). Obviously, this reaction can be driven on the reverse direction, *i.e.* the electrode oxidizes a reduced product (*Red*) and the produced oxidized species (*Ox*) react with a Y species in solution.

Let's first examine the situation where only equation 7.13 applies under stationary conditions, thus the substrate (for example *Ox*) is not continuously brought at the electrode (see Section 1.6.2.). Typically, in a CV experiment, at the starting potential, E1 (see Section 7.1.5.), catalysis does not occur, thus the current corresponds to the baseline (given by the non-faradaic current). As soon as the potential for the reaction under investigation is applied ($E \geq E^0$ for an oxidation or $E \leq E^0$ for a reduction), the electrode starts to convert the redox species (for example reducing *Ox* to *Red*), thus the current increases. However, under stationary conditions all the substrate is quickly converted *i.e.* depleted at the

electrode/solution interface, thus the current starts to decrease. Because of this reason, peak-current is observed. This is shown for example in **Figure VII-5-A**, for the reduction of $NADP^+$ from the FNR@ITO/Ti electrode (red trace, peaks at -0.35 V vs. SHE, for experimental conditions see Section 2.4.2.2.). When the potential applied becomes oxidative, the NADPH produced is re-oxidized to $NADP^+$ and a peak-current is obtained as explained above because of depletion. The Randles-Sevcik equation for the peak current is shown below:

$$I_{peak} = 0.4463 \left(\frac{F^3}{RT}\right)^{\frac{1}{2}} n^{\frac{3}{2}} A\, D_0^{\frac{1}{2}} c v^{\frac{1}{2}} \qquad (7.15)$$

In the equation (7.15) *F* is the faradaic constant, *R* is the gas constant, *T* the temperature, *z* is the number of electrons, *A* is the area, D_0 the diffusion constant, *c* is the concentration and *v* is the scan rate. Thus, the peak current changes with the bulk concentration of the redox couple and with the square root of the scan rate.

Let's now examine a situation where both equations 7.13 and 7.14 apply, which in this thesis corresponds for example to the introduction of a secondary dehydrogenase (E2) under stationary condition. By adding E2 the voltammetry changes its shape: the current loses its peak-like feature and it approaches the behaviour of a typical redox-species becoming sigmoidal (**Figure VII-5-B)**. For instance, **Figure VII-5-A** shows the CV of the FNR@ITO/Ti electrode with *Ox* and *X* species in solution. When the NADPH-dependent malic enzyme (ME) is injected to the FNR@ITO/Ti system in the presence of a X species (pyruvate), *Ox* ($NADP^+$) is never depleted at the electrode interface, because *Red* (NADPH) is immediately recycled by the secondary enzyme (ME) producing *Ox* ($NADP^+$) (**Figure VII-5-B**).

Thus, the current loses its peak-like feature. Note also that the oxidative current is not visible anymore and that reductive current upon injection of the secondary dehydrogenase increases dramatically. This is because the reduced species (NADPH) is consumed by ME: as a result, the oxidative current tends to zero and the flux of oxidized species ($NADP^+$) increases, thus the current is enhanced. The relation between flux (J_0), variation of the concentration of a species (*O*) over a given location x and time t, with current is described by equation 7.16,

$$-J_O(x,t) = \frac{i\,(t)}{zFA} = D_O\left[\frac{\partial C_0(x,t)}{\partial x}\right](x=0) \qquad (7.16)$$

In the equation, *i* is the current, *z* the number of electrons, *F* the faraday constant, D_0 is the diffusion constant and δC_0 is the change in concentration of a species over time.

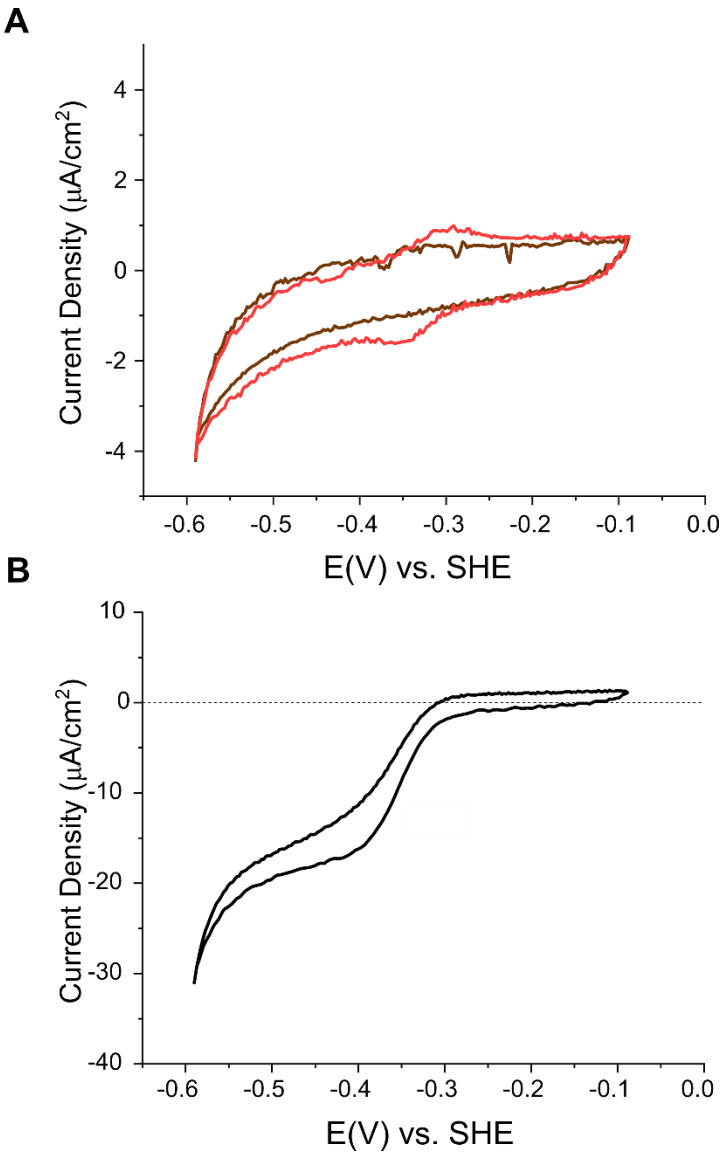


Figure VII-5. Catalytical voltammetry. A. Peak-like voltammetry of FNR@ITO/Ti electrode: the substrate ($NADP^+$) is depleted at the electrode interface (red trace, for experimental details see Section 2.4.2.1.). **B.** Sigmoidal curve after introduction of ME: the substrate is now never depleted as NADPH is constantly re-oxidised by ME: the shape is not peak-like anymore but sigmoidal. As a result, the flux of $NADP^+$ to the electrode increases, hence the current (for experimental details see Section 2.4.2.2.).

7.1.7 Reversibility

The shape of the voltammetry can give different information on the process under investigation. For instance, in this thesis it was shown the reversibility of the (FNR+ME)@ITO/Ti and (CA+FNR+ME+Fum+AspA)@ITO/Ti electrodes (see sections 2.4.2.2. and 4.4.1.). A difference between reversible and irreversible catalyst is shown in **Figure VII-6**.[178] In case of a reversible catalyst, by changing the potential of few mV from E^0 (as defined from the Nernst equation, see Section 7.1.4.) there is a substantial change in current in both oxidative and reductive direction: as a result the voltammetry cuts sharply the *x*-axis (blue curve). If the overpotential (η) applied is too large before observing a current the catalyst is considered irreversible (red curve).[178]

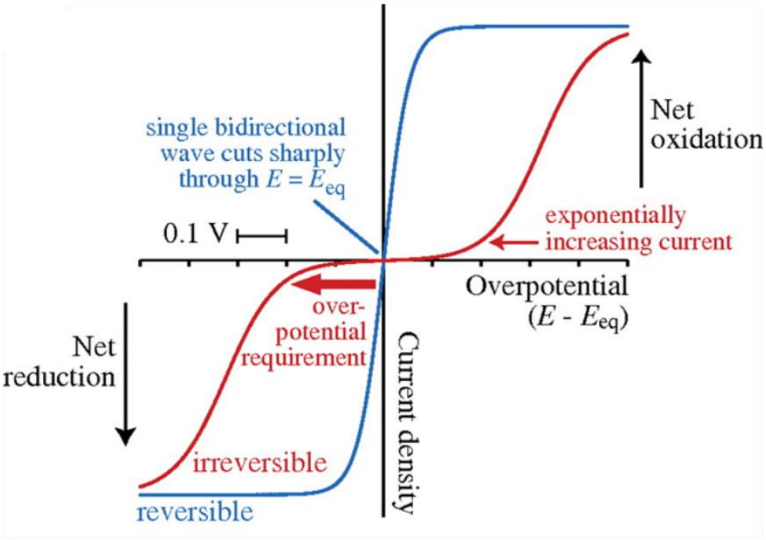


Figure VII-6. Difference between a reversible and irreversible electrocatalyst. In blue: representation of a reversible electrocatalyst; in red an irreversible electrocatalyst. Reprinted with permission from Hirst and Armstrong.[178]

7.1.8 Chronoamperometry

In chronoamperometry the potential is held constant and the current is measured against time. A plot of potential vs time in a chronoamperometry is shown in **Figure VII-7-A**. The figure shows also that during an experiment the applied potential (E_{app}) can be changed to a different value (E_{app2}).

Chronoamperometry in this thesis is mainly used to drive the formation of the product of interest through the (FNR+E_n)@ITO/Ti electrode (where E_n is either E2 or a set of enzymes). **Figure VII-7-B** shows the typical current vs. time plot (*i vs. t*) for a chronoamperometric reductive reaction. The integral of the curve shown in **Figure VII-7-B** is the charge passed (Q, unit: coulomb; grey area in **Figure VII-7-B**), which can be calculated using equation 7.17.

$$Q = \int i\, dt \tag{7.17}$$

In equation 7.17, *Q* is the charge passed, *i* is the current and *t* is the time expressed in seconds. If the faradaic efficiency (charge to the desired product) is 100% the number of moles produced during the experiment can be calculated using equation 7.18.

$$Q = zFN \tag{7.18}$$

In equation 7.18, *z* is the number of electrons involved (2 for the $NADP^+$/NADPH couple), F is the faraday constant (*F*, 96485 C mol^{-1}) and *N* is number of moles.

In chronoamperometric experiments described in this thesis, mass transport limitation was solved by stirring (unless stated otherwise), by purging the solution with inert gas (see Section 3.4.2.) or by electrode rotation (see Section 4.4.1.).

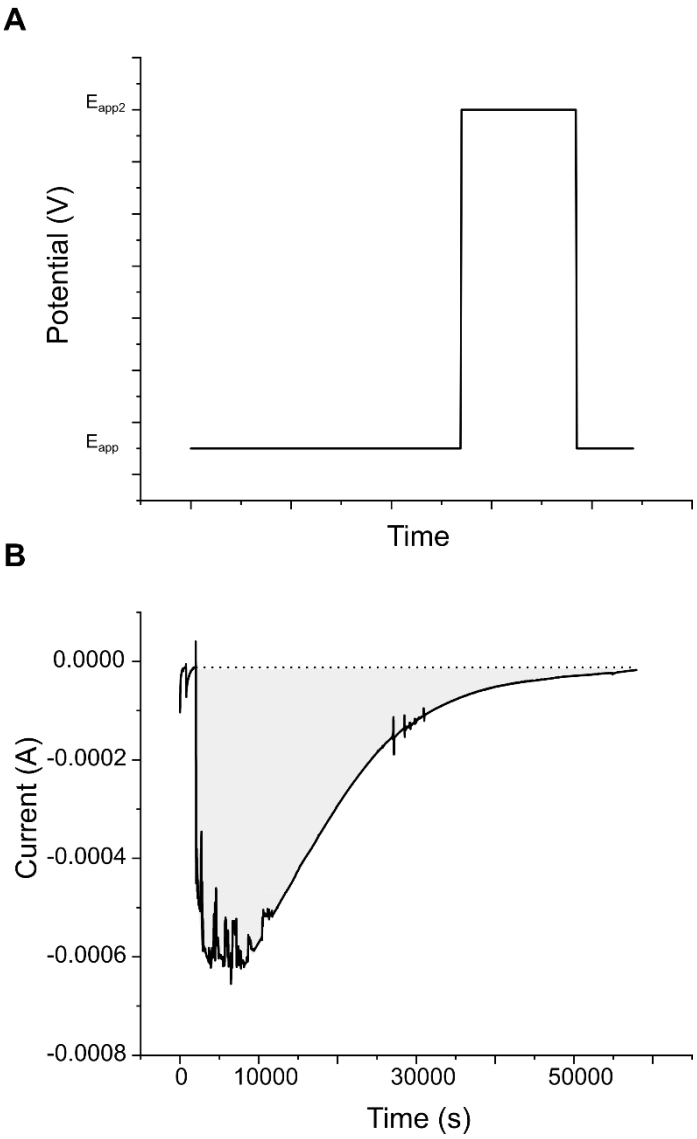


Figure VII-7. Chronoamperometry. The potential is held constant (E_{app}) over the time of the experiment or it can be jumped to another value (E_{app2}). **B.** During a chronoamperometric experiment the current flowing at the WE is measured against time. Integration of the current (grey area) can give a value of the moles of product formed if non-faradaic current is excluded and faradaic efficiency (FE) is known.

7.1.9 Diffusion

The movement of a molecule in an electrochemical experiment is governed by three forces, migration, diffusion and convection. Briefly convection is the movement of a species, because of stirring or rotation, and migration is the mechanism through which charge is transported through the electrolyte. Diffusion

is the movement of species through a concentration gradient. When a given substrate is converted to a product, a concentration gradient from the electrode surface to the bulk solution is established. Obviously, the concentration of the product is highest at the electrode surface and tends to the minimum in the bulk solution (especially for small surface area electrodes). In typical electrochemical experiments migration is not an issue as experiment are carried out in excess electrolyte. Thus, in stationary conditions (no convection) movement of charges is governed by diffusion. The Fick's law of diffusion (shown in equation 7.16) states that diffusion of a particle from an electrode depends on the change of concentration (c) over the change of distance (x) as shown in equation below:

$$rate\ of\ diffusion = D_O\ \frac{\partial c}{\partial x} = \frac{c - c_0}{\mu} \tag{7.19}$$

In equation 7.19, *c* is the concentration in the bulk solution and c_o on the surface, while μ is the thickness of the diffusion layer. Another version of this equation allows writing the change in concentration vs. the distance using equation 7.20[242],

$$c_{x,s} = c_0 \operatorname{erf}\left[\frac{x}{2(D_0 t)^{\frac{1}{2}}}\right] \tag{7.20}$$

The term ($2(D_0 t)^{\frac{1}{2}}$ = μ) corresponds to the thickness of the diffusion layer.[242] For a $D_O = 10^{-5}$ cm^{-1} s^{-1} and t = 1 ms the thickness of the diffusion layer is 1 μm. Obviously the smaller the term *t* the faster the concentration between electrode surface and bulk will be equal, as it can be observed by plotting equation 7.20. This section was relevant for the assumption of the rate of escape of intermediates in Section 4.4.3.

7.2 Semiconductor theory

Semiconductor materials are under intense research for the development of different application such as solar fuels and solar cells.[12,46,181] Their chemistry is based on the energy band model. The highest occupied energy state, which in case for discrete molecules such as in photosynthesis is normally called HOMO, is defined as valence band (VB), while the lowest unoccupied energy band is called conduction band (CB). The energy difference between these two levels shows whether the material is an insulator, a semiconductor or a conductor as depicted in **Figure VII-8**. In a conductor, the conduction and valence bands are almost overlapped, in an insulator the difference between the two energy levels is too large, thus no electron transition can occur. In a semiconductor the energy difference, called also band gap (E_g) is small (**Figure VII-8**). By shining light of an energy equal or bigger than E_g then an electron can transition into the CB, leaving a hole (h^+) in the VB of the material.

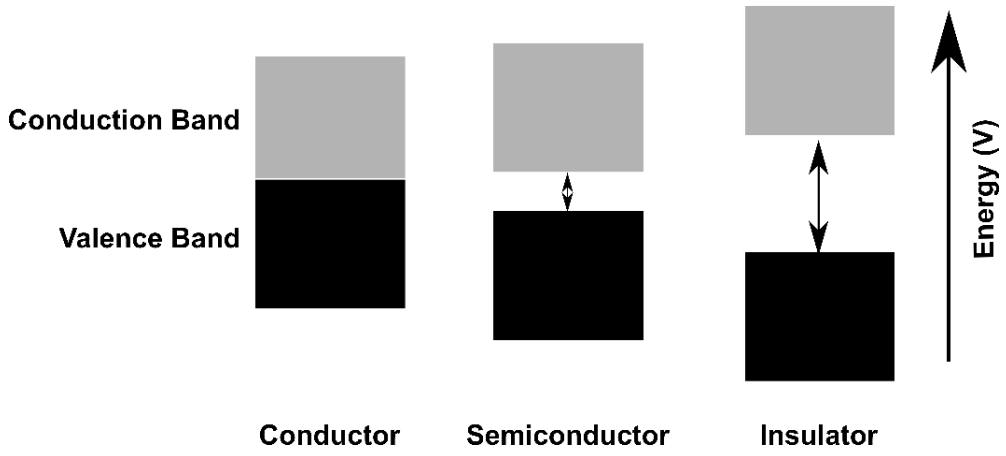


Figure VII-8. Difference between conductors, semiconductors and insulator. The difference between conduction band and valence band (band gap, E_g) is crucial to understand the behaviour of a material. Semiconductors have a small E_g so that energy transitions can occur.

Semiconductors are divided into intrinsic- or doped-materials. In the former the concentration of holes and electrons are the same, while different for the latter case. Doped-semiconductors have either a *n*-type or *p*-type behaviour. *N*-type semiconductors have a large concentration of electrons while the population of holes (h^+) is low, as such holes are the minority carriers. In *p*-type the situation is the opposite, electrons are the minority carriers. The Fermi level (E_F) is the energy level where there is 50% probability to find an electron. The E_F is closer to the CB for *n*-type while to the VB for *p*-type semiconductors (**Figure VII-9**). By extrinsically doping a material its conductivity can be increased or its behaviour reversed. For instance, an *n*-type can be modified to *p*-type by, for example introducing an electron-poor element, such as Mg^{2+} into α-Fe_2O_3.[290]

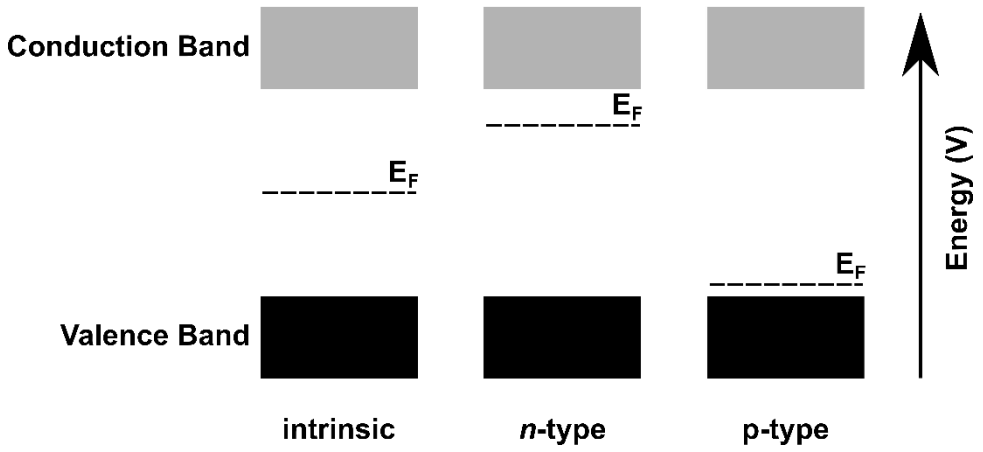


Figure VII-9. Difference between intrinsic, n-type and p-type semiconductors. The Fermi level (E_F) is at mid distance between conduction band and valence band in intrinsic semiconductors while closest to CB in *n*-type and to VB in *p*-type.

When semiconductors are immersed in solution, the energy level of the E_F equilibrates with the energy level of an electrolyte's solution, thus, band-bending occurs (*i.e*. a potential difference is established). For example, if the E_F has a higher energy level than the electrolytes, than electrons flow from the

semiconductor to the solution and a depletion region forms at the semiconductor interface (**Figure VII-10**). Opposite to that, with a *p*-type semiconductor, holes are the major charge carriers and the E_F is lower in energy than the electrons in the electrolyte: a potential difference is established in reverse and that causes bending of the band, as electrons are fed into the semiconductor to reach equilibrium.

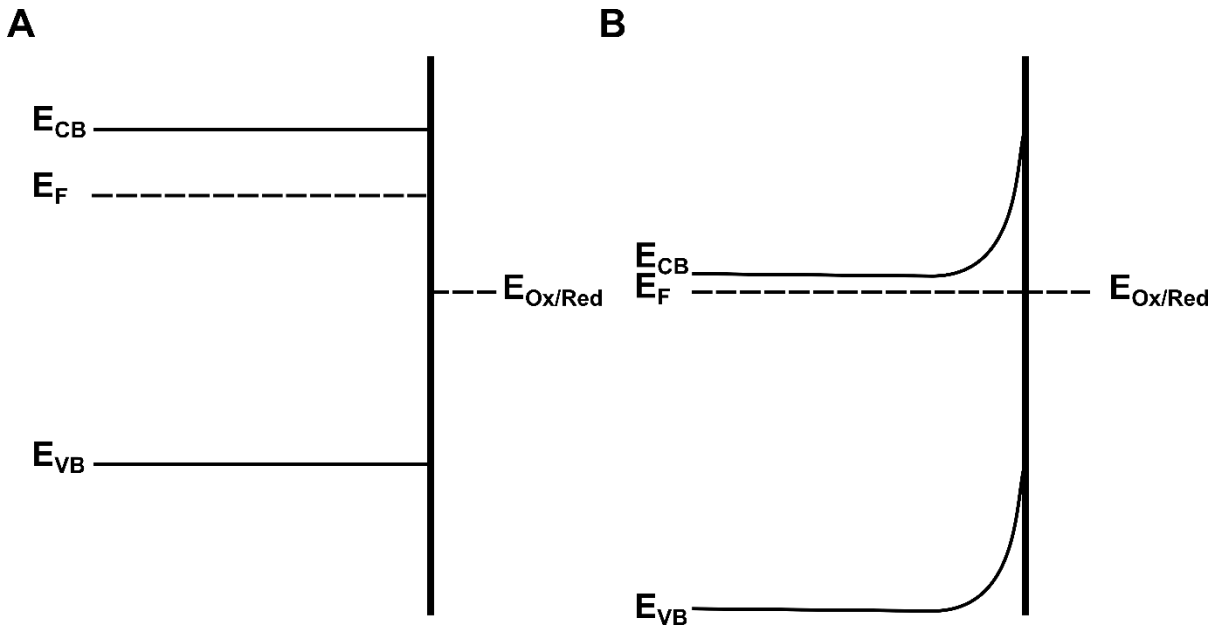


Figure VII-10. Equilibration of the semiconductor/solution interface. A. Before equilibration. **B.** After equilibration.

An important value for semiconductors is the flat-band potential (E_{fb}). At that potential the band is flat and charges do not flow. If a potential more positive than E_{fb} is applied ($E > E_{fb}$) then band bending occurs *i.e.* a potential difference is established so that electrons move to the back contact while holes to the semiconductor/electrolyte junction. As we mentioned before, in *n*-type semiconductors, concentration of holes is too low so that flow of charges can only occur by band excitation (by shining light). Upon light absorption electron-hole separation occurs, leaving a hole (h^+) in the VB (**Figure VII-11**). When a potential more negative than the E_{fb} is applied ($E < E_{fb}$) the opposite occurs: electrons flow

to the semiconductor/electrolyte junction while hole to the back contact. For *p*-type semiconductors the concentration of electrons is too low, hence, band excitation has to occur through light illumination. As a result, a *p*-type semiconductor can be used to drive a reduction reaction while, an *n*-type semiconductor for oxidation.

The requirement to drive band excitation is that the energy of the photon has to match or be bigger than the band gap. For wide-band gap semiconductors (such as in TiO_2 case) UV-light only can drive the transition (see Section 1.4.). Thus, to build a visible-light driven process ($\lambda > 420$ nm = 2.9 eV) the material's bandgap needs to be smaller than ≈ 2.9 eV. **Figure VII-11** shows the relevant case to this thesis: an *n*-type semiconductor under visible light illumination and at an applied potential, $E > E_{fb}$.

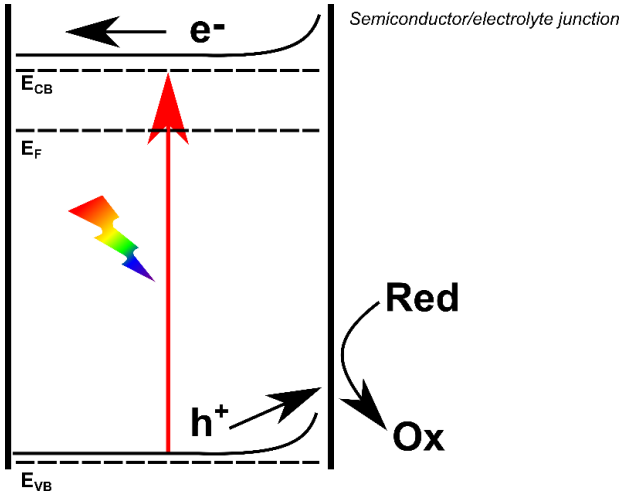


Figure VII-11. Charge separation and band bending in n-type semiconductor. Light triggers charge-hole separation. Electrons migrate towards the back contact of the semiconductor, while holes (the major carriers) migrate towards the semiconductor/electrolyte junction to drive oxidation of a species in solution.

This thesis investigates the light driven $NADP^+$ reduction using water as electron donor. The requirements to drive the process with visible light-only were (i) energy level of the valence band more positive than water oxidation potential and conduction-band energy level more negative than $NADP^+$ reduction potential. Moreover, a band gap (E_g) smaller than 2.9 eV was required (see above and

Sections 1.4 and 3.2 for more discussion). The materials investigated in this thesis (α-Fe_2O_3, $BiVO_4$) do not have the right energy level to drive the reduction reaction, thus an applied potential or a single junction solar cell was used to make the process feasible. Applying an additional potential shifts the fermi level, as CB, VB and E_g do not change.

Figure VII-12 shows the ideal and real behaviour of a typical *n*-type semiconductor. In the dark no current arises until very anodic potentials are applied (black trace). Ideally, when applying a potential higher than the flat-band potential, oxidative current should increase sharply to reach the maximum current within a short potential window. However, this ideal behaviour is not observed, and the real photocurrent is smaller and arises at more anodic potential. The potential at which catalysis starts to occur is called onset potential (**Figure VII-12**). Thus, in order to evaluate the performance of a material, important parameters to consider are amplitude of photocurrent and its onset potential.

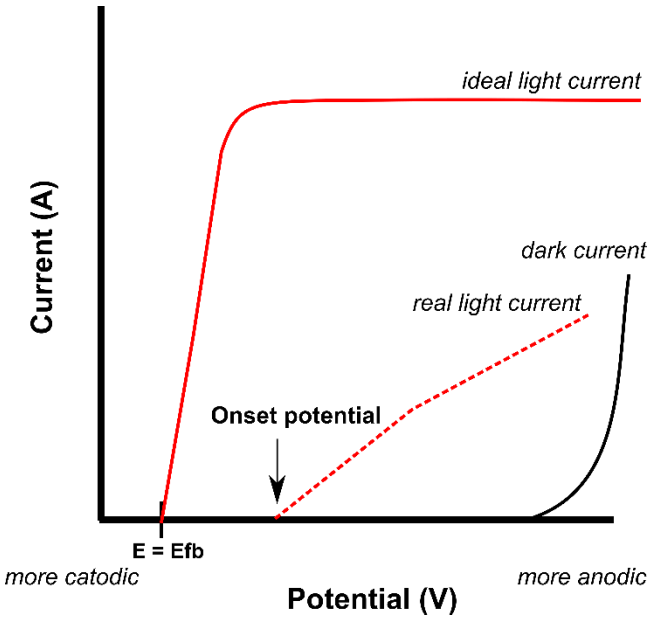


Figure VII-12. Ideal photoresponse of a *n*-type semiconductor used for water oxidation. In the dark catalysis is not observed until a high anodic potential is applied (black trace). The ideal behaviour of a photoanode should be an increase of oxidative current at a potential more positive than the flat band potential (E_{fb}). The photocurrent should reach its maximum within 0.1 V (red line). The real light current curve is shown in dotted line and the onset potential is the *E* at which light current is observed. Readapted from Iandolo *et al.*[43]

7.3 Experimental methods

7.3.1 Molecular Biology

7.3.1.1 ME cloning

Malic enzyme (*maeB*) from *E. coli* was amplified based on the sequence in the KEGG database (entry: B2463). The sequence was amplified using the following two primers (purchased from ThermoFischer):

Forward:

5′-GGTGATGATGATGACAAGATGGATGACCAGTTAAAACAAAGTGCAC-3′

Reverse:

5′-GGAGATGGGAAGTCATTATTACAGCGGTTGGGTTTGCGC-3′

A single colony of *E. coli* BL21 was suspended in sterile MQ-H_2O (under sterile conditions) and diluted 1:1 to generate the DNA template stock. The PCR reaction was set up into 50 µL tubes containing: 2.5 µL primer forward (0.5 µM), 2.5 µL primer reverse (0.5 µM), 10 µL buffer (New England Biolabs, NEB, stock 10x), 1 µL prepared-DNA template, 0.5 µL Q5 polymerase (NEB). The PCR cycle was as follows: initial denaturation 95°C for 5 minutes, 30 cycles of 95°C (30 seconds), 54°C (1 minute), 72°C (90 seconds) and a final elongation of 5 minutes at 72°C. At the end of the reaction 10 µl were loaded into a 0.8% agarose gel to check for a DNA product of 2.2 kb (TAE buffer (50X): 2 M Tris, 1 M acetic acid, 25 mM EDTA, pH 8.5; DNA loading dye from New England Biolabs; 100 V). Once it was established that the PCR was successful, PCR purification was performed. The sample was diluted with washing buffer 1 (5 M Guanidine hydrochloride, 20 mM Tris-HCl, 38% v/v ethanol, pH 6.6), loaded on a spin-column (12 g, 60 s). Supernatant was discarded and washing buffer 2 (20 mM NaCl, 2 mM Tris-HCl,

80% v/v ethanol, pH 7.5) was added. After discarding the supernatant, elution was performed by adding sterile MQ-H_2O (typically 15 µL) on the center of the spin column, for 5 minutes at 40°C and by spinning down at 12 g for 30 s. The elution was stored at -20°C and sent for sequencing to Source BioScience (University of Oxford) to confirm its sequence.

7.3.1.2 Ligation independent cloning

The amplified *maeB* was inserted into the vector pLATE51 by ligation independent cloning (Thermofisher, aLICator kit). Briefly, T4 DNA polymerase with 3'-5' exonuclease activity digests both the plasmid and PCR product (the plasmid contained a single cut). The reaction is then stopped with EDTA and the mixture is ready to be used directly for transformation. Ligation occurs directly in living cell after transformation.

7.3.1.3 AspA cloning

L-aspartate amino-lyase (AspA) from *E. coli* was amplified based on the sequence in the KEGG database (entry: B2463). The sequence was amplified using the following two primers (purchased from ThermoFischer):

Forward:

5′- GGTGATGATGATGACAAGATGTCAAACAACATTCGTATCGAAGAAGAT -3′

Reverse:

5′-GGAGATGGGAAGTCATTATTACTGTTCGCTTTCATCAGTATAGCGTTT-3′

A single colony of *E. coli* BL21 was dissolved into sterile MQ-H_2O (under sterile conditions) and diluted 1:1 to generate the DNA template stock. The PCR

reaction was setup into 50 µL tubes containing: primer forward, 2.5 µL (0.5 µM), primer reverse, 2.5 µL (0.5 µM), buffer (NEB) 10 µL (stock 10x), DNA template: 1 µL, Q5 polymerase (NEB) 0.5 µL. PCR cycle: initial denaturation 95°C for 5 minutes, 30 cycles of 95°C (30 seconds), 59°C (1 minute), 72°C (60 seconds) and a final elongation of 5 minutes at 72°C. At the end of the reaction 10 µl were loaded into a 0.8% agarose gel to check for an DNA product of 1.3 kb. Once, established that the PCR was successful a PCR purification kit was performed as described in Section 7.3.1.1.

7.3.1.4 Transformation

Competent DH5-α cells (NEB) were transformed as in the manufacturer protocol. Briefly, the cells were first thawed in ice for 10 minutes, then 5 µL of transformation mixture (after LIC or using a closed vector) were added into the cells and left on ice for 30 minutes (under sterile conditions). Heat shock was then performed at 42°C for 30 s and the cells were left in ice for 5 minutes. Then, medium (SOC, NEB, 950 µL) was added into the tube; the cells were left growing for 1 hour. Afterwards, the cells were spun down and concentrated to ≈ 20 µL which were plated onto solid LB (agar 20 g/L, LB 25 g/L) supplemented with ampicillin (to 100 $\mu g m L^{-1}$).

7.3.1.5 Miniprep

One single colony was inoculated into liquid LB (25 g/L) supplemented with ampicillin (to 100 $\mu g m L^{-1}$) at 37°C for 16 hours. Then the culture was centrifuged at 3000 rpm for 10 minutes, the medium discarded and the cells were suspended (250 µL) in resuspension buffer (50 mM Tris-HCl, 10 mM EDTA and RNase A to

50 µg/ml, pH 8). Then 250 µL of lysis buffer (0.4 M NaOH and 2% w/v SDS) was added, followed by 350 µL neutralization and binding buffer (4 M guanidine hydrochloride and 0.5 M potassium acetate, pH 4.2). The solution was loaded on a spin column, centrifuged (12 g) and the supernatant discarded. The centrifugation step was repeated after each addition of buffers. Afterwards, washing buffer 1 (5 M Guanidine hydrochloride, 20 mM Tris-HCl, 38% v/v ethanol, pH 6.6) was added, followed by washing buffer 2 (20 mM NaCl, 2 mM Tris-HCl, 80% v/v ethanol, pH 7.5). Elution was performed by adding sterile MQ-H_2O (typically 15 µL) on the center of the spin column, left for 5 minutes at 40°C and by spinning down at 12 g for 30 s. The elution was stored at -20°C and sent for sequencing to Source BioScience (University of Oxford) to confirm its sequence.

7.3.1.6 ME expression and purification

Transformation of competent *E. coli* BL21 (NEB) was carried out as described in Section 7.3.1.4. (using *pLATE51:maeB*) with the only difference that heat shock was done for 10 seconds. A single colony was then inoculated into 100 mL of LB (25 g/L) supplemented with ampicillin (100µgmL^{-1}) for 16 h hours at 37°C. The culture was then scaled up into 500 mL of LB medium (25 gL^{-1}) by transferring 15 mL per flask (typically total volume 5 L). The cells were first grown at 37°C for 3 hours then IPTG was added to 0.5 mM for induction. Cells were left for 20 h at 15°C (180 rpm). Cells were harvested at 6000 rpm for 30 minutes at 4°C and resuspended in buffer (pH 7.4) containing 50 mM HEPES, 150 mM NaCl, 10% glycerol supplemented with two tablets of EDTA free protease inhibitors (Sigma). The cells were then frozen at -80°C. The next day the cells were thawed first for 10 minutes in ice than left shaking at room temperature in a water bath. Cell lysis

was performed with a French press (20 psi, 2 cycles). The lysate was then ultracentrifuged at 45000 rpm for 1 hour at 4°C. The supernatant was loaded in a Ni^{2+} column pre-equilibrated with buffer A (50 mM HEPES, 500 mM NaCl, 50 mM imidazole, 1 mM DTT, pH 7.4) with an ÄKTA system. The lysed cells were then loaded to the column. Buffer A was used for equilibration and washing and buffer B (50 mM HEPES, 500 mM NaCl, 300 mM Imidazole, 1 mM DTT, pH 7.4) for elution. The relevant fractions were selected by looking at the absorbance (280 nm) and by doing a solution assay (Section 7.3.1.12). Fractions (volume from 20 mL to 40 mL) were then concentrated using a centrifugal tube equipped with a 50 kDa membrane (4°C, 3000 rpm). After reaching a final volume of ≈1 mL, dyalisis overnight was performed in a buffer (pH 7.4) containing 50 mM HEPES, 150 mM NaCl, 20 mM $MnCl_2$, 10% glycerol. The protein was then aliquoted (20 µL each), flash-frozen with liquid N_2 and stored at -80°C for further usage.

7.3.1.7 FNR expression and purification

E. coli BL21 was transformed with *pLATE51:fnr* (codifying for a *N*-term His-tagged FNR).[134] A single colony was inoculated into a 100 mL LB (25 gL^{-1}) supplemented with ampicillin (to 100 μgmL^{-1}); then the culture was scaled up to 500 mL (total volume typically 3 L). The cells were grown at 37°C (200 rpm) for 3 h and induction was carried out by adding IPTG (to 1 mM); cells were then left at 37°C for 3 hours (200 rpm) and harvested at 6000 rpm, 4°C for 30 minutes. They were resuspended in buffer (pH 7.4) containing 50 mM HEPES, 150 mM NaCl, 10% glycerol. The cells were then frozen at -80°C. The next day, cells were thawed for 10 minutes, lysed with a French press (20 psi, 2 cycles) and centrifuged at 45000 rpm 4°C for 1 hour. The supernatant was loaded into a Ni^{2+} column

equilibrated and washed with buffer A (50 mM HEPES, 500 mM NaCl, pH 7.4). Buffer B (50 mM HEPES, 500 mM NaCl, 250 mM imidazole, pH 7.4) was used for elution. The relevant fractions were chosen by looking at absorbance (280 nm and 460 nm; the latter for the FAD). The proteins were concentrated with a centrifugal tube equipped with 10 kDa cut-off membrane (4°C, 3000 rpm). A desalting column (Cytiva), equilibrated with buffer A, was used to remove all excess salts. The protein was then aliquoted and frozen at -80°C.

7.3.1.8 AspA expression and purification

AspA was purified with the same protocol as described for ME but using IPTG to a final concentration of 1 mM (see Section 7.3.1.6.).

7.3.1.9 FumC expression

FumC plasmid (pASK40:*fumC*) was kindly provided by Prof. Judy Hirst (University of Cambridge with permission granted by Prof. Todd Weaver from the University of Wisconsin) and purification was carried out with a modified protocol from literature.[172,291] Cells were selected in solid LB (25 g/L, agar 20 g/L) supplemented with ampicillin (50 $\mu g mL^{-1}$). Culture volume was first 100 mL and then scaled up to 500 mL (total volume 3 L). The cells were grown at 32°C (180 rpm), induced with 1 mM IPTG and left at 20°C overnight. They were then harvested at 6000 rpm for 30 min at 4°C. Supernatant was discarded and the pellet resuspended in buffer (100 mL, pH 7.8) containing 50 mM HEPES, 300 mM NaCl and two protease-inhibitor tablets. Cells were lysed with a French press system (20 psi, 2x) and centrifuged at 45000 rpm for 1 h at 4°C. The lysate was loaded on

a Ni^{2+} column. Buffer A (50 mM Hepes, 300 mM NaCl, 60 mM Imidazole, pH 7.8) was used for equilibration and washing and buffer B (50 mM Hepes, 300 mM NaCl, 400 mM Imidazole, pH 7.8) was used for elution. The cells were then dialysed in buffer (pH 7.8) containing 50 mM HEPES, 150 mM NaCl, 10% Glycerol and flash frozen as described for ME (see Section 7.3.1.6.). Solution assay in Section 7.3.1.12.

7.3.1.10 Protein concentration: Bradford method

Protein concentration was measured with the Bradford method.[275]

7.3.1.11 SDS gel

A precast gel (NuPage 4-12% Bis-Tris Midi Gel) was purchased from ThermoFischer. A voltage of 200 V was applied using a running buffer containing (500 mL, diluted 20 times in the final solution): 104.6 g MOPS, 60.6 g Tris Base, 10 g SDS, 3.0 g EDTA, pH 7.7. Protein molecular weight marker was purchased from NEB. For staining concentrated InstantBlue (Sigma) was added to a container containing the gel at room temperature for 20 minutes. The staining solution was discarded and the gel washed with DI H_2O.

7.3.1.12 Solution assay

ME: NADPH consumption or production was monitored by measuring the absorbance at 340 nm. Buffers: 50 mM Tris-HCl, 4 mM $MgCl_2$, 50 mM Malate, 1 mM $NADP^+$, pH 7.4 (Section 2.4.1.); To study steady-state kinetics, CO_2-saturated buffer for reductive carboxylation: 0.05 M HEPES, 4 mM $MgCl_2$, 1 mM $MnCl_2$, (pH 7.5). For oxidative decarboxylation: 0.05 M MOPS, 4 mM $MgCl_2$, 1 mM $MnCl_2$, (pH

7.5). Pyruvate was added to 0, 1, 2, 4, 6, 8, 10, 20, 50 mM and malate to 0, 0.05, 0.1, 0.5, 1, 2, 4, 6, 8, 10, 20, 50 mM. ME final concentration was: 0.11 µM (downstream direction) and 0.011 µM (upstream).

FumC and AspA: fumarate consumption or production was monitored by looking at the absorbance at 250 nm (for production) and 250 nm and 293 nm (for consumption at concentration lower than 1 mM and for concentration higher than 1 mM, respectively, because of the high extinction coefficient, see Section 4.6.6.). Buffer in the downstream: 0.05 M HEPES, 4 mM $MgCl_2$, 1 mM $MnCl_2$, (pH 7.5). Buffer upstream: 0.05 M MOPS, 4 mM $MgCl_2$, 1 mM $MnCl_2$, (pH 7.5). Concentrations of substrate: for malate 0, 0.05, 0.1, 0.5, 1, 2, 4, 6, 8, 10, 20, 50 mM; for fumarate from 0, 0.02, 0.1, 0.25, 0.5, 0.9 mM (tested at 250 nm) and 1, 2, 4, 8, 10, 20 mM (tested at 293 nm); for aspartate 0.02, 0.05, 0.1, 0.5, 1, 2, 4, 8, 10, 20, 50 mM. FumC final concentration: 0.409 µM; AspA, 0.0584 µM. Lambert-Beer law was used to convert absorbance into mol/L, using literature values of ε: for NADPH 6.22 mM^{-1} cm^{-1},[176] while for fumarate 1.45 mM^{-1} cm^{-1} at 250 nm. and 0.082 mM^{-1} cm^{-1} at 293 nm.[243]

4-enzyme cascade: reduction of Benzyl viologen (BV) was monitored by looking at absorbance at 600 nm in an anaerobic atmosphere. Reactions were carried out in 0.05 M MOPS, 4 mM $MgCl_2$, 1 mM $MnCl_2$, 50 mM BV, 20 µM $NADP^+$. Aspartate was injected to a final concentration of 20 mM. Enzyme stocks were diluted accordingly to obtain in solution a ratio of 5 FNR/1 ME/1 FumC/1 AspA where 1 = 0.86 nmol. This amount was decreased to 0.086, 0.043 and 0.17 nmol in experiments with diluted enzymes. The literature ε value of reduced BV at 600 nm was used to convert the absorbance to a concentration (7.2 mM^{-1} cm^{-1}). The slope value at highest rate was used to calculate the rate.

7.3.2 Electrode preparation

FTO glass was used as a support for the photoanode, the collector and the generator electrode, while titanium foil (Ti foil) and ITO glass for the cathode. The materials were first cut into 1x2 cm size and cleaned in deionized (dd)-H_2O, ethanol and acetone in a sonication bath for 15 minutes each step.

7.3.2.1 Cathode preparation

7.3.2.1.1 Electrophoretic deposition (EPD)

Indium tin oxide (ITO, Sigma, < 50 nm) and α-Fe_2O_3 (see Section 7.3.2.2.1.) were deposited by EPD[192] either on titanium or conductive glass support. An EPD deposition bath was prepared by suspending a metal oxide and iodine. For ITO: 0.02 g ITO and 0.01 g I_2; for α-Fe_2O_3: 0.1 g α-Fe_2O_3 and 0.02 g I_2 in 20 mL of acetone. The deposition condition was 10 V for 6 minutes per side (in case of ITO), while 10 s for α-Fe_2O_3. The electrodes were then dried, stored and rinsed before any usage. The mechanism through which electrophoretic deposition occurs was investigated by Koura et al.[192] The authors observed an increase of the conductivity of the acetone bath in presence of I_2. Koura *et al*. suggested that the first step is keto-enol tautomerization of acetone (step 1, see below), followed by iodination of the enol resulting in the formation of HI (step 2, see below). The metal oxide nanoparticles become positively charged after the adsorption of H^+ to the surface. The overall proposed mechanism is described in the equations below.

$$Step\ 1: CH_3COCH_3 \overset{H_2O}{\rightleftarrows} CH_3C(OH)CH_2$$

$$Step\ 2: CH_3C(OH)CH_2 + I_2 \rightarrow CH_3COCH_2I + I^- + H^+$$

Through application of an electric potential between two electrodes the positively charged nanoparticles migrate to the negative counter electrode.

7.3.2.1.2 PGE electrodes

PGE electrodes were prepared as reported previously.[287]

7.3.2.1.3 Introduction of controlled-size pores (Doctor blade)

A paste for a doctor blade method was prepared with a modified protocol from the reported protocol for the preparation of mesoporous TiO_2 paste.[292] First, ITO (0.5 g) was mixed with MQ-H_2O (2 mL) and ethanol (4 mL). The suspension was diluted with ethanol (70 mL), stirred for 15 minutes, and sonicated for 30 minutes. Then, 2 g of α–terpineol (Insight Biotechnology) was added. The suspension was stirred and sonicated again (15 min and 30 min, respectively). A volume of 100 mL of ethanol containing 0.3 g ethyl-cellulose (dissolved by sonication) was then mixed with the nanoparticle solution (15 min stirring and 30 min sonicating). Then the suspension was concentrated by heating the sample at 70°C until obtaining a paste. The suspension was then painted directly on the electrode and sintered at 550°C for 1 hour with a heat ramp of 5°C/min.

Addition of PS beads (see Section 6.2.2) of size: 1 µM, 0.5 µM, 0.1 µM was performed by mixing them with ITO in a ratio of 2:1 (by weight, PS beads:ITO). The total mass was reduced to 50 mg and protocol above was changed accordingly.

7.3.2.2 Photoanode preparation

7.3.2.2.1 Hematite

α-Fe_2O_3 was prepared with two protocols (see Section 3.4.1.). A solution of 0.2 M urea and 0.1 M $FeCl_2$ was heated at 150 °C for 10 hours in a Teflon-lined autoclave. A cleaned FTO glass was left inside, with the conducting side facing the Teflon wall. The product, FeOOH, was washed in MQ-H_2O three times, and dried in the oven. The powder was then calcined at 550 °C for 1.5 hours (10°C/min). Electrophoretic deposition was performed as described in Section 7.3.2.1.1. The electrodes then were calcined at 800°C for 10 minutes, without letting them to cool down inside the furnace. The resulting electrodes were defined as EPD-prepared hematite. In case of the FTO left inside the autoclave, this was rinsed and calcined at 550°C for 1.5 hours (10°C/min). Then, it was calcined at 800°C for 10 minutes and taken immediately out of the furnace.

Cobalt borate was photo-electrodeposited (Xe lamp: 300 W) by doing a chronoamperometry in a three electrode system in one compartment cell (CE: Pt, RE: Ag/AgCl) using a solution of 0.1 M $Co(NO_3)_2$ in 12.5 mM $Na_2B_4O_7$.

7.3.2.2.2 Bismuth Vanadate

Bismuth Vanadate ($BiVO_4$) was deposited using a literature reported procedure.[84] Briefly, in order to prepare a 2%Mo:$BiVO_4$ three separate precursor solutions were prepared: 0.2 M $BiNO_3$ in acetic acid, 0.03 M VO(acac) in acetylacetone and 0.03 M Mo(acac) in acetylacetone. The solutions were mixed in a Bi:(V + Mo) = 1 atomic ratio and sonicated for 1 hour until a green precursor was formed. Then, 60 µL of the solution was deposited onto a 1 cm^2 area on the

FTO glass which was then calcined at 550°C for 1 hour. The electrodes were then stirred in 1 M NaOH to get rid of remaining vanadium oxide.

FeOOH deposition was performed in a three-electrode system in a one compartment cell (CE: Pt, RE: Ag/AgCl) using a 0.1 M Fe_2SO_4 solution which was first purged with argon for 1 h. A potential of 0.2 V was applied to oxidise Fe^{2+} to Fe^{3+} on the electrode surface under light illumination (for 600 s). Afterwards, an electrodeposition at 1.2 V vs. Ag/AgCl for 60 seconds was carried out to cover completely the electrode surface with FeOOH.

7.3.2.3 FNR loading

FNR was deposited by either dropping 5 µL from the concentrated stock (1.8 mM) or by stirring overnight in a 50 mM borate buffer, pH 8 containing FNR (15 µM, 2.5 mL). The electrode was rinsed thoroughly with MQ-H_2O and then used for electrochemical experiments.

7.3.2.4 Loading of 4-enzyme and 5-enzyme cascade

The ITO/Ti electrode was prepared as described in Section 7.3.2.1.1. A mixture of the enzymes (for the four enzymes: FNR/ ME/ FumC/ AspA) and (for the five enzymes: CA/ FNR/ME/ FumC/ AspA) were mixed by preparing a concentrated enzyme solution (droplet) where 1 enzyme equivalent is equal to a final concentration in the droplet of 0.1 mM. Hence, in 20 µL, 1 enzyme equivalent = 2 nmol; in 10 uL = 1 nmol. In case of higher surface area a larger volume (same final concentrations) was used; a volume of 20 µL was dropped on each 1.6±0.3 cm^2 used to reach the final surface area. In Section 4.4.3. and 4.6.6. the relative ratio between the enzymes was varied. Note that in all the enzymes ratios, 1 enzyme

equivalent is relative to 2 nmol/1.6±0.3 cm^2. In case of a PGE electrode the volume was 10 µL for 0.03 cm^2. The enzyme mixture was left absorbing for 20 min and then thoroughly rinsed to remove any unbound protein.

7.3.3 Electrochemistry of the cathode:

7.3.3.1 Cyclic voltammetry

(FNR+ME)@ITO/Ti: cyclic voltammetry of the FNR@ITO electrode was performed at (1 mV/s, 25°C, continuous flow of CO_2 in the headspace) in CO_2-saturated buffer (pH 7.5) containing 0.2 M HEPES 0.1 M $KHCO_3$, 4 mM $MgCl_2$ using Pt as CE and Ag/AgCl as RE. Scan from -0.8 to -0.4 V vs Ag/AgCl. $NADP^+$ was typically added to a final concentration of 20 µM and ME to 2.5 µM. CO_2 was used in the headspace when reductive carboxylation was investigated. Results in Sections 2.4.2.

Cascade: after preparation of the electrode (EPD in Section 7.3.2.1.1. and enzyme loading in 7.3.2.4.) cyclic voltammetry (1 mV/s, stationary, 25°C, CE: Pt; RE: Ag/AgCl) in a buffered solution was carried out in 0.05 M HEPES, 0.1 M $KHCO_3$, 0.1 M NH_4Cl, 4 mM $MgCl_2$, 1 mM $MnCl_2$, 20 mM pyruvate (pH 7.5, argon purging). When unbuffered, the solution contained 0.1 M ammonium carbonate, 4 mM $MgCl_2$, 1 mM $MnCl_2$, 20 mM pyruvate (initial pH 7.5). The 4-enzyme cascade (no carbonic anhydrase included) was performed in CO_2-saturated buffer containing 0.2 M MOPS, 0.1 M $KHCO_3$, 0.1 M NH_4Cl, 4 mM $MgCl_2$, 1 mM $MnCl_2$, 20 mM pyruvate (initial pH 7.5). In all the three cases $NADP^+$ was injected to 20 µM and aspartate to 20 mM. Results in Sections 4.4.1. and 4.6.1.

7.3.3.2 Chronoamperometry

(FNR+ME)@ITO/Ti: Different surface areas were used (from 1 cm^2 to 16 cm^2). Buffers used were 0.2 M HEPES, 0.1 M $KHCO_3$, 4 mM $MgCl_2$, pH 7.5 (Chapter II, III), 0.2 M HEPES 0.1 M $NaHCO_3$, 4 mM $MgCl_2$ (pH 7.5, see Section 2.4.2.1.). A potential of –0.45 V vs. SHE was applied at 25°C, under stirring and continuous flow of CO_2. $NADP^+$ was injected to 20 µM (1 µM in Section 2.4.2.5.), pyruvate to 20 mM.

Cascade: different surface areas were used (from 0.03 cm^2 to 12 cm^2). Buffer for reduction (-0.45 V vs. SHE, stirring, 25°C, under anaerobic atmosphere in a glove box): 0.05 M HEPES, 0.1 M NH_4Cl, 4 mM $MgCl_2$, 1 mM $MnCl_2$, pH 7.5. $NADP^+$ was injected to 20 µM and $KHCO_3$ to 0.1 M unless stated otherwise. Buffer for oxidation (+0.1 V vs. SHE, stirring, 25°C, under argon – except for experiment in Section 4.4.2.): 0.05 M MOPS, 0.1 M $KHCO_3$, 4 mM $MgCl_2$, 1 mM MnCl2, pH 7.5. The oxidative deamination reaction was investigated at pH 8 in buffer containing 0.05 M Borate 0.1 mM $KHCO_3$, 0.1 M NH_4Cl, 4 mM $MgCl_2$, 1 mM $MnCl_2$ (see Section 4.6.5.). Electrodes prepared as described in 7.3.2.1.1. and 7.3.2.4. $NADP^+$ was injected to 20 µM and aspartate to 20 mM.

7.3.3.3 Solution exchange

Buffer exchange experiments were performed in sections 2.4.2.5., 3.4.6., 4.4.2., 4.6.4. The solution after 20 h (unless stated otherwise) of a chronoamperometric experiment was discarded, and the cell was washed 10 times with mq-H_2O and once with fresh buffer. Then fresh buffer without any substrate was reintroduced in the cell. Reaction was then restarted by injecting $NADP^+$

(typically to 20 µM, unless otherwise stated) or $KHCO_3$ to 0.1 M or aspartate to 20 mM.

7.3.3.4 CO_2 titration

Carbon dioxide titration was carried out both by cyclic voltammetry and chronoamperometry. The experiment was carried out in buffer (pH 7.5) containing 0.2 M HEPES, 4 mM $MgCl_2$. The FNR@ITO/Ti electrode was prepared as described in Section 7.3.2.1.1. and 7.3.2.3. The reaction was continuously purged with argon. At the same time an aliquot of the buffer (15 mL) was saturated with CO_2. $NADP^+$ was injected to a final concentration of 20 µM and ME to 2.5 µM. A cyclic voltammetry was performed as described in Section 7.3.3.1 and a chronoamperometry was carried out by applying a potential -0.45 V vs. SHE, stirring, 25°C, under Argon.

After two hours from ME injection, aliquots of the CO_2-saturated buffer were then added to the cell to reach final CO_2 concentration (0.4, 1, 2, 4, 10, 20, 50, 100%). Immediately after each injection the gas composition in the headspace was changed with the usage of two mass flow controllers (MFCs), connected to 100% Argon and CO_2 cylinder (either 4% CO_2 to perform the first four injections or 100% CO_2 for the rest). In the CV the current at –0.45 V vs. SHE was used as the catalytic rate. The normalized relative increase of current was calculated with the following equation:

$$\text{Normalized current } (i) \text{ increase} = \frac{i - i(0\%\ CO_2)}{i(100\%\ CO_2)}$$

The obtained values were plotted against CO_2 percentage and fitted to the Michaelis-Menten equation. Results are shown in Section 2.4.2.3.

7.3.3.5 Rotation dependence experiment with the five-enzyme cascade

An ITO/PGE electrode was prepared as described in 7.3.2.1.2. and the 5-enzymes cascade loaded as in Section 7.3.2.4. The experiment was carried out in a glove box in a two-compartments cell using Pt as CE (in the same compartment as WE) and Ag/AgCl as RE. Buffer for the reduction: 0.05 M HEPES,0.1 M $KHCO_3$, 0.1 M NH_4Cl, 4 mM $MgCl_2$, 1 mM $MnCl_2$. $NADP^+$ was injected to 20 µM. Initial rotation rate: 1000 rpm. A chronoamperometry (-0.45 V vs. SHE) was started and rotation rate was changed at specific time points from 1000 rpm to 0 rpm. After 1 h the solution was discarded, the cell washed 10 times with MQ-H_2O and once with buffer. Then. fresh buffer (pH 7.5) containing 0.05 M MOPS, 4 mM $MgCl_2$, 1 mM $MnCl_2$ was added to the cell. A potential of +0.1 V vs. SHE was then applied to drive the oxidation reaction. Rotation rate was then investigated as described above (see Section 4.4.2.).

7.3.4 Nuclear magnetic resonance (NMR)

Analysis by ^{1}H-NMR was carried out with a Bruker AVIIHD 400 instrument. Samples of the reactions were either treated by adding concentrated HCl (5 sample:1 HCl) or EDTA (pH 8, 0.5 mM); for the latter it was added to a final concentration of 10 mM. Then, a solution mixture of 90:10% of H_2O:D_2O was prepared. Moreover, a capillary containing an internal standard 3-(Trimethylsilyl)propionic-2,2,3,3-d4 acid sodium salt (TMSP, 1.24 mM in Chapter II and III and 4.2 mM in Chapter IV) was inserted in the NMR tube for quantification, knowing that TMSP gives a singlet due to 9 H^+ at 0 ppm.

The TMSP standard was prepared by filling and sealing glass capillaries with TMSP (to 10 mM) and the apparent concentration of the capillary was calculated by comparing the area of the standard with the peak of a known compound (here α-ketoglutarate, to 25 mM). The average peak area was taken into account for quantification. NMR are shown in Sections 2.4.2.4, 3.4.5. and 4.4.3.

7.3.5 Linear sweep of the photoanode

Hematite performance was investigated in 0.05 M borate (pH 8), while $BiVO_4$ in 0.5 M borate pH 9 containing 4 mM $MgCl_2$. Both were investigated at 25°C in a single compartment cell using Pt as CE and Ag/AgCl as RE. First three scans were performed in the dark followed then by 3 scans in the light (Xe lamp, 300 W, held at 6.5 cm, 0.92 sun). Results in Section 3.4.1.

7.3.6 Light-driven NADPH production

Light-driven NADPH production was performed in a buffer (typically 4 mL, pH 8) containing 0.05 M borate using FNR@ITO/Ti as WE electrode (2 cm^2, prepared as described in Sections 7.3.2.1.1. and 7.3.2.3.). The photoanode (hematite, see Section 7.3.2.2.1.) was used as both CE and RE and a potential was applied using the potentiostat (typically −1.2 V vs. CE, unless state otherwise). Argon was continuously flushed in the cell. The experiment was first carried out in the dark, then Xe-lamp (300 W, 0.92 sun) was switched on. $NADP^+$ was injected to reach a final concentration of 100 µM (unless stated otherwise). Aliquots (500 µL) were taken from the cell and NADPH production was monitored by looking at the absorbance at 340 nm. Results in Section 3.4.2.

7.3.7 Light-driven reductive carboxylation

A typical light driven experiment was setup in a two compartments-cell separated by a Nafion-115 membrane (prior to the experiment the membrane was treated with H_2O, H_2O_2, 0.5 M H_2SO_4 for one hour each), then glued with epoxy in the joints of an *in-house* electrochemical cell. The anode compartment contained 0.5 M Borate, 4 mM $MgCl_2$ (pH 9) while the cathode compartment 0.05 M phosphate, 0.1 M $KHCO_3$, 4 mM $MgCl_2$, 80 mM Pyruvate (pH 7.5). Photoanode: 2%Mo:$BiVO_4$/FeOOH (see Section 7.3.2.2.2.); cathode: FNR@ITO/Ti (12 cm^2, see Section: 7.3.2.1.1. and 7.3.2.3.). WE: FNR@ITO/Ti; CE/RE: 2%Mo:$BiVO_4$/FeOOH or 2%Mo:$BiVO_4$/FeOOH-Si solar cell. The solar cell provided 1 V and its potential was cut off with the use of a set of resistors to 0.5 V.

The cathode compartment was continuously flushed with CO_2 at 10 scc/m. The anode compartment was sealed and flushed with Argon in order to allow electrochemical oxygen quantification. Electrochemical O_2 quantification was carried out with a secondary potentiostat using a two-electrode system described in Section 7.3.8. The experiment was started in the dark and light was provided by a Xe-lamp held at 6.5 cm from the photoanode (0.92 sun). $NADP^+$ was injected to 50 µM and ME to 2.5 µM. Samples of the cathode compartment were taken for NMR analysis. Results in Section 3.4.5.

7.3.8 Oxygen and hydrogen gas detection

Gas chromatography was used to detect hydrogen in the cathode compartment at 30°C for 10 minutes. Oxygen was quantified by using a modified protocol of the collection generator system reported by Sherman *et al*.[206] Briefly a FTO collector electrode was held at a 1-2 mm close to the photoanode and a Pt wire was glued to its non-conductive side. The FTO collector was held at a negative

potential (–1.8 V vs. Pt) to reduce the oxygen being produced by the photoanode. The collector generator was first calibrated to measure the collection efficiency using a secondary FTO (generator) held at an oxidative potential to catalyse water oxidation (3.0 V vs. Pt). By measuring the average of the ratio between charge passed at the collector and at the generator, the collection efficiency was calculated as follows:

$$FE_{col\,eff} = {Q_{col}}/{Q_{gen}}$$

To calculate the faradaic efficiency of the system the following equation was used:

$$FE_{O_2} = \left({Q_{col}}/{Q_{gen}}\right) \times \left(\frac{1}{FE_{col\,eff}}\right)$$

In the equation above $Q_{col,}$ is the charge passed at the collector, Q_{gen} is the charge passed at the generator – the photoanode. Results in Sections 3.4.4. and 3.4.5.

7.3.9 Faradaic efficiency dependence on the applied potential

A light driven reductive carboxylation was carried out in a two-compartment cell. Here, the cathode surface area was 2 cm^2 and no solar cell was used. Hence, initially a potential of 0.5 V vs. photoanode was applied. At the beginning the dark current was recorded, then light was switched on. $NADP^+$ was injected to 50 µM and ME to 2.5 µM. Solution exchange was carried out by switching off the light, washing the cathode compartment 10 times with MQ-H_2O and once with buffer. Then, fresh buffer with no substrate and enzyme was reinjected in the electrochemical cell and a different potential vs. photoanode was applied. The potential was changed from 0.5 V to 0.8 V. Light was switched on and when the

current was stable substrates ($NADP^+$ and pyruvate to 50 µM and 80 mM) were injected. Faradaic efficiency at each potential was calculated using the following equation (results in Section 3.4.6.):

$$FE = \frac{total\ current - current\ without\ substrates}{total\ current}$$

7.3.10 Development of a sensor for biocatalyst discovery

7.3.10.1 Preparation of cell lysate

E. coli BL21 cells were transformed as in Section 7.3.1.4. Two parallel single colonies were grown in separate tubes containing 20 mL LB (25 gL^{-1}) supplemented with ampicillin (100 μgmL^{-1}) for 3 h. In one, IPTG was added to a final concentration of 1 mM and expression was carried out at 37 C for 3 h. Cells were harvested at 3000 rpm and resuspended in cell lysis buffer (1 mL, pH 7.5) containing 50 mM HEPES, 150 mM NaCl, 1 mM DTT, 30 µg/mL lysozyme, 10% glycerol. Cell lysis was performed by sonication (20 kHz, 10 s pulse and 30 s rest in ice, 10x). Lysates were frozen at -80°C.

7.3.10.2 Electrochemical experiments with the proposed sensor

A chronoamperometry was carried out as in CO_2-saturated buffer (pH 7.5) containing 0.2 M HEPES, 0.1 M $KHCO_3$, 4 mM $MgCl_2$, 1 mM $MnCl_2$, 20 µM $NADP^+$. Pyruvate was included to the buffer to 80 mM unless stated otherwise. Induced-cell lysate was injected to the electrochemical cell, unless stated otherwise. Results in Section 5.4.

7.3.11 Light-driven $NADP^+$ reduction using FNR-g-C_3N_4 composite

Graphitic-carbon nitride (g-C_3N_4) was synthesized by calcination of 5 g of urea at 550°C for 1 h. The resulting powder was stirred with FNR (15 µM) for 2 h. Then the supernatant was discarded and buffer (pH 8) containing 0.05 M borate and 0.1 M TEA as electron donor was supplemented. $NADP^+$ was injected to 100 µM. Light was switched on and aliquots (600 µL) were taken at each hour. Prior to UV-vis analysis cell samples were spun down at 3000 rpm to discard the nanoparticles. Results in Section 3.4.3.

APPENDIX

A.1. Cloning and purification of AspA

Aspartate ammonia-lyase catalyses the reversible amination of fumarate to aspartate. This enzyme is ubiquitous and used for the industrial production of L-aspartate from fumarate. This section describes cloning and purification of His-tagged AspA. The gene encoding for AspA was cloned by colony PCR using two sets of primers:

Forward:

5′-GGTGATGATGATGACAAGATGTCAAACAACATTCGTATCGAAGAAGAT-3′

Reverse:

5′-GGAGATGGGAAGTCATTATTACTGTTCGCTTTCATCAGTATAGCGTTT-3′

Product amplification was confirmed by electrophoresis (0.8% agarose gel), as shown in **Figure A-1**. The purified PCR product was inserted into the vector pLATE51 (ThermoFisher, to insert an N-terminal His-tag, generating pLATE51:*aspa*) by ligation-independent cloning (LIC) and then used to transform *E. coli* DH5-α cells. After isolating the plasmid, the sequence of ASPA was confirmed by SourceBioScience (Oxford).

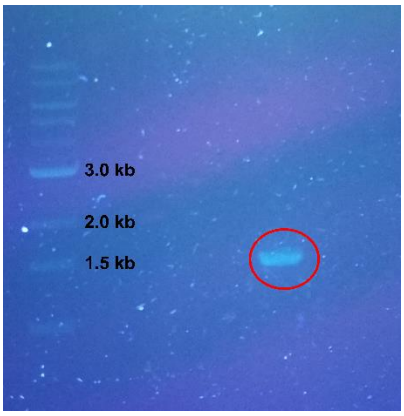


Figure A-1. Agarose gel (0.8%) showing the amplified gene ASPA (1.3 kb). Stained with Red safe and visualized with near UV-light.

The resulting plasmid was used to transform *E. coli* BL21 cells and a glycerol stock was prepared and stored at −80°C for further use. *E. coli* BL21, was transformed with pLATE51:*aspa* and expression was induced with 1 mM IPTG and for 20 hours of expression at 20°C. Elution was performed with a Ni^{2+} column using a linear gradient of an elution buffer containing 300 mM imidazole. A typical elution trace, (see Chapter VII for further details) is shown in **Figure A-2**. A single peak at 280 nm was obtained after optimisation and the protein-containing fractions between 23 mL and 43 mL were selected and concentrated.

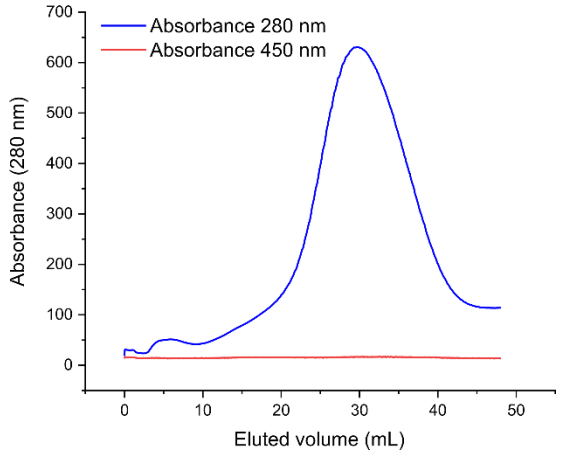


Figure A-2. Elution trace of aspartate ammonia-lyase via Ni^{2+} chromatography. Linear gradient from 50 mM to 300 mM imidazole in 42 minutes. Absorbance at 450 nm was used to monitor the presence of a contaminant, which was observed for ME purification and absorbance at 280 nm was used to monitor protein elution (Chapter II).

In order to confirm enzyme activity, a solution assay monitoring the decrease of absorbance at 250 nm (measuring fumarate consumption) was performed (**Figure A-3**). The extinction coefficient (ε) at 250 nm for fumarate is 1.45 mM^{-1} cm^{-1}, therefore a small concentration was initially used in the assay (93 µM).[238] Injection of the enzyme initiated catalysis and substrate was titrated in increasing amounts, resulting in an higher initial absorbance value (because of higher fumarate concentration) and increased rates of the reaction confirming the

enzyme was active. Above 930 µM fumarate the absorbance reaches values above 1 because of the high extinction coefficient of fumarate (see above). As previously reported, this enzyme is strictly dependent on Mg^{2+}.[239] In the absence of Mg^{2+}, no amination activity was detected if the NH_4^+ concentration was lower than 500 mM. No catalysis was detected when buffer was injected into the cuvette as a negative control. The optimisation for the production of AspA was highly successful and the purified enzyme was confirmed as active.

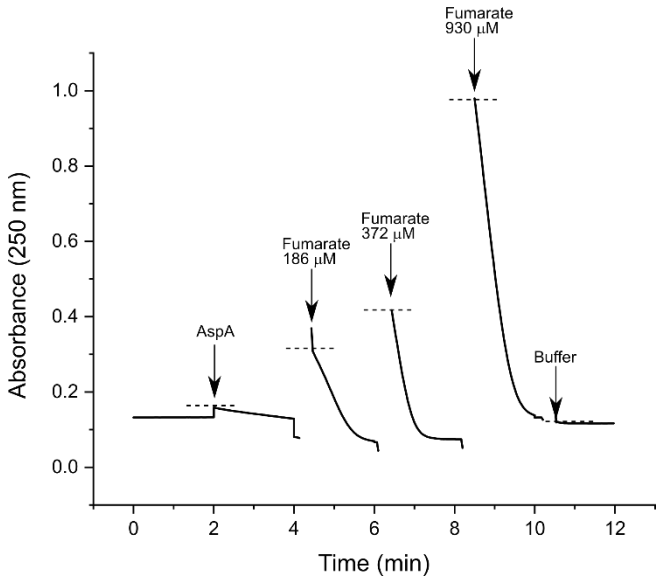


Figure A-3. The catalytic activity of AspA monitored by solution assay. Absorbance at 250 nm attributable to fumarate consumption was monitored. Initial concentration of fumarate was 93 µM. Buffer: 0.2 M HEPES, 0.1 M $KHCO_3$, 0.1 M NH_4Cl, 4 mM $MgCl_2$. Injection of enzyme initiates catalysis and subsequent injections of fumarate to 186, 372 and 930 µM. Control: injection of buffer confirms catalysis is initiated only by injection of enzyme or substrate (fumarate).

A.2. Cloning and purification of Fumarase

The gene encoding for FumC was amplified by colony PCR and ligation-independent cloning was performed with the final goal of using the plasmid (pLATE51, Thermofisher) which encodes for an N-terminal His-tag. The following primers were designed to amplify the gene encoding for FUMC.

Forward:

5′-GGTGATGATGATGACAAGATGAATACAGTACGCAGCGAAAAAG-3′

Reverse:

5′-GGAGATGGGAAGTCATTATTAACGCCCGGCTTTCATACTG-3′

Amplification was confirmed by DNA gel electrophoresis (agarose gel 0.8%) (**Figure A-4**) and the sequence was confirmed by SourceBioScience (Oxford).

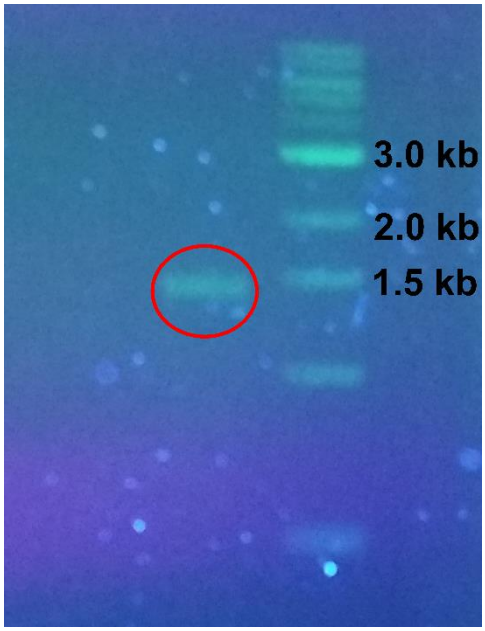


Figure A-4. Agarose gel (0.8%) for FumC (1.3 kb) amplification. Stained with Red safe and visualized with near UV-light.

Initial attempts to express and purify the N-terminal-His-tagged enzyme were unsuccessful. **Figure A-5-A** shows that during elution of the N-term-His tagged FumC a peak at 280 nm was not observed. Typically, the column is washed with H_2O after elution and in that instance, a large peak was observed (**Figure A-5-B**). This may have been the protein, but a solution assay using fractions form the peak, confirmed no activity even after concentrating the elutions from the peak in a repeat experiment. Addition of the His-tag at the N-terminus could have affected the protein structure.

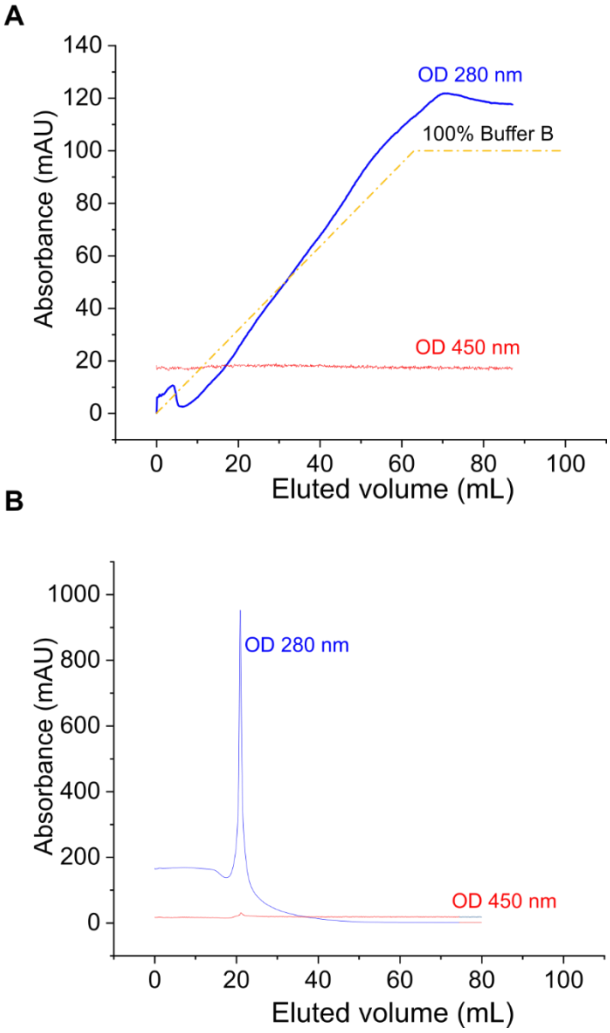


Figure A-5 A. Initial Ni^{2+} chromatography trial for the expression and purification of N-terminal His-tagged FumC from *E. coli* BL21. Plasmid: *pLATE51:fumc*. **A.** Linear gradient from 50 mM to 300 mM imidazole in 42 minutes. Elution trace: no peak was observed. **B.** Washing step after elution shows a very big peak but no enzymatic activity of that fraction was observed.

The crystal structure of FumC from *E. coli* (homotetramer) is available (*pdb*: 1FUO, **Figure A-6**)[293] and shows that both the N-terminus (blue) and C-terminus (orange) of the protein protrude from its surface. However, the N-terminus is closer to the enzyme catalytic sites and highly conserved regions (in green) whilst the C-terminus is further away. Possibly, the N-terminal His-tag could interfere with the correct folding and expression of the enzyme.

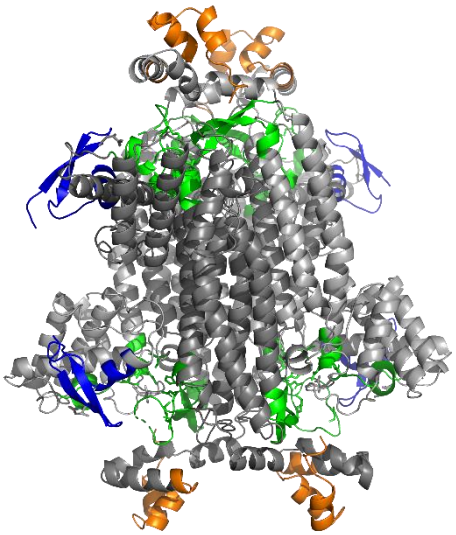


Figure A-6. Crystal structure of FumC (*pdb*: 1FUO, tetramer). The enzyme is a homotetramer consisting of two symmetric dimeric units (in grey). Blue: the N-terminus of the protein; orange: the C-terminus. Both protrude from the protein structure. The four catalytic sites and highly conserved regions are shown in green.[293]

Expression of C-terminus His-tagged FumC was attempted and a plasmid (pASK40:*fumC*) was kindly provided by Prof. Judy Hirst (University of Cambridge with permission granted by Prof. Todd Weaver from the University of Wisconsin). Purification was performed according to a modified protocol from Jones and Hirst.[172,291] The elution trace from Ni^{2+} chromatography is shown in **Figure A-7**. Fractions from 15 mL to 42 mL of the eluted volume were taken further for concentration and dialysis.

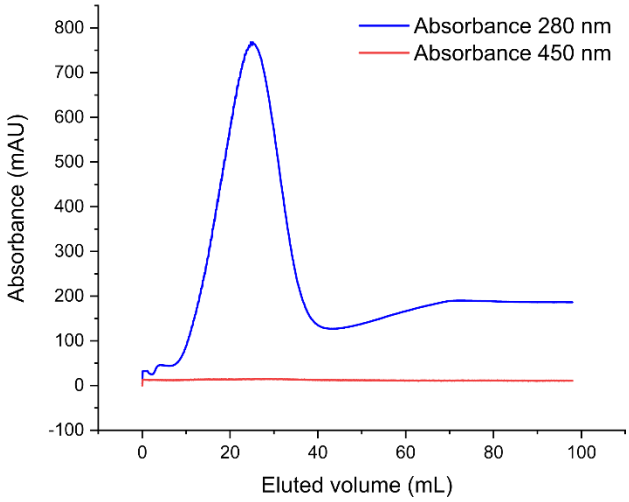


Figure A-7 Elution of C-term His tagged FumC by Ni^{2+} chromatography. Strain: *E. coli* BL21; plasmid: pASK40:*fumC*. Conditions: Ni^{2+} column; linear gradient from 50 mM to 400 mM imidazole in 42 minutes. Fractions from 15 mL to 42 mL were selected for further concentration and dialysis.

A solution assay was performed in a buffer containing 0.2 M HEPES, 0.1 M $KHCO_3$, 4 mM $MgCl_2$ to confirm enzyme activity. Fumarate formation was monitored by looking at the increase of absorbance at 250 nm and malate was injected at different concentrations (from 0.5 mM to 50 mM, **Figure A-8**); the result confirmed that the enzyme was indeed very active.

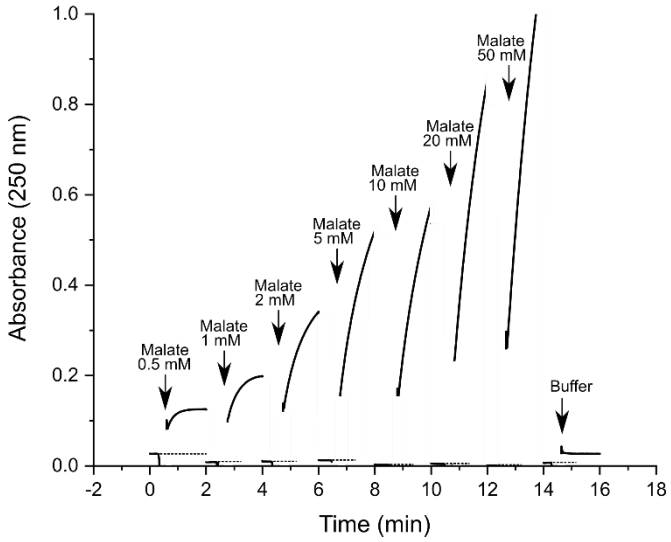


Figure A-8 Solution assay experiment of FumC monitoring fumarate formation (absorbance: 250 nm). Enzyme concentration: 0.028 mM. Buffer: 0.05 M HEPES, 0.1 M $KHCO_3$, 4 mM $MgCl_2$, pH 7.5. Malate was titrated at different concentrations (from 0.5 mM to 50 mM). Control: buffer injection confirmed that catalysis is observed upon enzyme and substrate injection only.

The enzymes which were cloned, expressed and purified as described were visualised and compared to all the other enzymes used in this Thesis via SDS-page (**Figure A-9**). ME, AspA, FumC and FNR were expressed as described (FNR purification described in Siritanaratkul *et al.*)[134], while CA was purchased from Sigma.

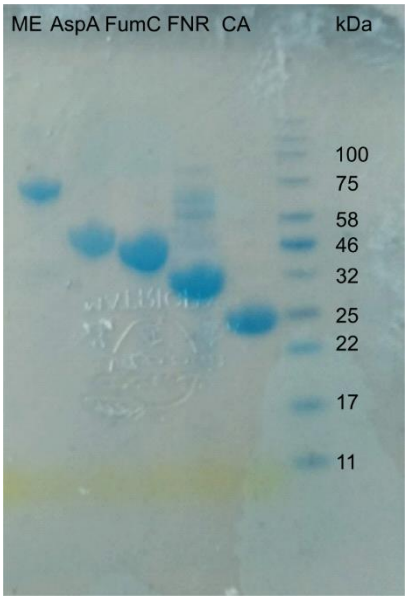


Figure A-9 The cascade enzymes visualised using SDS-gel. ME was cloned, expressed and purified as described in Chapter II. FumC was expressed using pASK40:*fumC* and purified as described above; AspA was cloned, expressed and purified as described in Section 4.6.7. FNR was purified as described in Siritanaratkul *et al.*[134] CA (bovine erythrocytes) was purchased from Sigma.

A.3. Malate oxidative decarboxylation in the absence of CO_2

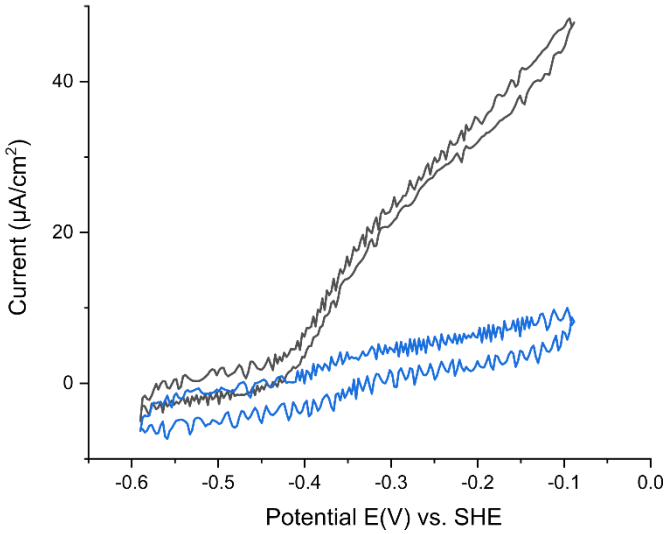


Figure A-10. Malate oxidative decarboxylation current is suppressed by CO_2. Cyclic voltammetry of a (FNR+ME)@ITO/Ti electrode (1 cm^2) in buffer (pH 7.5) containing 0.2 M HEPES, 0.1 M $KHCO_3$, 4 mM $MgCl_2$, 1 mM $MnCl_2$, 50 mM malate, 50 mM pyruvate under a continuous flow of argon. Blue trace represents injection of $NADP^+$ (to 20 µM) and in black the injection of ME (to 2.5 µM). Note that after each injection the electrochemical cell was purged with argon for 3 minutes. In the absence of CO_2, the oxidative decarboxylation catalysed by ME is faster than in its presence (see Figure II-10 for the CV carried out under 100% CO_2). Inhibition by CO_2 supports the result obtained in Chapter IV where the aspartate oxidative deamination current in 100% CO_2 was 4x smaller than the oxidative current obtained in its absence. The traces were corrected for a small offset of 5 µA.

REFERENCES

1. Hoegh-Guldberg, O. *et al.* Impacts of 1.5°C of Global Warming on Natural and Human Systems. *In: Global Warming of 1.5°C. An IPCC Special Report on the impacts of global warming of 1.5°C above pre-industrial levels and related global greenhouse gas emission pathways, in the context of strengthening the global response to the threat of climate change, sustainable development, and efforts to eradicate poverty* (2018).
2. World Health Organization. *Ambient air pollution: a global assessment of exposure and burden of disease*. (2016).
3. Foley, J. A. *et al.* Solutions for a cultivated planet. *Nature* **478**, 337–342 (2011).
4. World Health Organization. *COP24 special report health and climate change* (2018).
5. United Nations. *Paris agreement* (2015).
6. Norgård, J. S. Happy degrowth through more amateur economy. *J. Clean. Prod.* **38**, 61–70 (2013).
7. Lamont, L. A. *History of Photovoltaics*. *Comprehensive Renewable Energy* **1**, (Elsevier Ltd., 2012).
8. King, R. R. *et al.* Solar cell generations over 40 % efficiency. *Prog. Photovoltaics Res. Appl.* 801–815 (2012).
9. Green, M. A., Emery, K., Hishikawa, Y., Warta, W. & Dunlop, E. D. Solar cell efficiency tables (Version 45). *Prog. Photovoltaics Res. Appl.* 1–9 (2015).
10. Feldman, D., Zwerling, M. & Margolis, R. Solar Industry Update. 1–48 (2019).
11. Hammarström, L. & Hammes-schiffer, S. Artificial Photosynthesis and Solar Fuels. *Acc. Chem. Res.* **42**, 1859–1860 (2009).
12. Hisatomi, T. & Domen, K. Introductory lecture: Sunlight-driven water splitting and carbon dioxide reduction by heterogeneous semiconductor systems as key processes in artificial photosynthesis. *Faraday Discuss.* **198**, 11–35 (2017).
13. Ringsmuth, A. K., Landsberg, M. J. & Hankamer, B. Can photosynthesis enable a global transition from fossil fuels to solar fuels, to mitigate climate change and fuel-supply limitations? *Renew. Sustain. Energy Rev.* **62**, 134–

163 (2016).

14. Nelson, D. L. & Cox, M. M. *Lehninger, Principle of Biochemistry*. (Palgrave Macmillan, 2017).
15. Renger, G. Overview of Primary Processes of Photosynthesis. in *Primary Processes of Photosynthesis, Part 1: Principles and Apparatus* (ed. Renger, G.) (RSC Publishing, 2008).
16. Berg, J. M., Tymoczko, J. L. & Stryer, L. *Biochemistry*. (New York: W H Freeman, 2017).
17. Kirilovsky, D. & Büchel, C. Evolution and function of light-harvesting antenna in oxygenic photosynthesis. in *Advances in Botanical Research* **91**, 247–293 (Elsevier Ltd, 2019).
18. Barros, T. & Kühlbrandt, W. Crystallisation, structure and function of plant light-harvesting Complex II. *Biochim. Biophys. Acta* **1787**, 753–772 (2009).
19. Reimers, J. R. *et al.* Challenges facing an understanding of the nature of low-energy excited states in photosynthesis. *BBA - Bioenerg.* **1857**, 1627–1640 (2016).
20. Renger, G. & Renger, T. Photosystem II: The machinery of photosynthetic water splitting. *Photosynth. Res.* **98**, 53–80 (2008).
21. Kato, M., Zhang, J. Z., Paul, N. & Reisner, E. Protein film photoelectrochemistry of the water oxidation enzyme photosystem II. *Chem. Soc. Rev.* **43**, 6485–6497 (2014).
22. Nelson, N. & Junge, W. Structure and Energy Transfer in Photosystems of Oxygenic Photosynthesis. *Annu. Rev. Biochem.* **84**, 659–683 (2015).
23. Volgusheva, A., Kruse, O., Styring, S. & Mamedov, F. Changes in the Photosystem II complex associated with hydrogen formation in sulfur deprived *Chlamydomonas reinhardtii*. *Algal Res.* **18**, 296–304 (2016).
24. Pavlou, A., Jacques, J., Ahmadova, N., Mamedov, F. & Styring, S. The wavelength of the incident light determines the primary charge separation pathway in Photosystem II. *Sci. Rep.* **8**, 1–11 (2018).
25. Voet, D., Voet, J. G. & Pratt, C. W. *Fundamentals of Biochemistry*. (2006).
26. Hames, D. & Hooper, N. *Biochemistry*. (Garland Science, 2011).
27. Skjånes, K., Rebours, C. & Lindblad, P. Potential for green microalgae to

produce hydrogen, pharmaceuticals and other high value products in a combined process. *Crit. Rev. Biotechnol.* **33**, 172–215 (2013).

28. Melis, A. & Happe, T. Hydrogen Production. Green Algae as a Source of Energy. *Plant Physiol.* **127**, 740–748 (2001).
29. Siebel, J. F. *et al.* Hybrid [FeFe]-hydrogenases with modified active sites show remarkable residual enzymatic activity. *Biochemistry* **54**, 1474–1483 (2015).
30. Zalutskaya, Z., Minaeva, E., Filina, V., Ostroukhova, M. & Ermilova, E. Regulation of sulfur deprivation-induced expression of the ferredoxin-encoding FDX5 gene *Chlamydomonas reinhardtii* in aerobic conditions. *Plant Physiol. Biochem.* **123**, 18–23 (2018).
31. Melis, A. Photosystem-II damage and repair cycle in chloroplasts: what modulates the rate of photodamage in vivo? **4**, 130–135 (1999).
32. Yao, D. C. I., Brune, D. C. & Vermaas, W. F. J. Lifetimes of photosystem I and II proteins in the cyanobacterium *Synechocystis* sp. PCC 6803. *FEBS Lett.* **586**, 169–173 (2012).
33. Tsygankov, A. A., Kosourov, S. N., Tolstygina, I. V., Ghirardi, M. L. & Seibert, M. Hydrogen production by sulfur-deprived *Chlamydomonas reinhardtii* under photoautotrophic conditions. *Int. J. Hydrogen Energy* **31**, 1574–1584 (2006).
34. Kosourov, S. *et al.* The Effect of Sulfur Re-Addition on H_2 Photoproduction by Sulfur-Deprived Green Algae. *Photosynth. Res.* **85**, 295–305 (2005).
35. Volgusheva, A., Styring, S. & Mamedov, F. Increased photosystem II stability promotes H_2 production in sulfur-deprived *Chlamydomonas reinhardtii*. *Proc. Natl. Acad. Sci.* **110**, 7223–7228 (2013).
36. Nagy, V. *et al.* The mechanism of photosystem-II inactivation during sulphur deprivation-induced H_2 production in *Chlamydomonas reinhardtii*. *Plant J.* **94**, 548–561 (2018).
37. Krishna, P. S., Morello, G. & Mamedov, F. Characterization of the transient fluorescence wave phenomenon that occurs during H_2 production in *Chlamydomonas reinhardtii*. *J. Exp. Bot.* **70**, 6321–6336 (2019).
38. Krishna, P. S., Styring, S. & Mamedov, F. Photosystem ratio imbalance

promotes direct sustainable H_2 production in: *Chlamydomonas reinhardtii*. *Green Chem.* **21**, 4683–4690 (2019).

39. Englund, E., Shabestary, K., Hudson, E. P. & Lindberg, P. Systematic overexpression study to find target enzymes enhancing production of terpenes in *Synechocystis* PCC 6803, using isoprene as a model compound. *Metab. Eng.* **49**, 164–177 (2018).
40. Fields, F. J., Ostrand, J. T., Tran, M. & May, S. P. Nuclear genome shuffling significantly increases production of chloroplast- based recombinant protein in *Chlamydomonas reinhardtii*. *Algal Res.* **41**, 101523 (2019).
41. Miao, R., Xie, H. & Lindblad, P. Biotechnology for Biofuels Enhancement of photosynthetic isobutanol production in engineered cells of *Synechocystis* PCC 6803. *Biotechnol. Biofuels* **11**, 267 (2018).
42. Chaves, J. E. & Melis, A. Engineering isoprene synthesis in cyanobacteria. *FEBS Lett.* **592**, 2059–2069 (2018).
43. Iandolo, B., Wickman, B., Zorić, I. & Hellman, A. The rise of hematite: origin and strategies to reduce the high onset potential for the oxygen evolution reaction. *J. Mater. Chem. A* **3**, 16896–16912 (2015).
44. Zhang, B. & Sun, L. Artificial photosynthesis: opportunities and challenges of molecular catalysts. *Chem. Soc. Rev.* **48**, 2216–2264 (2019).
45. Fujishima, A. & Honda, K. Electrochemical photolysis of water at a semiconductor electrode. *Nature* **238**, 37–38 (1972).
46. Sivula, K. & Van De Krol, R. Semiconducting materials for photoelectrochemical energy conversion. *Nat. Rev. Mater.* **1**, 1–13 (2016).
47. Le Formal, F. *et al.* Passivating surface states on water splitting hematite photoanodes with alumina overlayers. *Chem. Sci.* **2**, 737–743 (2011).
48. Steier, L. *et al.* Understanding the role of underlayers and overlayers in thin film hematite photoanodes. *Adv. Funct. Mater.* **24**, 7681–7688 (2014).
49. Wang, G. *et al.* Facile Synthesis of Highly Photoactive α-Fe_2O_3-Based Films for Water Oxidation. *Nano Lett.* **11**, 3503–3509 (2011).
50. Nocera, D. G. The artificial leaf. *Acc. Chem. Res.* **45**, 767–776 (2012).
51. Kato, H., Sasaki, Y., Shirakura, N. & Kudo, A. Synthesis of highly active rhodium-doped $SrTiO_3$ powders in Z-scheme systems for visible-light-driven

photocatalytic overall water splitting. *J. Mater. Chem. A* **1**, 12327–12333 (2013).

52. Wang, Q., Hisatomi, T., Ma, S. S. K., Li, Y. & Domen, K. Core/Shell Structured La- and Rh-codoped $SrTiO_3$ as a Hydrogen Evolution Photocatalyst in Z-scheme Overall Water Splitting under Visible Light Irradiation. *Chem. Mater.* **26**, 4144–4150 (2014).
53. Wang, Q. *et al.* Particulate photocatalyst sheets for Z-scheme water splitting : advantages over powder suspension and photoelectrochemical systems and future challenges. *Faraday Discuss.* **197**, 491–504 (2017).
54. Shinde, P. S. *et al.* Surfactant and TiO_2 underlayer derived porous hematite nanoball array photoanode for enhanced photoelectrochemical water oxidation. *Chem. Eng. J.* **320**, 81–92 (2017).
55. Bessekhouad, Y., Robert, D. & Weber, J.-V. Photocatalytic activity of Cu_2O/TiO_2, Bi_2O_3/TiO_2 and $ZnMn_2O_4/TiO_2$ heterojunctions. *Catal. Today* **101**, 315–321 (2005).
56. Inoue, H., Yamachika, M. & Yoneyama, H. Photocatalytic Conversion of Lactic-Acid to Malic-Acid through Pyruvic-Acid in the Presence of Malic Enzyme and Semiconductor Photocatalysts. *J. Chem. Soc. Trans.* **88**, 2215–2219 (1992).
57. Cendula, P. *et al.* Calculation of the Energy Band Diagram of a Photoelectrochemical Water Splitting Cell. *J. Phys. Chem. C* **118**, 29599–29607 (2014).
58. Grätzel, M. Photoelectrochemical cells. *Nature* **414**, 338–344 (2001).
59. Zhang, L., Can, M., Ragsdale, S. W. & Armstrong, F. A. Fast and Selective Photoreduction of CO_2 to CO Catalyzed by a Complex of Carbon Monoxide Dehydrogenase, TiO_2, and Ag Nanoclusters. *ACS Catal.* **8**, 2789–2795 (2018).
60. Lyu, H. *et al.* An Al-doped $SrTiO_3$ photocatalyst maintaining sunlight-driven overall water splitting activity for over 1000 h of constant illumination. *Chem. Sci.* **10**, 3196–3201 (2019).
61. Dotan, H., Sivula, K., Grätzel, M., Rothschild, A. & Warren, S. C. Probing the photoelectrochemical properties of hematite (α-Fe_2O_3) electrodes using hydrogen peroxide as a hole scavenger. *Energy Environ. Sci.* **4**, 958–964

(2011).

62. Shen, S. Toward efficient solar water splitting over hematite photoelectrodes. *J. Mater. Res.* **29**, 29–46 (2014).

63. Sivula, K., Le Formal, F. & Grätzel, M. Solar water splitting: Progress using hematite (α-Fe_2O_3) photoelectrodes. *ChemSusChem* **4**, 432–449 (2011).

64. Chen, Y. H. & Lin, C. C. Effect of nano-hematite morphology on photocatalytic activity. *Phys. Chem. Miner.* **41**, 727–736 (2014).

65. Sivula, K. *et al.* Photoelectrochemical water splitting with mesoporous hematite prepared by a solution-based colloidal approach. *J. Am. Chem. Soc.* **132**, 7436–7444 (2010).

66. Bora, D. K. Fabrication of silicon doped hematite photoelectrode with enhanced photocurrent density via solution processing of an in-situ TEOS modified precursor. *Mater. Sci. Semicond. Process.* **31**, 728–738 (2015).

67. Kim, T. W. & Choi, K.-S. Nanoporous $BiVO_4$ Photoanodes with Dual-Layer Oxygen Evolution Catalysts for Solar Water Splitting. *Science* **343**, 990–994 (2014).

68. Kim, J. H. *et al.* Hetero-type dual photoanodes for unbiased solar water splitting with extended light harvesting. *Nat. Commun.* **7**, 13380 (2016).

69. Park, Y., McDonald, K. J. & Choi, K.-S. Progress in bismuth vanadate photoanodes for use in solar water oxidation. *Chem. Soc. Rev.* **42**, 2321–2337 (2013).

70. Higashi, M., Domen, K. & Abe, R. Highly stable water splitting on oxynitride TaON photoanode system under visible light irradiation. *J. Am. Chem. Soc.* **134**, 6968–6971 (2012).

71. Ong, W.-J., Tan, L.-L., Ng, Y. H., Yong, S.-T. & Chai, S.-P. Graphitic Carbon Nitride (g-C_3N_4)-Based Photocatalysts for Artificial Photosynthesis and Environmental Remediation: Are We a Step Closer to Achieving Sustainability? *Chem. Rev.* **116**, 7159–7329 (2016).

72. Caputo, C. A. *et al.* Photocatalytic Hydrogen Production using Polymeric Carbon Nitride with a Hydrogenase and a Bioinspired Synthetic Ni Catalyst. *Angew. Chemie Int. Ed.* **53**, 11538–11542 (2014).

73. Liu, J. *et al.* Metal-free efficient photocatalyst for stable visible water splitting

via a two-electron pathway. *Science* **347**, 970–974 (2015).

74. Wang, X. *et al.* A metal-free polymeric photocatalyst for hydrogen production from water under visible light. *Nat. Mater.* **8**, 76–80 (2009).

75. Wombwell, C., Caputo, C. A. & Reisner, E. [NiFeSe]-Hydrogenase Chemistry. *Acc. Chem. Res.* **48**, 2858–2865 (2015).

76. Brown, K. A. *et al.* Light-driven dinitrogen reduction catalyzed by a CdS:nitrogenase MoFe protein biohybrid. *Science* **352**, 448–450 (2016).

77. Uekert, T., Kuehnel, M. F., Wakerley, D. W. & Reisner, E. Plastic waste as a feedstock for solar-driven H_2 generation. *Energy Environ. Sci.* **11**, 2853–2857 (2018).

78. Hu, C.-C., Nian, J.-N. & Teng, H. Electrodeposited p-type Cu_2O as photocatalyst for H_2 evolution from water reduction in the presence of WO_3. *Sol. Energy Mater. Sol. Cells* **92**, 1071–1076 (2008).

79. Septina, W., Prabhakar, R. R., Wick, R., Moehl, T. & Tilley, S. D. Stabilized Solar Hydrogen Production with CuO/CdS Heterojunction Thin Film Photocathodes. *Chem. Mater.* **29**, 1735–1743 (2017).

80. Anandan, S., Wu, J. J., Bahnemann, D., Emeline, A. & Ashokkumar, M. Crumpled Cu_2O-*g*-C_3N_4 nanosheets for hydrogen evolution catalysis. *Colloids Surfaces A Physicochem. Eng. Asp.* **527**, 34–41 (2017).

81. Kim, W. & Frei, H. Directed Assembly of Cuprous Oxide Nanocatalyst for CO_2 Reduction Coupled to Heterobinuclear ZrOCoII Light Absorber in Mesoporous Silica. *ACS Catal.* **5**, 5627–5635 (2015).

82. Esswein, A. J., Surendranath, Y., Reece, S. Y. & Nocera, D. G. Highly active cobalt phosphate and borate based oxygen evolving catalysts operating in neutral and natural waters. *Energy Environ. Sci.* **4**, 499–504 (2011).

83. Bediako, D. K. *et al.* Structure-activity correlations in a nickel-borate oxygen evolution catalyst. *J. Am. Chem. Soc.* **134**, 6801–6809 (2012).

84. Lee, Y. W. *et al.* Unbiased biocatalytic solar-to-chemical conversion by FeOOH/$BiVO_4$/perovskite tandem structure. *Nat. Commun.* **9**, 4208 (2018).

85. Malara, F. *et al.* α-Fe_2O_3/NiOOH: An Effective Heterostructure for Photoelectrochemical Water Oxidation. *ACS Catal.* **5**, 5292–5300 (2015).

86. Mersch, D. *et al.* Wiring of Photosystem II to Hydrogenase for

Photoelectrochemical Water Splitting. *J. Am. Chem. Soc.* **137**, 8541–8549 (2015).

87. Wilker, M. B. *et al.* Electron transfer kinetics in CdS nanorod-[FeFe]-hydrogenase complexes and implications for photochemical H_2 generation. *J. Am. Chem. Soc.* **136**, 4316–4324 (2014).
88. Sakai, T., Mersch, D. & Reisner, E. Photocatalytic hydrogen evolution with a hydrogenase in a mediator-free system under high levels of oxygen. *Angew. Chemie Int. Ed.* **52**, 12313–12316 (2013).
89. Chaudhary, Y. S. *et al.* Visible light-driven CO_2 reduction by enzyme coupled CdS nanocrystals. *Chem. Commun.* **48**, 58–60 (2012).
90. Morello, G., Siritanaratkul, B., Megarity, C. F. & Armstrong, F. A. Efficient Electrocatalytic CO_2 Fixation by Nanoconfined Enzymes via a C3-to-C4 Reaction That Is Favored over H_2 Production. *ACS Catal.* **9**, 11255–11262 (2019).
91. Turner, N. J. & Kumar, R. Biocatalysis and biotransformation : The golden age of biocatalysis. *Curr. Opin. Chem. Biol.* **43**, A1–A3 (2018).
92. Wang, X. *et al.* Cofactor NAD(P)H Regeneration Inspired by Heterogeneous Pathways. *Chem* **2**, 621–654 (2017).
93. Hildebrand, F., Kohlmann, C., Franz, A. & Lütz, S. Synthesis, characterization and application of new rhodium complexes for indirect electrochemical cofactor regeneration. *Adv. Synth. Catal.* **350**, 909–918 (2008).
94. Bornscheuer, U. T., Hauer, B., Jaeger, K. E. & Schwaneberg, U. Directed Evolution Empowered Redesign of Natural Proteins for the Sustainable Production of Chemicals and Pharmaceuticals. *Angew. Chemie Int. Ed.* **58**, 36–40 (2019).
95. Zha, D., Wilensek, S., Hermes, M., Jaeger, K. E. & Reetz, M. T. Complete reversal of enantioselectivity of an enzyme-catalyzed reaction by directed evolution. *Chem. Commun.* **1**, 2664–2665 (2001).
96. Packer, M. S. & Liu, D. R. Methods for the directed evolution of proteins. *Nature Reviews Genetics* **16**, 379–394 (2015).
97. Zhou, C., Xue, Y. & Ma, Y. Evaluation and directed evolution for

thermostability improvement of a GH 13 thermostable aα-glucosidase from Thermus thermophilus TC11. *BMC Biotechnol.* **15**, 97 (2015).

98. Scheiblbrandner, S. *et al.* Evolving stability and pH-dependent activity of the high redox potential Botrytis aclada laccase for enzymatic fuel cells. *Sci. Rep.* **7**, 13688 (2017).
99. Morimoto, Y., Honda, K., Ye, X., Okano, K. & Ohtake, H. Directed evolution of thermotolerant malic enzyme for improved malate production. *J. Biosci. Bioeng.* **117**, 147–152 (2014).
100. Reetz, M. T., Soni, P., Fernández, L., Gumulya, Y. & Carballeira, J. D. Increasing the stability of an enzyme toward hostile organic solvents by directed evolution based on iterative saturation mutagenesis using the B-FIT method. *Chem. Commun.* **46**, 8657–8658 (2010).
101. Ma, S. K. *et al.* A green-by-design biocatalytic process for atorvastatin intermediate. *Green Chem.* **12**, 81–86 (2010).
102. Van Der Donk, W. A. & Zhao, H. Recent developments in pyridine nucleotide regeneration. *Curr. Opin. Biotechnol.* **14**, 421–426 (2003).
103. Al-Saryi, N. A. *et al.* Two NAD-linked redox shuttles maintain the peroxisomal redox balance in *Saccharomyces cerevisiae*. *Sci. Rep.* **7**, 11868 (2017).
104. Fukuzumi, S., Lee, Y.-M. & Nam, W. Catalytic recycling of NAD(P)H. *J. Inorg. Biochem.* **199**, 110777 (2019).
105. France, S. P., Hepworth, L. J., Turner, N. J. & Flitsch, S. L. Constructing Biocatalytic Cascades: In Vitro and in Vivo Approaches to de Novo Multi-Enzyme Pathways. *ACS Catal.* **7**, 710–724 (2017).
106. Song, J. W., Seo, J. H., Oh, D. K., Bornscheuer, U. T. & Park, J. B. Design and engineering of whole-cell biocatalytic cascades for the valorization of fatty acids. *Catal. Sci. Technol.* **10**, 46–64 (2020).
107. Garzón-Posse, F., Becerra-Figueroa, L., Hernández-Arias, J. & Gamba-Sánchez, D. Whole Cells as Biocatalysts in Organic Transformations. *Molecules* **23**, (2018).
108. de Carvalho, C. C. C. R. Whole cell biocatalysts: essential workers from Nature to the industry. *Microb. Biotechnol.* **10**, 250–263 (2017).
109. Stampfer, W., Kosjek, B., Moitzi, C., Kroutil, W. & Faber, K. Biocatalytic

asymmetric hydrogen transfer. *Angew. Chemie Int. Ed.* **41**, 1014–1017 (2002).

110. Wolberg, M., Hummel, W., Wandrey, C. & Müller, M. Highly regio- and enantioselective reduction of 3,5-dioxocarboxylates. *Angew. Chemie Int. Ed.* **39**, 4306–4308 (2000).
111. Yasohara, Y. *et al.* Stereoselective reduction of alkyl 3-oxobutanoate by carbonyl reductase from *Candida magnoliae*. *Tetrahedron Asymmetry* **12**, 1713–1718 (2001).
112. Paddon, C. J. *et al.* High-level semi-synthetic production of the potent antimalarial artemisinin. *Nature* **496**, 528–532 (2013).
113. Porro, D. *et al.* Replacement of a Metabolic Pathway for Large-Scale Production of Lactic Acid from Engineered Yeasts. *Appl. Environ. Microbiol.* **65**, 4211–4215 (1999).
114. Porro, D. *et al.* Development of Metabolically Engineered *Saccharomyces cerevisiae* Cells for the Production of Lactic Acid. *Biotechnol. Prog.* **11**, 294–298 (1995).
115. Tomás-Pejó, E., Oliva, J. M., Ballesteros, M. & Olsson, L. Comparison of SHF and SSF processes from steam-exploded wheat straw for ethanol production by xylose-fermenting and robust glucose-fermenting *Saccharomyces cerevisiae* strains. *Biotechnol. Bioeng.* **100**, 1122–1131 (2008).
116. Buijs, N. A., Siewers, V. & Nielsen, J. Advanced biofuel production by the yeast saccharomyces cerevisiae. *Curr. Opin. Chem. Biol.* **17**, 480–488 (2013).
117. Ascue Avalos, G. A., Toogood, H. S., Tait, S., Messiha, H. L. & Scrutton, N. S. From Bugs to Bioplastics: Total (+)-Dihydrocarvide Biosynthesis by Engineered *Escherichia col*i. *ChemBioChem* **20**, 785–792 (2019).
118. Zebec, Z. & Scrutton, N. S. Genome Editing for the Production of Natural Products in *Escherichia coli*. *Adv. Biosyst.* **2**, 1–6 (2018).
119. Toogood, H. S. & Scrutton, N. S. Retooling microorganisms for the fermentative production of alcohols. *Curr. Opin. Biotechnol.* **50**, 1–10 (2018).
120. Hepworth, L. J. *et al.* Enzyme Cascades in Whole Cells for the Synthesis of

Chiral Cyclic Amines. *ACS Catal.* **7**, 2920–2925 (2017).

121. Eckstein, M., Daußmann, T. & Kragl, U. Recent developments in NAD(P)H regeneration for enzymatic reductions in one- and two-phase system. *Biocatal. Biotransformation* **22**, 89–96 (2004).
122. Lauterbach, L., Lenz, O. & Vincent, K. A. H_2-driven cofactor regeneration with $NAD(P)^+$-reducing hydrogenases. *FEBS J.* **280**, 3058–3068 (2013).
123. Adlercreutz, P. Cofactor regeneration in biocatalysis in organic media. *Biocatal. Biotransformation* **14**, 1–30 (1996).
124. Al-Shameri, A. *et al.* Synthesis of: *N*-heterocycles from diamines via H_2-driven NADPH recycling in the presence of O_2. *Green Chem.* **21**, 1396–1400 (2019).
125. Hollmann, F. & Schmid, A. Electrochemical regeneration of oxidoreductases for cell-free biocatalytic redox reactions. *Biocatal. Biotransformation* **22**, 63–88 (2004).
126. Hollmann, F., Arends, I. W. C. E. & Buehler, K. Biocatalytic Redox Reactions for Organic Synthesis: Nonconventional Regeneration Methods. *ChemCatChem* **2**, 762–782 (2010).
127. Willner, I., Mandler, D. & Riklin, A. Photoinduced carbon dioxide fixation forming malic and isocitric acid. *J. Chem. Soc. Chem. Commun.* 1022–1024 (1986).
128. Zhang, L., Vilà, N., Kohring, G. W., Walcarius, A. & Etienne, M. Covalent Immobilization of (2,2′-Bipyridyl) (Pentamethylcyclopentadienyl)-Rhodium Complex on a Porous Carbon Electrode for Efficient Electrocatalytic NADH Regeneration. *ACS Catal.* **7**, 4386–4394 (2017).
129. Steckhan, E. *et al.* Analytical Study of a Series of Substituted (2,2′-Bipyridyl) (pentamethylcyclopentadienyl)rhodium and -iridium Complexes with Regard to Their Effectiveness as Redox Catalysts for the Indirect Electrochemical and Chemical Reduction of $NAD(P)^+$. *Organometallics* **10**, 1568–1577 (1991).
130. Yuan, M., Kummer, M. J., Milton, R. D., Quah, T. & Minteer, S. D. Efficient NADH Regeneration by a Redox Polymer-Immobilized Enzymatic System. *ACS Catal.* **9**, 5486–5495 (2019).

131. Carrillo, N. & Ceccarelli, E. A. Open questions in ferredoxin-NADP$^+$ reductase catalytic mechanism. *Eur. J. Biochem.* **270**, 1900–1915 (2003).

132. Musumeci, M. A., Ceccarelli, E. A. & Catalano-Dupuy, D. L. The Plant–Type Ferredoxin-NADP$^+$ Reductases. in *Advances in Photosynthesis - Fundamental Aspects* (IntechOpen, 2012).

133. Musumeci, M. A., Botti, H., Buschiazzo, A. & Ceccarelli, E. A. Swapping FAD binding motifs between plastidic and bacterial ferredoxin-NADP(H) reductases. *Biochemistry* **50**, 2111–2122 (2011).

134. Siritanaratkul, B. *et al.* Transfer of photosynthetic NADP$^+$/NADPH recycling activity to a porous metal oxide for highly specific, electrochemically-driven organic synthesis. *Chem. Sci.* **8**, 4579–4586 (2017).

135. Aliverti, A., Pandini, V., Pennati, A., de Rosa, M. & Zanetti, G. Structural and functional diversity of ferredoxin-NADP$^+$ reductases. *Arch. Biochem. Biophys.* **474**, 283–291 (2008).

136. Deng, Z. *et al.* A productive NADP$^+$ binding mode of ferredoxin-NADP$^+$ reductase revealed by protein engineering and crystallographic studies. *Nat. Struct. Biol.* **6**, 847–853 (1999).

137. Piubelli, L. *et al.* Competition between *C*-terminal tyrosine and nicotinamide modulates pyridine nucleotide affinity and specificity in plant ferredoxin-NADP$^+$ reductase. *J. Biol. Chem.* **275**, 10472–10476 (2000).

138. Shin, M. Ferredoxin-NADP$^+$ Reductase from Spinach. *Methods Enzymol.* **23**, 440–447 (1971).

139. Megarity, C. F. *et al.* Electrified Nanoconfined Biocatalysis with Rapid Cofactor Recycling. *ChemCatChem* **11**, 5662–5670 (2019).

140. Hurley, J. K. *et al.* Structure-function relationships in *Anabaena* ferredoxin/ferredoxin:NADP$^+$ reductase electron transfer: Insights from site-directed mutagenesis, transient absorption spectroscopy and X-ray crystallography. *Biochim. Biophys. Acta* **1554**, 5–21 (2002).

141. Siritanaratkul, B. Enzyme-material composites for solar-driven reactions. (DPhil Thesis, University of Oxford, 2017).

142. Daido, T. & Akaike, T. Electrochemistry of cytochrome c: influence of coulombic attraction with indium tin oxide electrode. *J. Electroanal. Chem.*

344, 91–106 (1993).

143. Rodkey, F. L. & Donovan Jr., J. A. Oxidation-reduction potentials of the triphosphopyridine nucleotide system. *J. Biol. Chem.* **234**, 677–680 (1959).
144. Wan, L., Megarity, C. F., Siritanaratkul, B. & Armstrong, F. A. A hydrogen fuel cell for rapid, enzyme-catalysed organic synthesis with continuous monitoring. *Chem. Commun.* **54**, 972–975 (2018).
145. Wan, L. *et al.* Enzyme-catalysed enantioselective oxidation of alcohols by air exploiting fast electrochemical nicotinamide cycling in electrode nanopores. *Green Chem.* **21**, 4958–4963 (2019).
146. Megarity, C. *et al.* Electrocatalytic Volleyball: Rapid Nanoconfined Nicotinamide Cycling for Organic Synthesis in Electrode Pores. *Angew. Chemie Int. Ed.* **58**, 4948–4952 (2019).
147. Aleku, G. A. *et al.* A reductive aminase from *Aspergillus oryzae*. *Nat. Chem.* **9**, 961–969 (2017).
148. Ziegelmann-Fjeld, K. I., Musa, M. M., Phillips, R. S., Zeikus, J. G. & Vieille, C. A *Thermoanaerobacter ethanolicus* secondary alcohol dehydrogenase mutant derivative highly active and stereoselective on phenylacetone and benzylacetone. *Protein Eng. Des. Sel.* **20**, 47–55 (2007).
149. Lim, R. J. *et al.* A review on the electrochemical reduction of CO_2 in fuel cells, metal electrodes and molecular catalysts. *Catal. Today* **233**, 169–180 (2014).
150. Schwander, T., Von Borzyskowski, L. S., Burgener, S., Cortina, N. S. & Erb, T. J. A synthetic pathway for the fixation of carbon dioxide in vitro. *Science* **354**, 900–904 (2016).
151. Nitopi, S. *et al.* Progress and Perspectives of Electrochemical CO_2 Reduction on Copper in Aqueous Electrolyte. *Chem. Rev.* **119**, 7610–7672 (2019).
152. Gao, D., Arán-Ais, R. M., Jeon, H. S. & Roldan Cuenya, B. Rational catalyst and electrolyte design for CO_2 electroreduction towards multicarbon products. *Nat. Catal.* **2**, 198–210 (2019).
153. Resasco, J. *et al.* Promoter Effects of Alkali Metal Cations on the Electrochemical Reduction of Carbon Dioxide. *J. Am. Chem. Soc.* **139**, 11277–11287 (2017).

154. Hori, Y. Electrochemical CO_2 Reduction on Metal Electrodes. in *Modern Aspects of Electrochemistry* (ed. Springer) **42**, 89–189 (2008).

155. Andrei, V., Reuillard, B. & Reisner, E. Bias-free solar syngas production by integrating a molecular cobalt catalyst with perovskite–$BiVO_4$ tandems. *Nat. Mater.* **19**, 189–194 (2020).

156. Ross, M. B. *et al.* Designing materials for electrochemical carbon dioxide recycling. *Nat. Catal.* **2**, 648–658 (2019).

157. Wang, Y., Liu, J., Wang, Y., Wang, Y. & Zheng, G. Efficient solar-driven electrocatalytic CO_2 reduction in a redox-medium-assisted system. *Nat. Commun.* **9**, 5003 (2018).

158. Klinkova, A. *et al.* Rational Design of Efficient Palladium Catalysts for Electroreduction of Carbon Dioxide to Formate. *ACS Catal.* **6**, 8115–8120 (2016).

159. Zhou, Y. *et al.* Dopant-induced electron localization drives CO_2 reduction to C2 hydrocarbons. *Nat. Chem.* **10**, 974–980 (2018).

160. De Luna, P. *et al.* What would it take for renewably powered electrosynthesis to displace petrochemical processes? *Science* **364**, (2019).

161. Bachmeier, A., Hall, S., Ragsdale, S. W. & Armstrong, F. A. Selective visible-light-driven CO_2 reduction on a p-type dye-sensitized NiO photocathode. *J. Am. Chem. Soc.* **136**, 13518–13521 (2014).

162. Noji, T., Jin, T., Nango, M., Kamiya, N. & Amao, Y. CO_2 photoreduction by formate dehydrogenase and a Ru-complex in a nanoporous glass reactor. *ACS Appl. Mater. Interfaces* **9**, 3260–3265 (2017).

163. Miller, M. *et al.* Interfacing Formate Dehydrogenase with Metal Oxides for the Reversible Electrocatalysis and Solar-Driven Reduction of Carbon Dioxide. *Angew. Chemie Int. Ed.* **58**, 4601–4605 (2019).

164. Durall, C., Lindberg, P., Yu, J. & Lindblad, P. Increased ethylene production by overexpressing phosphoenolpyruvate carboxylase in the cyanobacterium *Synechocystis* PCC 6803. *Biotechnol. Biofuels* **13**, 1–13 (2020).

165. Durall, C., Rukminasari, N. & Lindblad, P. Enhanced growth at low light intensity in the cyanobacterium *Synechocystis* PCC 6803 by overexpressing phosphoenolpyruvate carboxylase. *Algal Res.* **16**, 275–281 (2016).

166. Greene, D. N., Whitney, S. M. & Matsumura, I. Artificially evolved *Synechococcus* PCC6301 Rubisco variants exhibit improvements in folding and catalytic efficiency. *Biochem. J.* **404**, 517–524 (2007).

167. Mattozzi, M. d., Ziesack, M., Voges, M. J., Silver, P. A. & Way, J. C. Expression of the sub-pathways of the *Chloroflexus aurantiacus* 3-hydroxypropionate carbon fixation bicycle in *E. coli*: Toward horizontal transfer of autotrophic growth. *Metab. Eng.* **16**, 130–139 (2013).

168. Antonovsky, N. *et al.* Sugar Synthesis from CO_2 in *Escherichia coli*. *Cell* **166**, 115–125 (2016).

169. Schwander, T., Von Borzyskowski, L. S., Burgener, S., Cortina, N. S. & Erb, T. J. A synthetic pathway for the fixation of carbon dioxide in vitro. *Science* **354**, 900–904 (2016).

170. Morimoto, Y., Honda, K., Ye, X., Okano, K. & Ohtake, H. Directed evolution of thermotolerant malic enzyme for improved malate production. *J. Biosci. Bioeng.* **117**, 147–152 (2014).

171. Bologna, F. P., Andreo, C. S. & Drincovich, M. F. *Escherichia coli* malic enzymes: Two isoforms with substantial differences in kinetic properties, metabolic regulation, and structure. *J. Bacteriol.* **189**, 5937–5946 (2007).

172. Jones, A. J. Y. & Hirst, J. A spectrophotometric coupled enzyme assay to measure the activity of succinate dehydrogenase. *Anal. Biochem.* **442**, 19–23 (2013).

173. Ohno, Y., Nakamori, T., Zheng, H. & Suye, S. Reverse Reaction of Malic Enzyme for HCO_3^- Fixation into Pyruvic Acid to Synthesize L -Malic Acid with Enzymatic Coenzyme Regeneration. *Biosci. Biotechnol. Biochem.* **72**, 1278–1282 (2008).

174. Fukuda, W., Ismail, Y. S., Fukui, T., Atomi, H. & Imanaka, T. Characterization of an archaeal malic enzyme from the hyperthermophilic archaeon *Thermococcus kodakaraensis* KOD1. *Archaea* **1**, 293–301 (2005).

175. KEGG, MaeB sequence. Available at: https://www.genome.jp/dbget-bin/www_bget?eco:b2463.

176. Klingenberg, M. Nicotinamide-Adenine Dinucleotides (NAD, NADP, NADH, NADPH). in *Methods of Enzymatic Analysis* 2045–2072 (1974).

177. Chang, H. C., Chou, W.-Y. & Chang, G.-G. Effect of metal binding on the structural stability of pigeon liver malic enzyme. *J. Biol. Chem.* **277**, 4663–4671 (2002).

178. Armstrong, F. A. & Hirst, J. Reversibility and efficiency in electrocatalytic energy conversion and lessons from enzymes. *Proc. Natl. Acad. Sci.* **108**, 14049–14054 (2011).

179. Evans, R. M. *et al.* The value of enzymes in solar fuels research-efficient electrocatalysts through evolution. *Chem. Soc. Rev.* **48**, 2039–2052 (2019).

180. Frei, H. Photocatalytic fuel production. *Curr. Opin. Electrochem.* **2**, 128–135 (2017).

181. Jiang, C., Moniz, S. J. A., Wang, A., Zhang, T. & Tang, J. Photoelectrochemical devices for solar water splitting – materials and challenges. *Chem. Soc. Rev.* **46**, 4645–4660 (2017).

182. Walter, M. G. *et al.* Solar Water Splitting Cells. *Chem. Rev.* **110**, 6446–6473 (2010).

183. Miyauchi, M., Nukui, Y., Atarashi, D. & Sakai, E. Selective growth of *n*-type nanoparticles on *p*-type semiconductors for *Z*-scheme photocatalysis. *ACS Appl. Mater. Interfaces* **5**, 9770–9776 (2013).

184. Brown, K. A. *et al.* Photocatalytic Regeneration of Nicotinamide Cofactors by Quantum Dot-Enzyme Biohybrid Complexes. *ACS Catal.* **6**, 2201–2204 (2016).

185. Brown, K. A. *et al.* Photocatalytic Regeneration of Nicotinamide Cofactors by Quantum Dot-Enzyme Biohybrid Complexes. *ACS Catal.* **6**, 2201–2204 (2016).

186. Grätzel, M. The rise of highly efficient and stable perovskite solar cells. *Acc. Chem. Res.* **50**, 487–491 (2017).

187. Saliba, M. *et al.* Cesium-containing triple cation perovskite solar cells: Improved stability, reproducibility and high efficiency. *Energy Environ. Sci.* **9**, 1989–1997 (2016).

188. Bai, S. *et al.* Planar perovskite solar cells with long-term stability using ionic liquid additives. *Nature* **571**, 245–250 (2019).

189. Kim, J. H. *et al.* Wireless Solar Water Splitting Device with Robust Cobalt-

Catalyzed, Dual-Doped $BiVO_4$ Photoanode and Perovskite Solar Cell in Tandem: A Dual Absorber Artificial Leaf. *ACS Nano* **9**, 11820–11829 (2015).

190. Chen, X., Wang, M., Chen, J. & Shen, S. Electrophoretic deposition of nanostructured hematite photoanodes for solar hydrogen generation. *J. Mater. Res.* **31**, 1547–1553 (2016).
191. Annamalai, A. *et al.* Activation of hematite photoanodes for solar water splitting: Effect of FTO deformation. *J. Phys. Chem. C* **119**, 3810–3817 (2015).
192. Koura, N., Tsukamoto, T., Shoji, H. & Hotta, T. Preparation of various oxide films by an electrophoretic deposition method: A study of the mechanism. *Jpn. J. Appl. Phys.* **34**, 1643–1647 (1995).
193. Tilley, S. D., Cornuz, M., Sivula, K. & Grätzel, M. Light-induced water splitting with hematite: Improved nanostructure and iridium oxide catalysis. *Angew. Chemie Int. Ed.* **49**, 6405–6408 (2010).
194. Pihosh, Y. *et al.* Photocatalytic generation of hydrogen by core-shell WO3/BiVO4 nanorods with ultimate water splitting efficiency. *Sci. Rep.* **5**, 11141 (2015).
195. Kim, J. Y. *et al.* Single-crystalline, wormlike hematite photoanodes for efficient solar water splitting. *Sci. Rep.* **3**, 2681 (2013).
196. Patil, S. S. *et al.* One-pot in situ hydrothermal growth of $BiVO_4$/Ag/rGO hybrid architectures for solar water splitting and environmental remediation. *Sci. Rep.* **7**, 8404 (2017).
197. Fukuzumi, S., Lee, Y. M. & Nam, W. Solar-Driven Production of Hydrogen Peroxide from Water and Dioxygen. *Chem. - A Eur. J.* **24**, 5016–5031 (2018).
198. Berryottaway, P. Stability of vitamins in food in *The Technology of Vitamins of Food* (1993).
199. Sorigué, D. *et al.* An algal photoenzyme converts fatty acids to hydrocarbons. *Science* **357**, 903–907 (2017).
200. Lakavath, B. *et al.* Radical-based photoinactivation of fatty acid photodecarboxylases. *Anal. Biochem.* **600**, 113749 (2020).
201. Abe, R., Higashi, M. & Domen, K. Facile fabrication of an efficient oxynitride TaON photoanode for overall water splitting into H_2 and O_2 under visible light

irradiation. *J. Am. Chem. Soc.* **132**, 11828–11829 (2010).

202. Pei, L. *et al.* Nanostructured TaON/Ta_3N_5 as a highly efficient type-II heterojunction photoanode for photoelectrochemical water splitting. *Dalt. Trans.* **47**, 8949–8955 (2018).
203. Higashi, M., Tomita, O. & Abe, R. Porous TaON Photoanodes Loaded with Cobalt-Based Cocatalysts for Efficient and Stable Water Oxidation Under Visible Light. *Top. Catal.* **59**, 740–749 (2016).
204. Ye, S., Wang, R., Wu, M.-Z. & Yuan, Y.-P. A review on g-C_3N_4 for photocatalytic water splitting and CO_2 reduction. *Appl. Surf. Sci.* **358**, 15–27 (2015).
205. Zhang, Y., Liu, J., Wu, G. & Chen, W. Porous graphitic carbon nitride synthesized via direct polymerization of urea for efficient sunlight-driven photocatalytic hydrogen production. *Nanoscale* **4**, 5300–5303 (2012).
206. Sherman, B. D., Sheridan, M. V., Dares, C. J. & Meyer, T. J. Two Electrode Collector-Generator Method for the Detection of Electrochemically or Photoelectrochemically Produced O_2. *Anal. Chem.* **88**, 7076–7082 (2016).
207. Walter, M. G. *et al.* Solar water splitting cells. *Chem. Rev.* **110**, 6446–6473 (2010).
208. Yang, Y. *et al.* Photochemical Charge Separation at Particle Interfaces: The *n*-$BiVO_4$-*p*-Silicon System. *ACS Appl. Mater. Interfaces* **7**, 5959–5964 (2015).
209. Tachibana, Y., Vayssieres, L. & Durrant, J. R. Artificial photosynthesis for solar water-splitting. *Nat. Photonics* **6**, 511–518 (2012).
210. Liang, A. D., Serrano-Plana, J., Peterson, R. L. & Ward, T. R. Artificial Metalloenzymes Based on the Biotin-Streptavidin Technology: Enzymatic Cascades and Directed Evolution. *Acc. Chem. Res.* **52**, 585–595 (2019).
211. Kao, H. P., Abney, J. R. & Verkman, A. S. Determinants of the Translational Mobility of a Small Solute in Cell Cytoplasm. *J. Cell Biol.* **120**, 175–184 (1993).
212. Sweetlove, L. J. & Fernie, A. R. The role of dynamic enzyme assemblies and substrate channelling in metabolic regulation. *Nat. Commun.* **9**, 2136 (2018).
213. An, S., Kumar, R., Sheets, E. D. & Benkovic, S. J. Reversible

compartmentalization of de novo purine biosynthetic complexes in living cells. *Science* **320**, 103–106 (2008).

214. Hwang, E. T. & Lee, S. Multienzymatic Cascade Reactions via Enzyme Complex by Immobilization. *ACS Catal.* **9**, 4402–4425 (2019).
215. Fryszkowska, A. & Devine, P. N. Biocatalysis in drug discovery and development. *Curr. Opin. Chem. Biol.* **55**, 151–160 (2020).
216. Faber, K., Fessner, W.-D. & Turner, N. J. Biocatalysis: Ready to Master Increasing Complexity. *Adv. Synth. Catal.* **361**, 2373–2376 (2019).
217. Renata, H., Wang, Z. J. & Arnold, F. H. Expanding the enzyme universe: Accessing non-natural reactions by mechanism-guided directed evolution. *Angew. Chemie Int. Ed.* **54**, 3351–3367 (2015).
218. Arnold, F. H. Directed Evolution: Bringing New Chemistry to Life. *Angew. Chemie Int. Ed.* **57**, 4143–4148 (2018).
219. Huffman, M. A. *et al.* Design of an in vitro biocatalytic cascade for the manufacture of islatravir. *Science* **366**, 1255–1259 (2019).
220. Rudroff, F. Whole-cell based synthetic enzyme cascades—light and shadow of a promising technology. *Curr. Opin. Chem. Biol.* **49**, 84–90 (2019).
221. Sheldon, R. A. & Brady, D. The limits to biocatalysis: Pushing the envelope. *Chem. Commun.* **54**, 6088–6104 (2018).
222. Parmeggiani, F. *et al.* One-Pot Biocatalytic Synthesis of Substituted D-Tryptophans from Indoles Enabled by an Engineered Aminotransferase. *ACS Catal.* **9**, 3482–3486 (2019).
223. Klumbys, E., Zebec, Z., Weise, N. J., Turner, N. J. & Scrutton, N. S. Bio-derived production of cinnamyl alcohol: Via a three step biocatalytic cascade and metabolic engineering. *Green Chem.* **20**, 658–663 (2018).
224. Good, M. C., Zalatan, J. G. & Lim, W. A. Scaffold proteins: Hubs for controlling the flow of cellular information. *Science* **332**, 680–686 (2011).
225. Vonck, J. & Van Bruggen, E. F. J. Architecture of peroxisomal alcohol oxidase crystals from the methylotrophic yeast Hansenula polymorpha as deduced by electron microscopy. *J. Bacteriol.* **174**, 5391–5399 (1992).
226. Good, M., Tang, G., Singleton, J., Remenyi, A. & Lim, W. A. Scaffold-Assisted Catalysis: A Novel Domain In the Ste5 Scaffold Protein is Required

to Unlock the MAPK Fus3 for Phosphorylation by the MAPKK Ste7. *Cell* **136**, 1085–1097 (2009).

227. Vázquez-González, M., Wang, C. & Willner, I. Biocatalytic cascades operating on macromolecular scaffolds and in confined environments. *Nat. Catal.* **3**, 256–273 (2020).
228. Chen, W. H., Vázquez-González, M., Zoabi, A., Abu-Reziq, R. & Willner, I. Biocatalytic cascades driven by enzymes encapsulated in metal–organic framework nanoparticles. *Nat. Catal.* **1**, 689–695 (2018).
229. Wang, X. *et al.* Bioinspired approach to multienzyme cascade system construction for efficient carbon dioxide reduction. *ACS Catal.* **4**, 962–972 (2014).
230. Fu, J. *et al.* Multi-enzyme complexes on DNA scaffolds capable of substrate channelling with an artificial swinging arm. *Nat. Nanotechnol.* **9**, 531–536 (2014).
231. Ke, G. *et al.* Directional Regulation of Enzyme Pathways through the Control of Substrate Channeling on a DNA Origami Scaffold. *Angew. Chemie Int. Ed.* **55**, 7483–7486 (2016).
232. Chen, Y. *et al.* A Synthetic Light-Driven Substrate Channeling System for Precise Regulation of Enzyme Cascade Activity Based on DNA Origami. *J. Am. Chem. Soc.* **140**, 8990–8996 (2018).
233. Lim, S., Kim, J., Kim, Y., Xu, D. & Clark, D. S. CRISPR/Cas-directed programmable assembly of multi-enzyme complexes. *Chem. Commun.* **56**, 4950–4953 (2020).
234. Nguyen, T. M., Nakata, E., Saimura, M., Dinh, H. & Morii, T. Design of Modular Protein Tags for Orthogonal Covalent Bond Formation at Specific DNA Sequences. *J. Am. Chem. Soc.* **139**, 8487–8496 (2017).
235. Zakeri, B. *et al.* Peptide tag forming a rapid covalent bond to a protein, through engineering a bacterial adhesin. *Proc. Natl. Acad. Sci.* **109**, E690–E697 (2012).
236. Al-Shameri, A. *et al.* Powering artificial enzymatic cascades with electrical energy Ammar. *Chem. Eng. Sci.* **59**, 10929–10933 (2020).
237. Weaver, T. M., Levitt, D. G., Donnelly, M. I., Stevens, P. P. W. & Banaszak,

L. J. The multisubunit active site of fumarase c from escherichia coli. *Nat. Struct. Biol.* **2**, 654–662 (1995).

238. Karsten, W. E., Gates, R. B. & Viola, R. E. Kinetic Studies of L-Aspartase from *Escherichia coli*: Substrate Activation. *Biochemistry* **25**, 1299–1303 (1986).
239. Ellfolk, N. Studies on Aspartase. II. On the Chemical Nature of Aspartase. *Acta Chem. Scand.* **7**, 1155–1163 (1953).
240. Falzone, C. J., Karsten, W. E., Conley, J. D. & Viola, R. E. L-Aspartase from *Escherichia coli*: Substrate Specificity and Role of Divalent Metal Ions. *Biochemistry* **27**, 9089–9093 (1988).
241. Morello, G., Megarity, C. F. & Armstrong, F. A. The power of electrified nanoconfinement for energising, controlling and observing long enzyme cascades. *Nat. Commun.* **12**, 340 (2021).
242. Bard, A. J. & Faulkner, L. R. *Electrochemical Methods*. (John Wiley & Sons, 2001).
243. Ida, N. & Tokushige, M. L-Aspartate-Induced Activation of Aspartase. *J. Biochem.* **98**, 35–39 (1985).
244. Idan, O. & Hess, H. Origins of activity enhancement in enzyme cascades on scaffolds. *ACS Nano* **7**, 8658–8665 (2013).
245. Zhao, X. *et al.* Substrate-driven chemotactic assembly in an enzyme cascade. *Nat. Chem.* **10**, 311–317 (2018).
246. Ma, L. *et al.* Induced Rebuilding of Aspartase Conformation. *Ann. N. Y. Acad. Sci.* **672**, 60–65 (1992).
247. Zhang, Y., Tsitkov, S. & Hess, H. Proximity does not contribute to activity enhancement in the glucose oxidase-horseradish peroxidase cascade. *Nat. Commun.* **7**, 13982 (2016).
248. Zhang, Y., Wang, Q. & Hess, H. Increasing Enzyme Cascade Throughput by pH-Engineering the Microenvironment of Individual Enzymes. *ACS Catal.* **7**, 2047–2051 (2017).
249. Heider, J., Ma, K. & Adams, M. W. W. Purification, characterization, and metabolic function of tungsten- containing aldehyde ferredoxin oxidoreductase from the hyperthermophilic and proteolytic archaeon

Thermococcus strain ES-1. *J. Bacteriol.* **177**, 4757–4764 (1995).

250. Barnes, E. O., Chen, X., Li, P. & Compton, R. G. Voltammetry at porous electrodes: A theoretical study. *J. Electroanal. Chem.* **720**–**721**, 92–100 (2014).
251. Kätelhön, E. & Compton, R. G. Unscrambling illusionary catalysis in three-dimensional particle-modified electrodes: Reversible reactions at conducting particles. *Appl. Mater. Today* **18**, 100514 (2020).
252. Hemker, H. C. & Hemker, P. W. The kinetics of enzyme cascade systems. General kinetics of enzyme cascades. *Proc. R. Soc. London. Ser. B. Biol. Sci.* **173**, 411–420 (1969).
253. Sellés Vidal, L., Kelly, C. L., Mordaka, P. M. & Heap, J. T. Review of NAD(P)H-dependent oxidoreductases: Properties, engineering and application. *Biochim. Biophys. Acta - Proteins Proteomics* **1866**, 327–347 (2018).
254. Truppo, M. D. Biocatalysis in the Pharmaceutical Industry: The Need for Speed. *ACS Med. Chem. Lett.* **8**, 476–480 (2017).
255. Bornscheuer, U. T. *et al.* Engineering the third wave of biocatalysis. *Nature* **485**, 185–194 (2012).
256. Savile, C. K. *et al.* Biocatalytic Asymmetric Synthesis of Sitagliptin Manufacture. *Science* **329**, 305–310 (2010).
257. Cadwell, R. C. & Joyce, G. F. Manual Supplement III1 | 11 Mutagenic PCR. *Genome Res.* **3**, S136–S140 (1994).
258. Stemmer, W. P. C. Rapid evolution of a protein in vitro by DNA shuffling. *Nature* **370**, 389–391 (1994).
259. Gibson, D. G. *et al.* Creation of a bacterial cell controlled by a chemically synthesized genome. *Science* **329**, 52–56 (2010).
260. Goto, H. *et al.* Microfluidic screening system based on boron-doped diamond electrodes and dielectrophoretic sorting for directed evolution of NAD(P)-dependent oxidoreductases. *Lab Chip* **20**, 852–861 (2020).
261. Tawfik, D. S. & Griffiths, A. D. Man-made cell-like compartments for molecular evolution. *Nat. Biotechnol.* **16**, 652–656 (1998).
262. Badran, A. H. & Liu, D. R. In vivo continuous directed evolution. *Curr. Opin.*

Chem. Biol. **24**, 1–10 (2015).

263. Boder, E. T. & Wittrup, K. D. Yeast surface display for screening combinatorial polypeptide libraries. *Nat. Biotechnol.* **15**, 553–557 (1997).
264. Martínez, A. T. *et al.* Oxidoreductases on their way to industrial biotransformations. *Biotechnol. Adv.* **35**, 815–831 (2017).
265. Oyobiki, R. *et al.* Toward high-throughput screening of NAD(P)-dependent oxidoreductases using boron-doped diamond microelectrodes and microfluidic devices. *Anal. Chem.* **86**, 9570–9575 (2014).
266. Mayer, K. M. & Arnold, F. H. A colorimetric Assay to Quantify Dehydrogenase Activity in Crude Cell Lysates. *J. Biomol. Screen.* **7**, 135–140 (2002).
267. Johannes, T. W., Woodyer, R. D. & Zhao, H. Directed evolution of a thermostable phosphite dehydrogenase for NAD(P)H regeneration. *Appl. Environ. Microbiol.* **71**, 5728–5734 (2005).
268. Gielen, F. *et al.* Ultrahigh-throughput-directed enzyme evolution by absorbance-activated droplet sorting (AADS). *Proc. Natl. Acad. Sci.* **113**, E7383–E7389 (2016).
269. Bähr, S. *et al.* Selective Enzymatic Oxidation of Silanes to Silanols. *Angew. Chemie Int. Ed.* (2020).
270. Chen, K. & Arnold, F. H. Engineering Cytochrome P450s for Enantioselective Cyclopropenation of Internal Alkynes. *J. Am. Chem. Soc.* **142**, 6891–6895 (2020).
271. Brandenberg, O. F., Chen, K. & Arnold, F. H. Directed Evolution of a Cytochrome P450 Carbene Transferase for Selective Functionalization of Cyclic Compounds. *J. Am. Chem. Soc.* **141**, 8989–8995 (2019).
272. Kan, S. B. J., Lewis, R. D., Chen, K. & Arnold, F. H. Directed evolution of cytochrome c for carbon-silicon bond formation: Bringing silicon to life. *Science* **354**, 1048–1051 (2016).
273. Alissandratos, A. In vitro multi-enzymatic cascades using recombinant lysates of *E. coli*: an emerging biocatalysis platform. *Biophys. Rev.* **12**, 175–182 (2020).
274. ThermoFischer. NanoOrange™ Protein Quantitation Kit. Available at:

https://www.thermofisher.com/order/catalog/product/N6666#/N6666.

275. Bradford, M. M. A Rapid and Sensitive Method for the Quantitation of Microgram Quantities of Protein Utilizing the Principle of Protein-Dye Binding. *Anal. Biochem.* 248–254 (1976).

276. Lim, S., Kim, J., Kim, Y., Xu, D. & Clark, D. S. CRISPR/Cas-directed programmable assembly of multi-enzyme complexes. *Chem. Commun.* **56**, 4950–4953 (2020).

277. Luo, Y. *et al.* Enhancing the biocatalytic manufacture of the key intermediate of atorvastatin by focused directed evolution of halohydrin dehalogenase. *Sci. Rep.* **7**, 42064 (2017).

278. Strohmeier, G. A., Schwarz, A., Andexer, J. N. & Winkler, M. Co-factor demand and regeneration in the enzymatic one-step reduction of carboxylates to aldehydes in cell-free systems. *J. Biotechnol.* **307**, 202–207 (2020).

279. Winkler, M. Carboxylic acid reductase enzymes (CARs). *Curr. Opin. Chem. Biol.* **43**, 23–29 (2018).

280. Gahloth, D. *et al.* Structures of carboxylic acid reductase reveal domain dynamics underlying catalysis. *Nat. Chem. Biol.* **13**, 975–981 (2017).

281. France, S. P. *et al.* One-Pot Cascade Synthesis of Mono- and Disubstituted Piperidines and Pyrrolidines using Carboxylic Acid Reductase (CAR), ω-Transaminase (ω-TA), and Imine Reductase (IRED) Biocatalysts. *ACS Catal.* **6**, 3753–3759 (2016).

282. Yuan, B. *et al.* A plasma metabolite panel as biomarkers for early primary breast cancer detection. *Int. J. Cancer* **144**, 2833–2842 (2019).

283. Hashim, N. A. A., Ab-Rahim, S., Suddin, L. S., Saman, M. S. A. & Mazlan, M. Global serum metabolomics profiling of colorectal cancer. *Mol. Clin. Oncol.* **11**, 3–14 (2019).

284. Wulff, P., Thomas, C., Sargent, F. & Armstrong, F. A. How the oxygen tolerance of a [NiFe]-hydrogenase depends on quaternary structure. *J. Biol. Inorg. Chem.* **21**, 121–134 (2016).

285. Armstrong, F. A. *et al.* Guiding Principles of Hydrogenase Catalysis Instigated and Clarified by Protein Film Electrochemistry. *Acc. Chem. Res.*

49, 884–892 (2016).

286. Léger, C. *et al.* Enzyme electrokinetics: Using protein film voltammetry to investigate redox enzymes and their mechanisms. *Biochemistry* **42**, 8653–8662 (2003).
287. Evans, R. M. *et al.* Mechanistic Exploitation of a Self-Repairing, Blocked Proton Transfer Pathway in an O_2-Tolerant [NiFe]-Hydrogenase. *J. Am. Chem. Soc.* **140**, 10208–10220 (2018).
288. Evans, R. M. *et al.* Mechanistic Exploitation of a Self-Repairing, Blocked Proton Transfer Pathway in an O_2-Tolerant [NiFe]-Hydrogenase. *J. Am. Chem. Soc.* **140**, 10208–10220 (2018).
289. Monk, P. M. S. *Fundamentals of Electroanalytical Chemistry*. (John Wiley & Sons, 2001).
290. Lin, Y. *et al.* Growth of *p*-Type Fe_2O_3 by Atomic Layer Deposition and Its Utilization for Improved Solar Water Splitting. *J. Am. Chem. Soc.* **134**, 5508–5511 (2012).
291. Weaver, T. M., Levitt, D. G., Donnelly, M. I., Stevens, P. P. W. & Banaszak, L. J. The multisubunit active site of fumarase c from *escherichia coli*. *Nat. Struct. Biol.* **2**, 654–662 (1995).
292. Wei, M. *et al.* Highly efficient dye-sensitized solar cells composed of mesoporous titanium dioxide. *J. Mater. Chem.* **16**, 1287–1293 (2006).
293. Weaver, T. & Banaszak, L. Crystallographic studies of the catalytic and a second site in fumarase C from *Escherichia coli*. *Biochemistry* **35**, 13955–13965 (1996).